BIOMECHANICAL ANALYSIS OF FEMORAL FRACTURE FIXATION USING THE EXPERT ADOLESCENT LATERAL FEMORAL NAIL SYSTEM

by

Darshan. Srishail. Angadi

A thesis submitted to the University of Birmingham
for the degree of DOCTOR OF MEDICINE

School of Clinical and Experimental Medicine
College of Medical and Dental Sciences
University of Birmingham

Abstract

Femoral fracture in adolescents is a severe injury. Recent studies of intramedullary nail fixation with rigid titanium alloy helical nail viz. Expert adolescent lateral femoral nail (ALFN) have reported good results. However, there is no *in vitro* biomechanical data available on this nail in the literature.

Experimental testing and finite element analysis (FEA) were used to establish the stiffness parameters of small composite femurs with simulated fractures stabilised using ALFN. In comparison to intact femur, construct stiffness ranged from maximum (114%) to minimum (20%) for healed fracture and segmental fracture, respectively. Simulation testing in SolidWorks™ was performed with validated FEA model to evaluate the effect of clinical and implant factors. Maximum predicted stress in the distal interlocking screw remained in an acceptable range (160.25 - 188.51 MPa) irrespective of the level of femoral shaft fracture with a relative decrease in stress values as the fracture callus healed over a 16 week period. The relative angle between the ALFN and proximal interlocking screw and implant material were two significant factors influencing stress at the interlocking screw and nail interface.

In conclusion, a rigid helical titanium alloy femoral intramedullary nail can perform satisfactorily under physiological loading conditions experienced in the perioperative period.

Dedication

I dedicate this work to my family. I express my gratitude to my parents - Dr S. F. Angadi and Mrs R. S. Angadi for their unwavering support in my life and work. I thank my wife, Priyanka for her love, patience and help throughout the course of this work. Finally, my daughter, Vedhika who has been a source of joy and happiness.

Acknowledgements

I am grateful to my supervisors Prof. T.G. Barrett, Prof. D.E.T. Shepherd and Mr. R. Vadivelu for their guidance, support and encouragement during the course of this research work.

I thank Mr C Hingley and team for their help with the experimental study.

I would like to thank Mr M.J. Porteous for corresponding with the implant manufacturer and giving me flexibility with my clinical work enabling me to complete this research.

I am grateful to the AO Foundation, UK for the grant towards this research project.

Finally, I would like to thank the following organisations:

- DePuy Synthes for providing the intramedullary nails to conduct the study.
- MTS Systems for providing technical help and support with the testing machines.
- Heraeus Medical for providing the PMMA to fabricate supports and molds.

Table of Contents

List of Figures

List of Tables

List of Terminology

EXP	Experimental testing
FEA	Finite element analysis
TTJ	Torsion test jig
FAC	Femur and adolescent lateral femoral nail construct
Ax	Axial
Be	Four point bending
Ir	Internal rotation (torsion)
Er	External rotation (torsion)
k	Stiffness
Int	Intact femur group
Tra	Transverse fracture group
Com	Comminuted fracture group
Seg	Segmental defect fracture group

1 INTRODUCTION

1.1 Background

Femoral fractures in children have an incidence of 20 - 33 per 100,000 a year (1). The common modes of injury in adolescents include road traffic collisions and falls from height (2). Management of femoral fractures in adolescents poses unique challenges due to the growth plate and relatively small size of femur (3). Treatment options of these complex injuries have evolved over the last few decades (4, 5). Flexible intramedullary nails used initially had poor outcome in heavier, older children with unstable fractures due to loss of length and rotation at the fracture site (6). Rigid intramedullary interlocking nails help overcome the limitations of the flexible nails and have been well described in the current literature (7-9). Numerous types of rigid intramedullary nails have been described in the literature to fix adolescent femoral fractures (7, 10-14).

The concept of helical intramedullary implants which allow a lateral entry portal was first described in 2002 by Fernandez Dell'Oca (15). The helical design of the nail enables the surgeon to use an entry point on the outer surface of the greater trochanter thereby minimising the risk of damage to the vascularity of the femoral head and/or the superior gluteal nerve (15). Furthermore the constant radius of curvature in the helical nail would enable an uniform bone-to-nail fit (15). This paper briefly mentions a limited case series of 5 children aged between 13-15 years with femoral fracture fixation using a solid titanium femoral nail (UFN, Synthes®) modified into a helical shape. However, further information on the functional outcome or complications are unavailable. Interestingly, biomechanical and anatomical studies have also noted a design mismatch between femur and the commonly available rigid intramedullary commercial nails (15-18). Rigid intramedullary fixation with helical nail design viz. Expert adolescent lateral femoral nail (ALFN) has been suggested as a treatment option due to the perceived advantages of stable fixation and avoiding iatrogenic damage to growth plate (19) (Figure 1-1). However, there are no biomechanical studies on this design of nail in the literature. Hence the current study.

Figure 1-1 Paediatric femur with Adolescent Lateral Femoral Nail (ALFN) *in-situ* (20). Illustration representative of fixation mode used for shaft fractures (highlighted in blue)

1.2 Current evidence

1.2.1 Clinical studies

Numerous types of rigid intramedullary nails have been described to treat adolescent femoral fractures (8, 14, 21-23). Due to the lack of consistency on reported outcomes comparison of various rigid nails is difficult and subject to observer variability. Based on their initial experience, Flynn and colleagues proposed criteria to grade the clinical outcome following fixation of femoral fractures (24). They classified a major complication and/or lasting morbidity, limb length discrepancy > 2.0 cm and malunion > 10° as a poor result. Similar outcome criteria for rigid intramedullary nail fixation are not clearly agreed in the literature (3-5). Initial papers (7, 8, 25) on this topic reported on the radiographic parameters described by Edgren (26). On the other hand some studies have not reported on the radiological outcomes (12, 27). Therefore, to ensure objective comparison of different nails the reported clinical outcomes from the various studies were analysed based on the major complications (avascular necrosis, limb length discrepancy >2.0 cm, malunion > 10°) and the Oxford Centre for Evidence-Based Medicine 2011 levels of evidence (28).

In order to collate and evaluate the available evidence for management of diaphyseal femoral fractures in adolescents using rigid intramedullary nails an English medical literature search was undertaken using the NHS healthcare database website (http://www.library.nhs.uk/hdas). The databases searched were Medline, CINAHL, Embase and the Cochrane library.

The Medline search was performed using boolean statements and the wildcard symbol (*). The search criteria: "(femur* OR femoral*) AND (shaft* OR diaph*) AND fracture* AND (child* OR pediat* OR paediat* OR adolescent*) AND (intramedullary OR rod OR nail)". An Embase search was performed using boolean statements and the wildcard symbol ($). The search criteria: "(femur$ OR femoral$) AND (shaft$ OR diaph$) AND fracture$ AND (child$ OR pediat$ OR paediat$ OR adolescent$) AND (intramedullary OR rod OR nail)". CINAHL database was searched using the following criteria: "(femur* OR femoral*) AND (shaft* OR diaph*) AND fracture* AND (child* OR pediat* OR paediat* OR adolescent*) AND (intramedullary OR rod OR nail)". A review of the Cochrane database for relevant articles was performed.

The above database search and adjunctive bibliography search returned 1849 articles of which 51 relevant articles were identified. Of the 51 articles, 23 were duplicates which left a total of 28 articles to be reviewed (as shown in Table 1-1).

Table 1-1 Results of literature search

	Database				**Total**
	Medline	**Embase**	**CINAHL**	**Cochrane**	
Search results	794	787	240	28	1849
Relevant articles	23	24	3	0	51
Duplicates					-23
Articles reviewed					28

A summary of the various studies on rigid nails identified from the literature search is presented below (Table 1-2).

Table 1-2 List of relevant clinical studies in literature

(MC - Major complications, LOE - Level of evidence, AO - Arbeitsgemeinschaft für Osteosynthesefragen, S&N-Smith and Nephew, R-T – Russell–Taylor, G-K – Grosse & Kempf)

Author	Type of Nail	Number of Patients	Age range (years)	Average Weight (Kg)	MC reported Y / N	LOE
Reynolds *et al*. (2012) (29)	Adolescent Lateral Femoral	15	10-16	59.6	N	2b
Park *et al*. (2012) (30)	AO Humeral	23	8.2-16.1	49.4	N	2b
Park *et al*. (2012) (31)	Unreamed Tibial & Sirus femoral	21	11-17.2	51.2	N	1b
Garner *et al*. (2011) (32)	N/A	15	14.3-16.4	60.4	Y	2b
Ramseier *et al*. (2010) (33)	N/A	37	11-17.6	55.2	Y	2b
Keeler *et al*. (2009) (23)	S&N Humeral	78	8.2-18.4	70	N	2b
Jencikova-Celerin *et al*. (2008) (34)	Biomet Interlocking	58	9.9-14.1	47.4	N	2b
Mehlman *et al*. (2007) (35)	Synthes locked tibial	6	9-15	69.1	N	4
Kanellopoulos *et al*. (2006) (22)	R-T & Targon	20	11-16	N/A	N	2b
Gordon *et al*. (2004) (14)	S&N Humeral	15	8.2-17.1	N/A	N	2b

Table 1-2 continued						
Letts *et al*. (2002) (36)	AO / G-K / R-T	54	11.4-17.1	60	Y	2b
Tortolani *et al*. (2001) (37)	R-T adult tibial	9	11-15	N/A	N	2b
Townsend *et al*. (2000) (27)	R-T / Delta II	34	10.2-17.6	N/A	N	2b
Momberger *et al*. (2000) (38)	Zimmer Titanium / R-T / Steel	48	10-16	N/A	N	2b
Stans *et al*. (1999) (11)	N/A	13	11.1-16.2	50.2	Y	2b
Buford *et al*. (1998) (12)	Solid Titanium	54	6-15	N/A	Y	1b
Skak *et al*. (1996) (39)	Kűntscher / Street-Hansen /AO	25	8-17	N/A	N	2b
Gregory *et al*. (1995) (21)	Kűntscher / R-T	10	11.4-16.1	N/A	N	2b
Gonzalez-Herranz *et al*. (1995) (13)	Kűntscher	22	3-14	N/A	Y	2b
Beaty *et al*. (1994) (40)	R-T	30	10-15	N/A	Y	2b
Galpin *et al*. (1994) (8)	G-K / AO	22	11-16	N/A	Y	2b
Maruenda-Paulino *et al*. (1993) (25)	Kűntscher	29	7-16	N/A	Y	2b
Timmerman *et al*. (1993) (41)	Kűntscher / AO / G-K	22	10-14	N/A	Y	2b

Table 1-2 continued

Reeves *et al*. (1990) (42)	Kűntscher / AO	33	11-16.8	N/A	N	2b
Herndon *et al*. (1989) (9)	Kűntscher / Interlocking	16	11-16	N/A	N	2b
Ziv *et al*. (1984) (7)	Kűntscher	8	6-12	N/A	N	2b
Valdserri *et al*. (1983) (10)	Kűntscher	17	6-12	N/A	N	4
Kirby *et al*. (1981) (43)	Kűntscher	13	10.8-15.6	N/A	N	2b

The Küntscher nail has been used for fixation of femoral fractures in children (7, 10, 13, 25) but resulted in growth disturbance (7, 13). This prompted some authors to question the use of the Küntscher nail in children (13). Numerous biomechanical studies (44-46) exist in the literature regarding this implant but none of them have focused on femoral fractures in children. Furthermore biomechanical testing indicated that the Küntscher nail did not provide adequate stability for comminuted fractures in torsion and compression (45). Hence the use of the Küntscher nail was largely abandoned in favour of new nail designs.

With the introduction of the interlocking technique Grosse-Kempf nail (8, 36, 41), Russell-Taylor nail and its delta version (with triangular section, thicker wall and thinner diameter) were used in adolescents (22, 27, 40). However, their use was an extension of indication from the adult variety with a limited understanding of the intricate vascularity of proximal femoral epiphysis in adolescents. This resulted in the growth disturbances noted in patients of these series (22, 40). The current literature has descriptions of different rigid intramedullary nails like Street-Hanson (39), tibial nails (31, 37) and flexible interlocking intramedullary nail (FIIN) (34). However, they represent a limited series as these devices have not been reported from other centres.

Avascular necrosis or death of femoral head due to lack of blood supply (AVN), limb length discrepancy (>2 cm) and malunion (>10°) are significant complications that have been associated with intramedullary nail fixation of adolescent femoral fractures (3, 5, 13, 47, 48). The early nail designs (Küntscher / Grosse-Kempf) were noted to have high rate of limb length discrepancy (5-9%). It is interesting that AVN was not reported in the earlier series (7, 10, 43). However, this may represent a combination of limited understanding of this complication and the lack of widespread availability of investigations like magnetic resonance imaging (MRI) at the time. The reporting of subclinical AVN in the later series (12, 22) using MRI is indicative of this development. Russell-Taylor nail results represent a good improvement with a lower incidence of limb length discrepancy (2.8%). The multiplanar nails have by and large been reported not to be associated with such complications. Two studies (11, 33) have reported on AVN and limb length discrepancy but the lack of detail regarding the type or design of nail limits their interpretation.

Earlier studies with nails requiring a pyriformis entry point had patients with complications like avascular necrosis (12), coxa valga and growth arrest of the greater trochanter (13). Subsequent studies of nail designs with a lateral entry point over the greater trochanter report no such complication (14, 30). Hence the entry point of the intramedullary nail has been a subject of much debate due to the potential impact on the vascularity of the femoral head (3) and malalignment or iatrogenic fractures (49). The entry point is largely dictated by the type / design of the nail (15). Recent nails (14, 23, 29) have a multiplanar / helical design to avoid the piriformis entry point which has been shown in a recent systematic review to be associated with a higher rate of avascular necrosis (50).

Some authors advocate rigid intramedullary fixation of femoral fractures in children ≥9 years (51). This is largely due to the increased complication rate reported following the use of flexible nails in this subset of patients (52). The recent consensus on age limit for rigid intramedullary fixation is in children of ≥11 years (3, 5). Adolescents ≥49 kg have poor outcome following other modalities of treatment for femoral fractures (5, 6). Hence these heavier adolescents are better managed with a rigid, locked intramedullary nail (3, 30, 51). Excessive weight has also been shown to be an independent predictor of increased postoperative complications (6).

The findings from the above study have been published (53). The key findings of the systematic literature review are listed below:

- Clinical use of rigid multiplanar nail design has increased in the past decade especially amongst heavier adolescents (5)
- Postoperative rehabilitation is facilitated as the rigid nails permit earlier weight bearing (expert adolescent nail 4.1 weeks vs. flexible nails 9.4 weeks) (29)
- No evidence of growth disturbance associated with use of lateral entry point during rigid intramedullary nail fixation (50)

No biomechanical study is available in the current literature on the adolescent lateral femoral nail.

1.2.2 Biomechanical studies

Several biomechanical studies to evaluate different femoral fracture fixation methods in the paediatric population have been reported in the current literature. As described in the previous section a database search was performed using NHS healthcare database website (http://www.library.nhs.uk/hdas). The databases searched were Medline, CINAHL and Embase.

In total the database search returned 1167 articles of which 23 relevant articles were identified. Adjunctive bibliography search from the above articles identified one additional article. A brief survey of the relevant studies is presented in the table below

Table 1-3 List of biomechanical studies using a paediatric femur model

(T-transverse, C-comminuted, LO-long oblique, SD-segmental defect, S-spiral, O-oblique, B-butterfly, OW-opening wedge, CW-closing wedge, LCP-locking compression plate)

Author	**Biomechanical model of femur**	**Specimen dimensions (mm)**		**Type of fracture or osteotomy**	**Implants tested**
		Length	**Canal diameter**		
Dogan *et al*. (2013) (54)	Sawbone®	N/R	N/R	T / C	Titanium flexible nail
Porter *et al*. (2012) (55)	Sawbone® (Third generation)	445	10.0	LO	Titanium flexible nail LCP
Volpon *et al*. (2012) (56)	Sawbone® (Third generation)	350	9.5	SD	Titanium flexible nail

Table 1-3 continued					
Kaiser *et al*. (2012) (57)	Sawbone® (Fourth generation)	450	10.0	S	Stainless steel flexible nail
Liao *et al*. (2012)	Cadaver	N/R	N/R	O	Anatomic plate Recon plate
Doser *et al*. (2011) (58)	Sawbone® (Fourth generation)	455	13.0	T	Titanium flexible nail
Kaiser *et al*. (2011) (59)	Sawbone® (Fourth generation)	450	10.0	S	Titanium flexible nail
Kaiser *et al*. (2011) (60)	Sawbone® (Fourth generation)	450	10.0	S	Titanium and Stainless steel flexible nails
Sagan *et al*. (2010) (61)	Sawbone® (Third generation)	N/R	13.0	T	Titanium flexible nail
Abosala *et al*. (2010) (62)	Sawbone® (Third generation)	380	12.0	SD	Titanium flexible nail
Li *et al*. (2008) (63)	Sawbone®	350	9.5	T	Titanium flexible nail
Perez A *et al*. (2008) (64)	Sawbone® (Third generation)	420	9.0	T	Titanium and Stainless steel flexible nails
Mahar *et al*. (2007) (65)	Sawbone®	380	9.0	C	Titanium flexible nail
Goodwin *et al*. (2007) (66)	Sawbone®	N/R	9.0	C	Titanium flexible nail
Mehlman *et al*. (2006) (67)	Sawbone®	455	10.0	T	Titanium flexible nail

Table 1-3 continued					
Mani *et al*. (2006) (68)	Sawbone®	450	9.0	T / C	Titanium and Stainless steel flexible nails External fixator
Crist *et al*. (2006) (69)	Sawbone®	N/R	16.0	T / C	Titanium flexible nail
Green *et al*. (2005) (70)	Sawbone® (Second generation)	280	8.0	T	Titanium flexible nail
Mahar *et al*. (2004) (71)	Sawbone®	380	9.0	T / C	Titanium and Stainless steel flexible nail
Gwyn *et al*. (2004) (72)	Sawbone®	N/R	10.0	T / C / S / O / B	Titanium flexible nail
Fricka *et al*. (2004) (73)	Sawbone®	380	9.0	T / C	Titanium flexible nail
Kiely *et al*. (2002) (74)	Tufnol	280	10.0	N/R	Titanium flexible nail
Lee *et al*. (2001) (75)	Sawbone®	380	9.0	T / C	Ender nail
Greis *et al*. (1993) (76)	Sawbone®	N/R	N/R	OW / CW	Stainless steel plates (90° Infant blade plate, 120° Angled plate)

The majority of the biomechanical studies of paediatric femur have evaluated different aspects of flexible intramedullary nail fixation. However, no biomechanical study is available in the current literature addressing rigid intramedullary nail fixation using the adolescent lateral femoral nail.

1.2.3 Finite element analysis (FEA) studies

There is paucity in the current literature in terms of FEA studies using a paediatric femur model. In contrast to the adult femur FEA model, to date only two studies (77, 78) have described evaluation of intramedullary nails using a paediatric femur FEA model. Furthermore the standardised FEA model of sawbone (available as an open source download - http://www.biomedtown.org) is based on the geometry of an adult femur (79).

In their study Perez *et al*. (77) used the bone model available for download from the aforementioned source. The femur FEA model measured 420 mm in length with a canal diameter of 9 mm. They evaluated the influence of elastic modulus of two different materials (stainless steel and titanium) on the biomechanical stability of a midshaft transverse fracture having two 3.5 mm flexible nails in a retrograde ‘C’ pattern. They used gap closure and nail slippage as the outcome measures to assess stability of the construct. Following static analyses they concluded that titanium nails performed better and slipped less with a gap closure of 0.69 mm in comparison to 1.03 mm noted with stainless steel nails. Additionally they observed that the titanium nails distributed stresses more evenly along the nail axis.

Krauze *et al*. (78) performed biomechanical analysis comparing flexible intramedullary nails of two different materials (316L stainless steel and titanium alloy – Ti-6Al-4V). The femur FEA model in this study is reported to be based on a 5-7 year old child. However, the details regarding development of the femur FEA model and its dimensions are not provided in the paper. They evaluated oblique fracture at two levels with the fracture located at the midshaft in the first FEA model and in the second model the fracture level was 25 mm proximal. In both these fracture configurations they observed following the FEA that the stresses in both the stainless steel and titanium alloy nails did not exceed the yield point.

In summary the literature review of the current clinical, biomechanical and FEA studies demonstrated no *in vitro* biomechanical study pertaining to the ALFN.

1.3 Aims and outline of the study

The aims of this research work are listed below:

1. The primary aim was to assess the biomechanical stability of an adolescent femoral shaft fracture fixed using the ALFN. This was performed using a combination of laboratory based experimental testing and finite element based simulation testing to assess the stiffness parameters of a composite femur and ALFN construct under axial, four-point bending and torsional loading conditions anticipated in the perioperative period.

2. The secondary aims were to use the validated finite element model to identify any potential modes of failure of femoral fracture fixation using ALFN. Variation in the finite element model parameters allowed
    a. To study the effect of routine factors (fracture type / fracture level / stage of fracture healing) encountered in clinical decision making
    b. Evaluate the influence of common intramedullary nail design factors (viz. diameter of interlocking screw / relative angle between the ALFN and proximal interlocking screw / thickness of nail / implant material) on the stress at the interlocking screw and nail interface

3. The final aim was to develop a better understanding of the relative biomechanical advantages (or disadvantages) of the ALFN by comparing data from the current study with data from biomechanical studies available in the literature regarding other commonly used devices (viz. flexible intramedullary nails / plate and screws) to treat femoral fractures in the adolescent population.

A schematic outline of the study is presented in the figure below (Figure 1-2)

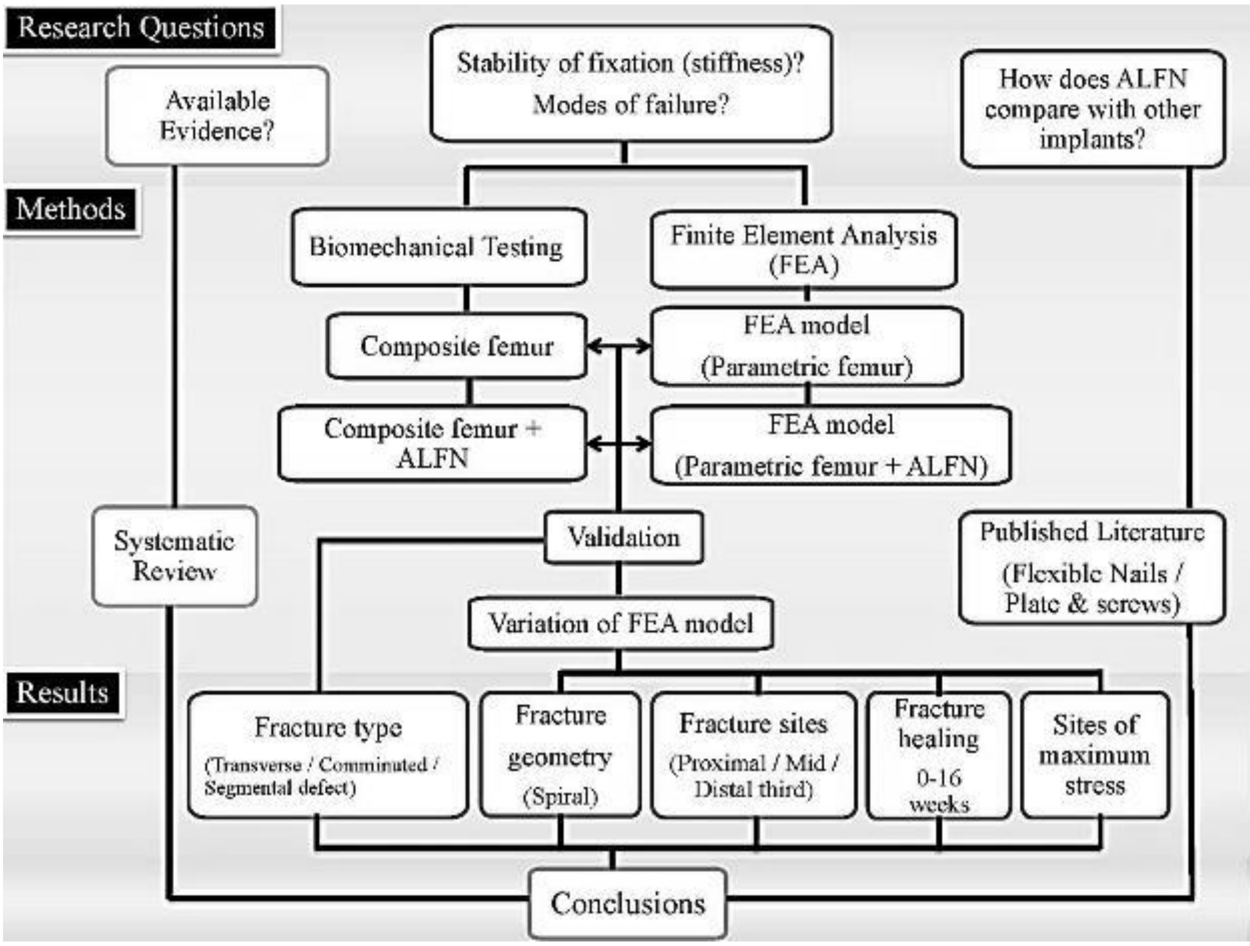

Figure 1-2 Outline of the current study

1.4 Guide to the thesis chapters

Chapter 1 presents the current evidence on the topic and highlights the gap in the knowledge with respect to the biomechanical features of the ALFN.

Chapter 2 presents the macroscopic and microscopic structure and properties of an adolescent femur including embryology, growth and development, relevant ossification centers, vascular supply and its clinical significance. The mechanical properties of long bones, biology of fracture healing and relevant internal fixation methods used in management of adolescent femoral fracture are also discussed in this chapter.

Chapter 3 discusses the different aspects of rigid intramedullary nail fixation. This chapter presents the history and development of rigid intramedullary nail fixation and discusses the key biomechanical characteristics and relevant physiological effects of intramedullary nail fixation. A brief introduction to the ALFN including clinical indications, design features and components are presented in the last three sections of this chapter.

In Chapter 4 the mechanical testing of small composite femur specimens used as an experimental model in this study and results are described. A brief introduction to finite element analysis and the SolidWorks™ simulation software is presented in Chapter 5. The subsequent section describes a novel technique of development of a simplified finite element model of paediatric femur using standardised orthogonal digital radiographs as a template. The simulation results and validation of the finite element model using the results of mechanical testing of composite femurs is presented in the last section of Chapter 5.

Chapter 6 describes the mechanical testing of the composite femurs following surgical implantation with ALFN. The technique of standardised osteotomy to produce transverse, comminuted and segmental defect types of fractures in the composite femurs is described in the next section. The last two sections discuss the results of the mechanical testing.

In Chapter 7, the development of computer aided design (CAD) models of the ALFN and interlocking screws and the methodology used to undertake virtual insertion of the ALFN in paediatric femur using digital radiograph templates is presented. Subsequently simulation tests using SolidWorks™ software and validation of the paediatric femur fracture fixation FEA model are described.

Chapter 8 describes the use of the above validated FEA model of paediatric femur fracture fixation using ALFN to investigate the effect of routine clinical factors namely fracture level and geometry, stage of fracture healing and implant properties. The variation in the biomechanical parameters like stiffness and stress as a result of the above factors are analysed and discussed.

Finally, Chapter 9 collates the key findings of the current research work including the conclusions and the potential areas for future research.

2 ADOLESCENT FEMUR

2.1 Macroscopic architecture

The femur is the largest and strongest long bone in the human body (80, 81). It can contribute upto a quarter of an individual's overall height (80). It consists of a shaft, proximal and distal regions (Figure 2-1). The shaft is predominantly cylindrical in shape with an anterior curvature (81). The proximal region consists of the head, neck, greater and lesser trochanter. The distal region comprises of the medial and lateral condyles with a groove in between them. The surface of the femur provides for the origin and insertion of the various muscles and ligaments which enable weight bearing and movement (81).

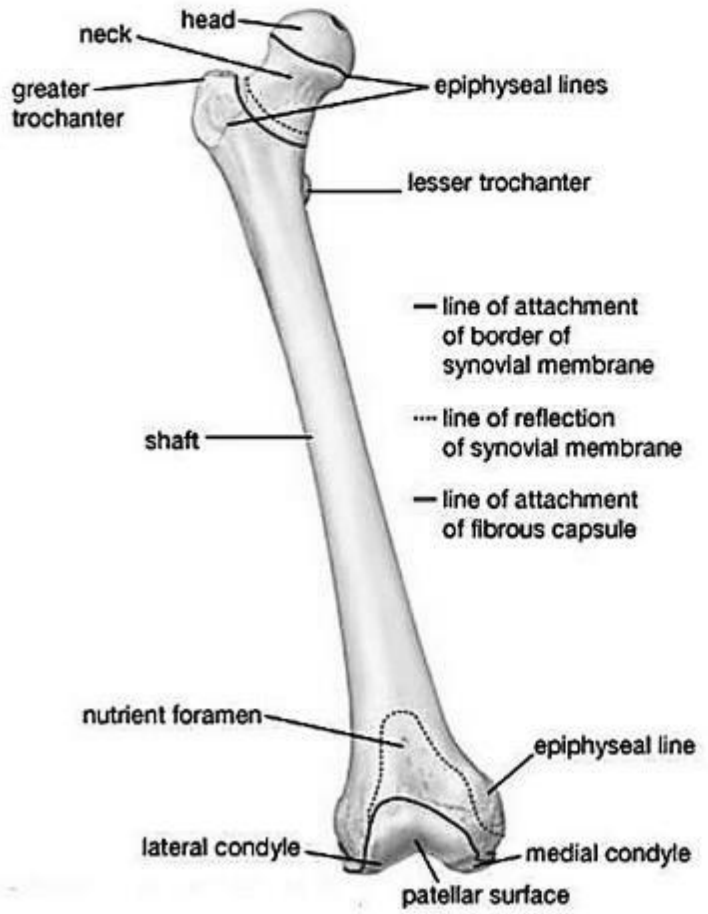

Figure 2-1 Illustration of the adolescent femur

From an anatomical perspective the structure of a long bone like the femur is described to consist of a diaphysis, metaphysis and epiphysis (81, 82). The widened section of femur at either end is referred to as the epiphysis. The diaphysis represents the shaft and the junctional area of the epiphysis with the diaphysis is called the metaphysis (82-84). The metaphysis contains a layer of hyaline cartilage allowing bone growth referred to as the epiphyseal plate (growth plate) (82).

The outer surface of the femur is covered with a membrane called the periosteum. This layer is vital for providing nutrients to the cortical bone as it contains blood vessels in addition to nerves and lymphatics. It has two layers: a dense and fibrous outer layer and an inner layer comprising of vascular and cellular elements (85). The inner layer consists of cells which have the potential of bone formation (osteoblasts) and is also referred to as the osteogenic layer or cambium (86). The cells of this layer play an important role in fracture healing (87).

2.2 Microscopic architecture

2.2.1 Hierarchical organisation of bone

Bone is a living, dense, connective tissue that forms a part of the skeletal system. Bone tissue performs multiple functions such as mechanical support for movement (88, 89), mineral and acid-base homeostasis (90-92), structural protection of vital organs (80, 88, 89) and red blood production (hematopoiesis) (93-95). As bone tissue performs a multitude of mechanical and biological functions its individual components are therefore highly organised and follow a hierarchical arrangement (86, 93, 96, 97). Individual components of bone tissue can range in size from nanometer to millimeter-sized structures (Figure 2-2).

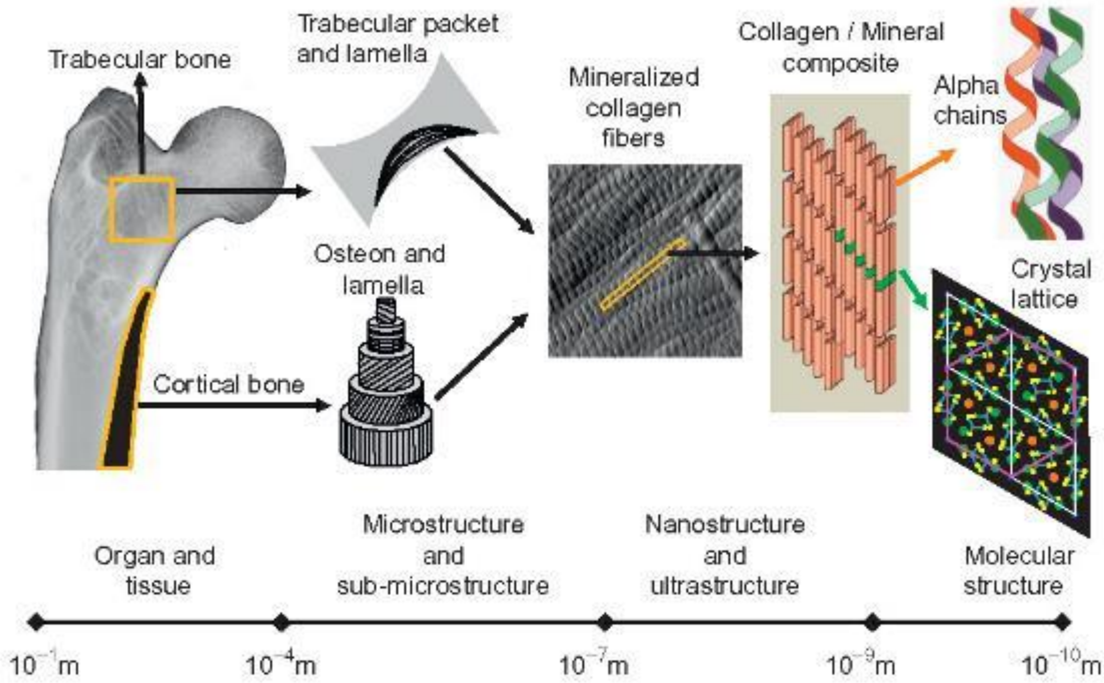

Figure 2-2 Multiscale hierarchical organisation of bone [Reproduced from Burr DB and Akkus O (93)]

The microscopic structural unit of compact bone is called the osteon or Haversian system (98) (Figure 2-3). Calcified matrix is arranged in a concentric ring pattern called lamella around a central canal or Haversian canal which contains blood vessels, nerves and lymph vessels. Branches of these vessels and nerve enter the perforating canal or Volkmann's canal (99) to traverse towards the periosteum and endosteum. Bone cells (osteocytes) are housed in spaces called lacunae. Smaller canals (canaliculi) contain the cell processes of osteocytes and connect lacunae with each other and the central canal (86, 100).

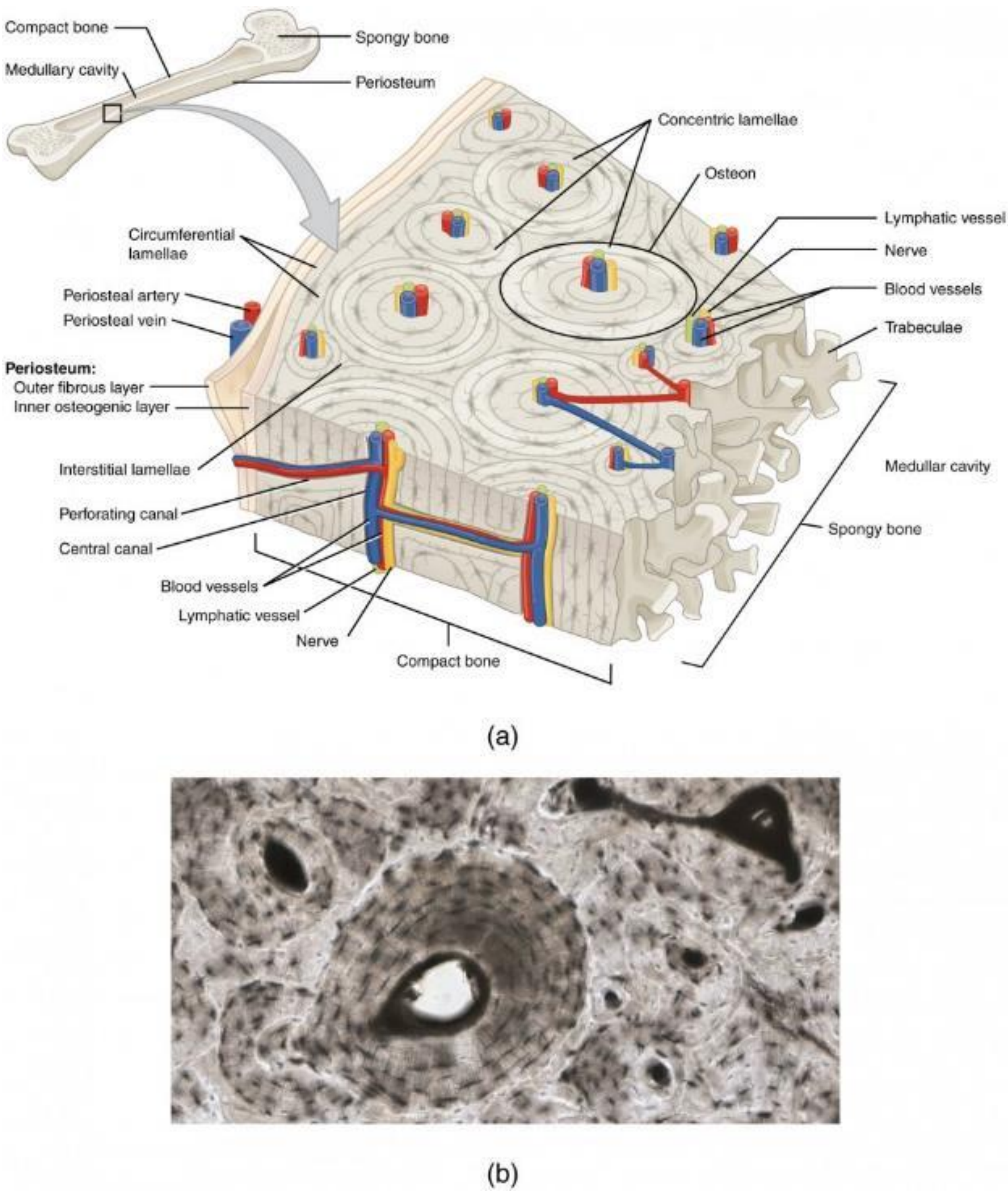

Figure 2-3 Microstructure of compact bone (a-diagram Haversian system, b-micrograph of an osteon) [Reproduced from Thanos *et al*. (82)]

2.2.2 Biology and composition of bone

Whole bone is a specialised structure and consists of cellular (bone cells, blood vessels, nerve fibres and bone marrow) and non-cellular components (86, 93, 101). Bone cells constitute a relatively small percentage of bone tissue but perform vital functions like bone formation and resorption, mineral homeostasis and repair of bone (82, 86, 87, 102). Bone cells are either mesenchymal (osteoblasts, osteocytes, bone-lining cells and undifferentiated cells) or haematopoietic (osteoclasts, pre-osteoclasts and circulating or marrow monocytes) in origin (86).

The non-cellular components of bone tissue are as below -

i. Inorganic matrix (65% of weight) - is composed of carbonated apatite mineral in a poorly crystalline form (86, 93).
ii. Organic matrix (25% of weight) - is mainly made up of type I collagen fibrils (90%) with the remainder 10% coming from non-collagenous proteins, proteoglycans and phospholipids (103).
iii. Water (10% of weight) - is present in either a bound or unbound state. Bound water is associated with the collagen-mineral composite whereas unbound water flows freely amongst the canalicular and vascular channels of bone (93).

2.2.3 Physis

Physis or the growth plate is present in the immature bone and contributes to the longitudinal growth (82, 104). The physis is an organised cartilage layer entrapped between the epiphysis and metaphysis. It is connected to the latter two structures via the zone of Ranvier and the perichondrial ring of LaCroix (105) (Figure 2-4). Zone of Ranvier appears as a circumferential notch-like structure at the periphery of the physis containing fibers, cells (osteoblasts, chondrocytes and fibroblasts) and bony lamina contributing to appositional growth (106).

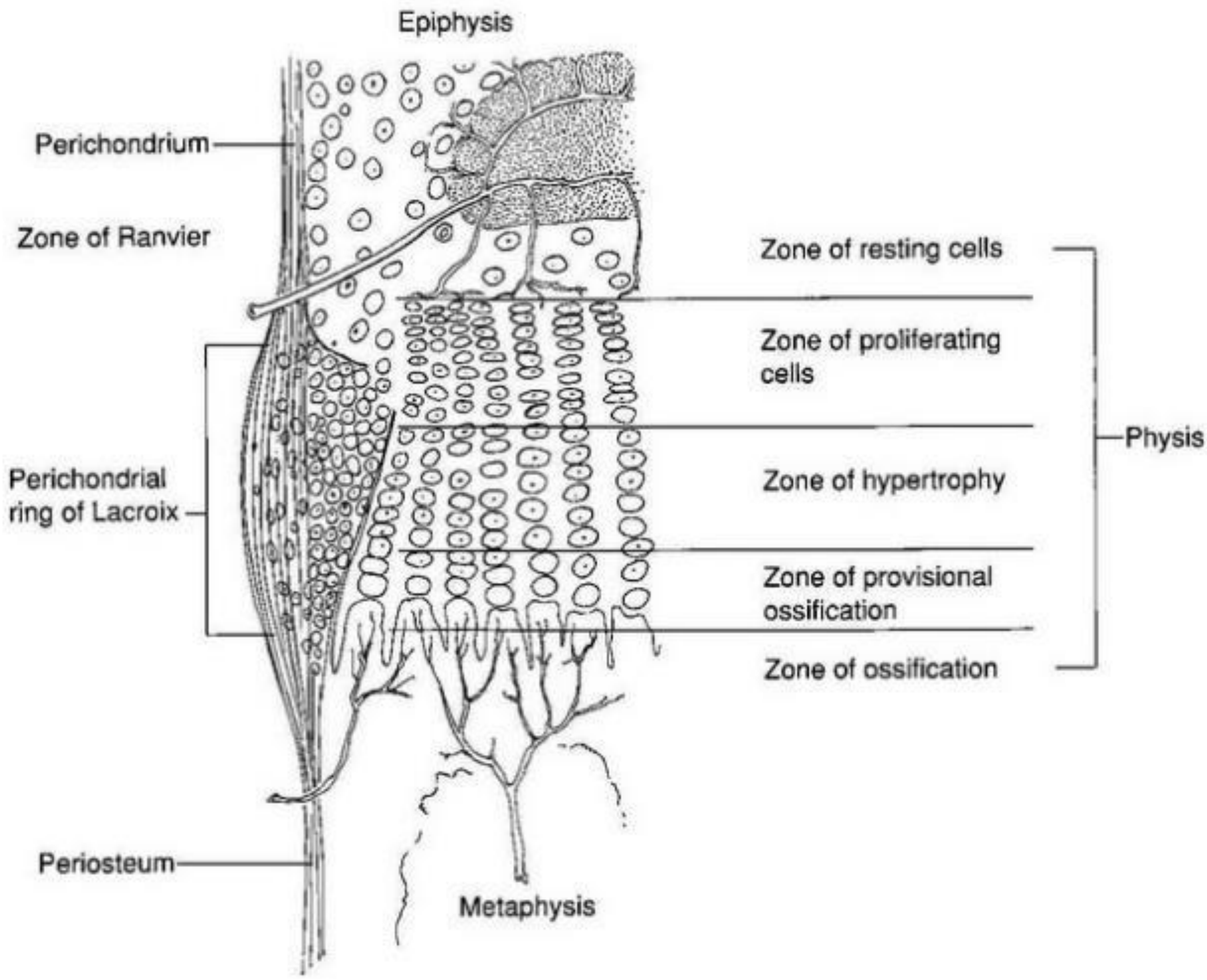

Figure 2-4 Diagram of growth plate

The periosteum is firmly attached around the perichondrium of the epiphysis and the zone of Ranvier and may act as a restraint for uncontrolled longitudinal growth (107). The perichondrial ring of LaCroix is a strong ring of fibrous tissue that secures the epiphysis to the metaphysis. It may act as a potential reservoir for growth plate germ cells (108). The perichondrial ring of LaCroix contains a thin extension of the metaphyseal cortex and provides a circumferential support to the growth plate (105). Histologically the physis consists of three zones namely reserve zone, proliferative zone and hypertrophic zone representing the cartilage cells (chondrocytes) at various stages of differentiation (104, 109)

2.3 Early development, ossification centers and growth zones of femur

During the embryonic stage the femur develops from the mesodermal layer at around 4 weeks (110, 111). Subsequently by the seventh week it progresses into a cartilaginous model of the femur including the head, neck, both trochanters and condyles (111, 112). Ossification of the femur is accomplished with the emergence of the primary and secondary ossification centers (Figure 2-5).

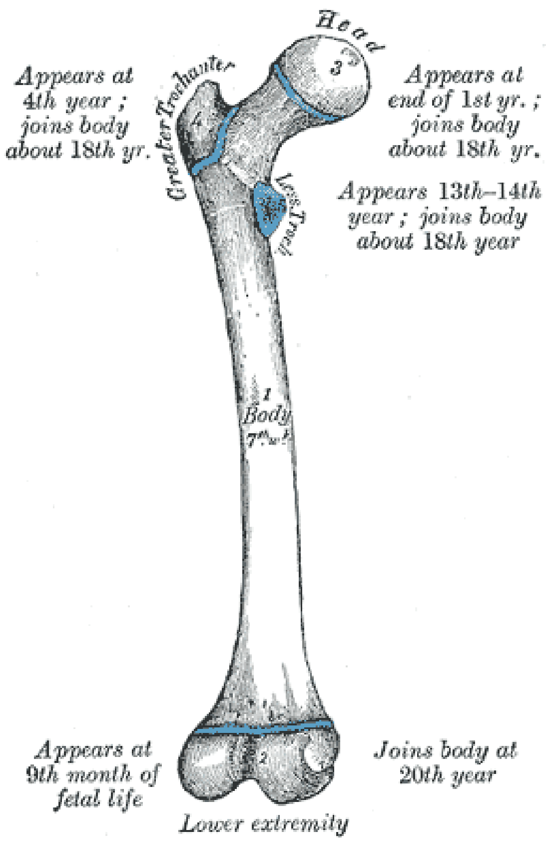

Figure 2-5 Illustration of ossification centers of the femur (reproduced from Gray, H (81))

The primary ossification center appears around 8 weeks in the diaphysis as a bony collar (111, 112). Subsequently, bone formation in the shaft proceeds in both proximal and distal directions (111) such that it reaches the neck area proximally and the distal epiphysis by 12 weeks (110). At 16 weeks ossification of the entire femoral shaft is completed (111). Following the above development in the femur secondary ossification centers corresponding to the femoral head, greater and lesser trochanters and the distal end appear in stages. The cartilaginous parts of the femur in the proximal region which are not ossified form the main growth zones (Figure 2-6).

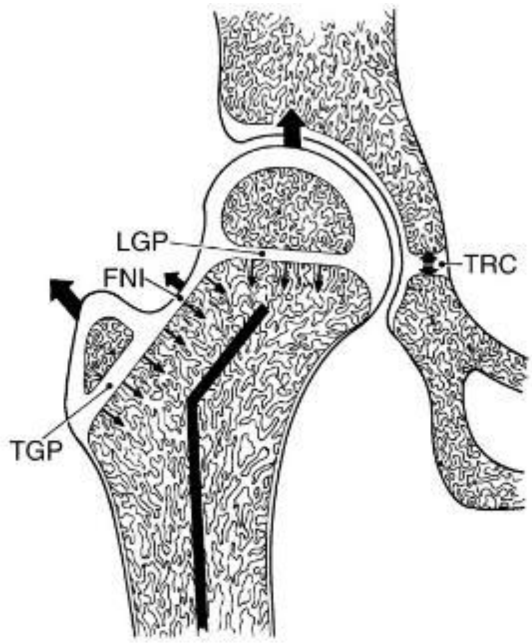

Figure 2-6 Growth zones of proximal femur (LGP - longitudinal growth plate, FNI - femoral neck isthmus, TGP - trochanteric growth plate, TRC - triradiate cartilage) [Reproduced from Siffert *et al*. (113)]

Three growth zones namely longitudinal growth plate, trochanteric growth plate and femoral neck isthmus have been described (111, 113). These growth zones play a vital role in the longitudinal growth of the femur including the shape of the proximal femur with an anterior bow. The cartilaginous parts at the distal end of the femur proximal to the secondary ossification center develop into the distal growth plate (physis). It contributes to 70% growth in the length of femur (114).

2.4 Vascular supply of proximal femur and its clinical relevance

Blood supply to the proximal end of the femur mainly consists of an extracapsular arterial ring, intracapsular ascending cervical arteries and an intracapsular subsynovial ring (111, 115). The extracapsular arterial ring is situated at the base of the femoral neck and is formed by the anastomosis from the branches of the medial and lateral femoral circumflex arteries. The ascending cervical arteries emerge from the extracapsular arterial ring and pierce the hip joint capsule and traverse the neck towards the femoral head (115). The subsynovial ring is formed from the anastomosis of the ascending cervical vessels at the junction of the femoral neck and articular cartilage of head. The intricate vasculature of the proximal femur has certain clinical implications. Three different entry points have been used by orthopaedic surgeons whilst performing rigid intramedullary nail fixation of femoral fractures (50) (Figure 2-7).

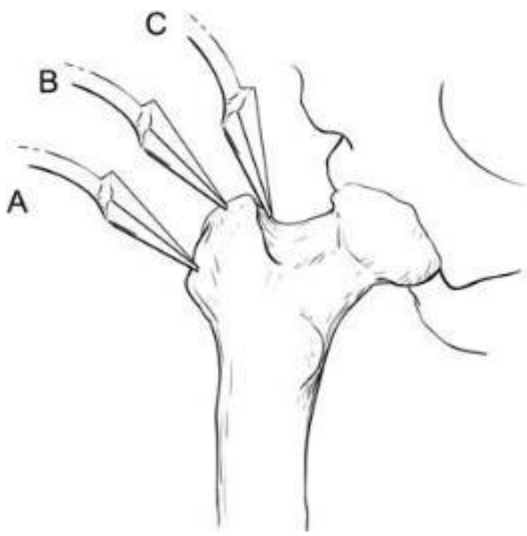

Figure 2-7 Entry points for intramedullary nail insertion A-lateral aspect of greater trochanter, B-tip of greater trochanter, C-piriform fossa [Reproduced from MacNeil *et al*. (50)]

The proximity of the above three entry points to the femoral head vasculature is shown below (Figure 2-8). Intramedullary nail fixation using either the pyriformis fossa or tip of the greater trochanter entry points have an inherent risk of iatrogenic damage to the blood vessels due to the close proximity (3, 50). This is a subtle complication and the clinical symptoms may appear several months later secondary to avascular necrosis of the femoral head (12). However, an entry point located over the lateral aspect of the greater trochanter is less likely to disrupt the blood supply to the femoral head (23, 29).

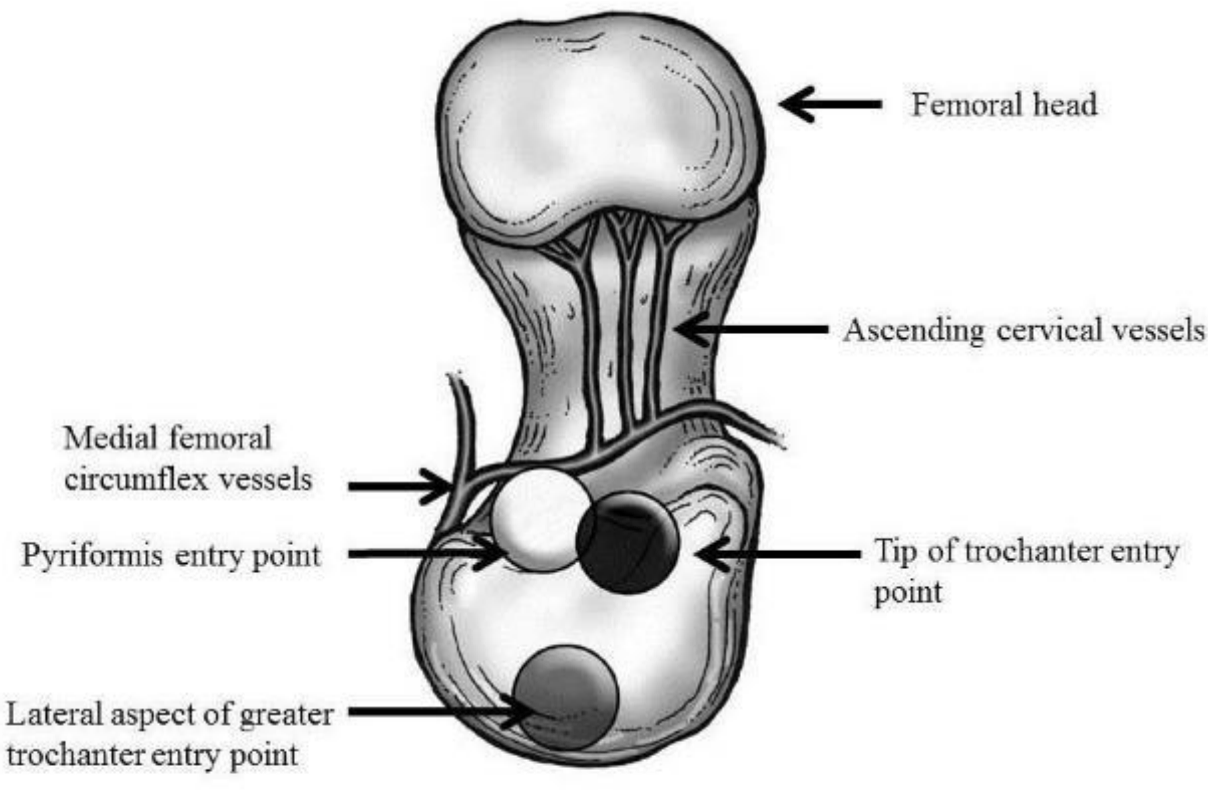

Figure 2-8 Superior view of femoral head with vasculature and three entry points used for intramedullary nail fixation. [Reproduced from Keeler *et al*. (23)]

2.5 Mechanical properties of long bones

The mechanical properties of bone tissue are a reflection of the complex hierarchical organisation and composition as outlined above. The relative content of inorganic and organic matrix within a given bone tissue determines its mechanical behavior (116, 117). In general bone with deficient inorganic mineral content is pliable whereas bone with deficient organic content is brittle. The current literature has numerous studies and surveys providing data regarding mechanical properties of different bone tissues (118-134). However, it must be noted that there is considerable variation in the reported literature. Careful interpretation of data is essential as mechanical properties of bone can be affected by the site and size of specimens (119, 130), quality of specimens (135), specimen storage and preparation (136, 137), temperature at which tests are carried out (137, 138), testing standards and protocols (120) followed by different authors. It is also vital to differentiate the structural and material properties of bone. Whilst structural properties refer to the whole bone properties, material properties refer to specific bone segments (machined section of cortex). Structural properties are useful in global stress analysis whereas material properties are helpful in evaluating bone pathologies and to study bone adaptation around implants (126).

2.5.1 Cortical bone

Mechanical properties of cortical bone have been well documented using traditional testing techniques such as uniaxial tensile or compressive testing, three-point or four-point bending and torsional testing. In general terms it has been observed that the tensile strength is about 2/3 that of compression strength. The torsional (shear) strength is approximately 1/3 to 1/2 of the values of the longitudinal strength whereas the torsional (shear) modulus is only about 1/6 to 1/5 of the longitudinal modulus. A brief summary of the data available in the literature is presented below. (Table 2-1)

Table 2-1 Mechanical properties of cortical bone in human femur

Superscript: a - range of average values from different subjects, b - Means ± SD

(Adapted from An *et al*. (139))

Test method	Specimen Dimensions	Strength (MPa)	Elastic Modulus (GPa)	Reference
Compression Test	2 × 2 × 6 mm 2 × 2 × 6 mm 3 mm	167-215[a] 179-209[a] 205-206[a]	14.7-19.7[a] 15.4-18.6[a] -	Reilly *et al*. (136) Burstein *et al*. (140) Cezayirlioglu *et al*. (141)
Tensile Test	3.8 × 2.3 × 76 mm 2 × 2 × 6 mm 2 × 2 × 6 mm 3 mm	66-107[a] 107-140[a] 120-140[a] 133-136[a]	10.9-20.6[a] 11.4-19.7[a] 15.6-17.7[a] -	Evans *et al*. (142) Reilly *et al*. (124) Burstein *et al*. (140) Cezayirlioglu *et al*. (141)
Torsional Test	N/A 2 × 2 × 6 mm 3 × 3 × 6 mm 3 mm	54 ± 0.6[b] - 65-71[a] 68-71[a]	3.2 3.1-3.7[a] - -	Yamada *et al*. (143) Reilly *et al*. (124) Reilly *et al*. (123) Cezayirlioglu *et al*. (141)
Bending Test	2 × 5 × 50 mm 2 × 3 × 30 mm 0.4 × 5 × 7 mm 2 × 3.4 × 40 mm	181 103-238[a] 225± 28[b] 142-170[a]	15.5 9.82-15.7[a] 12.5 ± 2.1[b] 9.1-14.4	Sedlin *et al*. (144) Keller *et al*. (145) Lotz *et al*. (146) Currey *et al*. (147)

Evans and Lebow (1951) demonstrated that cortical bone is mechanically heterogenous (142). In femoral shaft specimens they noted that the middle third had the highest ultimate strength and elastic modulus whereas the lower third had the lowest average strength and modulus. Furthermore the lateral quadrant of the shaft had the highest ultimate tensile strength whilst the anterior quadrant had the lowest. The mechanical properties of cortical bone depend on the direction of the load application during testing (139). It has been noted that the longitudinal elastic modulus is the highest and the transverse elastic modulus is the lowest. The moduli of the specimens taken at any angles in between 0 and 90° have intermittent values (126, 148-150). This property is referred to as anisotropy (Figure 2-9).

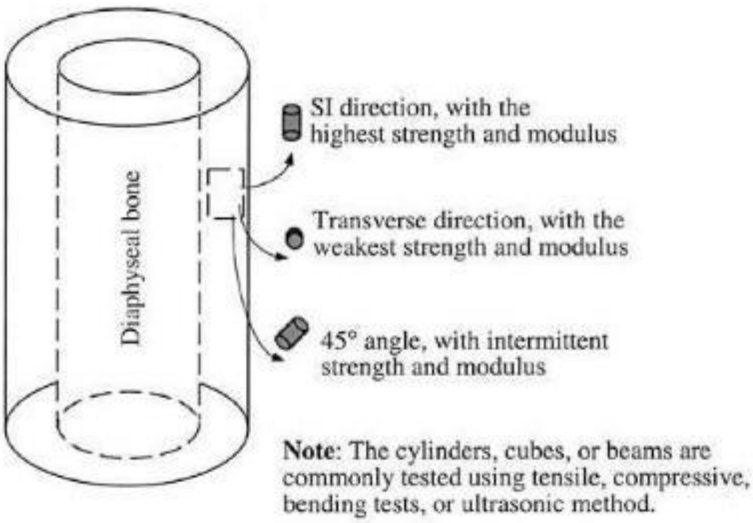

Figure 2-9 Anisotropic characteristics of cortical bone (reproduced from An *et al*. (139))

This behavior of cortical bone is due to the longitudinally oriented collagen fibers and osteons (151). Sasaki *et al*. used the X-ray pole figure analysis technique to evaluate the orientation of hydroxyapatite crystals in bovine femurs (152). They noted that the c-axis of hydroxyapatite was parallel to the longitudinal axis of bone. However, a significant amount was also oriented in other directions including perpendicular to the longitudinal axis. They concluded that the nonlongitudinal (off bone) axial distribution of hydroxyapatite contributed to the anisotropic quality of bone.

2.5.2 Cancellous bone

A brief summary of data regarding human cancellous bone mechanical properties is presented below (Table 2-2).

Table 2-2 Mechanical properties of cancellous bone of different sites in human specimens Superscript: a - range of average values from different subjects, N/A - data not available (Adapted from An *et al*. (139))

Site	Specimen Dimensions	Ultimate Strength (MPa)	Elastic Modulus (MPa)	Apparent Density (g/cm^3)	Ash Density (g/cm^3)	Reference
Femoral head	8 mm cylinder	9.3±4.5	900±710	N/A	N/A	Martens *et al*. (121)
Proximal femur	8 mm cylinder	6.6±6.3	616±707	N/A	N/A	Martens *et al*. (121)
Distal femur	8 mm cube	5.6±3.8	298±224	0.43±0.15	0.26±0.08	Kuhn *et al*. (153)
	10.3 mm cylinder	1.5-45[a]	10-500[a]	0.24±0.09	N/A	Carter *et al*. (154)
	7.5 mm cylinder	5.96	103-1058[a]	0.46	N/A	Odgaard et al. (155)
Proximal tibia	7.5 mm cylinder	5.3±2.9	445±257	N/A	N/A	Linde *et al*. (156)
Vertebral body	N/A	N/A	165±110	0.14±0.06	N/A	Keaveny *et al*. (157)

Cancellous bone is characterised by the presence of bony trabecular columns and struts along with marrow-filled cavities giving it a porous appearance. This two-phase structure of cancellous bone provides a unique mechanical property (154). Under excessive loads the trabeculae collapse allowing the cancellous bone to undergo large compressive strains at approximately constant stress. Thus large amounts of energy generated from impacts can be absorbed without generation of high stress akin to engineering foams (158). The structural properties of cancellous bone are much smaller than those of cortical bone. As cancellous bone is considerably more porous than cortical bone, its apparent density (the mass of bone tissue divided by the bulk volume of the test specimen including mineralised bone and bone marrow spaces) has been studied by several authors (131, 155, 157). The apparent density of cortical bone is 1.8 - 1.9 g/cm^3 (159-162) whilst that of cancellous bone ranges from 0.1 - 1.0 g/cm^3 (154, 155, 157, 162). The apparent density of cancellous bone significantly influences its compressive stress-strain behavior (130, 163). A comparison of the stress-strain response of cortical and trabecular bone is shown in Figure 2-10.

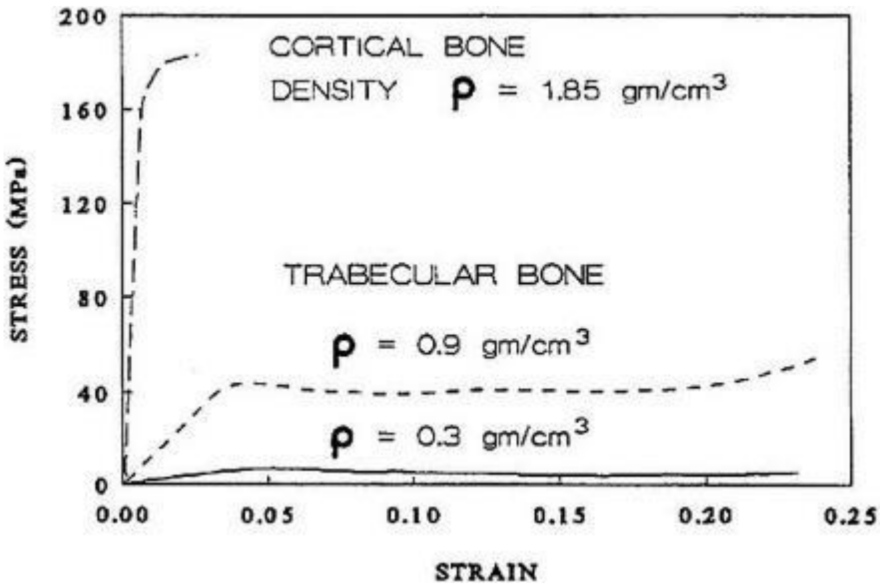

Figure 2-10 Typical stress-strain curves for trabecular bone of different apparent densities [Reproduced from Hayes *et al*. (164)]

In contrast to cortical bone the stress-strain curve of trabecular bone demonstrates an initial elastic region followed by yield as the fracture of trabeculae occurs. This is followed by a long plateau region representing the progression of the fracturing process. As a result the marrow spaces are sequentially filled with the debris of fractured trabeculae. At a strain of approximately 0.50 closure of the pores occurs and any continued load results in marked increase in specimen modulus. A strong correlation between the mechanical properties of cancellous bone (strength / stiffness) and its apparent density and mineral (or ash) density has been reported (139). The compressive strength (σ in MPa) and compressive modulus (E in MPa) of trabecular bone vary as a power-law function of its apparent density (ρ in g/cm^3) (165, 166). The compressive strength of trabecular bone is related to its apparent density such that $\sigma = 60\rho^2$ whereas the compressive modulus $E = 2915\rho^2$. Hence a small variation in apparent density can have a large effect on trabecular bone mechanical properties.

Viscoelasticity: Cortical bone and cancellous bone to a lesser extent exhibit a time-dependent material behavior which is referred to as viscoelasticity. The rate at which the load is applied along with the duration of load application influences the biomechanical response of bone. Bone is stiffer and exhibits a higher load to failure when loads are applied at higher rates (167). Sammarco *et al*. (168) demonstrated this phenomenon using paired canine tibiae subjecting them to a high (0.01 second) and very low (200 second) loading rates. It was observed that the load to failure almost doubled whereas the deformation within the specimen did not change significantly. Furthermore the amount of energy stored before failure nearly doubled at the higher loading rate. Clinically this has an implication on the type of fracture and the associated soft tissue trauma following an injury. At a higher loading rate the energy within the bone cannot be rapidly dissipated through the initial fracture. This results in a multi-fragmentary type of fracture with associated soft tissue damage. On the other hand at a low loading rate the energy in the bone can be dissipated through the formation of a single crack. Thus minimal soft tissue damage occurs with relatively small displacement of the fracture fragments.

Analysis of physiological strain rates reveals that a strain rate of 0.002 s^{-1} is attained at a speed of 1.0 m s^{-1}. This can increase upto 0.01 s^{-1} during running at a speed of 2.2 m s^{-1} and 1.0 s^{-1} during impact causing fracture (169). In general when activity becomes more strenuous the strain rate correspondingly increases (170). Bone is approximately 30% stronger during brisk walking than for slow walking (Figure 2-11). Several physical processes like thermoelastic and piezoelectric coupling, inhomogeneous deformation, molecular modes in collagen and motion of fluid in bone canals have all been attributed to cause viscoelastic effects in bone (171).

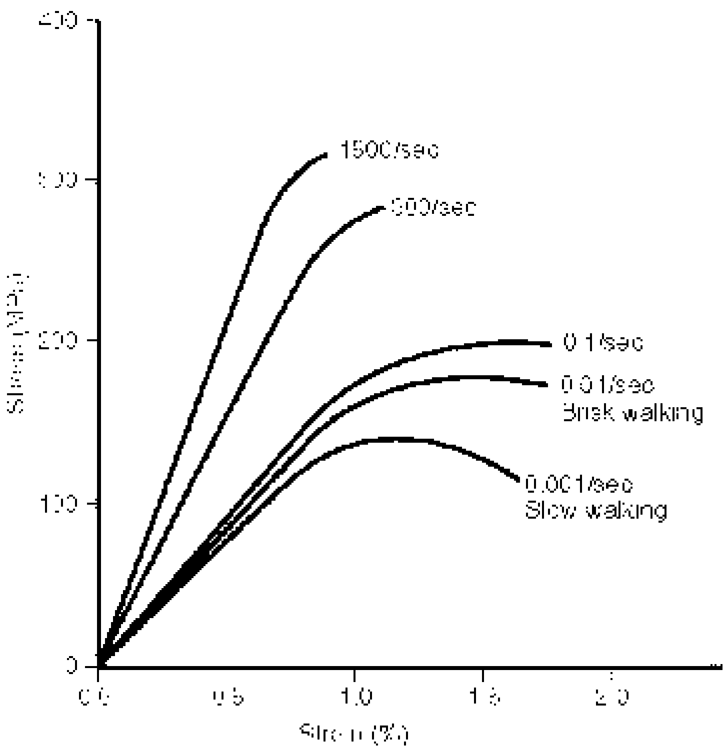

Figure 2-11 Rate dependency of cortical bone demonstrated at five strain rates [Adapted from McElhaney *et al.* (170)]

2.6 Fracture and biology of fracture healing

Fracture is defined as a break or discontinuity in the cortex of a bone. The magnitude and mechanism of trauma usually determines the location and pattern of fracture in a bone (167). Direct trauma to the bone can either result in a transverse fracture low energy or multi-fragmentary fracture high energy. Indirect trauma in the form of a disruptive biomechanical force can cause different patterns of fracture. Tractional force causes transverse fracture perpendicular to the force whereas a bending force causes a transverse fracture with a butterfly fragment. Torsion often results in spiral fracture and oblique fracture occurs due to a combination of bending and torsional force (172).

2.6.1 Stages

The process of fracture healing commences immediately following trauma due to the activation of complex biological processes (173-175). Unlike damaged soft tissues which heal by replacement of the injured tissue with collagen scar tissue bone heals by replacing the fractured area with normal bony tissue (176).

Fracture healing can be either primary or secondary types (177). Primary (direct) healing is characterised by osteonal bone remodeling and is observed with fracture fixation methods like plate and screws which provide absolute stability (178). Secondary (indirect) healing by callus formation is observed with fixation methods that provide relative stability (flexible nails) (178). For descriptive purposes fracture healing can be broadly divided into three stages as below (Table 2-3).

Table 2-3 Stages of fracture healing

Stage	Salient features
Inflammatory	
	Fracture causes vascular endothelial damage and haematoma Migration of inflammatory cells and release of immunoregulatory cytokines (Interleukin 1, Interleukin 6, transforming growth factor beta) (177) Organisation of fracture haematoma into fibrovascular tissue matrix rich in collagens I, III and V (179) Duration - 3-4 days (180) Clinically characterised by pain and oedema
Reparative	
Fibrocartilage callus	Development of new blood vessels at fracture site and cartilage Callus – combination of fibrous tissue, cartilage and woven bone Appearance of macrophages, chondroblasts, chondrocytes, osteoclasts, fibroblasts (177) Duration – 1 week to 1 month (181)
Bony callus	Intramembranous and endochondral ossification with laying down of new woven bone Calcified soft callus is resorbed by chondroclasts Neovascularisation bringing in osteoblast precursors to produce osteoid followed by mineralisation to form hard/bony callus Duration – 1-4 months (181) Clinically fracture is united and pain free on movement (181)
Remodelling	
	Mechanical optimisation of callus by arrangement of cells with osteoclasts at the apex of cone causing bone resorption and trailing osteoblasts laying down new bone (cutting cone) (182) Duration – upto several years

Due to normal development bones in children undergo a process of modeling continuously. The physes are known to undergo reorientation with asymmetric growth following fracture. This can be either due to decreased longitudinal growth from compression (Hueter-Volkmann law) (183) or increased growth due to tension on the physis (Delpech’s law). Hence the potential for bones in children to remodel following a fracture is higher than adult bones (176). This is significant as it implies that any residual deformity in the bone following fracture union will correct over the course of time. Axial and translational deformities have better potential to remodel compared to rotational deformity (184). Wallace *et al*. (185) retrospectively reviewed 28 children with unilateral middle third femoral shaft fractures with angular deformity of 10° to 26° after union. They noted that 74% of the angulation correction due to remodeling occurred at the physes and only 26% at the fracture site. Of the physeal remodeling, 53% was at the proximal and 47% at the distal physis of the femur. They concluded that malunion by upto 25° in any plane will remodel to give normal alignment of joint surfaces.

In summary fracture healing in a bone involves complex interplay of physical and biological factors to restore the geometry and original structural integrity.

2.6.2 Treatment and fixation of adolescent femoral fracture

The purpose of fracture treatment is to promote acceptable bone healing whilst preserving soft tissues with an ultimate goal of restoration of function (186). The treatment of fractures is a vast and complex topic. Hence a brief overview of the routine methods used in the management of femoral fractures (3, 4, 187, 188) is presented below. Treatment methods are broadly divided into nonoperative and operative modalities. Nonoperative modalities like bracing, hip spica cast are not used in the adolescent patients as they do not provide adequate fracture stability and are not practical (4, 5). Operative treatment modalities include flexible intramedullary nails (24), plate and screw fixation (189, 190), external fixation (33) and rigid intramedullary nails (29).

I. Flexible intramedullary nails - This technique is well documented (191-194) and is also referred to as elastic stable intramedullary nailing (ESIN) in the literature (195, 196). This method relies on the principle of preservation of the soft tissues namely the periosteum which is thicker in children. Two nails of identical diameter are prebent and to achieve a three-point fixation by anchorage firstly at the entry points and secondly in the metaphysis at the other end of the bone (Figure 2-12). The combination of two nails acts as a balanced insertion construct and resists rotational forces due to the inherent elastic properties of their material (197). The dense metaphyseal bone in children offers good fixation for the nail tips.

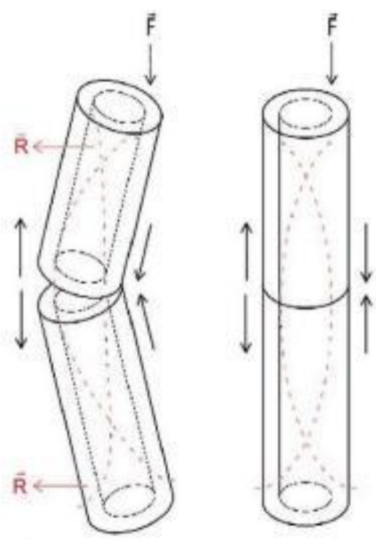

Figure 2-12 Resistance to angular displacement at fracture site due to recoil of elastic nails F- deforming force, R- resistance of elastic nails [Reproduced from Hunter *et al*. (198)]

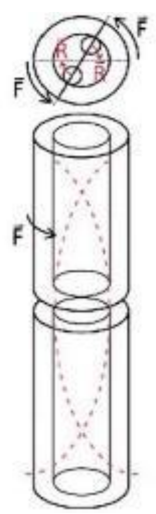

Figure 2-13 Resistance of elastic nails to rotational deformity F- deforming force, R- resistance of elastic nails [Reproduced from Hunter *et al*. (198)]

Titanium or stainless steel nails varying in diameter from 2.5-4.0 mm are used such that the diameter should be equivalent to a third of that of the medullary canal as measured on radiographs (196). Flexible nails are mainly indicated for fracture of femoral diaphysis but their use has been extended to metaphyseal and some epiphyseal fractures (198). It must be noted that clinical studies have reported poor outcomes using this method to treat unstable femoral fractures especially in heavier adolescents (52, 199, 200).

II. Plate and screws - Treatment of adolescent femoral fractures using a locking compression plate (LCP) (31, 201), low contact dynamic compression plate (LC-DCP) (201), distal femoral plate (189), distal femoral condylar plate (189) has been reported in the literature. Internal fixation using a plate and screws has evolved over the past few decades based on a better understanding of the mechanical and biological factors involved in fracture healing and their close interaction (175, 202). This has resulted in the development of the concept termed as 'biological internal fixation' using locked internal fixators with minimal contact between the plate and bone, long-span bridging and fewer screws to achieve fixation (202). Minimally invasive percutaneous osteosynthesis (MIPO) is a technique of fracture fixation based on this principle wherein a locking plate is used in the submuscular plane without disturbing the biology of the fracture site. It has been used by some authors in the management of adolescent femoral fractures with satisfactory results in terms of fracture alignment and union rates (31, 189, 203-206). A general drawback of using metalwork to fix fractures is that it needs a second procedure for removal of metalwork following union of the fracture. This procedure can be challenging and can be associated with complications (207-209). Bone overgrowth at the leading edge of the plate has been reported following fracture healing making the removal procedure more difficult than plate insertion (210). Stripping of the hexagonal recess of locking screws has also been reported (31, 211-213) forcing the operating surgeon to use additional aggressive tools like high speed carbide-tipped burr to cut and remove the implant (31). Thus plate and screw fixation of adolescent femoral fracture is a useful method but has its own drawbacks and limitations.

III. External fixation - This method of fracture treatment has been used in patients with unstable femoral fractures, multiple injuries and/or contaminated open fractures (11, 199, 214-220). External fixator systems are available in different designs and materials but in general consist of five basic components: half pins, clamps, couplings, central body and a compression/distraction system (197) (Figure 2-14). Due to the increased rate of complications like pin track infections, pin site scarring, delayed union and re-fracture the use of external fixators has declined in the recent past (216, 220-223).

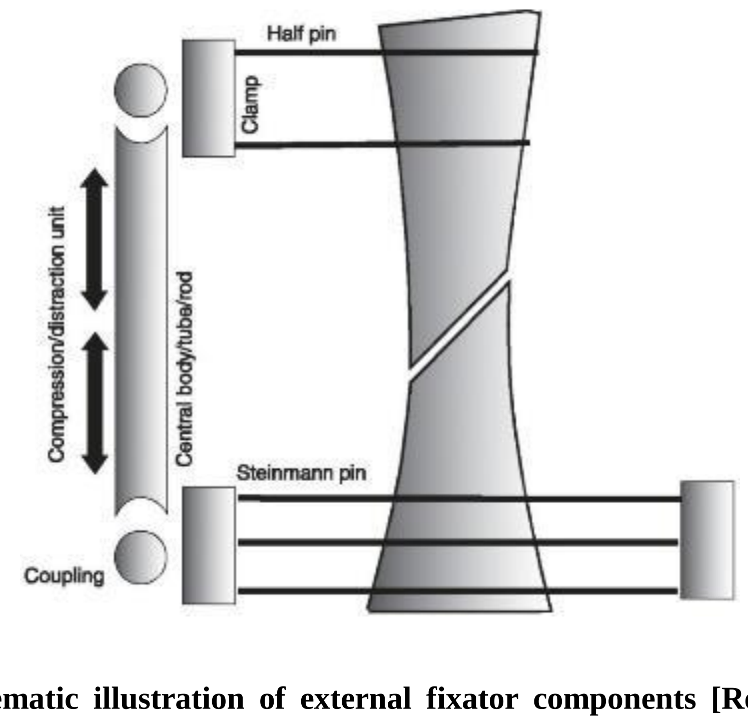

Figure 2-14 Schematic illustration of external fixator components [Reproduced from Thakur *et al*. (197)]

IV. Rigid intramedullary nails - Numerous types of rigid intramedullary nails have been described in the literature to fix adolescent femoral fractures (7, 8, 12, 27, 29, 30, 40, 41, 51). A detailed description of the salient biomechanical principles of intramedullary nailing including the adolescent lateral femoral nail is presented in the next chapter.

2.7 Summary

It can be noted from the above that the adolescent femur has a complex macro and micro architecture which plays a crucial role in routine functions like weight bearing and load transmission. The wellbeing of the physes in the proximal aspect of the growing femur is vital for the overall growth and development of the femur. Hence injuries in this region both traumatic and iatrogenic can result in significant morbidity. Therefore, ideal treatment modalities should not only promptly restore the biomechanical functions of the femur but also cause least amount of biological disruption in terms of the vascularity and fracture callus. The new generation of intramedullary nails with entry point on the lateral aspect of the greater trochanter (ALFN) are based on this objective. The next chapter provides further information on this topic.

3 EXPERT ADOLESCENT LATERAL FEMORAL NAIL (ALFN)

3.1 History and development of intramedullary nail fixation

The recorded practice of intramedullary nail fixation dates back to the sixteenth century (224, 225). Bernardino de Sahagun an anthropologist travelled to Mexico and noted the Aztec physicians treating nonunion of bone with wooden sticks. A couple of centuries later Bircher reported intramedullary fixation using ivory pegs (226). Gluck described an interlocking fixation device also made from ivory (227). The American surgeon Nicholas Senn (1893) described the use of a 'perforated bone ferrule' prepared from the femur of an ox to directly fix and stabilise oblique fractures of the femur and humerus, compound fractures and ununited fractures (228). His contemporary from Norway, Nicolaysen suggested that increasing the length of intramedullary nails provided biomechanical advantage whilst describing biomechanical principles of proximal femoral fracture management with this technique (229).

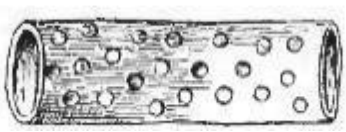

Figure 3-1 Perforated intra osseous bone splint [Reproduced from Senn (228)]

Sporadic application of intramedullary nail fixation techniques to address different fractures and conditions is noted during this period. Lilienthal (1911) based at the Bellevue Hospital in New York described treatment of femoral shaft fracture using an intramedullary aluminum splint (230). In 1913, Georg Schöne reported fixation of six forearm fractures using silver nails inserted at a distance from the fracture (231). Frédéric François Burghard (1914) in "A System of Operative Surgery" stated that the best method for holding bone surfaces together is by nails, pegs or screws (232). Subsequently in 1917 Hoglund from the United States reported use of bone for intramedullary fixation (233) and a year later in England HeyGroves published three cases of intramedullary nailing using solid metal rod in gunshot wounds (234). More than a decade later Smith-Petersen's work demonstrated successful treatment of femoral neck fractures using stainless steel nails (235). In 1940 Küntscher reported use of a V-shaped nail as an internal splint to achieve union at the fracture site (236). However at the time this concept was dismissed by his contemporaries in Germany as "merely a fashion" (237). With the advent of World War II successful management of fractures in German soldiers with the principles of intramedullary fixation proposed by Küntscher led to better recognition. Between 1940 and 1949 Böhler and colleagues performed nearly 700 nailing procedures and recommended Küntscher's method for treatment of variety of conditions like femoral fractures including open fractures, osteotomies and non-unions (238). Subsequently in the late 1940's Küntscher collaborated with Pohl to change the design of the nail from a V-shape to a cloverleaf shape. He hypothesised that this shape provided better fixation with elastic expansion of the compressed nail as it engaged within the medullary isthmus (237) (Figure 3-2).

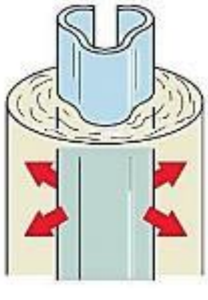

Figure 3-2 Fixation of Küntscher cloverleaf shape nail with elastic expansion in the isthmus

In 1942 Fischer reported the use of flexible intramedullary reaming to increase the contact area between the nail and the bone to improve stability of fixation (239).

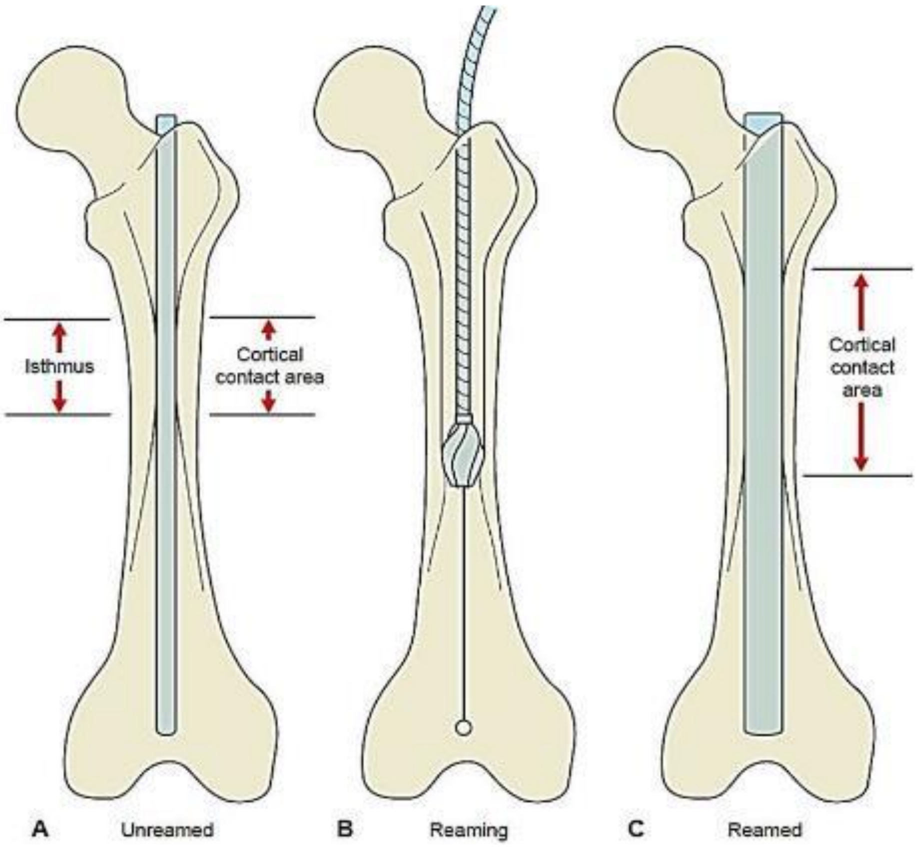

Figure 3-3 Illustration of reaming medullary canal to insert bigger nail

Modny and Bambara introduced the transfixion intramedullary nail in 1953 (240). This nail had multiple holes which allowed for placement of screws perpendicular to each other. This interlocking screw concept has since evolved over the decades (224, 237, 241, 242). Advancements in fluoroscopy leading to image intensification also promoted rapid adoption of intramedullary nail fixation techniques (224). In summary this development of intramedullary nails based on design and material technology is useful to categorise nails broadly into four generations (243) (Table 3-1).

Table 3-1 Generation of intramedullary nails

Generation of Intramedullary Nail	Design features	Example(s)
First	Cloverleaf shape Stainless steel	Küntscher nail (244)
Second	Interlocking screws	Grosse-Kempf nail (242) Russell-Taylor nail (245)
Third	Fatigue resistant titanium alloy	Gamma nail (246)
Fourth	Multiplanar curvature Angle stable locking Virtual real time imaging for distal locking	ALFN (29) ASLS (247) Sureshot™ (248)

3.2 Biomechanical features of intramedullary nails

Intramedullary nails stabilise fractured bones by functioning as internal splints. They form a composite structure with the host bone wherein both the intramedullary nail and the bone both contribute towards the stability of the structure. Intramedullary nails bear most of the load initially in a fractured bone and then gradually transfer it to the bone as the fracture heals (249). Hence this load-sharing quality of intramedullary nails is fundamental to their behavior. The load an intramedullary nail has to sustain can be large and either static or dynamic depending upon the activity undertaken (249). The biomechanical performance of an intramedullary nail *in vivo* depends on several factors. For descriptive purposes they can be broadly divided into the following

I. **Structural properties** - The geometry and design parameters of an intramedullary nail dictate its biomechanical behavior (250, 251). Intramedullary nails can be solid or hollow; open-sectioned (slotted) or closed sectioned; cylindrical, rectangular, diamond, square, cloverleaf or triflanged in cross section. The shape, diameter and the area of the nail determine its bending and torsional rigidity (252). Russell *et al*. (253) carried out four point bending tests on AO, Russell-Taylor and Grosse- Kempf nails. Bending stiffness and strength were noted to be similar in all three designs. This was due to the cross-sectional design of each nail whereby the nails had similar second moments of area (I) around the bending axis. Miles *et al*. (254) conducted three point bending tests to evaluate the AO and Russell-Taylor nails. They observed that slotted and non-slotted nails had a comparable stiffness in bending. During torsional tests, Russell *et al*. (253) and Miles *et al*. (254) both noted that the non-slotted Russell-Taylor nail was approximately thirty times more rigid compared to the slotted AO nail. Using midshaft fractured cadaveric femora and five different intramedullary nails from different manufacturers Tencer *et al*. (252) demonstrated that for the same nominal size there was a twofold difference in flexural rigidity and three fold difference in torsional modulus (Figure 3-4). It can be noted that rigidity increases significantly with nail diameter as the moment of inertia is approximately proportional to the fourth power of the radius. A 16 mm nail is 1.5 times as stiff as a 14 mm nail and 2.5 times as stiff as a 12 mm nail (197).

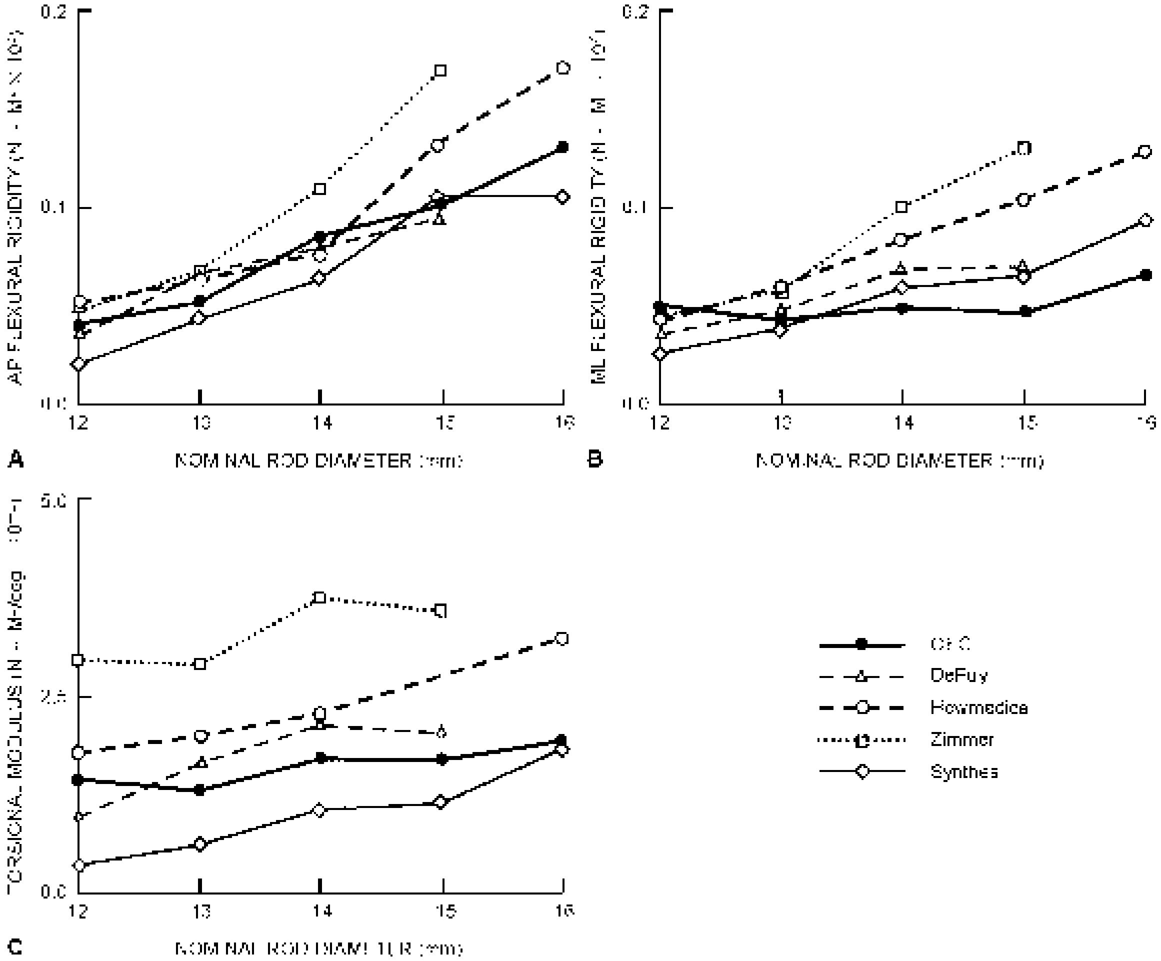

Figure 3-4 Variation in flexural rigidity and torsional modulus of different intramedullary nails A - anteroposterior flexural rigidity, B - mediolateral flexural rigidity, C - torsional modulus [Reproduced from Tencer *et al*. (252)]

Thus it can be inferred that intramedullary nails will have similar bending stiffness when their second moments of area (I) are similar. On the other hand the polar second moment of area (J) for a closed circular section or non-slotted nail is significantly higher than that of an open circular section or slotted nail. Hence a closed section nail will be more rigid in torsion.

The influence of nail length on its biomechanics depends on the total nail length, length of nail-bone contact and working length. Total nail length is based mainly on the anatomy of the host bone. The length of nail-bone contact is the total surface area of contact between the nail and bone. In general, a larger contact area results in higher resistance to motion. Working length is defined as the length of a nail spanning the fracture site from its distal point of fixation in the proximal fragment to its proximal point of fixation in the distal fragment (197). Working length represents the unsupported portion of the nail between two major fragments and is the length of nail carrying the majority of the load across the fracture site. Thus a nail has a shorter working length for a transverse fracture than a comminuted fracture. Surgeons use medullary reaming and interlocking screws to optimise the working length. Serial reaming of the medullary canal improves nail-bone fixation and reduces the working length. (Figure 3-3). Interlocking screws provide fixed points for load transfer between the nail and the bone thereby increasing the torsional stability. The bending stiffness of a nail is inversely proportional to the square of its working length whereas the torsional stiffness is inversely proportional to its working length (197). Kyle *et al*. (255) used a midshaft cadaveric femur fracture model to evaluate the effect of varying combinations of interlocking screws on torsional rigidity. They noted that nails without any interlocking and those with just one proximal interlocking screw had very low torsional rigidity. In comparison the femurs with proximal and either one of the distal screws exhibited a higher torsional rigidity by approximately four times. When all the three interlocking screws were used torsional rigidity was higher by approximately four and half times. They also observed that the group with all three interlocking screws had the greatest ability to spring back following the withdrawal of the torsional deforming load.

Distal third femoral fracture fixation was evaluated by Hajek *et al*. (256) using cadaveric femora implanted with Klemm-Schellman nails. This study addressed the clinically relevant question of whether to use one or two distal interlocking screws. They demonstrated that during axial loading although the load to failure was similar the mode of failure was different in the two groups of femurs. In femurs with a single distal interlocking screw the screw failed whereas in constructs with two screws the nail failed. There was no difference between the two groups in terms of rotational stiffness. They concluded that with a slotted nail system a single distal screw provided adequate stability in distal third femoral fractures.

II. **Material properties** - The most ideal material for manufacturing intramedullary nail is still an area of ongoing research. Key requirements of the ideal material are biocompatibility, biomechanical equivalence and clinical compliance (257). A material which is systemically nontoxic, non-immunogenic and non-carcinogenic qualifies as biocompatible. Biomechanical equivalence refers to the ability to restore physiological loading and result in strains and stresses that are compatible with the requirements of the adjacent bony and soft tissue structures. Additionally the material should be safe for implantation and allow easy removal following fracture healing without undergoing corrosion or degradation. It should allow all imaging modes like ultrasound, magnetic resonance imaging and computed tomography without induction of artefacts.

Bone is a living tissue that responds to mechanical loads (170). Homeostasis of bone mineral content and fracture healing rely on continuous load transmission. However, if bone tissue does not experience physiological loads then it begins to lose mineral content leading to relative osteopenia a phenomenon termed as stress shielding (202, 258, 259). It is therefore vital that the materials used to manufacture a load sharing device like an intramedullary nail have the ability to distribute stress to both the nail and the bone appropriately. In order to achieve this elastic modulus of the material should be similar to that of the bone. The elastic modulus of titanium alloys is 6 times greater than that of cortical bone. In comparison the elastic modulus of stainless steel is 12 times greater (260). Therefore titanium alloys are better implant materials for the prevention of stress shielding.

Fracture fixation implants require a material with high yield strength and high fatigue resistance. Intramedullary nails were initially manufactured from 316L stainless steel but increasingly titanium alloys are becoming the material of choice (257). Titanium alloys like Ti-6Al-4V (TAV) and Ti-6Al-7Nb (TAN) are used in the current generation of intramedullary nails. Due to the absence of chromium and nickel, TAV is recommended for patients with allergy to these metals. The material properties are listed in Table 3-2.

Table 3-2 Material properties of metals and alloys used in manufacture of intramedullary nails

SS-stainless steel, CP-commercially pure [Adapted from Mazocca *et al*. (260)]

Material	Yield Strength (MPa)	Ultimate Tensile Stress (MPa)	Fatigue Strength (MPa) (10^7 cycles)	Elastic Modulus (GPa)
316L SS	690	860	310	200
CP Titanium ASTM F-67 (261)	485	550	240	104
Ti-6Al-4V ASTM F-136 (262)	795	860	520	114
Ti-6Al-7Nb ASTM F-1295 (263)	800	900	600	105
Cortical bone	130	150	-	17

The Russell-Taylor reconstruction nail (Smith and Nephew) (245) and the ZMS reconstruction nail (Zimmer) (264) are made from cold-worked stainless steel; the Uniflex reconstruction nail (Biomet, Warsaw, IN) (265), the CFX nail (Howmedica) (266), and the TriGen nail system (Smith and Nephew) (267) are made from titanium alloy.

III. **Fracture configuration and location** - Bucholz *et al*. (268) performed finite element analysis following a retrospective review of failure of interlocking nails in seven patients with distal third femoral fractures. They reported that the risk of fatigue failure significantly increased if the fracture was located at a distance of five centimeters or less from the more proximal of the two distal interlocking screw holes. A fracture in the distal aspect of the femur results in a longer moment arm (the perpendicular distance from the load to the fracture site) and correspondingly higher stresses (269). Intramedullary nail fixation of distal third femoral fractures can be technically more demanding and the corner of the screw hole can be nicked by the drill or whilst inserting the interlocking screw. This can result in an additional stress riser and contribute to the fatigue process. The distal aspect of the femur flares laterally around the metaphyseal region. Hence a relatively longer length of interlocking screw is required. If the screw is not well supported by trabecular bone but mainly by the cortex, then its stiffness and strength decrease with the 3rd power of its length between cortices. If the screw length doubles, the deformation of the screw under the same load increases by a factor of 8 (269).

Using synthetic femurs Antekeier *et al*. (270) simulated distal third fractures at a distance of 1, 2, 3 and 4 cm from the more proximal of the distal locking screw of a titanium nail system and subjected them to compression/bending cycles. They noted that the antegrade titanium alloy nail survived 1 million bending / compression cycles when the fracture was located ≥3 cm from the more proximal of the two distal locking screws. Awareness of these potential problems has led to design optimisation like increasing material thickness around the interlocking screw holes, closing the proximal section of the nail and cold forming amongst others to improve the fatigue performance (269).

IV. **Host bone quality** - Poor bone quality is detrimental to normal physiology and contributes to pathological fractures. It also affects fracture healing and as a consequence increases the risk of complications following intramedullary nail fixation (271). Wähnert *et al*. (272) investigated four different fixation devices using a combination of osteoporotic synthetic bone model with AO/ASIF type 33-C2 fracture and eight pairs of fresh-frozen human cadaveric femora. They noted that the intramedullary nail with four-screw distal locking construct had the greatest torsional strength and axial stiffness.

3.3 Background

The Expert Adolescent Lateral Femoral Nail is an intramedullary nail fixation system manufactured by DePuy Synthes (273). It has been available for clinical use since 2009 (274). The unique helical shape of the nail has been developed based on an anatomical study by Ehmke *et al*. (16). Using a 3-dimensional motion tracking sensor embedded in a reamer they demonstrated the reamed canal of the femur to exhibit a multiplanar curvature. This curvature represented a helix with a 1000 mm radius and 0.6°/mm pitch. The helical shape of the ALFN allows an entry point through the greater trochanter (29). This has the potential advantage of decreasing the risk of iatrogenic damage to the vascular supply of femoral head and subsequent AVN (29, 50).

3.4 Indications

ALFN is indicated for use in adolescent patients with the following conditions:

i. Fractures of the femoral shaft
ii. Subtrochanteric fractures
iii. Ipsilateral neck / shaft fractures
iv. Impending pathologic fractures
v. Nonunion and malunion

In the current study only fixation of femoral shaft fractures (region highlighted in Figure 1-1) using ALFN was investigated.

3.5 Design features of ALFN system

The ALFN intramedullary nailing system consists of the following components:

i. ALFN - a rigid cannulated intramedullary nail manufactured from a titanium alloy (TAN - titanium-6% aluminium-7% niobium) with a helical fluted cross section (Figure 3-6). It is available in a range of lengths (240 mm to 400 mm, in 20 mm increments) with a diameter of 8.2 mm and 11 mm in the distal and proximal regions respectively. Subsequent to the commencement of this study two further variants (9 mm and 10 mm diameter) of the distal region have been released (275). Based on the laterality of use left or right sided ALFN can be selected in the above dimensions. ALFN has provision for proximal and distal interlocking screw placement depending on the site and pattern of fracture. Three types of standard proximal locking options can be used namely 120° antegrade locking, dynamic locking and static locking.

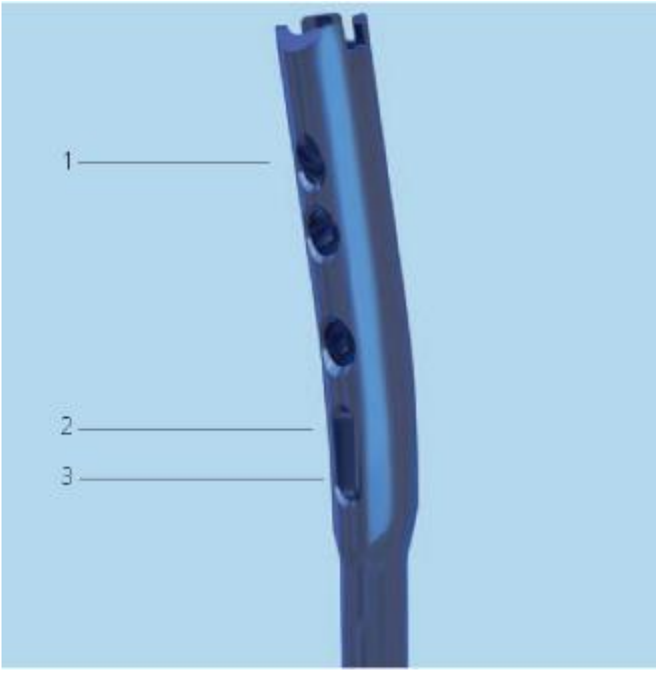

Figure 3-5 Proximal interlocking options - 1) 120° antegrade locking 2) dynamic locking 3) static locking

The first and the second distal interlocking holes are oriented transversely and are located at a distance of 42 mm and 12 mm respectively from the distal end of the nail (Figure 3-6).

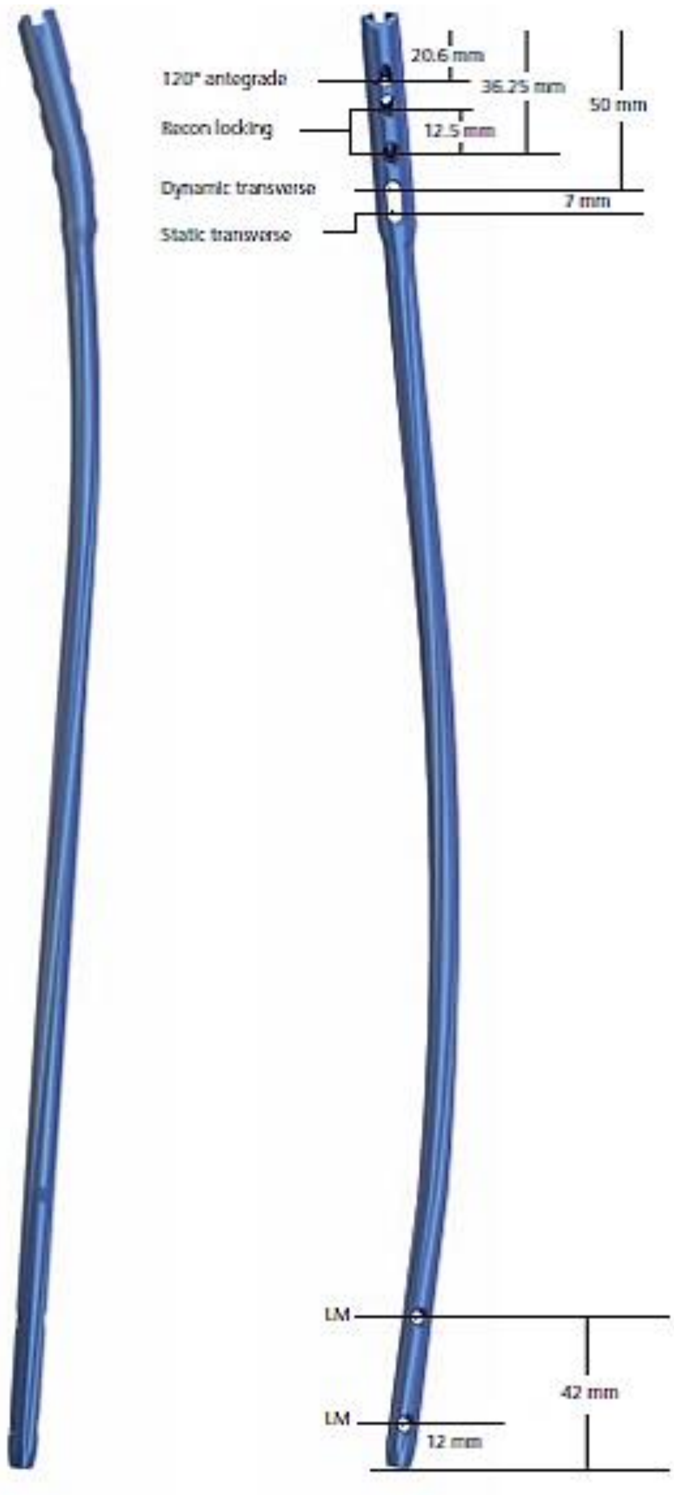

(a) (b)

Figure 3-6 Dimensions of Expert Adolescent Lateral Femoral Nail (20) a-anteroposterior view b-lateral view

The proximal interlocking screw hole is located at a distance of 20.6 mm from the proximal end and is set at an angle of 120° with respect to the long axis of the femur (Figure 3-7).

Figure 3-7 Illustration of 120 degree proximal interlocking screw

ii. Standard interlocking crews - The interlocking screws are manufactured from TAN with 4.0 mm diameter. The screws are fully threaded with a self-tapping blunt tip. The screws are available in a range of length (18-80 mm) with 2 mm increments.

Figure 3-8 Standard interlocking screw

iii. Hip screws - These TAN screws are 5.0 mm in diameter with a core diameter of 3.2 mm. They are partially threaded, self-tapping with a blunt tip and are available in a range of length (50-125 mm) with 5 mm increments. They are indicated in recon locking mode especially fractures of the femoral neck.

Figure 3-9 Illustration of recon locking with hip screws

iv. End caps - They are used at the proximal end of the ALFN to protect nail threads from tissue ingrowth and facilitate subsequent nail extraction. Endcaps are manufactured from TAN with an 8.2 mm diameter. The end caps are available in different sizes. 0 mm end cap sits flush with the nail whereas the other sizes (5 mm, 10 mm and 15 mm) extend the nail height in a scenario where the ALFN is over inserted.

Figure 3-10 Illustration of end cap insertion into proximal end of ALFN

The current study addressed fractures located in the femoral shaft. Hence the fixation comprised of ALFN with 120 degree proximal interlocking screw and two distal interlocking screws (Figure 1-1, Figure 3-7).

3.6 Summary

The technique of intramedullary nail fixation used to treat fractures has evolved to improve both the biomechanical performance of these implants and the clinical outcomes in patients. In general for any fracture fixation implant, complementary data from biomechanical and clinical studies contributes towards robustness of evidence. In the case of ALFN early clinical studies have reported good results (29). The current study aimed to address the paucity of *in vitro* biomechanical data regarding this implant using a combination of experimental testing and finite element analysis. The next chapter introduces the reader to the small composite femur which formed the basis of experimental testing in this study.

4 PAEDIATRIC FEMUR - EXPERIMENTAL MODEL

4.1 Introduction

This chapter describes the biomechanical testing of a paediatric femur to establish the stiffness parameters of an intact bone.

4.2 Basic biomechanical concepts

In general, biomechanics entails the study of internal and external forces acting on biological systems (viz. human musculoskeletal system including the bones, tendons, ligaments and adjunctive organs) and their resultant effects. Therefore biomechanical evaluation of the musculoskeletal system requires a good understanding of basic mechanics.

Mechanical properties of bone are basic parameters based on the structure and function of individual bone. These can be measured and analysed by testing whole bones or specimens (276). As noted in chapter 2, the mechanical behavior of a long bone like the femur and its resultant stiffness depends on several factors viz. magnitude of load, direction of load, rate of load application amongst others. Hence a brief description of the fundamental concepts, terminology and definitions relevant to biomechanical testing is presented in the section below.

Biomechanics encompasses two main branches of mechanics: statics and dynamics (276). Statics deals with forces acting on an object or biological structure at rest (277). Dynamics refers to the forces acting on an object or biological structure in motion and the resultant change in motion due to such forces (277). Dynamics is subdivided into kinematics and kinetics (276). Kinematics describes the relations among displacements, velocities and acceleration of on object or biological structure without regard to the forces involved (276). Kinetics on the other hand deals with the forces causing movement of an object or biological structure (276).

4.2.1 Force and displacement

Force (*F*) or load is a physical entity in mechanics that is used to describe the action of one body on another. Force is a vector quantity that has both magnitude and direction. Thus force or load acting on a body can result in either an external effect (change in velocity / displacement) or an internal effect (deformation of the body) (276). Three fundamental force components acting on a body are recognized namely compressive, tensile and shear.

During biomechanical tests a load (*F*) can be applied to a bone or a fracture fixation construct (fractured bone stabilised with a surgical implant). The resultant deformation/displacement (δ) is measured and plotted as a function of the load to obtain a load-displacement curve (Figure 4-1).

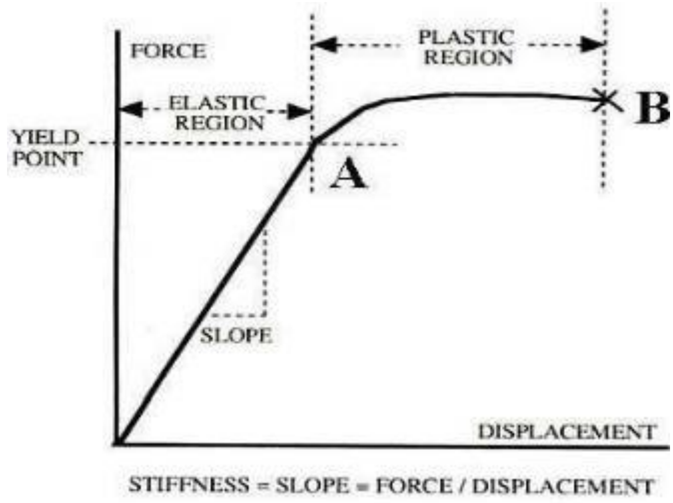

Figure 4-1 Typical load-displacement curve

A typical load-displacement curve consists of different regions. The initial part of the curve is characterised by a linear relationship between load and displacement. This region is referred to as the elastic region as the deformation induced by the load application is recovered following the removal of the load (277). The slope of the linear part of the curve is known as structural stiffness (k). The elastic limit (or yield point, A) of the bone specimen or fixation construct represents the load value at the upper limit of the elastic region. The region beyond the yield point is the plastic region wherein the linear relationship between the load and displacement is not maintained. Permanent deformation associated with yielding of the construct occurs in this region which cannot be recovered despite complete removal of the load. The area under the load-displacement curve is a measure of the energy absorbed by the bone or fixation construct as it is being deformed (277). Point B in the Figure 4-1 indicates the load at which mechanical failure of the bone or fixation construct occurs.

4.2.2 Stress and strain

Stress is the ratio between the applied load (F) and its area of application (A) (276). Depending on the direction of the applied load, stresses can be identified as normal (σ) or shear (τ). Normal stress occurs when the load is perpendicular to the area of application (A) whereas a load in parallel to the area of application (A*) results in shear stress (277).

$$\sigma = \frac{F}{A} \tag{1}$$

$$\tau = \frac{F}{A^*} \tag{2}$$

Stress is expressed in units of N/m^2 or Pascal (Pa). In a bone specimen stress due to load application occurs due to the bonds between molecules, between collagen fibers and the bonding between collagen and hydroxyapatite crystals (276).

Strain (ε) represents the change in dimension of a body under the action of a force or multiple forces (276). In response to a load if a given body with a unit length (L) undergoes a change in dimension (ΔL) then the strain is calculated as:

$$\varepsilon = \frac{\Delta L}{L} \tag{3}$$

Similar to the aforementioned load-displacement curve, the stress-strain curve (Figure 4-2) displays the relationship between applied stress and resultant strain in a bone or fixation construct during mechanical testing (276, 278).

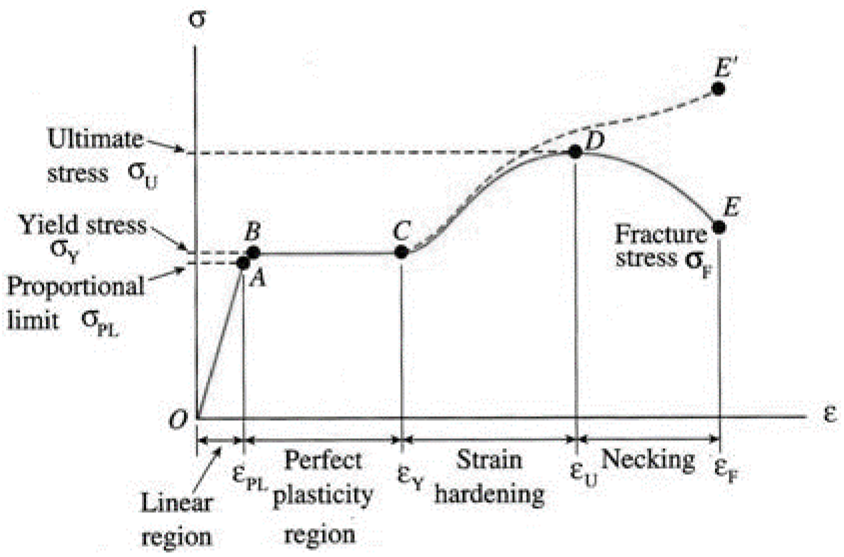

Figure 4-2 Typical stress-strain curve

The slope of the linear part of the stress-strain curve in the case of normal stress and strain is called the elastic modulus (E) (Equation (4)). Conventionally the elastic modulus determined in a tensile test is called Young's modulus.

$$E = \frac{\sigma}{\varepsilon} \tag{4}$$

From the above equation it can be observed that stress and strain are linearly related in an elastic material (Hooke's law) (Equation (5)).

$$\sigma = E\varepsilon \tag{5}$$

The mechanical properties of biological tissues like bone are not linear throughout their physiological range mainly due to the nonlinear behavior of their fluid component (276).

In the context of shear stress and strain plot, the slope is termed shear modulus or modulus of rigidity (G) (Equation (6))

$$G = \frac{\tau}{\gamma} \tag{6}$$

Compliance (C) is the inverse of stiffness or modulus. It is defined as the ratio of deformation to load (or strain) to stress (276).

$$C = \frac{\varepsilon}{\sigma} \tag{7}$$

Biological materials like cartilage, tendon and muscle have high compliance values and low E values. In comparison bone has low compliance values and relatively high E values. However, mechanical testing machines are constructed of considerably high-modulus materials (E of steel

≈ 200 GPa). Hence for all practical purposes their compliance is considered as zero when testing materials such as cortical bone (E= 5 to 21 GPa) or cancellous bone (E < 1GPa) (276).

4.2.3 Mechanics of beams, columns and shafts

Engineering design of a structure utilises beams, columns, shafts or a combination of all in order to support the structure and help distribute the load. As an integral part of the musculoskeletal system, bones (and fracture fixation implants) function as beams, columns or shafts capable of handling complex loading conditions *in vivo* (279) (197). In general, a beam sustains load between two supports, a shaft resists torsion and a column supports compressive loads (Figure 4-3).

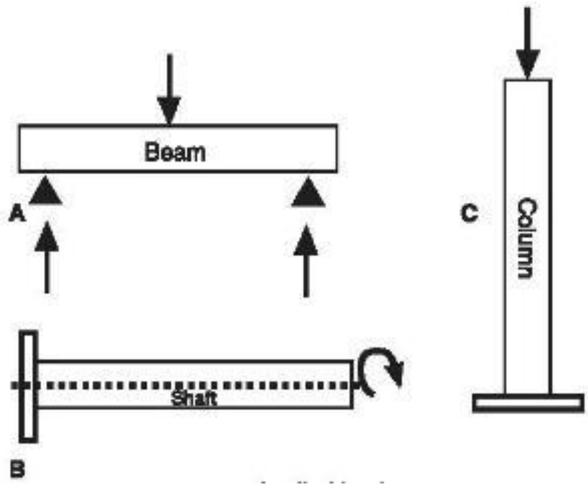

Figure 4-3 Three basic types of load bearing structures [Reproduced from Thakur *et al*. (197)]

A beam is a structure with one of its dimensions much larger than the other two (280) and normally supports transverse loads. Loading of beams with cantilever, three-point and four-point bending are described (197, 281). In cantilever bending the beam is supported at one end and the load is applied at any point along the length of the beam. During three-point bending of a beam, the top (concave) surface shortens resulting in compressive stress while the bottom (convex) surface lengthens resulting in tensile stress. In four-point bending, the load is applied in two points and the bending moment is constant between the two loading points. Therefore four-point bending test does not rely upon the exact position of the fracture or the callus. This phenomenon is clinically significant and is used by orthopaedic surgeons for the assessment of bone healing, callus stiffness or the quality of osteogenesis (197) (Figure 4-4).

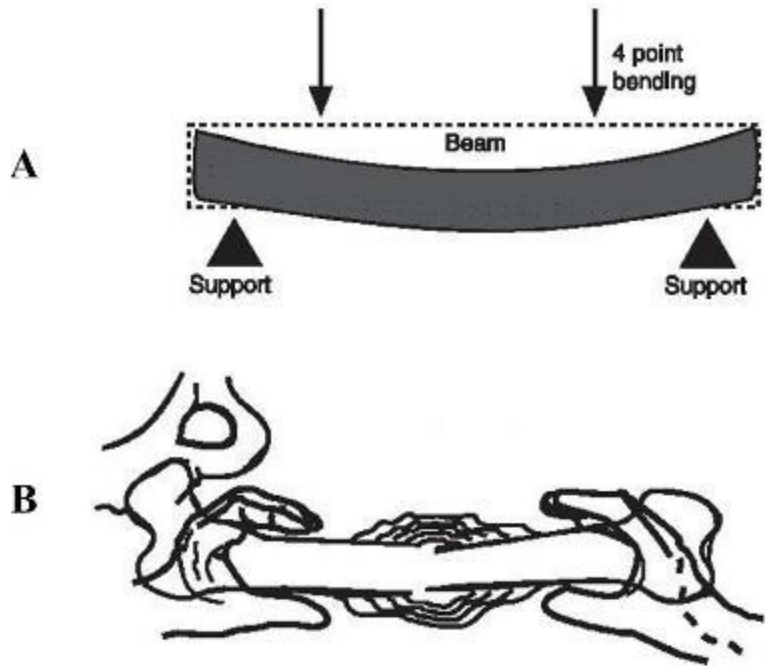

Figure 4-4 Clinical assessment of fracture callus in femur (B) similar to the four-point bending test of a beam (A). [Reproduced from Thakur *et al*. (197)]

Bending stiffness of a beam can be denoted as either the ratio of load over deformation (N / m) or the ratio of bending moment to angular deformation (N m/deg). Bending stiffness depends on the length (L) of the unsupported span of the beam and its cross sectional shape (area moment of inertia, I). For a rectangular cross-section beam, I is given by

$$I = \frac{w \times d^3}{12} \tag{8}$$

where w = dimension parallel to the bending plane and d = dimension vertical to the bending plane. In the case of a bone and an intramedullary nail which has a circular cross-section hollow beam, I is given by

$$I = \frac{\pi\,(D^4 - r^4)}{4} \tag{9}$$

where D = outer diameter and r = inner diameter of the hollow cylinder.

The maximum deflection at the center of a beam (d) undergoing a four-point bending load is given by

$$d = \frac{F}{EI} \times \frac{a}{24} \times (3L^2 - 4a^2) \tag{10}$$

where F = load on the beam, E = modulus of elasticity, I = moment of inertia, a = distance between support and loading point, L = length of the beam overlying the supports (Figure 4-5).

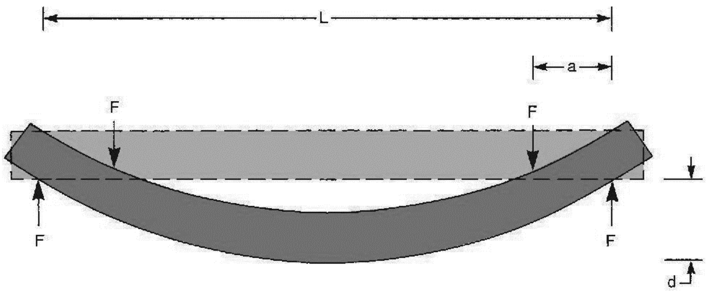

Figure 4-5 Four-point bending test of a beam. Original shape indicated by dashed lines and deformed shaped indicated by solid lines. [Reproduced from Hipp *et al*. (282)]

Bones function as columns to support compressive loads. When a load is applied to the central axis of a column, a uniformly distributed stress pattern is noted. However, if the load is applied off-center then the stress pattern changes such that it creates elements of compression and tension along the column due to bending. The more eccentric the loading, the greater the bending component generating higher stresses. The femur, being a weight bearing bone functions as a column in transmitting the load to the ground. Load applied on the femoral head generates tension (lateral cortex) and compression (medial cortex) stresses along the shaft (Figure 4-6).

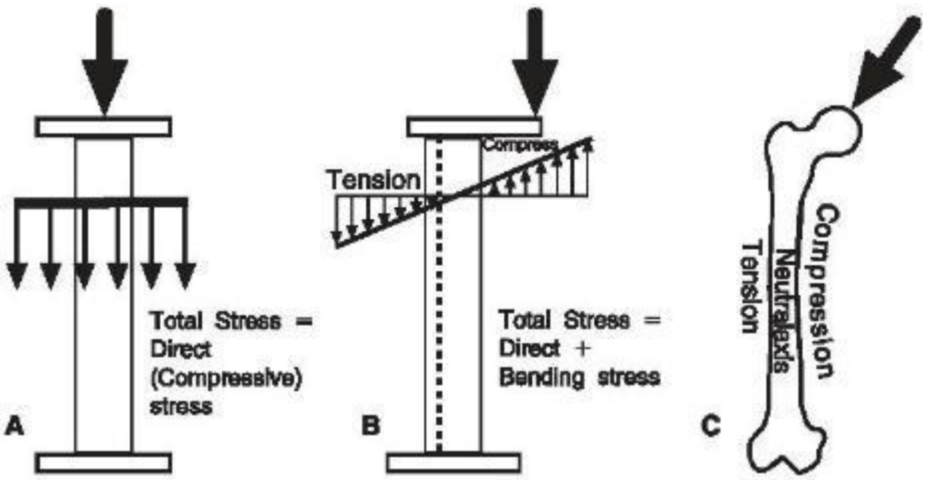

Figure 4-6 Loading patterns of a column A – uniaxial loading B – eccentric loading C – Stress pattern in weight bearing bone like femur [Reproduced from Thakur (197)]

If an axial load (F) is applied along the long axis of a structure of length (L), the resulting deformation ΔL (shortening or elongation) is given by the equation

$$\Delta L = \frac{F.L}{E.A} \tag{11}$$

where E = Young's modulus and A = mean cross-sectional area. The product $E.A$ is referred to as axial rigidity of that structure and is measured in Newtons (N). As per equation (11) it can be noted that

$$E.A = \frac{F.L}{\Delta L} \tag{12}$$

Axial stiffness (k) of a structure is defined as the force required to produce a unit deflection. It is measured in N / m or N / mm and is given by the equation

$$k = \frac{E.A}{L} \tag{13}$$

(Substituting $E.A = \frac{F.L}{\Delta L}$ in the above)

$$k = \frac{F}{\Delta L} \tag{14}$$

Long bones like the femur function as shafts to resist torsional loads. Torsion results from torque (twisting force) applied to the long axis of a cylindrical structure (shaft) (197). Subsequently there is a relative rotation of one end of the shaft with respect to the other through an angle (θ) (Figure 4-7)

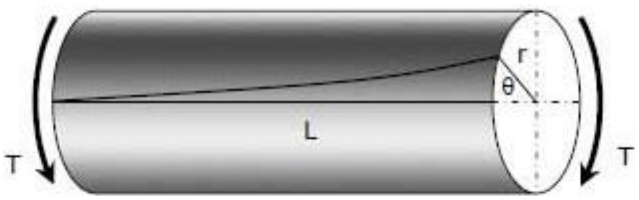

Figure 4-7 Torsion of a shaft

The resistance of a shaft to a torsional load depends on the length (L), the polar moment of inertia (J) and the shear modulus (G). The angle of twist (θ) which is measured in radians is given by

$$\theta = \frac{T.\ L}{G\ .\ J} \tag{15}$$

The polar moment of inertia is a quantitative measure describing the distribution of material about the long axis of a shaft undergoing torsion. For a hollow cylindrical structure it is given by the following equation

$$J = \frac{\pi\ (D^4 - r^4)}{32} \tag{16}$$

where D = outer diameter and r = inner diameter of the hollow cylinder.

Thus a small change in the shaft diameter can result in profound increase in J. Torsional rigidity of a shaft (expressed in $N.m^2$) is a product of shear modulus and polar moment of inertia (G.J). Torsional stiffness (G.J / L) represents the torque required to produce a unit of rotation at one end of the shaft relative to the other. It is expressed in N.m.

Normalising the stiffness of bone specimens or fixation constructs to the stiffness of intact bones allows the stiffness to be expressed as a percentage of intact stiffness. This methodology is used in the subsequent chapters of the thesis.

4.3 Objectives

The objectives of the experimental part of the study were as below:

i. Develop customised test jigs which allowed for consistent alignment and repeated testing of the experimental specimens (described in Appendix B).
ii. Define the stiffness parameters of interest for the composite femurs (axial, four-point bending and torsional).

4.4 Materials and methods

4.4.1 Experimental femur model

4.4.1.1 Rationale for use of synthetic composite femur

Cadaveric femurs have in the past been used for biomechanical investigation of intramedullary nails (283-285). However, the major limitation with cadaveric specimens in comparative biomechanical testing has been the inter-specimen variability and the number of tests required to ensure robust results (286). Additionally access to good quality, disease free cadaveric femurs is not only limited but requires extensive prior approval of the local ethics committee (287). Thus biomechanical researchers have adopted to using mechanically analogous synthetic bones. The advantages of a commercially available composite femur over a cadaveric femur include consistent geometry with low inter-specimen variability, ready availability, easy storage, no special requirement for specimen preparation and handling (286, 288-290). These validated composite femurs have been used extensively in paediatric biomechanical testing (291-299) (Table 1-3). Hence, a composite femur representative of paediatric femur was selected as an experimental model for the study (Figure 4-8).

4.4.1.2 Small left fourth generation composite femur Sawbone®

The small fourth generation composite femur Sawbone® (model 3414) was used as the experimental model in this study. It is manufactured by Pacific Research Laboratories Inc. Vashon, USA and is available in the UK through Sawbones Europe AB (Malmö, Sweden).

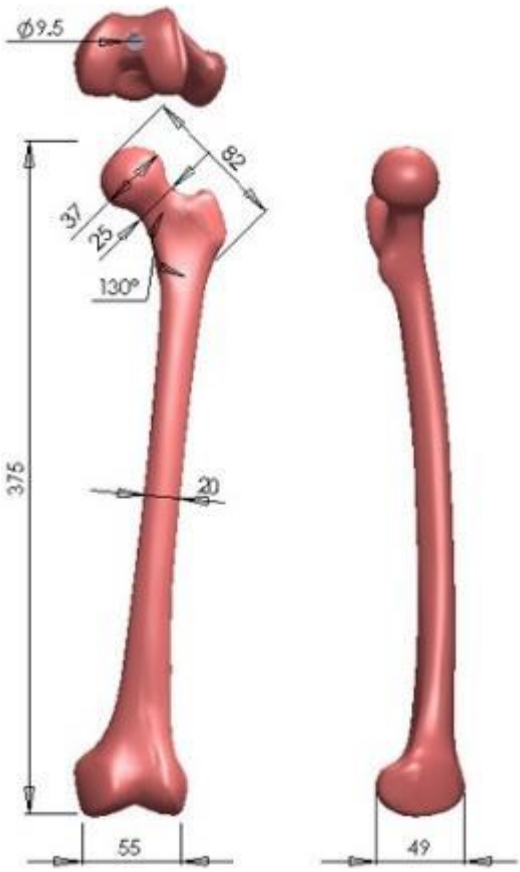

Figure 4-8 Small fourth generation composite femur with dimensions marked in millimeters

The above femur model has simulated cortical bone manufactured using a mixture of short glass fibers and epoxy resin pressure injected around a foam core. It has an intramedullary canal extending from the intercondylar notch to the intertrochanteric region (Figure 4-9). The typical mechanical properties of the simulated cortical and cancellous bone available from the manufacturer are given in Table 4-1 and Table 4-2 (300).

Table 4-1 Typical properties of simulated cortical bone (short fiber filled epoxy) [Reproduced from Sawbones® brochure (300)]

	Compressive		**Longitudinal Tensile**			**Transverse Tensile**	
Density (g/cc)	Strength (MPa)	Modulus (GPa)	Strength (MPa)	Modulus (GPa)	Strain (%)	Strength (MPa)	Modulus (GPa)
1.64	157	16.7	106	16.0	0.80	93	10.0

Table 4-2 Typical properties of simulated cancellous bone (rigid polyurethane foam) [Reproduced from Sawbones® brochure (300)]

		Compressive	
	Density (g/cc)	Strength (MPa)	Modulus (MPa)
Solid	0.27	6.0	155
Cellular	0.32	5.4	137

A set of three composite femurs (labelled as Sp1, Sp2 and Sp3) were used as the bone model. Following satisfactory visual inspection to ensure no cracks or surface irregularities were present, all the specimens underwent digital radiography in co-planar views (anteroposterior, lateral) to identify any potential internal inconsistencies (Figure 4-9). All three specimens were noted to be satisfactory.

Figure 4-9 Digital radiographs of composite femur with size template (left - anteroposterior, right - lateral view)

4.4.2 Design and development of test jigs and alignment molds

A preliminary requirement of any biomechanical testing is to ensure reliable fixtures that secure the test specimen, allow repeatable tests and do not interfere / interact with the test set up (139). In this regard test jigs and alignment molds play a significant role. However, only limited information is available on the topic from the previous biomechanical studies using the composite femur of paediatric dimensions (57, 59, 293). Hence custom test jigs and alignment molds were developed in the initial part of the study to enable:

i. Multiple tests on intact femur specimens in a repeatable and consistent manner
ii. Multiple tests of femur specimens following implantation with ALFN (next part of experimental testing described in chapter 6)
iii. Visual reference points to help the test set up

In addition to the above studies (57, 59, 293), the dimensions for test jigs recommended in the American Society for Testing and Materials (ASTM) standard pertaining to the test methods for intramedullary fixation devices (F1264) were appropriately scaled to suit the dimensions of the small composite femur and used to develop the test jigs (301). Split molds were fabricated using polymethylmethacrylate (PMMA) with the femur specimen held in relevant reference positions within the test jigs. This ensured a consistent alignment and an anatomical fit for all the femur specimens in the test jigs during testing. PMMA was selected as it is a viscoelastic material (302, 303) with easy handling and casting properties (304, 305). A detailed description of the design and development of test jigs and alignment molds is provided in Appendix B.

4.4.3 Biomechanical testing

Several methodologies and testing protocols have been described to establish the stiffness parameters of femurs and fracture fixation implants. However, only limited studies pertaining to paediatric femur fixation are available (Table 1-3). Amongst these considerable variation is noted with respect to the biomechanical testing criteria viz. magnitude of load, loading rate, orientation of specimen, pre-conditioning cycles, number and type of tests performed.

A brief survey of the test parameters used in the biomechanical studies using the composite femur of paediatric dimensions is presented in the tables (Table 4-3, Table 4-4 Table 4-5) below

Table 4-3 Axial load test parameters in the literature

PC – pre-conditioning, N – load in Newtons, N/R – not reported, y - yes, n - no

Author	Specimen orientation (Degree / Axis)	PC cycle	Preload (N)	Load to failure of construct (y / n)	Load (N)	Displacement rate (mm/s)	Number of tests
Flinck *et al*. (299)	Mechanical	N/R	50	n	425	0.07	N/R
Porter *et al*. (306)	25	N/R	N/R	y	3000	0.20	N/R
Volpon *et al*. (56)	11	1	8	n	85	0.10	N/R
Kaiser *et al*. (307)	9	1	N/R	n	150	0.05	3
Kaiser *et al*. (59)	9	1	N/R	n	100	0.05	3
Mahar *et al*. (296)	Mechanical	N/R	N/R	y	N/R	0.50	1
Mani *et al*. (291)	N/R	1	20	n	400	0.10	5
Green *et al*. (293)	N/R	N/R	N/R	n	85	0.10	1
Mahar *et al*. (292)	N/R	N/R	N/R	y	50	N/R	1
Lee *et al*. (75)	N/R	N/R	N/R	y	50	0.50	N/R

Table 4-4 Four-point bending test parameters in the literature

AP – anteroposterior, PA – posteroanterior, ML – mediolateral, LM – lateromedial, PC – pre-conditioning, N – load in Newtons, N/R – not reported, y - yes, n - no

Author	Bending load direction (AP / PA / ML / LM)	PC cycle	Preload (N)	Load to failure of construct (y / n)	Maximum load (N) / bending moment (N m)	Displacement rate (mm/s)	Tests
Flinck *et al*. (299)	ML, LM	N/R	N/R	n	7 N m	0.07	N/R
Flinck *et al*. (299)	AP, PA	N/R	N/R	n	22 N m	0.07	N/R
Volpon *et al*. (56)	PA	1	7	n	67 N	0.10	N/R
Doser *et al*. (58)	AP, LM	1	15	n	N/R	0.33	4
Kaiser *et al*. (59)	AP, PA, ML, LM	1	N/R	n	5 N m	0.05	3
Kaiser *et al*. (307)	AP, PA, ML, LM	1	N/R	n	5 N m	0.05	3
Li *et al*. (294)	N/R	N/R	0.01	y	N/R	0.10	N/R
Mehlman *et al*. (297)	ML	3	N/R	n	N/R	0.05	2
Mani *et al*. (291)	AP, LM	1	20	n	400 N	0.10	5
Green *et al*. (293)	AP	N/R	N/R	n	67 N	1.0	1

Table 4-5 Torsional load test parameters in the literature

ER – external rotation, IR – internal rotation, deg/s – degree per second, PC – pre-conditioning, N – load in Newtons N/R – not reported, y - yes, n - no

Author	Torsional load direction (ER / IR)	PC cycle	Axial load used (N)	Load to failure of construct (y / n)	Maximum load (N m)	Rotation rate (deg/s)	Number of tests
Porter *et al*. (306)	N/R	N/R	311.4	y	N/R	0.10	N/R
Volpon *et al*. (56)	ER	N/R	N/R	y	2	0.50	N/R
Kaiser *et al*. (59)	ER, IR	N/R	N/R	n	10	0.30	N/R
Kaiser *et al*. (307)	ER, IR	N/R	N/R	n	10	0.30	N/R
Mahar *et al*. (296)	ER, IR	N/R	20	n	2	0.50	1
Goodwin *et al*. (66)	ER, IR	N/R	20	n	1	0.50	10
Mehlman *et al*. (297)	ER, IR	N/R	N/R	n	10	0.75	N/R
Mani *et al*. (291)	N/R	N/R	N/R	n	20	0.30	5
Green *et al*. (293)	ER, IR	N/R	N/R	n	2	0.50	1
Lee *et al*. (75)	ER, IR	3	20	n	1	N/R	2

As evident from the above, different investigators have used different load parameters and test protocols whilst evaluating paediatric femoral fracture fixation implants. Furthermore the rationale for use of these parameters (viz. destructive or nondestructive testing / specimen orientation / preload / loading rate / number of preconditioning and data acquisition cycles) is sparse and not clearly stated in the methodology. This lack of standardisation is compounded by the fact that the majority of the published testing protocols to estimate whole bone stiffness are based on the adult femur (286, 288, 308, 309).

Numerous clinical studies have described the forces acting on the femur *in vivo* (310-317). It can be observed that this body of research has been undertaken on adult patients with femoral endoprostheses as a part of total hip replacement (THR). Nonetheless certain consensus points emerge from these studies:

i. Loads acting on the femur *in vivo* are complex
ii. Loads acting on the femur are significantly influenced by the position of the lower limb and activity being undertaken
iii. Muscles play a substantial role in balancing the loads acting on the femur
iv. Bony anatomy of the femur viz. neck anteversion affect the overall hip joint contact force and bending moment
v. Walking aids like crutches which are frequently used in the postoperative period can reduce the joint load by 20 to 50%

Pioneering work by Schneider *et al*. (249) has provided useful insight into *in vivo* loads acting on intramedullary nails used to stabilise a femur with a midshaft fracture. Using a telemeterised stainless steel nail (length of 400 mm, outer diameter of 16 mm) in an adult male weighing approximately 70 kg they recorded different force components (Figure 4-10).

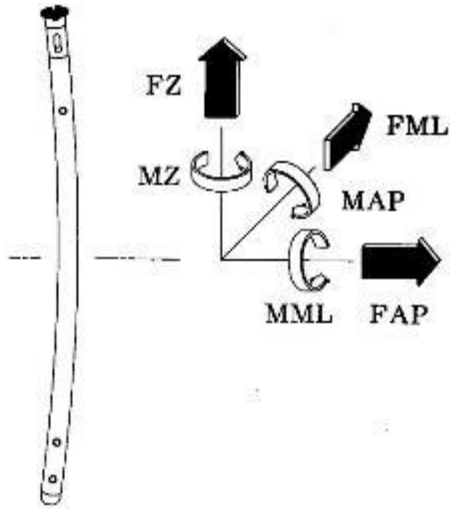

Figure 4-10 Force components acting on intramedullary nail in femur *in vivo*. The coordinate system is fixed to the midpoint of the central cross-section of the nail. FZ points upwards in the axial direction, FAP from posterior to anterior and FML from medial to lateral. MZ, MML and MMAP are the corresponding moments. [Reproduced from Schneider *et al*. (249)]

They reported an axial load (FZ) of 300.6 (± 26.7) N on the nail with the patient partially weight bearing at 250 N. In the same loading scenario they measured a bending moment in the anteroposterior plane (FAP) at -16.2 (± 5.4) N m whereas the torsional moment (MZ) along the long axis measured 5.6 (± 2.3) N m.

Rigid intramedullary nail like the ALFN is clinically indicated in children weighing more than 45 kg with femoral shaft fractures (29). Hence for the purpose of biomechanical testing a hypothetical adolescent with a body weight of 60 kg was considered. The load parameters described below (and in the subsequent part of the study) were based on this clinical scenario.

Stiffness parameters (axial, four-point bending and torsion) of the three intact small composite femur specimens (labelled as Sp1, Sp2 and Sp3) were established as described below.

4.4.3.1 Axial compression test

Each femur specimen was mounted onto an Instron TT-D materials testing machine (Instron, High Wycombe, UK) and aligned using custom designed jigs and PMMA split molds (318) (Figure 4-11). The following sequence of steps were performed during each test setup:

i. The circular aluminium base was mounted on the load cell of the Instron materials testing machine such that the screw marked ‘front’ faced anteriorly.
ii. The PMMA molds were applied around distal portion of the composite femur. This was placed flat on the circular aluminium base and lined up with the ‘front’ screw to enable correct alignment. Following visual checks the multidirectional screws were tightened to secure the femur in the base unit.
iii. The top unit was secured onto the crosshead of the testing machine and lowered into position such that the central socket in the epoxy resin block accomodated the femoral head.
iv. Following verification of the test setup, a compressive load of up to 600 N was applied at a displacement rate of 0.17 mm/s along the mechanical axis of the femur during the axial loading test (299, 319).

A set of 6 loading tests were performed on each composite femur. A 10 minute interval was allowed between each loading test for the viscoelastic properties of the bone to return to the normal state (286). After the completion of test cycles each specimen was closely inspected to note for surface defects or cracks and found to be satisfactory.

Figure 4-11 Intact femur aligned along mechanical axis in Instron materials testing machine during axial compression test

4.4.3.2 Four-point bending test

The midpoint of the diaphysis (located 175 mm below tip of greater trochanter) was marked on each femur specimen. A four-point bending test in the anteroposterior direction was performed with a force of 400 N applied through a top unit with two rollers separated by a distance of 70 mm (301) (Figure 4-12). The following sequence of steps were performed during each test setup:

i. The base unit was mounted onto the Instron materials testing machine. The composite femur was placed on the base unit such that the obliquely oriented proximal support was just distal to the lesser torchanter to provide a stable support for the composite femur. The distal femoral metaphysis rested on the perpendicularly oriented distal support.

ii. The top unit was secured onto the crosshead of the testing machine and lowered into position such that the two rollers were equidistant from the midpoint of the diaphysis

iii. Following verification of the test setup, a bending load of up to 400 N was applied at a displacement rate of 0.17 mm/s

Figure 4-12 Four-point bending test setup

A set of 6 loading tests were performed on each composite femur (286). A 10 minute interval was allowed between each loading test for the viscoelastic properties of the femur to return to the normal state (286). Each specimen was closely inspected to note for surface defects and cracks at the end of test cycle.

4.4.3.3 Torsion (internal rotation) test

During torsion tests the proximal and distal aspects of each femur was encased in PMMA split molds and placed inside proximal and distal aluminium cylindrical units, respectively. This arrangement aligned the mechanical axis of the composite femur to the mid-axis of the cylindrical units (320) (Figure 4-13). The following sequence of steps were performed during each test setup:

i. The distal PMMA molds were applied around the condyles of the femur and inserted into the distal aluminium cylindrical unit.
ii. The proximal PMMA molds were applied to encase the femoral head and the trochanters. The molds were then inserted into the proximal cylinder and the reference marks on the mold aligned with the corresponding marks on the cylinder. The reference marks ensured that the aluminium lever arm was in a true horizontal position ie. zero degree of rotation.
iii. Following satisfactory inspection of the alignment, the metal plate of the distal cylinder was secured to the base plate with washers and screws. The circumferential grub screws on the proximal and distal aluminium cylinders were tightened to secure the PMMA split molds contained in them.
iv. The digital inclinometer (Digi-Pas DWL-130, resolution of 0.05° with accuracy 0.05° at 0° & 90°) was switched on and referenced to zero degree
v. After verification of the test setup, torque was applied in 0.2 N m increments up to 4 N m using calibrated weights (0.988 N = 100.712 g) suspended on an aluminium lever arm (length = 202.5 mm) attached to the proximal cylindrical unit. The resultant internal rotation (°) was measured using a digital inclinometer mounted on the aluminium lever arm.

Each femur underwent 6 torsional loading tests. A 10 minute interval was allowed between each loading test for the viscoelastic properties of the bone to return to the normal state (286).

Subsequent to the test cycle each specimen was closely inspected to note for surface defects and cracks.

Figure 4-13 Torsional test (internal rotation) setup with calibrated weights

4.4.3.4 Torsion (external rotation) test

Following internal rotation tests, the grub screws on the proximal cylindrical unit were loosened and the unit with the lever arm was rotated 180° in a clockwise manner. The grub screws were subsequently tightened and the digital inclinometer was repositioned and reset to zero degree. Torque was applied in 0.2 N m increments up to 4 N m using calibrated weights suspended on an aluminium lever arm attached to the proximal cylindrical unit. The resultant external rotation (°) was measured using the digital inclinometer. Each specimen underwent six tests in total. A 10 minute interval was allowed between each loading test for the viscoelastic properties of the bone to return to the normal state (286).

4.4.4 Data analysis

Axial stiffness: Load and displacement data from the tests were entered into a spreadsheet (Microsoft Excel® 2010, Redmond, WA, USA). The displacement data was normalized to reflect a starting position of 0 mm and a load versus displacement graph was generated to determine the slope of load-displacement curve (321). The slope represented the stiffness in N/mm for the axial compression test.

Four-point bending stiffness: Load and displacement data from the tests were entered into a spreadsheet (Microsoft Excel® 2010, Redmond, WA, USA). The displacement data was normalized to reflect a starting position of 0 mm and a load versus displacement graph was generated to determine the slope of load-displacement curve (321). The slope represented the stiffness in N/mm for four-point bending test.

Torsional stiffness: Torque and angular rotation (°) data were entered into a spreadsheet (Microsoft Excel® 2010, Redmond, WA, USA). The angular rotation data was normalized to reflect a starting position of 0 degree and a torque versus angular rotation graph was generated to determine the slope of the torque-rotation curve (321). The slope represented the stiffness in N m / deg for the torsional loading test.

For each specimen the mean, standard deviation, coefficient of variation was calculated from the six test results. The mean value thus obtained represented the stiffness of the individual specimen (322, 323). As each of the three femur specimens (Sp1, Sp2 and Sp3) underwent six tests, a total of 18 results for each type of stiffness were obtained. These 18 results were further collated to determine the mean stiffness of intact femur ($k_{\mathrm{EXP}\ Int}$) group.

4.5 Results

4.5.1 Axial compression

The results of six tests on the three femur specimens are shown in Figure 4-14 and Table 4-6.

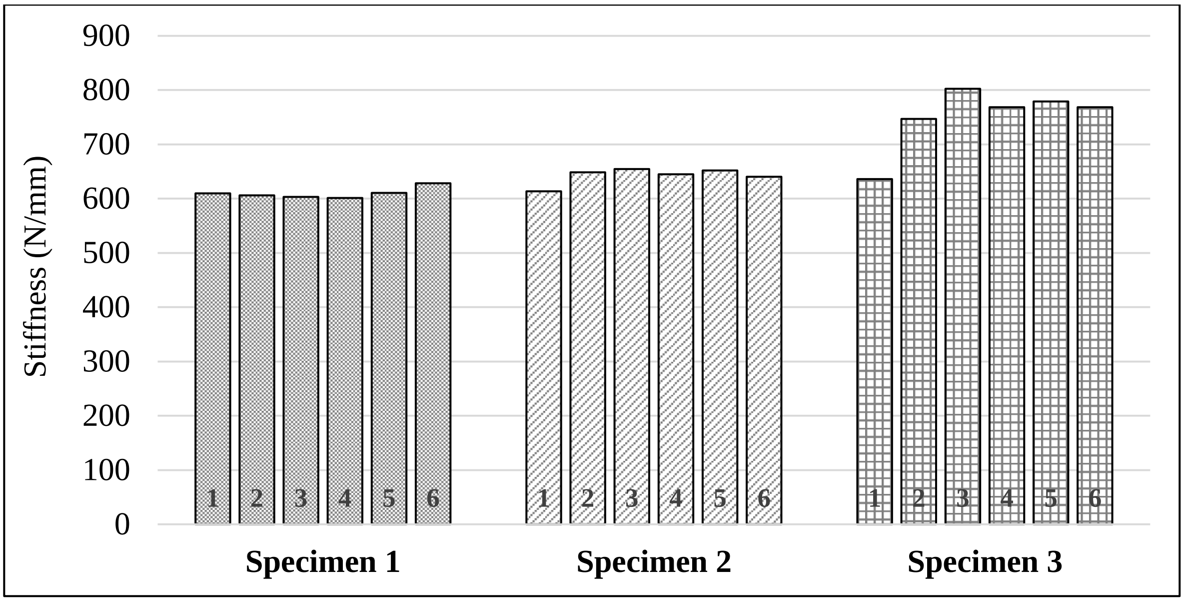

Figure 4-14 Axial stiffness test results of three intact femur specimens

Table 4-6 Axial stiffness of intact femur specimens

n – number of tests, SD – standard deviation, COV – coefficient of variation

Specimen	n	Mean (N/mm)	SD	COV (%)	Minimum (N/mm)	Median (N/mm)	Maximum (N/mm)
Sp1	6	609.79	9.74	1.60	601.17	607.83	628.25
Sp2	6	642.22	14.96	2.33	613.48	646.66	654.46
Sp3	6	750.15	58.77	7.83	635.96	768.41	802.33
Group							
Intact	18	667.39	70.15	10.51	601.17	642.54	802.33

The mean axial stiffness in axial compression of the three femur specimens ranged from 609.79 N/mm - 750.15 N/mm and the standard deviation from 9.74 – 58.77 N/mm. The overall mean axial stiffness of the three femur specimens (intact group) ($k_{\mathrm{EXP\ Ax}\ Int}$) was 667.39 N/mm with a standard deviation of 70.15 N/mm.

4.5.2 Four-point bending

The results of six tests on the three composite femur specimens are shown in Figure 4-15.

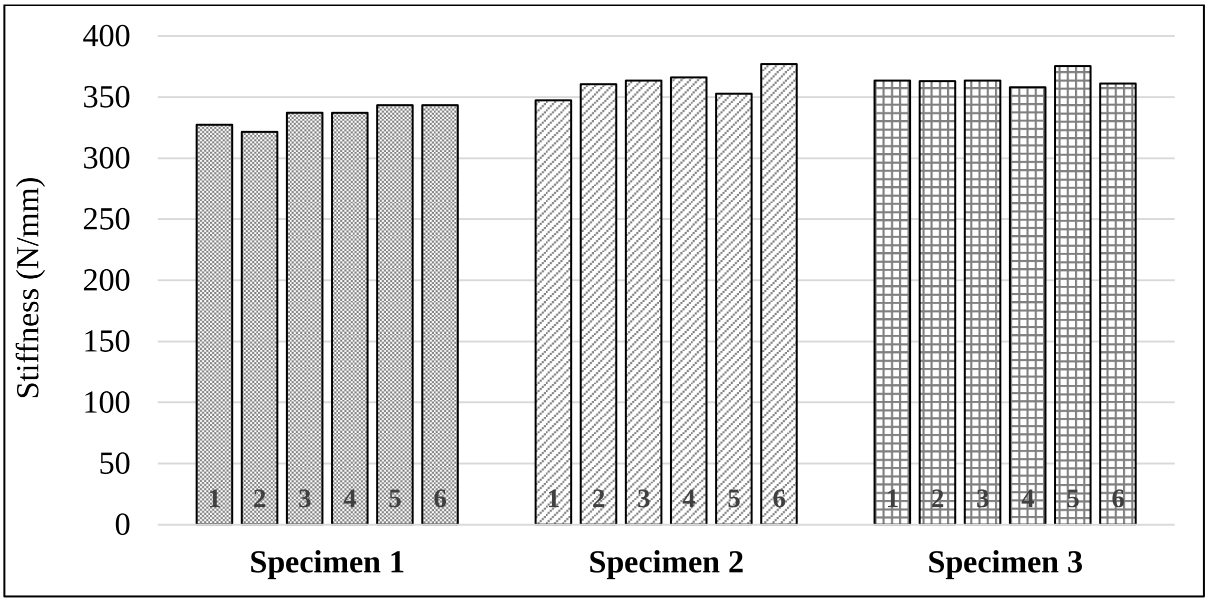

Figure 4-15 Four-point bending stiffness results of three intact femur specimens

The mean four-point bending stiffness of the three femur specimens ranged from 335.03 N/mm – 364.16 N/mm and the standard deviation from 8.83 – 10.42 N/mm. The overall mean four-point bending stiffness of the three femur specimens (intact group) ($k_{\mathrm{EXP\ Be}\ Int}$) was 352.49 N/mm with a standard deviation of 15.72 N/mm. (Table 4-7)

Table 4-7 Four-point bending stiffness of intact femur specimens

n – number of tests, SD – standard deviation, COV – coefficient of variation

Specimen	n	Mean (N/mm)	SD	COV (%)	Minimum (N/mm)	Median (N/mm)	Maximum (N/mm)
Sp1	6	335.03	8.83	2.63	321.55	337.20	343.41
Sp2	6	361.28	10.42	2.88	347.40	362.10	377.07
Sp3	6	364.16	5.90	1.62	358.10	363.35	375.42
Group							
Intact	18	352.49	15.72	4.45	321.55	359.35	377.07

4.5.3 Torsion (internal rotation)

The results of the six tests on the three composite femur specimens are shown in Figure 4-16.

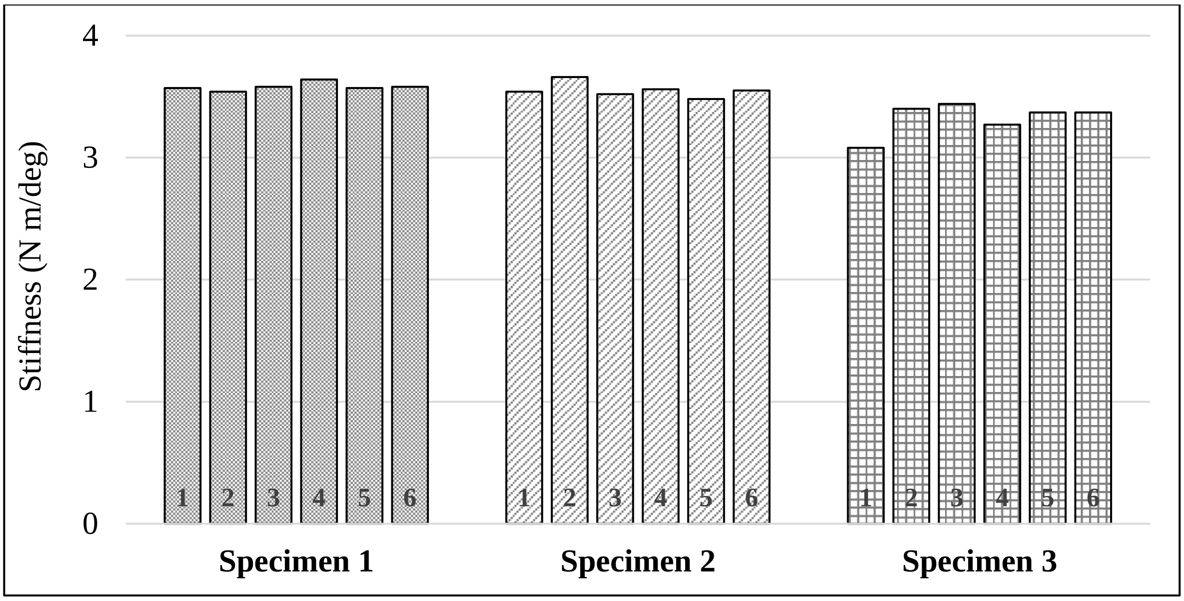

Figure 4-16 Torsional stiffness (internal rotation) results of three intact femur specimens

The mean torsional stiffness of the three femur specimens in internal rotation ranged from 3.32 N m/deg – 3.58 N m/deg and the standard deviation from 0.03 – 0.13 N m/deg. The overall mean torsional stiffness of the three femur specimens (intact group) ($k_{\mathrm{EXP\ Ir}\ Int}$) in internal rotation was 3.48 N m/deg with a standard deviation of 0.14 N m/deg. (Table 4-8)

Table 4-8 Torsional stiffness (internal rotation) of intact femur specimens

n – number of tests, SD – standard deviation, COV – coefficient of variation

Specimen	n	Mean (N m/deg)	SD	COV (%)	Minimum (N m/deg)	Median (N m/deg)	Maximum (N m/deg)
Sp1	6	3.58	0.03	0.92	3.54	3.58	3.64
Sp2	6	3.55	0.06	1.69	3.48	3.55	3.66
Sp3	6	3.32	0.13	3.95	3.08	3.37	3.44
Group							
Intact	18	3.48	0.14	4.12	3.08	3.54	3.66

4.5.4 Torsion (external rotation)

The results of the six tests on the three composite femur specimens are shown Figure 4-17 and Table 4-9. The mean torsional stiffness of the three femur specimens in external rotation ranged from 3.54 N m/deg – 3.63 N m/deg and the standard deviation from 0.17 – 0.23 N m/deg. The overall mean torsional stiffness of the three femur specimens (intact group) ($k_{\mathrm{EXP\ Er}\ Int}$) in external rotation was 3.58 N m/deg with a standard deviation of 0.18 N m/deg. (Table 4-9)

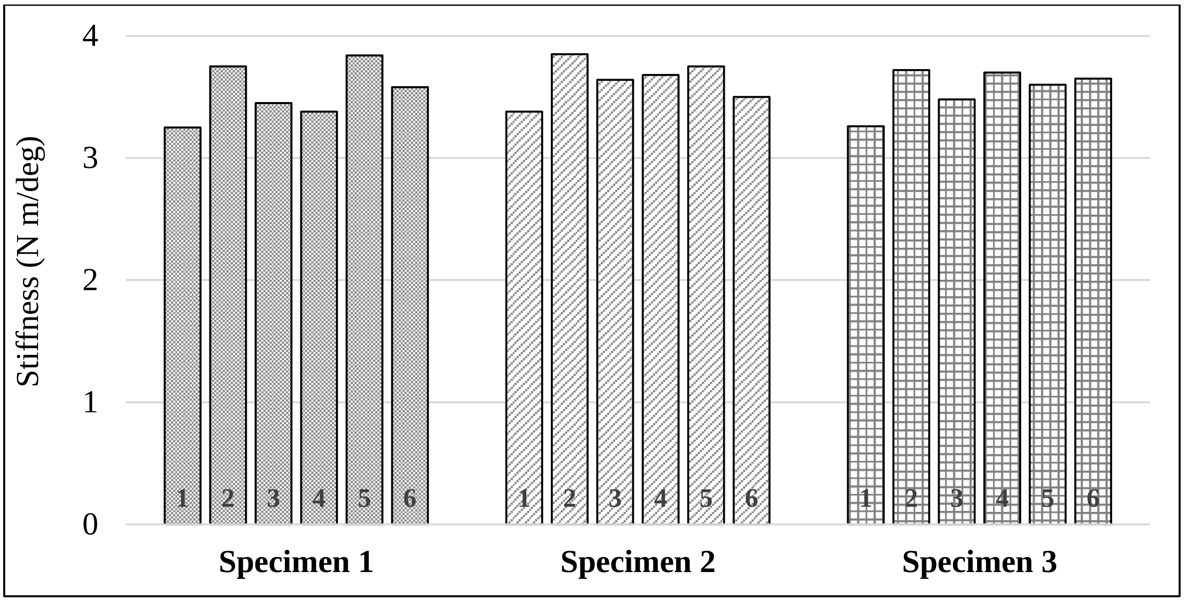

Figure 4-17 Torsional stiffness (external rotation) results of three intact femur specimens

Table 4-9 Torsional stiffness (external rotation) of intact femur specimens

n – number of tests, SD – standard deviation, COV – coefficient of variation

Specimen	n	Mean (N m/deg)	SD	COV (%)	Minimum (N m/deg)	Median (N m/deg)	Maximum (N m/deg)
Sp1	6	3.54	0.23	6.36	3.25	3.52	3.84
Sp2	6	3.63	0.17	4.68	3.38	3.66	3.85
Sp3	6	3.57	0.17	4.87	3.26	3.63	3.72
Group							
Intact	18	3.58	0.18	5.14	3.25	3.62	3.85

4.6 Discussion

In a rare clinical study, Chotel *et al*. performed an equivalent of three-point bending test in children undergoing osteotomy as a part of limb length corrective surgery (324, 325). They used an orthometer (Orthofix SRL, Verona, Italy) along with a goniometer to capture the force and angular displacement and reported the stiffness calculated by a hand-held microcomputer. The bending stiffness (in N m/deg) was taken as the quotient of the applied bending moment (N m) and resulting bending angle (°). Of the 11 children in their study, 7 (2 girls, 5 boys, age range 5.5-16.7 years) had bending stiffness measurements performed on the femur. The mean anteroposterior stiffness varied between 7.0-22.9 N m/deg. The mean mediolateral stiffness varied between 7.0-15.9 N m/deg. However, this parameter was measured in only 3 children (all boys) due to technical and intraoperative reasons.

The experimental testing of specimens provided stiffness parameters of the intact small composite femur under axial, four-point bending and torsional load application. Limited information is available from the aforementioned biomechanical investigations (Table 1-3, Table 4-3, Table 4-4, Table 4-5) which used a composite femur experimental model of paediatric dimensions regarding intact femur stiffness parameters.

Lee *et al*. performed biomechanical analysis of Ender nail fixation using five adolescent sized composite femurs measuring 380 mm in length with a 9 mm canal (75). Under a maximum axial load of 50 N they reported axial stiffness of 775 ± 71 N/mm in the intact specimens. For torsional stiffness test they used a maximum torque of 1 N m combined with 20 N axial compression to simulate muscle tension (Table 4-5). They reported torsional stiffness of 4.80 ± 0.28 N m/deg in the intact specimens. Subsequently in 2005, Jason *et al*. evaluated flexible intramedullary nail fixation using six second generation composite paediatric femur specimens which measured 280 mm in length with a 8 mm intramedullary canal (293). They reported average axial stiffness of 983 N/mm (maximum axial load 95 N), bending stiffness of 448 N/mm (maximum bending load 67 N), torsional stiffness of 2.25 N m/deg in external rotation and 1.78 N m/deg in internal rotation (maximum torsional load 2 N m). In comparison to the above two studies Porter *et al*. undertook destructive biomechanical testing to compare flexible intramedullary nails with locking plate construct and reported the load to failure in each group. They used third generation composite femurs with a canal of 10 mm and length of 445 mm. In their control group (number of specimens not reported), they used an axial load of 70 pounds with a torsional loading rate of 0.1° per second. The mean rotational stiffness of their intact specimens was 0.236 N m/rad (approximately 13.5 N m/deg). The stiffness results of the three intact femur specimens in this study are in agreement with the results reported in the current literature.

During axial compression test the intra specimen variability ranged from 1.60 % - 7.83 % and the corresponding inter specimen variability was 10.51 %. Intra specimen variability varied from 1.62% - 2.88% for four-point bending test whereas the inter specimen variability was 4.45%. Torsional loading (internal rotation) test showed the intra specimen variability to be lowest for Sp1 (0.92%) and highest for Sp3 (3.95%) with an inter specimen variability of 4.12%. Sp1 and Sp2 had the highest (6.36%) and lowest intra specimen variability during torsional loading (external rotation). Cristofolini *et al*. (286) observed that the deflection under axial loading is dependent on boundary compliance whereas the four-point bending test was more capable of demonstrating real inter specimen differences. Overall the results demonstrated that both the intra and inter-specimen variability were similar to other studies on composite femurs in the literature (286, 288-290). Additionally the results verified the design of the test jigs and test protocol adopted in the study.

4.7 Summary

The biomechanical testing helped to characterise the intact femur specimen stiffness properties both at an individual specimen level and collectively as a group (intact group) ($k_{\mathrm{EXP}\ Int}$). This data will be used for stiffness comparison of different fracture constructs in the subsequent sections of the study (in chapter 6). Additionally the above data from the three intact femur specimens is used for comparison and validation of a paediatric femur finite element model which is described in the next chapter (chapter 5).

5 PAEDIATRIC FEMUR - FINITE ELEMENT ANALYSIS

5.1 Introduction

This chapter describes the development of a finite element (FE) model based on the paediatric composite femur. Finite element analysis (FEA) is a numerical method of problem solving which has been extensively applied in many engineering disciplines (326). It is used by engineers to simulate real life conditions to evaluate product design thereby saving development costs and contributing towards design improvement (326-328). This technique has gained popularity in orthopaedic biomechanics research following the rapid advancement of computational technology in the past three decades (327, 329, 330). A number of commercial FEA software packages have been described in orthopaedic biomechanics research (327, 331-336). The current study used the Solidworks™ simulation software. Solidworks™ is an integrated suite of programs developed by Dassault Systèmes which in addition to the computer aided design (CAD) tools includes FEA module (Solidworks™ simulation) (328, 337)

The subject of FEA is vast with a multitude of concepts based on the research field or the engineering discipline to which it is applied. Hence a brief description of the fundamental concepts of FEA relevant to the current research and Solidworks™ simulation software are presented in the section below.

5.2 Basic definitions and concepts

In general, the finite element method (FEM) is based on the principle of converting the governing energy principles or differential equations of a given problem in to a system of matrix equations and subsequently solving the equations to provide an approximate solution (326, 338). The application of FEM to a specific field of analysis viz. stress analysis, thermal analysis or vibration analysis is termed as finite element analysis (FEA) (338).

Simulation is defined as the study of effects caused on an object due to real-world loading conditions (328). Computer simulation uses CAD models to represent experimental models which are subjected to different loading conditions to evaluate the real-world effects. In Solidworks™ simulation, the user can study the effect of various loads (viz. physiological loads in axial, four-point bending and torsional mode) on a constrained model (CAD model of composite paediatric femur) under predefined environmental conditions and check the results (visually and in the form of tabular data) (328). This forms the basis of FEA in the current study and will be elaborated in the subsequent sections of this chapter and in chapter 7.

When an external load is applied to a structure, like a femur, displacement occurs and stresses are generated. In solving this problem a simple linear equation like $F = kx$ (where F is the force, k is the stiffness and x is the resultant displacement) does not provide reliable results for the entire structure due to the underlying complex geometry of the femur. However, the above equation can still be valid for a small region of material within the complex structure. This approach forms the fundamental basis of the FEM. In solid mechanics, displacement represents the basic unknown or the field variable (328). Hence the finite element method reduces the unknowns to a finite number by dividing the solution region (or structure) into small parts called elements and by expressing the unknown field variables in terms of assumed approximating functions with each element (nodes). Hence the above equation for each element in the structure can be represented as below

$$[k]_e \delta_e = F_e \tag{17}$$

where $[k]_e$ is element stiffness matrix, δ_e is nodal displacement vector of element and F_e is nodal force vector.

By solving these simultaneous equations, a solution in terms of nodal unknowns (displacement values) is obtained. Using these nodal values additional parameters viz. stresses, strains, moments are computed (326, 328, 338).

For the above scenario, the resultant displacement and the generated stresses in the femur can be estimated using FEA. In this process the complex shape of femur is broken down into finite number of smaller structures (discretized) called the elements. This generates a mesh of elements which are interconnected at specific points called nodes. This allows simple equations to be solved for each of the elements with acceptable accuracy (where numerical approximations are valid). Subsequently an approximate solution for the entire femur is estimated by transferring solutions from one element to the next using successive computation. From a computational perspective this process is referred to as matrix gather and scatter (or assembly) operations (338) (Figure 5-1). Finite element mesh generation creates at least two data sets. The first (nodal set) represents the numbered list of all generated vertices along with their spatial coordinates. The second (element set) represents the numbered set of elements along with the list of element vertex numbers to which it is connected (element connectivity list). This data set allows automation of the FEA calculations (338). The gather operation involves bringing the nodal data in the full mesh back to a single element. On the other hand scatter or assembly operation involves partial summation of element data to the matrices associated with the corresponding mesh data (338).

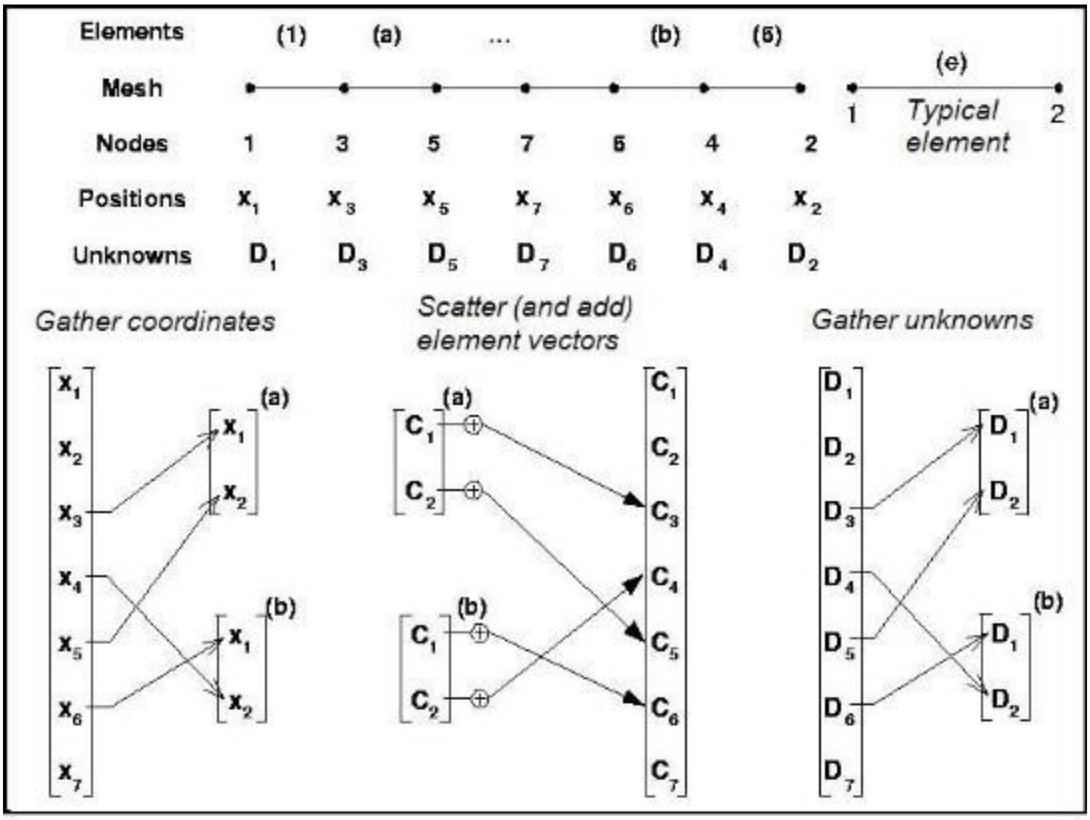

Figure 5-1 Example of matrix gather and scatter operation on data from linear elements. [Reproduced from Akin *et al*. (338)]

In general, FEA using a software package like Solidworks™ simulation can be broadly divided into three stages (327):

i. **Pre-processing** – it is the problem definition stage. It includes preparation of the finite element model based on the computer aided design (CAD) model. Subsequently the relevant geometric parameters and material properties are assigned for the model. The next step involves defining the loads and boundary conditions of the model. Boundary condition represents the set of assumptions made with respect to the interaction of the model with its surroundings. In other words it is the relationship that exists between the nodes and space. A region or part of the model can be selected for application of a load (axial / four-point bending / torsional). In mathematical terminology this is referred to as non-essential conditions or Neumann boundary conditions (338). Support or fixtures and restraints of the model are then defined. This is referred to as essential boundary conditions or Dirichlet boundary conditions (338). In Solidworks™ simulation several type of fixtures are available to accurately define the behavior of the model under different loading conditions. The fixed geometry fixture allows the user to rigidly fix the face, edge or point of the object (328). The roller/slider fixture allows the user to fix a face of the model in such a manner that it can slide/roll in its plane but cannot move perpendicular to the plane (328). Whilst assigning the boundary condition a critical decision is to define the contact type between two components of a given model along their shared faces viz. medullary canal of the femur and the outer surface of an intramedullary nail. In Solidworks™ simulation this is undertaken using the 'contact set' option. The 'no penetration' contact set option allows the faces of adjacent components to touch each other but does not allow them to penetrate (328).

ii. **Numerical analysis** – this stage involves discretization of the model into constituent elements to generate a mesh. Elements contain the material information of a given model and determine how the loads are transferred into displacements for all connected nodes. Based on the model under evaluation and its dimensions, different types of finite elements (interconnected geometrical entities) are used generate the mesh. These include one-dimensional line elements, two-dimensional plane elements and three-dimensional volume elements (Figure 5-2). The three-dimensional solid element is the most versatile type of element compared to the former two (337).

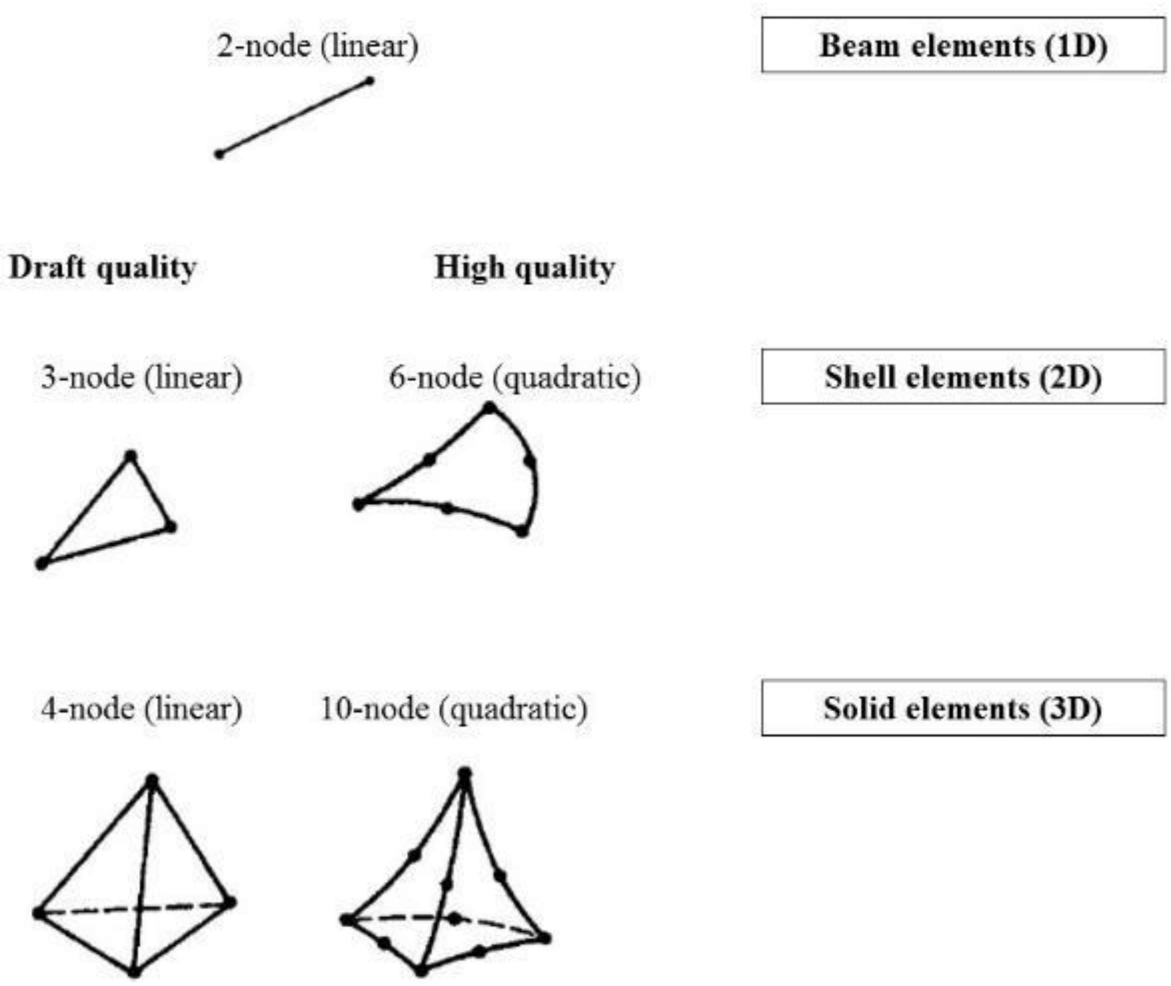

Figure 5-2 Types of finite elements.

Nodes are coordinate locations that locate/define the endpoints of all one-dimensional elements and the corners of all two and three dimensional elements. Degrees of freedom (DOF) are the unknown quantities associated with a node or the parameters that must be solved mathematically. Associated loads are loads of the same direction and type as the DOF. For structural FEA the DOF are displacements (or rotations) and the associated loads are forces (or moments). Solid elements have three translational DOF with 12 and 30 DOF for the linear and quadratic solids, respectively (338). It can be noted that for a particular node the user can set either the load or the displacement value but not both.

The process of mesh generation for a given model is automated in Solidworks™ simulation with two options available to the user. The first is the standard mesh generator based on the principle of Voronoi-Delaunay triangulation (339). The second option uses the advancing front meshing technique and generates a curvature based mesh (340). In this technique, tetrahedral elements are built progressively inward from a given triangulated surface. An active front is maintained where new tetrahedra are formed thereby creating more elements in higher-curvature areas automatically. Based on the volume, surface area and other geometric details the software estimates a global element size for the model (328). The tetrahedral solid elements can be first order elements (draft quality) or second order elements (high quality). First order tetrahedral elements have straight edges and flat faces which maintain that shape characteristic even after the deformation of the element following the application of load (Figure 5-3). Thus strain and consequently stress are both constant in first order elements which limits their applicability while evaluating a complex structure like the femur. Furthermore the straight edges and flat faces cannot adequately map the curvilinear geometry of the femur.

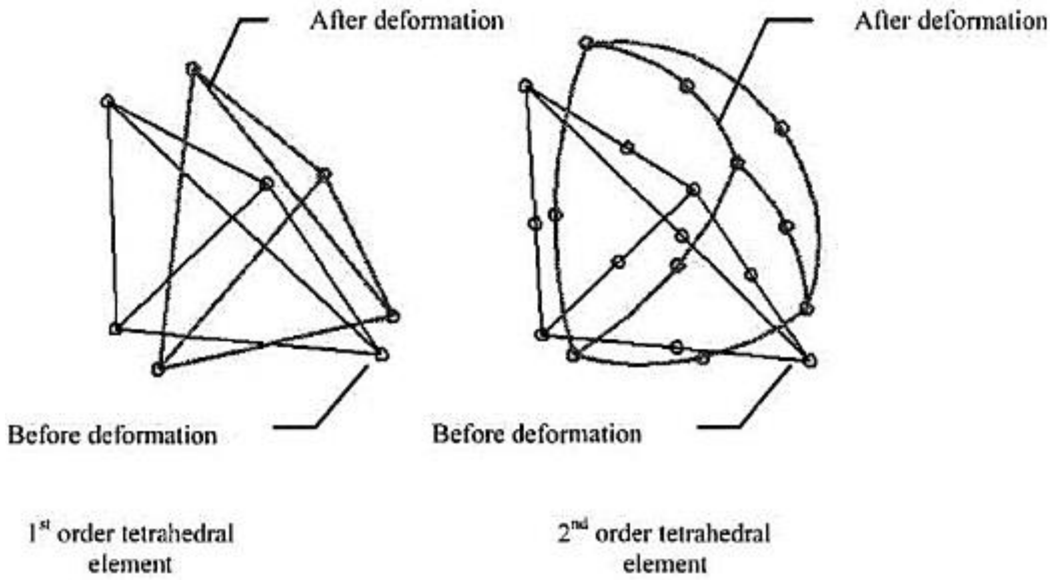

Figure 5-3 Illustration of deformation of first and second order elements [Reproduced from Kurowski *et al*. (326)]

Element distortion can impact the accuracy of the results (326, 328). This can occur due to the presence of a large sized element in a feature with tight curvature or due to rapid transition from one size to another. The quality of elements in the mesh can be estimated using two parameters in Solidworks™ simulation namely the aspect ratio check and Jacobian point check (341). The aspect ratio of an element is defined as the ratio between the longest edge and the shortest normal dropped from a vertex to the opposite face normalized with respect to a perfect tetrahedral (341) (Figure 5-4). The Jacobian ratio is a measure of the quality of second order elements (341). The Jacobian ratio increases as the curvatures of the edges increases. However, the Jacobian of an extremely distorted element becomes negative (326) (Figure 5-5). The automatic mesh generator algorithm available in Solidworks™ simulation helps to avoid development of distorted elements due to built-in empirical rules for avoiding them (328).

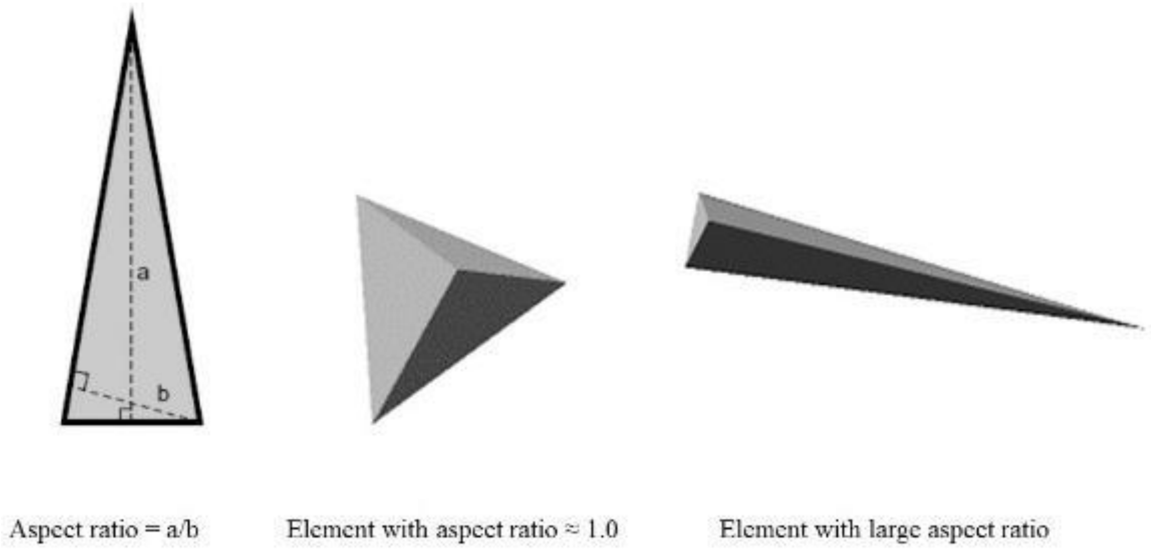

Figure 5-4 Illustration of element aspect ratio

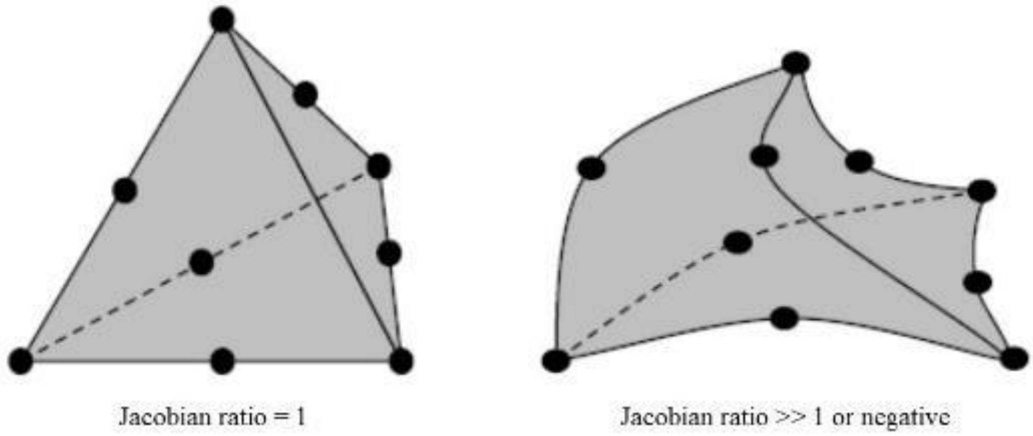

Figure 5-5 Illustration of element Jacobian ratio

Mesh control refers to specifying different element sizes at different regions in the model. This is especially important for regions of interest in the model viz. locations where displacement is expected, in areas where stress is expected following load application and around fixtures or restraints (337, 338).

FEA involves solving a set of matrix equations simultaneously (326, 338). Solvers are the software algorithms which compute a numerical solution to a given problem (342). In Solidworks™ simulation three solver options are available namely the Direct Sparse solver, FFEPlus solver and automatic (342, 343). The Direct Sparse solver uses exact numerical techniques to produce a solution. The 'Sparse' refers to the sparsity (zeroes) in the matrices that this algorithm uses to find a solution (343). FFEPlus is an iterative solver based on implicit integration method (326, 343). With each iteration the solution is assumed and errors are evaluated with the process continuing until errors are small enough / acceptable. Hence if a study contains more than 100, 000 DOF it can be more efficient and accurate to use this solver (343). The automatic solver is the default option wherein the software decides the optimum solver based on the problem and finite element model.

Following numerical analysis a solution is provided. However, the accuracy of a solution for a given finite element model must be determined by a process of mesh refinement and comparing the successive solutions obtained with the original. This is referred to as a convergence test (326, 328, 330). In general the improvement in accuracy of the solution is due to two reasons: a fine mesh results in a higher number of elements with associated nodes that are available for calculating displacement and fine mesh results in smaller size elements which minimize the discretization error by accurately mapping the geometry of the model (327, 338). It must be noted that higher accuracy does come at the cost of increased computational resources and time (326, 328, 338). Hence a balance is required when an optimum solution is sought and is guided by the primary research question which the finite element model is addressing (77, 327, 330, 331, 334, 335, 344-349).

The two most common methods used for convergence analysis are the h-method and p-method (337). The h-method improves results by using a finer mesh of the same type of element. This is achieved by dividing each existing element into two or more elements without changing the type of elements used (Figure 5-6).

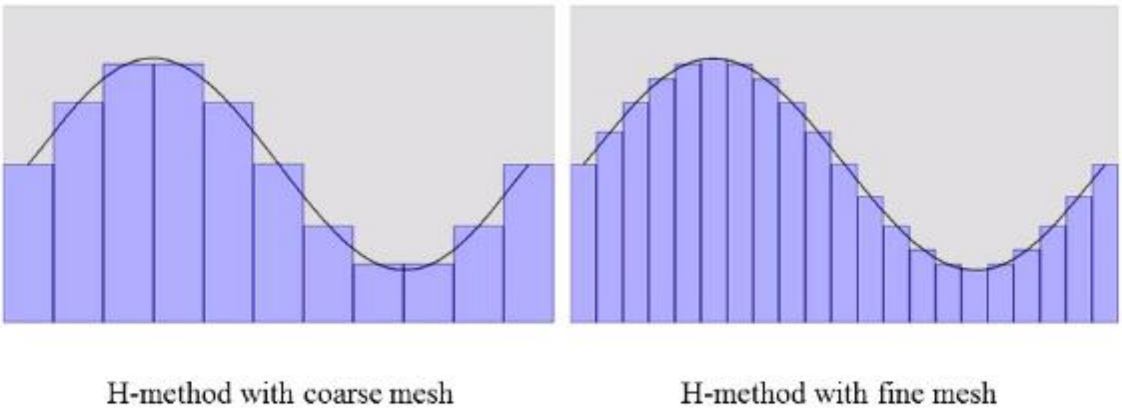

Figure 5-6 Illustration of H-method of convergence

The p-method increases the displacement accuracy in each element by increasing the degree of the highest complete polynomial (p). However, the number of elements used remains same but this method relies on large elements and complex shape functions (Figure 5-7).

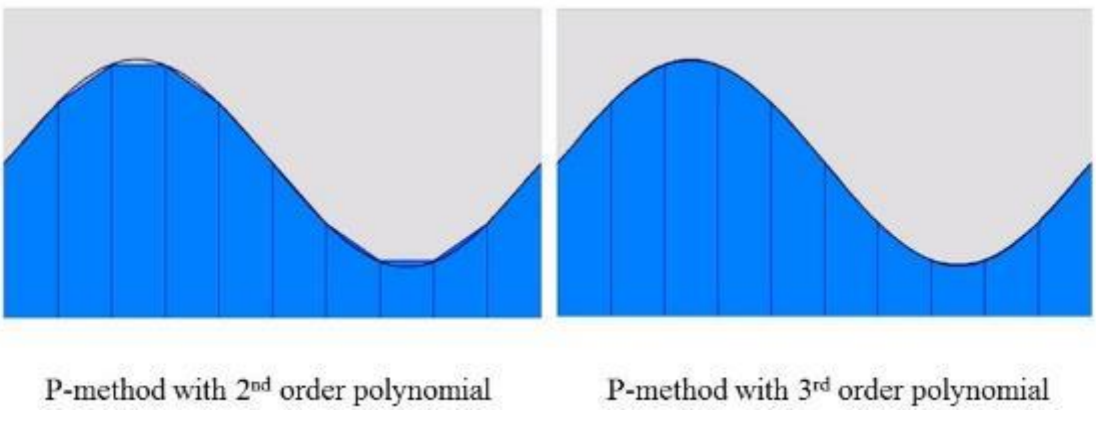

Figure 5-7 Illustration of P-method of convergence

Hence the p-method is computationally more intensive than the h-method (326). With both methods the desired accuracy is seldom achieved in a single step and several iterations are often required (349).

iii. **Post processing** – refers to the evaluation of the results from the numerical analysis in a systematic manner. The resultant displacement and stress in the different parts of the finite element model are visualised and recorded (327). Furthermore, the response of the finite element model to a load can be viewed in Solidworks™ simulation as an animation to assess the dynamic behavior. This can be useful to predict failure modes of fracture fixation implants.

5.3 Objectives

The objectives of this part of the study were to develop a finite element model that:

i. Was representative of a paediatric composite femur and allowed simulation testing in Solidworks™ simulation

ii. Enabled assessment of stiffness of the intact femur ($k_{\mathrm{FEA}\ Int}$) under axial compression, four-point bending and torsional loading conditions.

iii. Was versatile enough to allow the creation of different fracture configurations, virtual insertion of the CAD model of the ALFN (described in chapter 7) and evaluation of fracture healing and implant parameters (described in chapter 8)

5.4 Materials and methods

5.4.1 Development of paediatric femur finite element model using digital radiographs

A novel technique was developed in the current study to create a simplified finite element model of the paediatric femur. This technique has been recently published (350). Orthogonal views (anteroposterior / lateral) of the digital radiographs of a paediatric femur sawbone with radiographic size template (Figure 4-9) were initially processed using Adobe Photoshop CS4 (Adobe, San Jose, California) and imported into SolidWorks™ software (Dassault Systèmes, France). Digital radiograph dimensions were scaled in SolidWorks™ to accurately match the geometric parameters of composite femur (model 3414, Pacific Research Laboratories Inc, Vashon, USA). Subsequently the scaled orthogonal views of the digital radiographs were used as a template to develop the finite element model. Using the spline (351, 352) and sweep functions (352, 353) a FEA model based on a simplified geometry of the paediatric femur was developed.

The model consisted of two cylinders which intersected at 130°. The first hollow curved cylinder (length 350 mm, outer diameter 20 mm, inner diameter 9.5 mm, radius of curvature 1031.72 mm) represented the shaft whilst the second solid cylinder (length 96.92 mm, diameter 25 mm) represented the head, neck and trochanteric region (Figure 5-8). Similar approach to simplify the femur geometry has been used by other authors (354, 355).

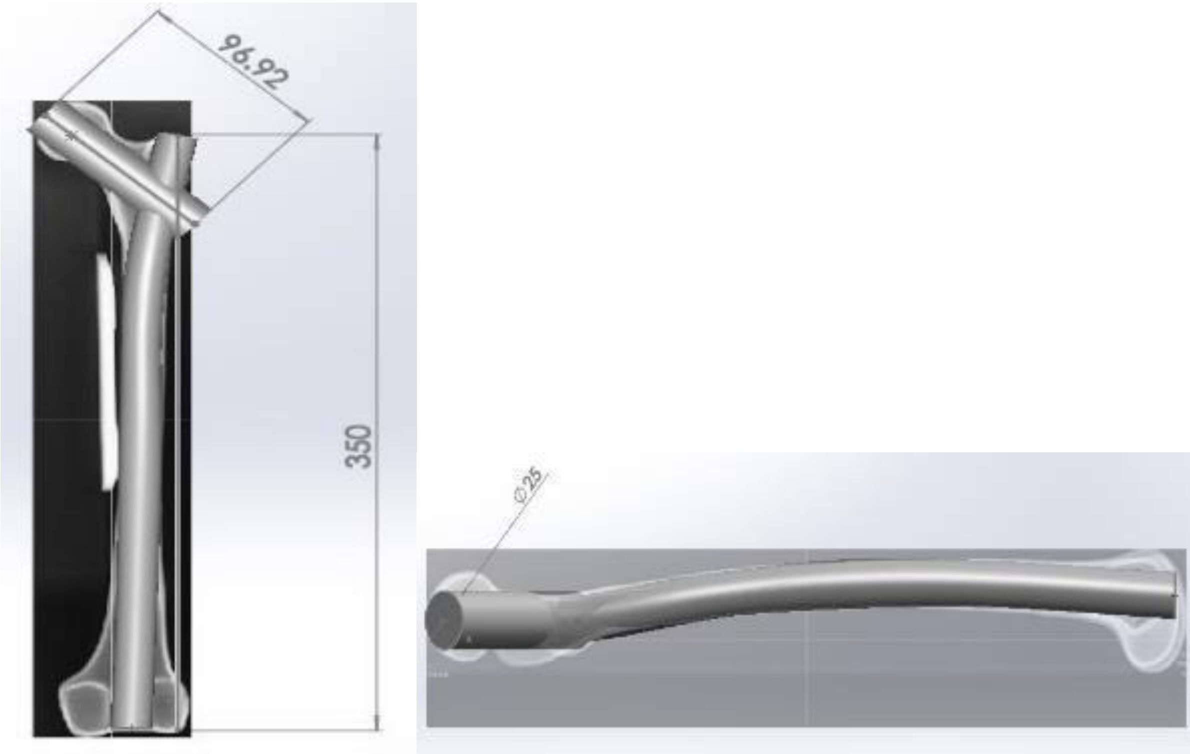

Figure 5-8 FEA model (left - anteroposterior view, right - lateral view)

5.4.2 SolidWorks™ simulation tests

5.4.2.1 Material properties and assumptions

Material properties of the composite femur (compressive strength = 157 MPa, compressive modulus = 16.7 GPa, yield strength = 93 MPa, Poisson's ratio = 0.26) (Table 4-1) were assigned to the model. The material properties of the FEA model were assumed to be isotropic and linearly elastic (348, 356-358).

5.4.2.2 Boundary conditions

The boundary conditions of all the simulation tests (axial compression / four-point bending / torsion) mirrored the corresponding experimental setup described in chapter 4 (345, 356, 359-364).

For the axial compression test the distal 50 mm of the FE model was fully constrained using the 'fixed geometry' option (365). Displacement of the femoral head in the anteroposterior direction was constrained (364, 366) (Figure 5-9). The 'split line' command was used to create an area representative of the acetabular socket with a depth of 28 mm through which axial load was applied during experimental testing. Axial load was applied on the superior surface representative of the femoral head similar to the experimental set up (Figure 5-10). Simulated axial load was initially applied at 60 N and subsequently in 60 N increments up to a maximum of 600 N. The predicted displacement in the superior-inferior axis (U_X in mm) (Figure 5-9 - right and Figure 5-10 - c) was noted for each load increment and axial stiffness ($k_{\text{FEA Ax } Int}$) was estimated as described earlier.

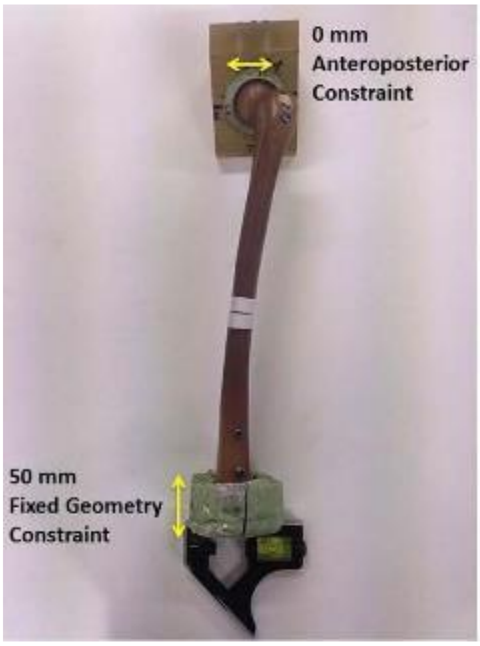

Figure 5-9 Axial compression test boundary condition (left - experimental setup, right – simulated axial compression)

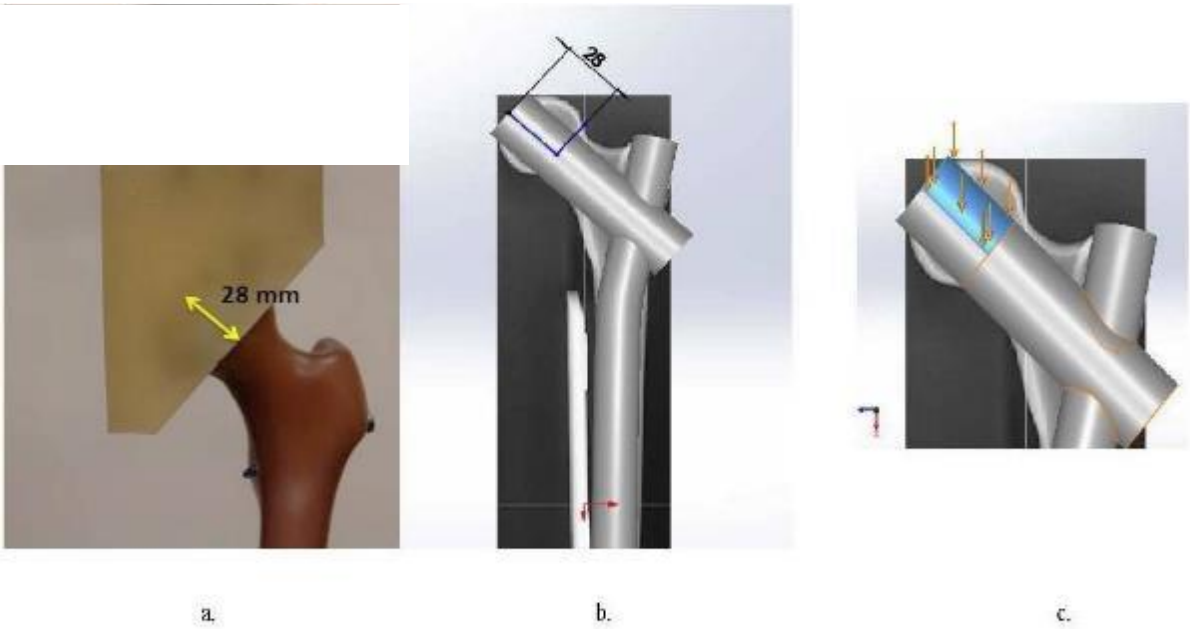

Figure 5-10 Axial compression test (a-experimental setup, b-split line of 28 mm, c-simulated axial compression)

For the simulated four-point bending test, the 'split line' command was used to create a set of four areas (2 at the base for support and 2 at the top for application of bending load) (328). The supports at the base were set at a distance of 260 mm whereas the top areas were 70 mm apart similar to the experimental setup (Figure 5-11). The 'advanced fixture' option was used to allow displacement in the plane only along the long axis of the femur. A similar approach has been used by other investigators to perform a simulated four-point bending test (367, 368). Simulated load was applied to the top areas at 40 N initially followed by 40 N increments up to 400 N. The predicted displacement from the solver in the anterior-posterior axis (U_Y in mm) (Figure 5-11- right) was noted for each simulated load and the four-point bending stiffness ($k_{\text{FEA Be } Int}$) was estimated as described earlier.

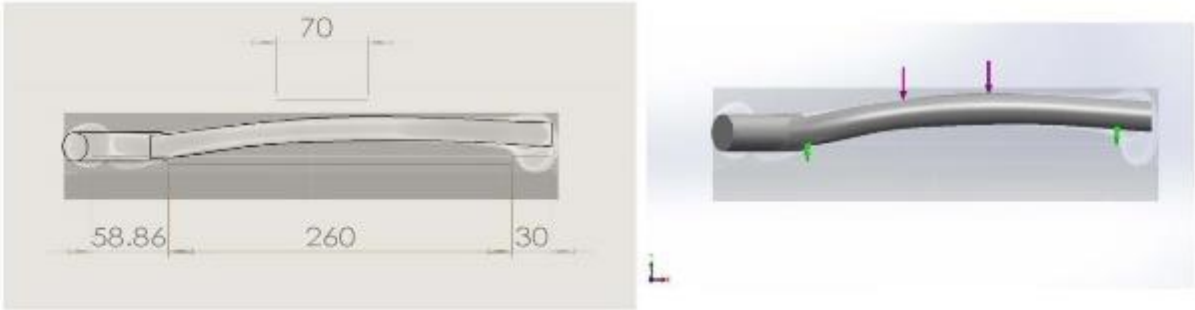

Figure 5-11 Four-point bending test [left – FE model with dimensions similar to the experimental setup, right – FE model showing simulated loading points (purple arrows) and supports (green arrows)]

For the torsion test, the 'fixed geometry' option was applied to the distal 65 mm of the femur model. The 'advanced fixture' (328) option was used for proximal end face which allowed rotational movement but prevented displacement in the anteroposterior and mediolateral directions (Figure 5-12).

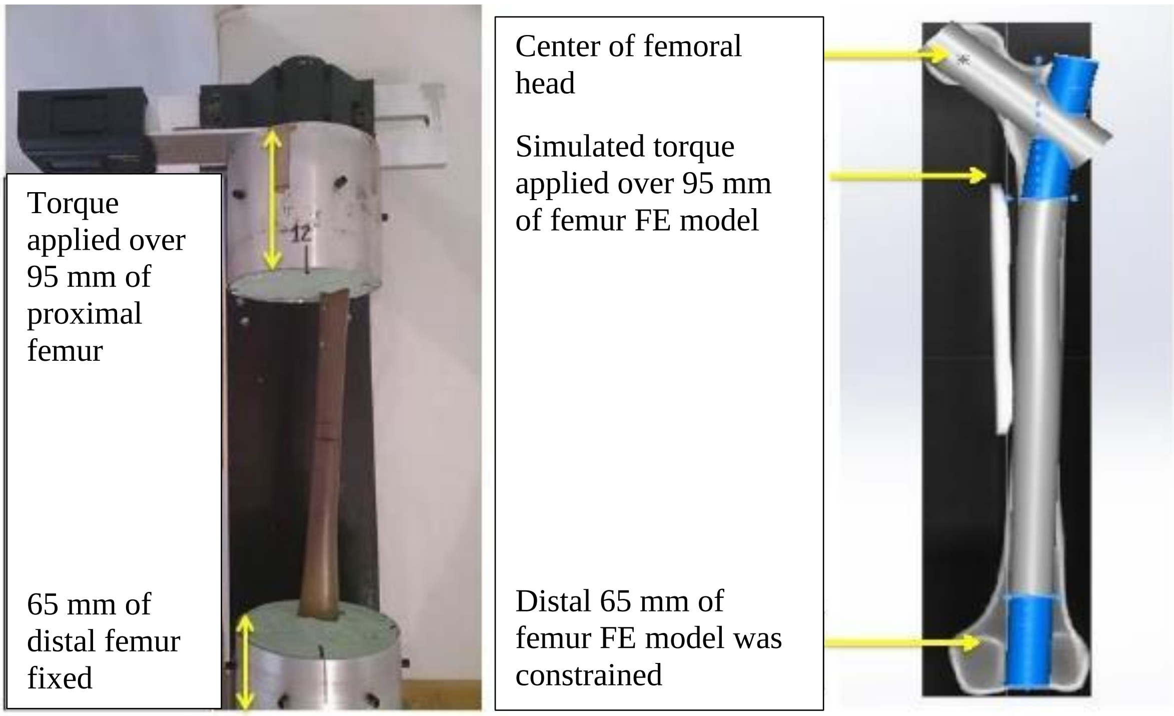

Figure 5-12 Boundary conditions of torsion test (left-experimental setup, right - FE model)

The long axis of the paediatric femur was marked along the length of the intramedullary canal (369) . The femoral offset (distance from the center of rotation of the femoral head to a line bisecting the long axis of the femur) (370) was estimated at 37 mm (Figure 5-13). Simulated torque was applied at the proximal aspect of the femoral shaft at 0.2 N m increments up to a maximum of 4 N m.

Figure 5-13 Estimation of femoral offset

Displacement of the point (arc length) corresponding to the center of rotation of the femoral head was noted for each increment of simulated torque (Figure 5-14). Angular displacement (in degrees) of the above point was calculated using arc of a circle principle wherein $\phi = (\text{Arc length} \times 180) / (\pi \times 37)$ (371). Torsional stiffness (N m/deg) was obtained by plotting the torque against the angular displacement and calculating the gradient.

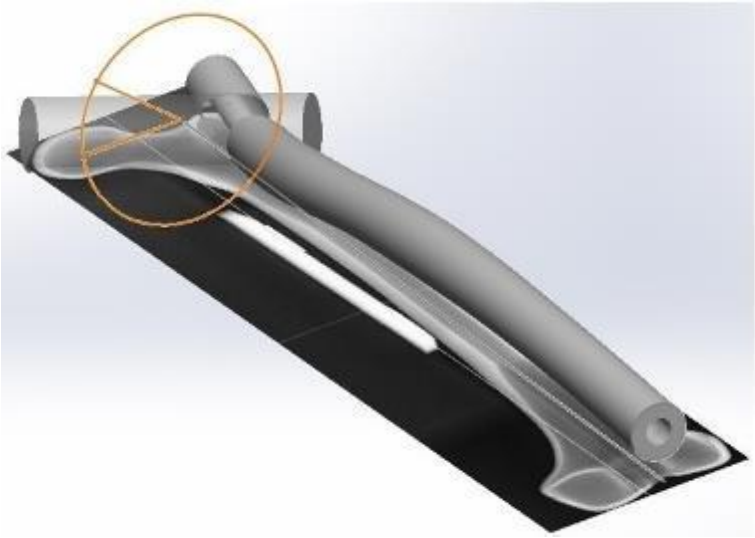

Figure 5-14 Displacement of the point (arc length) corresponding to the center of rotation of the femoral head

Positive torque produced internal rotation whereas negative torque resulted in external rotation (Figure 5-15).

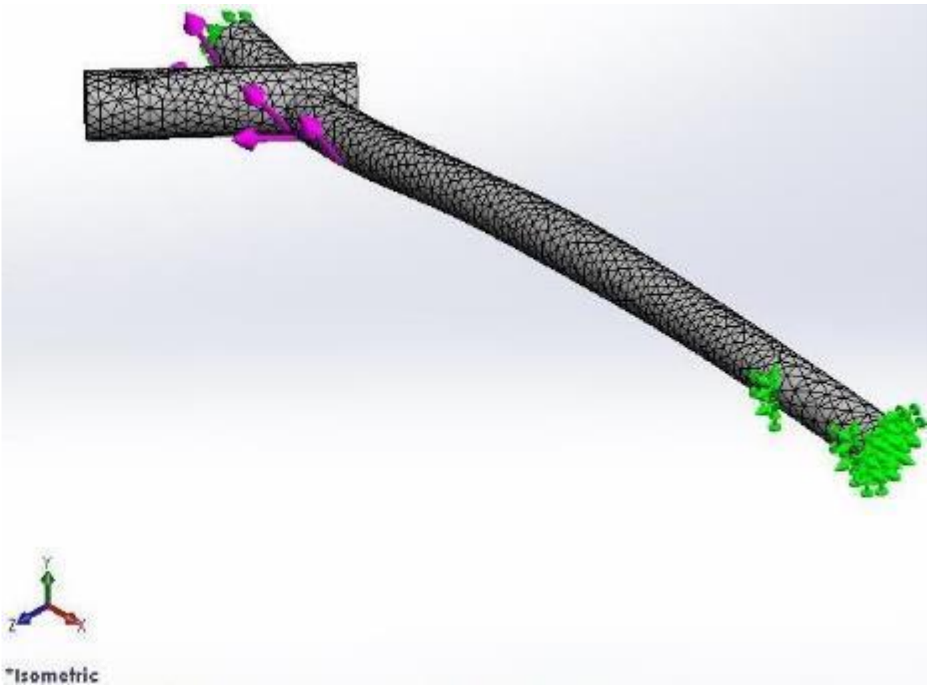

Figure 5-15 Simulated torque (external rotation) test

5.4.2.3 Mesh selection and convergence

The type of mesh was selected based on the following criteria: i) Ability of the generated mesh elements to appropriately represent the geometry and shape of the model components. ii) Total solver/computational time of each type of mesh for a given simulated load. iii) Flexibility of the mesh to allow subsequent modification during iterative testing of the model.

Preliminary tests conducted on the model showed that the curvature type mesh with three-dimensional (3D) tetrahedral elements available in Solidworks™ simulation met the above criteria and had the least computational time. Similar 3D tetrahedral finite elements have been used by other investigators during FEA of femoral intramedullary nail fixation (355, 358, 372-374). Subsequently convergence analysis was done to detect the influence of element size on displacement results for each of the simulated loading condition described above (373).

Based on the FE model and the boundary conditions, the automesher algorithm in Solidworks™ simulation provides a default element size (375). This formed the default or iteration 1 test during convergence analysis. Iterative tests were then performed on the FE model for all the above loading conditions at the lowest value of simulated load (viz. 60 N for axial compression test). The element size was sequentially decreased from the default size and numerical analysis repeated till the displacement results from the solver demonstrated a plateau effect (337, 338). The iteration at which the displacement result had plateaued was selected to apply further increments of simulated load. Additionally other factors like the quality of mesh (as indicated by the percentage of elements with aspect ratio < 3) and the total solution time were considered in accepting convergence of displacement result for a given simulated load (326, 337, 338, 373). This methodology was used for performing convergence analysis of the FE model described in this chapter and in the subsequent chapters of the thesis describing the FEA.

5.4.3 Validation and verification

In the context of FEA, validation can be defined as a process by which the model predictions are compared to the experimental data in order to determine the modeling error (330, 376). Verification refers to the process of determining that a given FE model accurately represents the conceptual description and solution to the model (376, 377). In other words validation informs the investigator if a given FE model is the right model and an accurate representation of the 'real world' whereas verification informs the investigator if a given FE model has been numerically modelled in an accurate manner. A comparison of FEA results with experimental results is mandatory for robust validation of the FE model and its inherent assumptions (327, 330, 331, 334, 344, 345, 356, 360, 376). Validation of the current FE model of paediatric composite femur was undertaken using the following two methods (361, 368, 376, 378, 379):

a) A quantitative analysis using linear regression was performed between the experimental observations and FE model predictions to determine the slope, intercept, 95% prediction interval and R^2 value

b) Estimation of the relative error between the experimental stiffness results and the predicted stiffness results from the FEA. The relative error (expressed as percentage) was calculated as below:

$$\text{Relative error} = \frac{(k_{\text{FEA}\ Int} - k_{\text{EXP}\ Int})}{k_{\text{EXP}\ Int}} \times 100 \qquad (18)$$

where $k_{\text{FEA}\ Int}$ = predicted stiffness of intact femur and $k_{\text{EXP}\ Int}$ = mean stiffness of intact femur group established from experimental testing (chapter 4).

The above were performed using the data analysis function in Microsoft Excel® 2010 (Redmond, WA, USA).

A schematic illustration of the FE model validation process used in this study is presented in Figure 5-16.

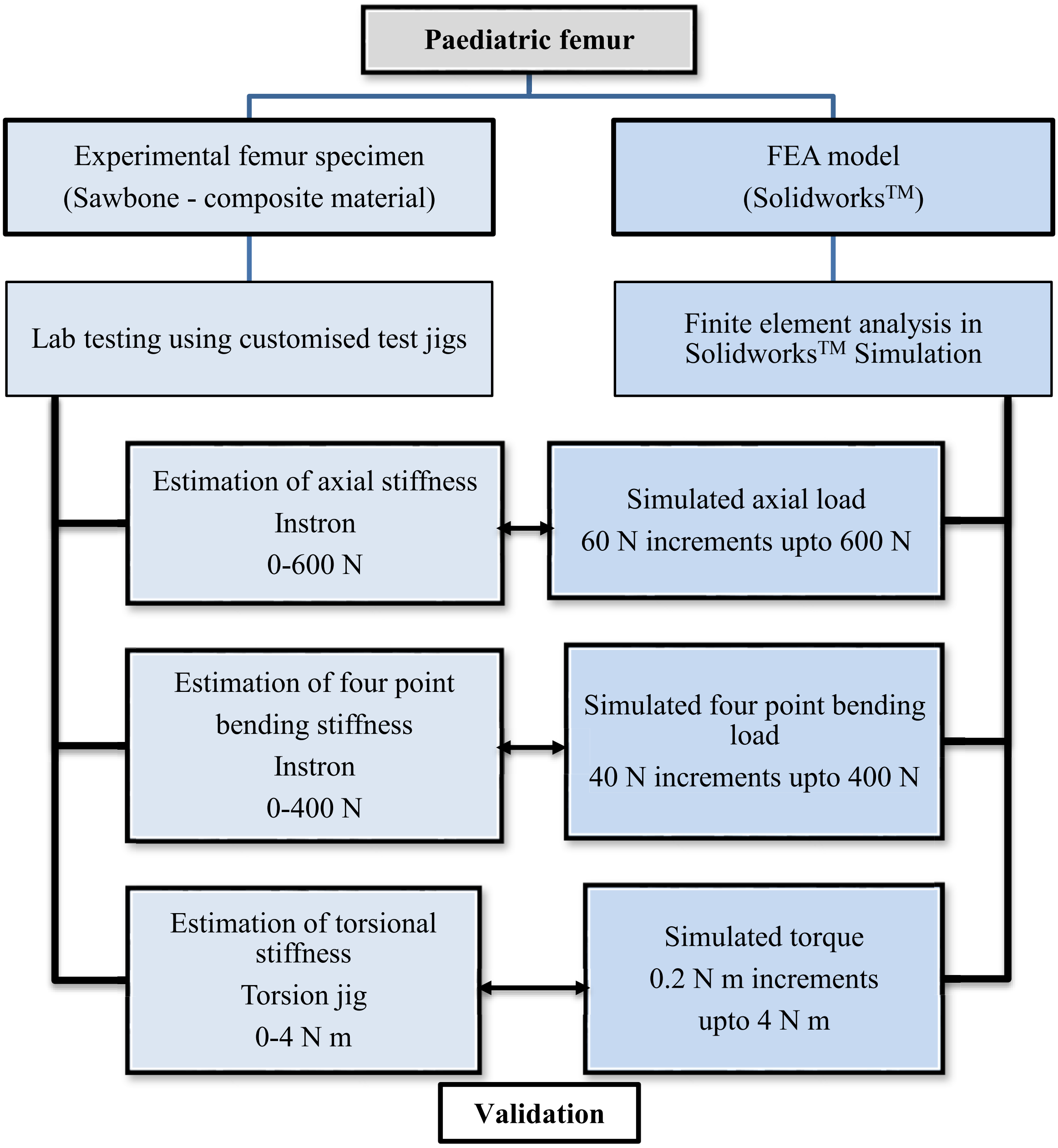

Figure 5-16 Validation of paediatric femur FEA model

5.5 Results

Simulation test results of the paediatric composite femur FE model are presented in the initial section below. The subsequent section presents the methodology used to validate the FE model including the comparative analysis of the FEA results and the results of experimental testing of the three composite femur specimens described in the previous chapter.

5.5.1 Axial compression

5.5.1.1 Convergence analysis

The displacement values (U_X in mm) obtained from simulated axial compression load of 60 N for different iterations of the of FE model are shown in Table 5-1 and Figure 5-17. Iteration 3 with 116,609 elements and 179,884 nodes with an element size of 2.5 mm displayed satisfactory convergence of displacement. This iteration was used to apply 60 N incremental loads and determine the predicted axial stiffness ($k_{\text{FEA Ax } Int}$) (Figure 5-18).

5.5.1.2 Predicted axial stiffness ($k_{\text{FEA Ax } Int}$)

The axial displacement results (U_X in mm) obtained using iteration 3 were plotted against simulated load. The predicted axial stiffness ($k_{\text{FEA Ax } Int}$) was 704.83 N/mm (Figure 5-18)

Table 5-1 Details of iterations tested during simulated axial compression test

DOF – degrees of freedom, Mesh quality = percentage of elements with aspect ratio < 3

Iteration	Element Size (mm)	Total Nodes	Total Elements	DOF	Mesh quality	U_X (mm)	Solution Time (s)
1	10	96344	62118	289032	91	0.072	4
2	5	105016	67781	315048	94	0.082	6
3	2.5	179884	116609	539652	97	0.085	8
4	1.25	833955	563735	2501865	98	0.085	27
5	0.625	5098778	3582544	15296334	99	0.085	179

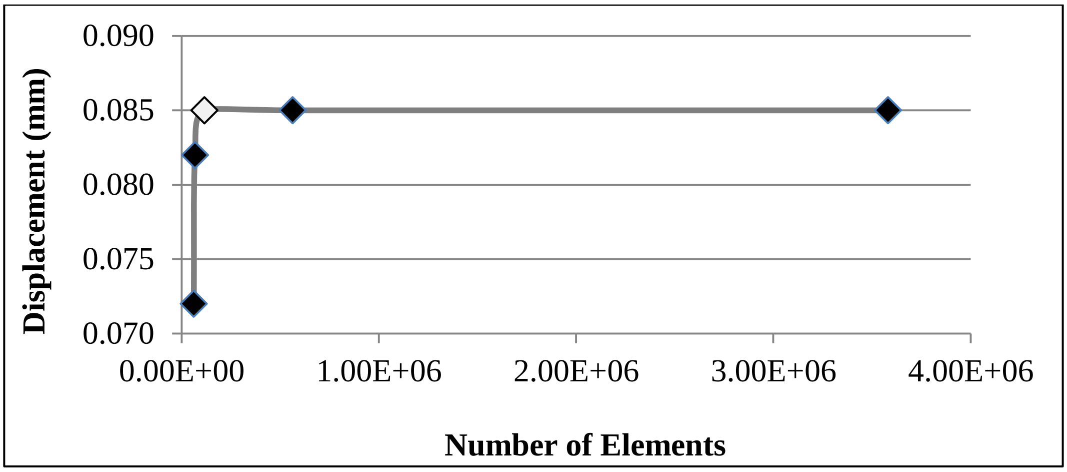

Figure 5-17 Convergence of displacement values during simulated axial compression test

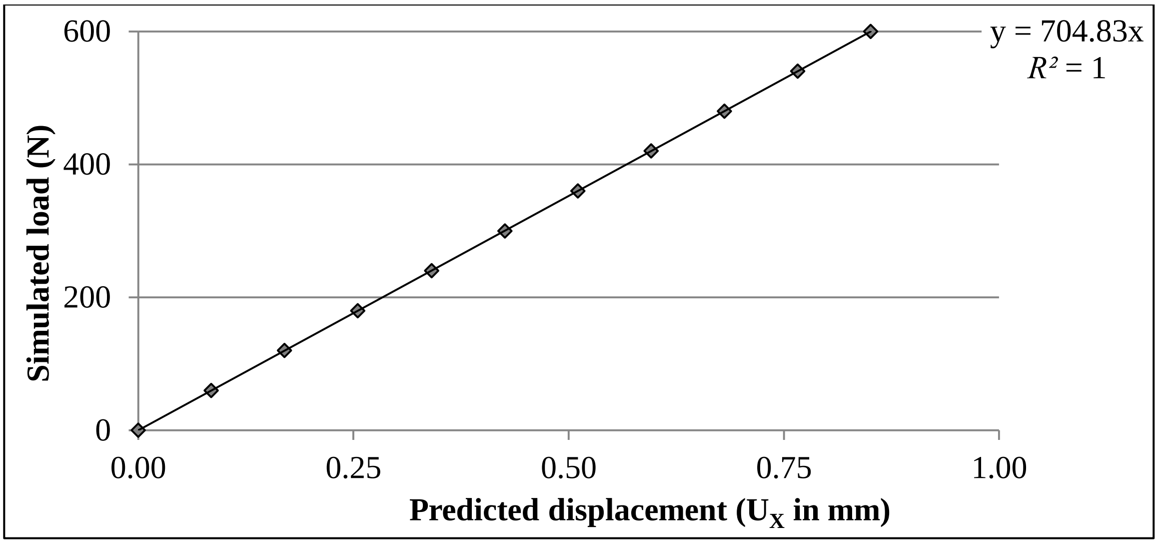

Figure 5-18 Predicted axial stiffness

5.5.2 Four-point bending

5.5.2.1 Convergence analysis

The displacement values (U_Y in mm) obtained for different iterations are shown in Table 5-2 and Figure 5-19. It was noted that for iteration 5 the software completed the meshing process.

However, the numerical analysis was not completed due to lack of memory required for the solver (380). Iteration 3 which predicted a displacement of 0.108 mm for a simulated bending load of 40 N was selected for further analysis (Figure 5-19) and estimation of four-point bending stiffness ($k_{\text{FEA Be } Int}$) (Figure 5-20).

Table 5-2 Details of iterations tested during simulated four-point bending test

DOF – degrees of freedom, Mesh quality = percentage of elements with aspect ratio < 3, N/R – no recordable solution due to solver running out of memory

Iteration	Maximum Element Size (mm)	Total Nodes	Total Elements	DOF	Mesh quality	UY (mm)	Solution Time (s)
1	8.00	12260	6649	36780	91.70	0.101	11
2	4.00	33438	20493	100314	98.7	0.103	26
3	2.00	204443	135832	613329	99.7	0.108	48
4	1.00	1340859	937175	4022577	99.8	0.108	182
5	0.50	8141009	5842964	24423027	99.8	N/R	N/R

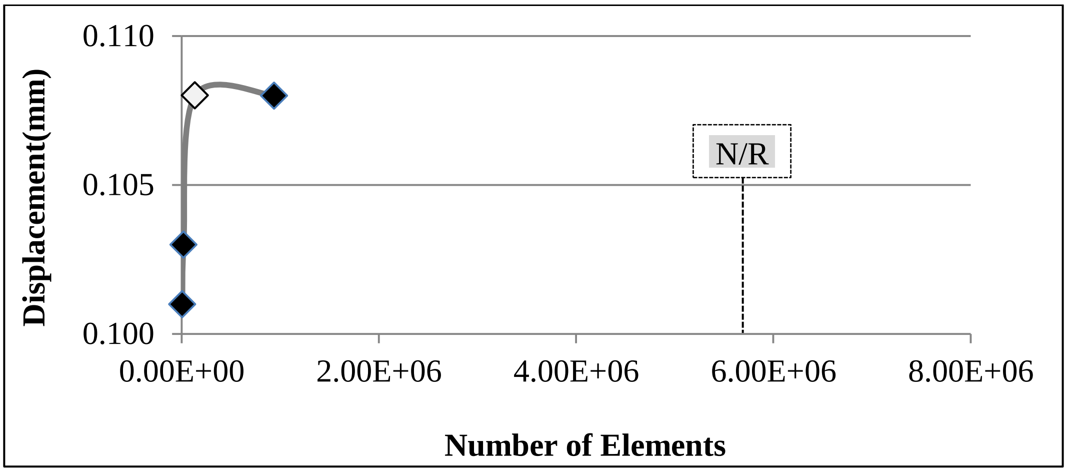

Figure 5-19 Convergence of displacement values during simulated four-point bending test (N/R – no recordable solution)

5.5.2.2 Predicted four-point bending stiffness ($k_{\text{FEA Be } Int}$)

Displacement of 1.084 mm (U_Y) was predicted by iteration 3 in response to maximum bending load of 400 N. The predicted four-point bending stiffness was 369.1 N/mm (Figure 5-20).

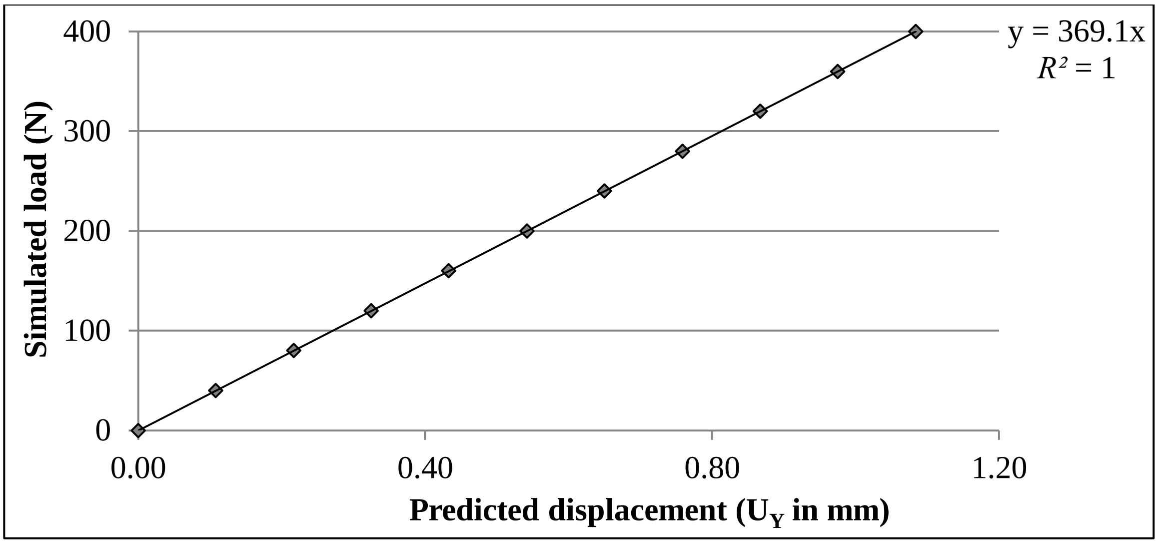

Figure 5-20 Predicted four-point bending stiffness

5.5.3 Torsion (internal rotation)

5.5.3.1 Convergence analysis

During simulated torsion test (internal rotation) it was noted that iteration 2 and 3 exhibited similar mesh quality and internal rotation value for a simulated torque of 0.2 N m. However the solution time for iteration 3 was more than four times longer (Table 5-3). This was contributed due the fact that total elements increased considerably (80524 to 556,966) from iteration 2 to iteration 3. Hence iteration 2 was chosen for further numerical analysis (Figure 5-21).

Table 5-3 Details of iterations tested during simulated torsion (internal rotation) test

DOF – degrees of freedom, Mesh quality = percentage of elements with aspect ratio < 3

Iteration	Maximum Element Size (mm)	Total Nodes	Total Elements	DOF	Mesh quality	ϕ_{IR} (°)	Solution Time (s)
1	5.0	26761	16181	80283	93.4	0.05	2
2	2.5	123650	80524	370950	99.6	0.05	5
3	1.25	807235	556966	2421705	99.7	0.05	23
4	0.625	5010658	3570710	15031974	99.7	0.05	176

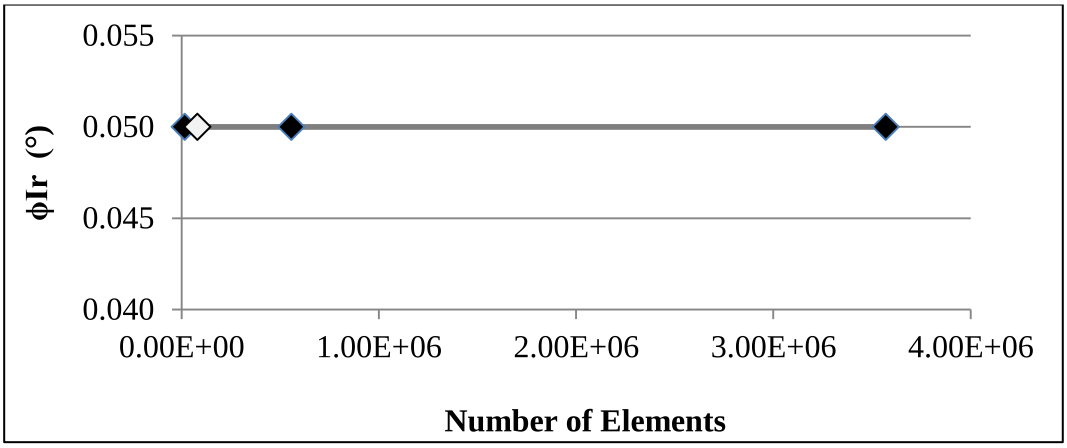

Figure 5-21 Convergence of rotation during simulated torsion (internal rotation) test

5.5.3.2 Predicted torsional stiffness (internal rotation) ($k_{\text{FEA Ir } Int}$)

Internal rotation of 1.14° was predicted at the maximum torque of 4 N m by iteration 2 of the FE model. The predicted torsional stiffness during internal rotation ($k_{\text{FEA Ir } Int}$) was 3.49 N m / deg (Figure 5-22).

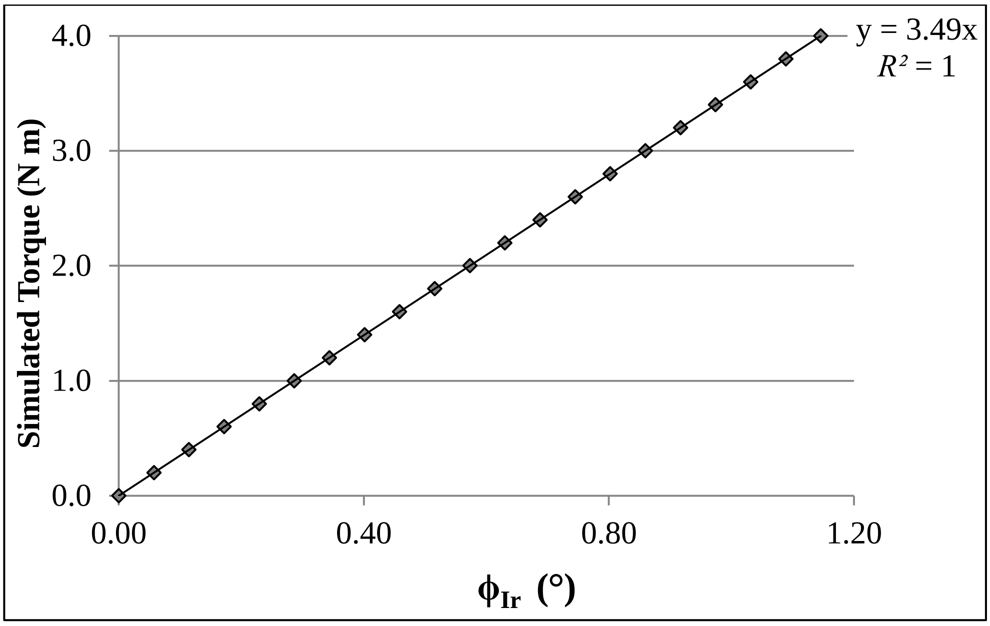

Figure 5-22 Predicted torsion (internal rotation) stiffness

5.5.4 Torsion (external rotation)

5.5.4.1 Convergence analysis

Iterative testing of the torsion FE model in external rotation demonstrated similar parameters (Table 5-4) to that of internal rotation described above. Thus iteration 2 was selected for estimation of torsional stiffness in external rotation ($k_{\mathrm{FEA\ Er}\ Int}$).

Table 5-4 Details of iterations tested during simulated torsion (external rotation) test

DOF – degree of freedom, Mesh quality = percentage of elements with aspect ratio < 3

Iteration	Maximum Element Size (mm)	Total Nodes	Total Elements	DOF	Mesh quality	ϕ_{ER} (°)	Solution Time (s)
1	5.0	26761	16181	80283	93.4	0.05	2
2	2.5	123650	80524	370950	99.6	0.05	5
3	1.25	807235	556966	2421705	99.7	0.05	23
4	0.625	5010658	3570710	15031974	99.7	0.05	176

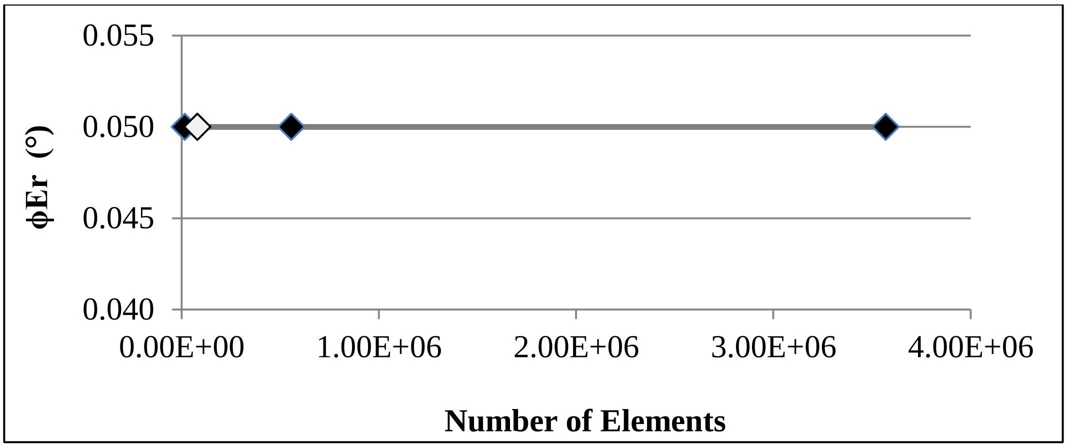

Figure 5-23 Convergence of rotation during simulated torsion (external rotation) test

5.5.4.2 Predicted torsional stiffness (external rotation) ($k_{\text{FEA Er}\,Fem}$)

The predicted torsional stiffness ($k_{\text{FEA Er}\,Fem}$) was 3.49 N m/deg (Figure 5-24).

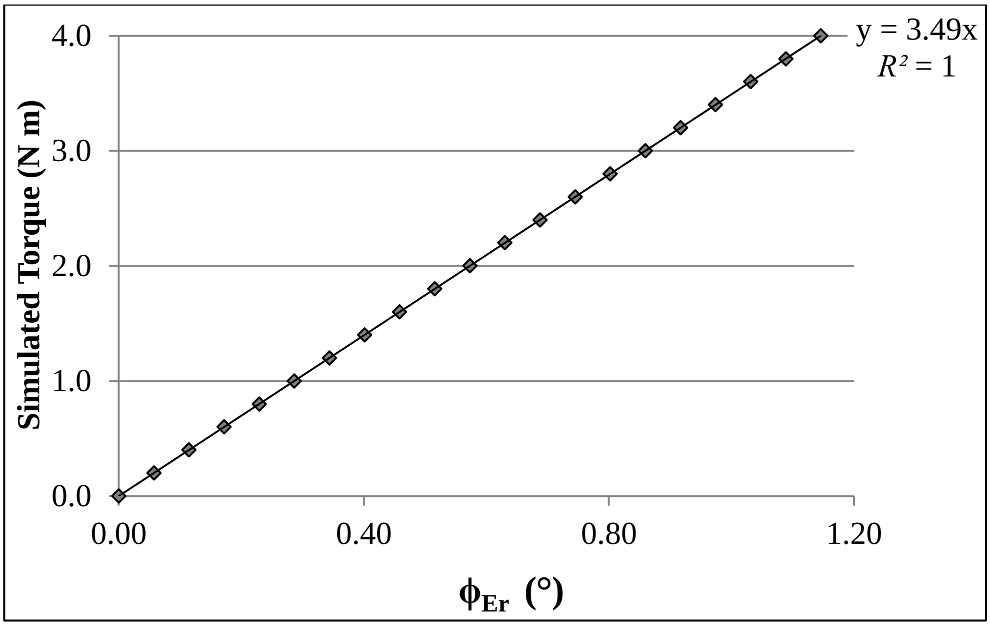

Figure 5-24 Predicted torsion (external rotation) stiffness

5.5.5 Comparison of FEA and experimental results

5.5.5.1 Linear regression analysis of experimental observations and FE predictions

a. Axial compression

The pooled displacement results from the three composite femur specimens (Sp1, Sp2 and Sp3) were compared with the predicted displacement values (U_X in mm) from the FE model (Figure 5-25).

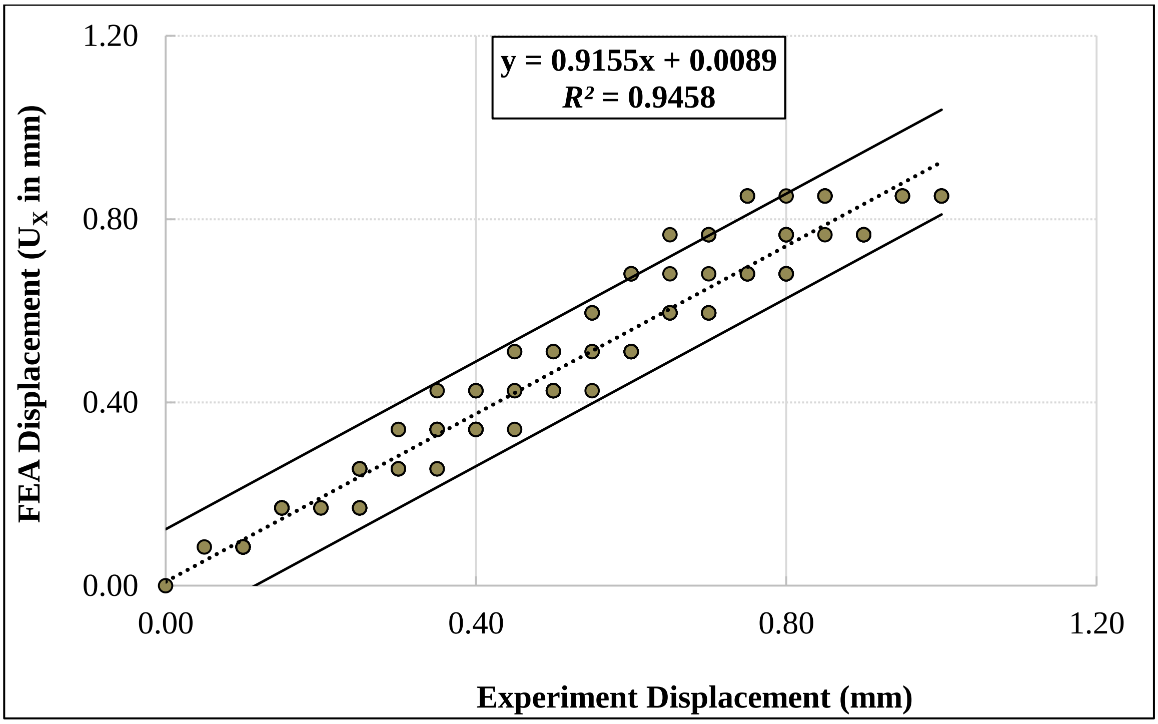

Figure 5-25 Correlation of displacement results from FEA and experimental testing for axial compression (dashed line = regression line, solid lines = 95% prediction interval)

A good correlation was noted between the experiment displacement results and the predicted results of the FE model indicated by the following regression parameters

$$U_{X\,FEA} = 0.915 \times U_{X\,EXP} + 0.008, \quad R^2=0.95 \qquad (19)$$

b. Four-point bending

The comparison of the displacement results obtained during experimental testing of the femur specimens and the predicted results (U_Y in mm) of the FE model are shown in Figure 5-26.

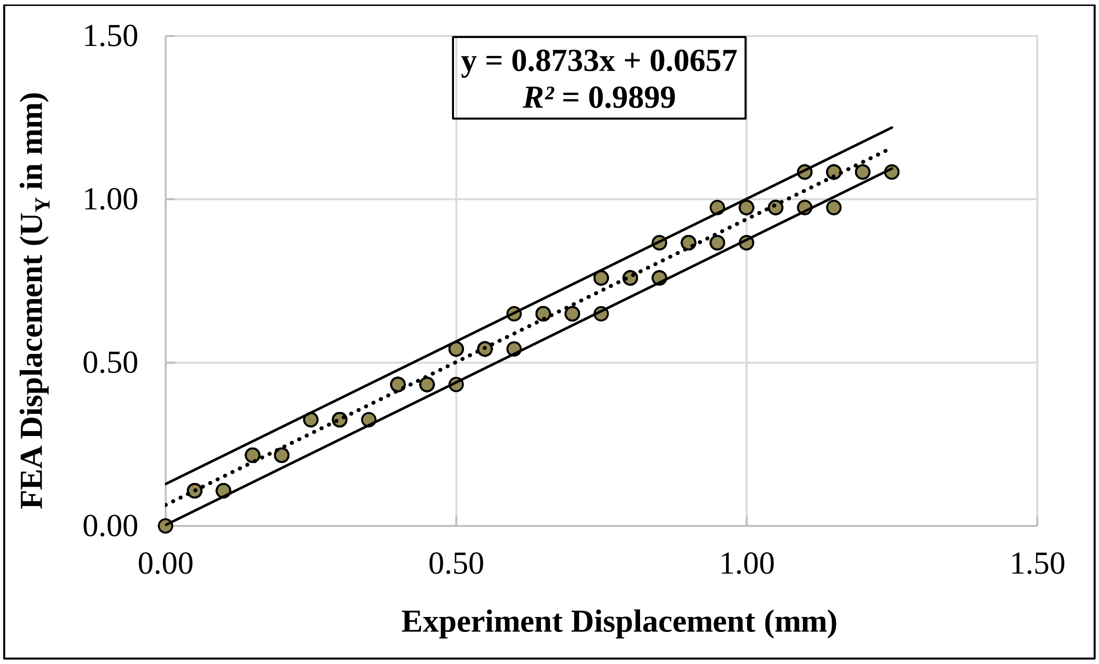

Figure 5-26 Correlation of displacement results from FEA and experimental testing for four-point bending (dashed line = regression line, solid lines = 95% prediction interval)

A linear correlation was noted between the experimental displacement results and the FE model predicted displacement results.

$$U_{Y\ FEA} = 0.873 \times U_{Y\ EXP} + 0.065, \quad R^2 = 0.99 \tag{20}$$

c. Torsion (internal rotation)

Angular rotation results from torsional loading of the three femurs in internal rotation ($\phi_{Ir\ EXP}$ in °) were compared with angular rotation results predicted by the FE model ($\phi_{Ir\ FEA}$ in °) (Figure 5-27)

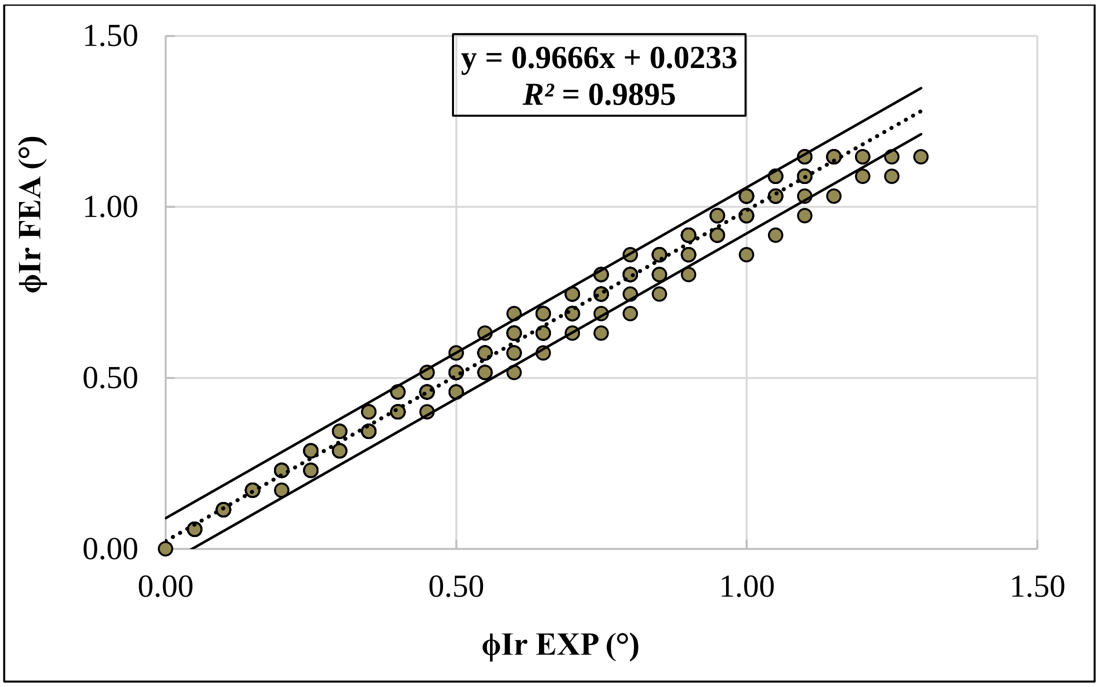

Figure 5-27 Correlation of torsion (internal rotation) results from FEA and experimental testing (dashed line = regression line, solid lines = 95% prediction interval)

An excellent correlation was noted between the experimental results and the FE model predictions manifested by the following regression parameters

$$\phi_{Ir\ FEA} = 0.966 \times \phi_{Ir\ EXP} + 0.023, \quad R^2{=}0.98 \qquad (21)$$

d. Torsion (external rotation)

Finally the angular rotation results from torsional loading of the three femurs in external rotation ($\phi_{Er\ EXP}$ in °) were compared with angular rotation results predicted by the FE model ($\phi_{Er\ FEA}$ in °)

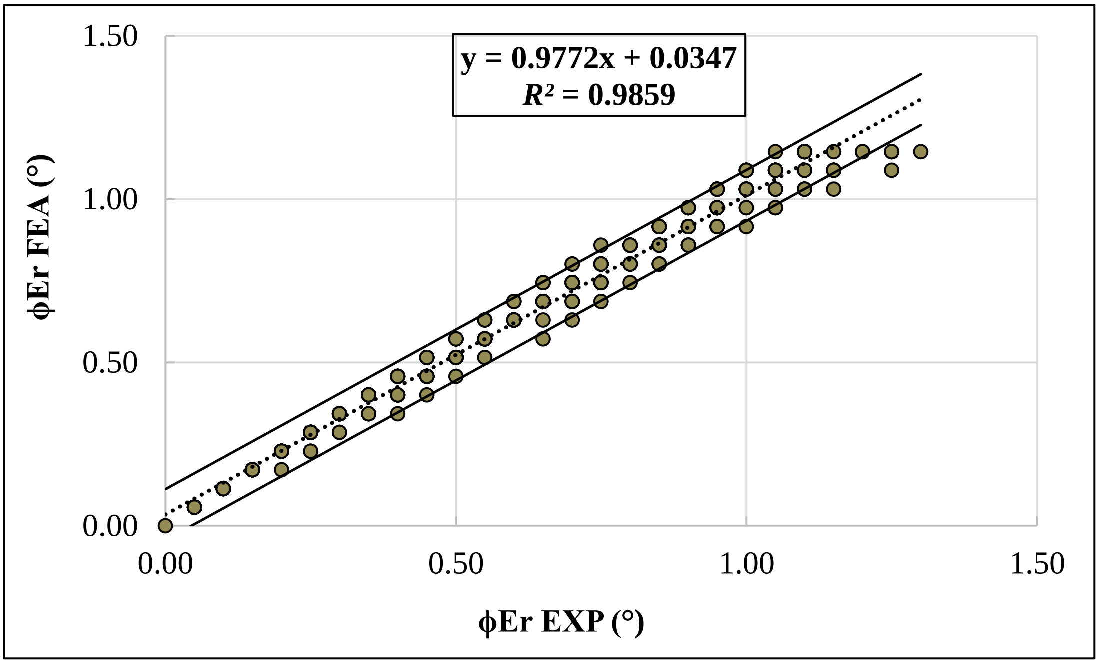

Figure 5-28 Correlation of torsion (external rotation) results from FEA and experimental testing (dashed line = regression line, solid lines = 95% prediction interval)

Regression analysis showed a good correlation between the experimental results and the FE model predictions for the angular rotation results in torsion during external rotation

$$\phi_{Er\ FEA} = 0.977 \times \phi_{Er\ EXP} + 0.034, \quad R^2 = 0.98 \tag{22}$$

5.5.5.2 Estimation of the relative error between the experimental stiffness (k_{EXP}) and the FEA predicted stiffness (k_{FEA}).

The mean (±standard deviation) axial stiffness of during experimental testing ($k_{\mathrm{EXP\ Ax}\ Int}$) was 667.39 (±70.15) N/mm. In comparison the axial stiffness predicted by the FE model ($k_{\mathrm{FEA\ Ax}\ Int}$) measured 704.83 N/mm representing a relative error of 5.61% (Figure 5-29).

Figure 5-29 Comparison of axial stiffness of intact femur

The mean (±standard deviation) four-point bending stiffness of the three femur specimens ($k_{\mathrm{EXP\ Be}\ Int}$) was 353.49 (±15.72) N/mm whereas the predicted axial stiffness from the FE model ($k_{\mathrm{FEA\ Be}\ Int}$) measured 369.1 N/mm with a relative error of 4.42% (Figure 5-30).

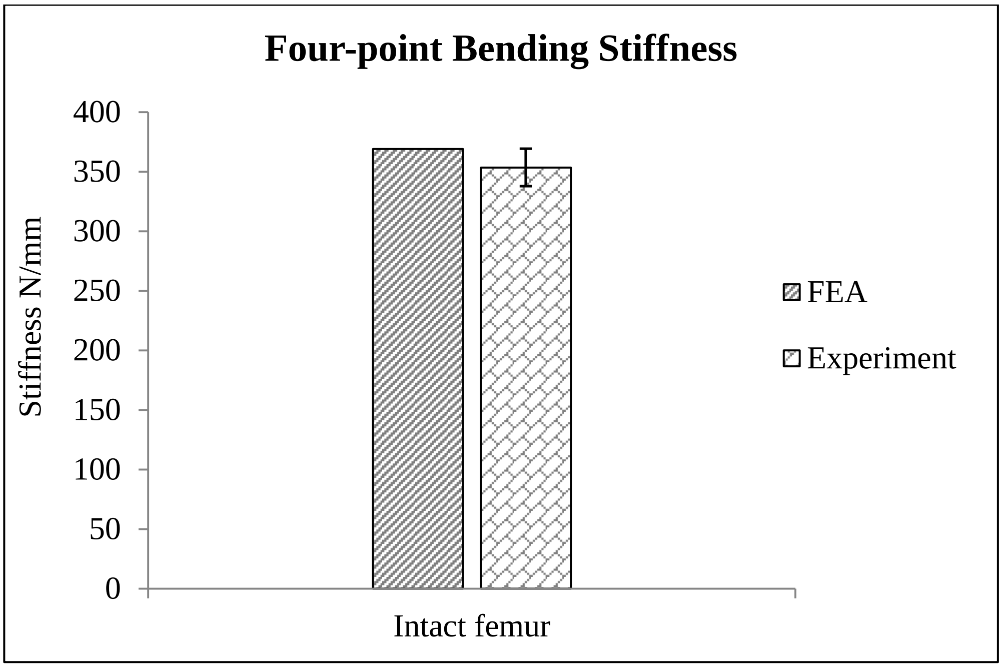

Figure 5-30 Comparison of four-point bending stiffness of intact femur

The FE model predicted torsional stiffness in internal rotation ($k_{\text{FEA Ir } Int}$) measured 3.49 N m /deg whereas experimental testing results showed the mean (±standard deviation) torsional stiffness ($k_{\text{EXP Ir } Int}$) to be 3.48 (±0.14) N m/deg representing a relative error of 0.16 % (Figure 5-31).

Comparison of torsional stiffness in external rotation estimated from experimental tests and the FE model gave a relative error of -2.54 %. This was due to the predicted torsional stiffness of the FE model ($k_{\text{FEA Er } Int}$) being relatively lower at 3.49 N m/deg in comparison to the mean (±standard deviation) torsional stiffness of the femurs ($k_{\text{EXP Er } Int}$) of 3.58 (±0.18) N m/deg (Figure 5-32).

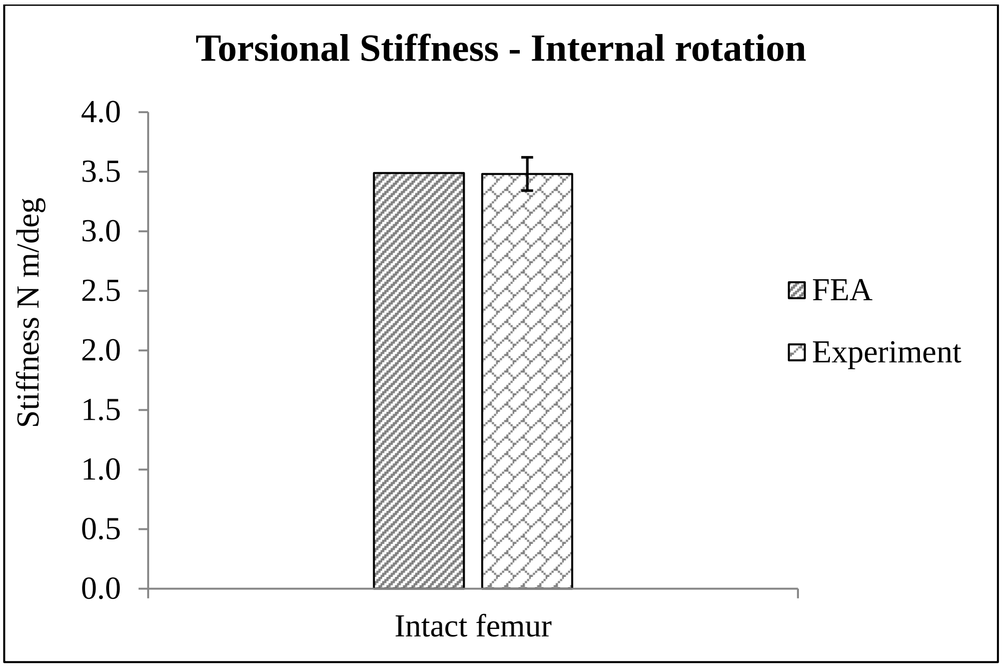

Figure 5-31 Comparison of torsional stiffness (internal rotation) of intact femur

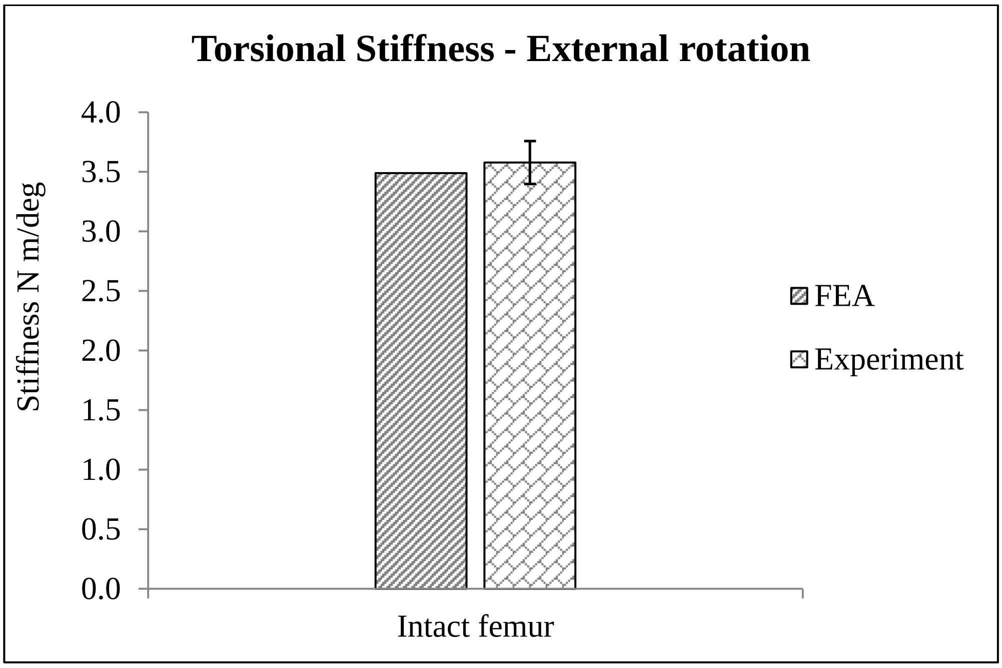

Figure 5-32 Comparison of torsional stiffness (external rotation) of intact femur

5.6 Discussion

FEA has been extensively used as a research tool in orthopaedic biomechanical studies of the femur (79, 268, 308, 327, 330, 331, 334, 336, 344-346, 348, 355, 356, 359-361, 373, 378, 379, 381). However, the majority of the described FE models pertain to the adult femur (330, 346, 382).

The various FE models of the femur described in the current literature have their origins in the initial numerical models described by Brekelmans *et al*. (383) and Rybicki *et al*. (384). Different approaches have been adopted by different investigators to develop a FE model of the femur to perform computational analysis (330, 346). The approaches used can be divided into two broad categories: 1) development of a simple representative FE model of the femur 2) development of a FE femur model based on anatomical and visual similarity. It can be noted that the approach used is largely dictated by the primary research question that the model was used to answer (330, 345, 385).

A simple representative FE model of the femur has been used to address several aspects of orthopaedic biomechanical research (268, 331, 348, 355, 386-389). Jade *et al*. (387, 388) investigated the influence of femoral curvature on the bending predictability and strength of femur. They modelled the diaphysis of the human femur as a hollow cylinder with circular cross section and different curvatures using ANSYS software. Additionally they also developed an anatomical FE model of the femur using CT scan data. They reported that under different loading conditions the von Mises stress distribution was similar amongst the two types of models. Efstathopoulos *et al*. (355) evaluated the stress fields in the distal interlocking screw of Fi-Nail (Dynamic Trochanteric Nail, Sanatmental Ltd, Hungary) using a hollow cylinder as a femur model which was three times as long as the nail. Rankovic *et al*. (386) modelled a comminuted femoral shaft fracture as two simple hollow cylinders representing the upper and lower bone segments. Subsequently one iteration of this model was stabilised with a stainless steel intramedullary nail whilst the second iteration was stabilised with a neutralisation plate. Numerical analysis was performed using PAK software to compare the stress distribution amongst the two fixation methods. Wang *et al*. (348) investigated the stress in the Gamma nail using a simplified 3D model of proximal femur developed using ANSYS finite element package. A similar approach to develop a 3D model of the proximal femur was used by Simpson whilst evaluating the Gamma nail fixation (331). The proximal femur model was developed using a series of reference points and lines followed by a skinning operation to create the desired areas and volumes. In their study, Mittlmeier *et al*. (390) modelled the femoral shaft geometry as a cylindrical tube with a height of 160 mm and an outer and inner diameter of 30 mm and 15 mm, respectively. They used this model in ABAQUS software to evaluate the effects of mechanical loading on human femoral diaphyseal geometry. Bucholz *et al*. (268) investigated the fatigue fracture of interlocking nails used to treat distal femoral shaft fractures. Using the ANSYS software code they developed an axisymmetric model of the femur which represented only the shaft. This model was 46 cm long and contained a 13 mm diameter Grosse-Kempf nail. This model lacked femoral head due to the axisymmetrical assumption. Huiskes *et al*. (389) reported a simplified model of intramedullary fixation system for THR stem wherein the femur was modelled as a cylinder with acrylic cement. A simple FE model takes less computational resource to develop, relatively less simulation time and has the potential to be developed further (345). However, this approach has certain inherent limitations as it is based on a simplified assumption of a complex structure like the femur. Thus the solutions from such FE models can help identify a trend and require validation using experimental methods (345).

Other investigators have applied the second approach to develop a femur FE model with the use of anatomical models having close visual similarity to the human femur (79, 308, 356, 359, 361, 391, 392). The standardized femur model (available for download in the public domain at http://www.biomedtown.org) has been proposed as a generic model to be used for all orthopaedic and biomechanical research (79). This model is based on the CAD geometry of a large synthetic femur and has been used by some authors (356, 361, 391) but Greer *et al*. (393) reported that it was not appropriate for stress analyses. The above approach has evolved into using subject specific models (308, 359) wherein a CT scan is used to capture the geometry of a patient's femur followed by segmentation and development of a CAD model (385). Material properties are then assigned using approximate values based on Hounsfield units or correlating the Hounsfield units from the CT scan with standardised bone mineral density phantoms (385). Additionally some studies (362, 392) have used approximation of the various muscle forces described by Bergmann (311) and Duda (314) to simulate *in vivo* load on the femur. However, this approach is evolving (382) and some investigators have questioned its use for all biomechanical research given the current lack of universal bone material laws (394) and uncertainties regarding the load and orientation of different muscles in the hip musculature (395, 396). The adolescent femur *in vivo* has a complex structure (consisting of osseous and physeal components as described in chapter 2) and geometry. There is no FE model in the current literature which accurately models these characteristics. It must be noted that the values of muscle forces reported in the literature from the aforementioned study (311) were obtained in adult patients with total hip replacement which may not be relevant to the paediatric patient. Furthermore muscle function is affected following intramedullary nail fixation of the femur in the perioperative period (397-400). It has therefore been suggested that more useful information can be gained from FEA if the main load components are applied to the bone individually rather than replicating a large number of loading conditions (345, 395). Hence this approach was adopted in the current study.

A major limitation with subject specific modelling approach is that it increases the numerical complexity of the model (385). It requires more computational time, resources and even supercomputers (329) to perform numerical analysis which may not be available to all the investigators (330, 345). FEA with this approach can produce a large amount of data but the relevance of it in the clinical scenario remains limited (92, 382, 385). Furthermore visual similarity of the model to the real femur gained by accurate geometric representation using CT scan based reconstruction does not guarantee an accurate result (381, 382). Hence in a review of the topic, Prendergast (382) included a succinct quote from Ferguson (401) regarding computer-based analysis for the design of orthopaedic implants: 'the successful design of real things in a contingent world will always be based more on art than on science'. In order to perform a useful FEA, it is therefore vital to strike a balance between complex models which visually mimic the bony structure and simple models which offer ease-of-analysis (331, 345, 360, 382).

Previous studies in this field (402, 403) have used specialised algorithms to develop 3D bone models from radiographs. However, the lack of widespread availability of such algorithms limits their applicability. Enhanced processing capability of computers has enabled the development of bone FEA models with good visual similarity through accurate geometric representation. However, this approach does not necessarily guarantee the numerical accuracy of the results predicted by such models (381). In their study Perez and colleagues (77) used the bone model available for download from the aforementioned source. The model measured 420 mm in length with a canal diameter of 9 mm which is probably representative of an adolescent femur. It has been noted that a change in the synthetic femur geometry from a large to small dimension can result in axial and torsional rigidity differences of 1.5 and 2.2 times respectively despite having the same Young's modulus for the cortical bone (347). It will be of interest to note the predictions from their model if the overall dimensions were scaled down to be representative of a child's small femur. Krauze (404) performed biomechanical analysis comparing flexible intramedullary nails of two different materials. The femur FE model in this study is reported to be based on a 5-7 year old child. However, the details regarding development of the femur FE model and its dimensions are not provided in the paper.

The primary objective of this part of the study was to develop a FE model that accurately predicted displacement and stiffness of the *in vitro* bone model. A FE model based on simplified geometry of the paediatric femur was successfully developed using orthogonal digital radiographs as a template (350). Digital radiographs enable development of FE model that is simple yet representative of the overall dimensions and features viz. radius of curvature of the paediatric femur (273). This is an important requisite of a femur FE model used to assess the biomechanical parameters of intramedullary implants (18). It has been demonstrated that omission of cancellous bone in the femur FE model does not significantly alter the overall stiffness results (356, 361). Therefore in the paediatric FE model cancellous bone tissue was not modelled separately to optimise computational time (395). Many software packages like ANSYS (268, 348, 392), ABAQUS (336, 379, 390), MENTAT (77) NASTRAN (332) have been described in the literature to perform FEA. This study used SolidWorks™ as it combined pre-processing (development of CAD model), numerical analysis and post-processing tools (simulation) in a single platform (328, 337, 338). Other investigators have used SolidWorks™ simulation to perform FEA of cannulated hip screws (405, 406), intramedullary fixation of distal third femoral shaft fracture (407), wrist arthroplasty implant (333), mandibular and dental implants (408-410), ankle joint (411) and prosthetic foot (412).

A comparison of FEA results with experimental results is mandatory for robust validation of the FE model and its inherent assumptions (327, 330, 331, 334, 344, 345, 356, 360, 376). However, both the aforementioned studies (77, 78) which evaluated paediatric femoral shaft fracture fixation using FEA did not provide any information on their validation methodology. The correlation coefficient (R^2) values for the current femur FE model ranged from 0.94 for axial compression to 0.98 for both simulated four-point bending and torsion loading tests. The relative error between the experimental stiffness (k_{EXP}) and the stiffness predicted by FE model (k_{FEA}) ranged from -2.54% (torsion in external rotation) to 5.61% (axial compression). These values are within the acceptable range published in the current literature for femur FE model validation (359, 361, 376, 378, 379, 413, 414).

5.7 Conclusions

Orthogonal digital radiographs can be used as a template to develop a simplified finite element model of a paediatric composite femur. A FE model based on simplified geometry can be used for evaluation of routine stiffness parameters of a paediatric composite femur.

So far a combination of experimental testing (chapter 4) and FEA (chapter 5) of intact paediatric composite femur specimens has been described. The baseline (intact femur) stiffness parameters have been established.

The next chapter presents the methodology of implantation of ALFN into the composite femur specimens, creation of standardised simulated fractures and experimental testing to assess construct stiffness.

6 PAEDIATRIC FEMUR FRACTURE FIXATION - EXPERIMENTAL MODEL

6.1 Introduction

This chapter describes the biomechanical testing of paediatric composite femur specimens following the implantation with ALFN. An overview of the methodology is presented in the initial section with description of the implantation of the ALFN in sawbones, standardised osteotomy technique to simulate common fracture types and the results of the biomechanical testing in the subsequent sections. Analysis of the results and relevant biomechanical studies of rigid femoral intramedullary nails in the literature are discussed in the final section of the chapter.

6.2 Overview of methodology

Following the completion of biomechanical tests on the native sawbones, estimation of the appropriate size of ALFN was undertaken using the guidelines in the manufacturer manual (20). ALFN (length-300 mm, outer diameter 11 mm in proximal and 8.2 mm in distal regions) was selected using the sizing template (273). As all the sawbones were of the same geometry, the above nail size was used for all the three femur specimens. The nails were inserted in the intact sawbones as per the surgical technique described in the manufacturer manual. This involved the following steps: insertion of the guidewire, serial reaming of the proximal femur (up to a depth of 75 mm) starting with 8.5 mm reamer and ending with 13.0 mm reamer, reaming of the medullary canal with 9.5 mm reamer, insertion of ALFN, insertion of proximal and distal interlocking screws under fluoroscopic guidance (further details of the surgical technique are provided in Appendix 3). Thus a composite femur and ALFN construct (FAC) was obtained. Following satisfactory visual inspection to rule out any surface cracks, orthogonal digital radiographs (anteroposterior and lateral views) were obtained for all the sawbones (Figure 6-1).

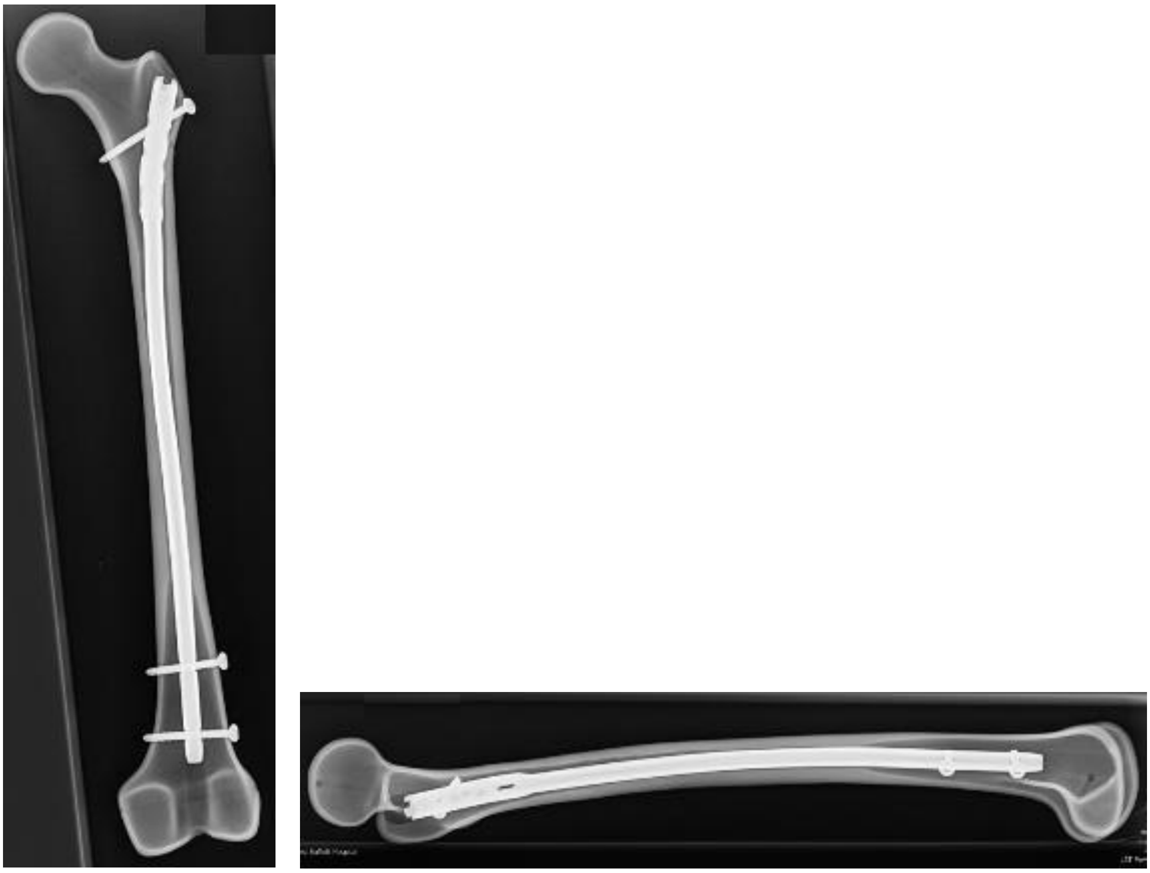

Figure 6-1 Digital radiographs of composite femur with ALFN *in situ* (left - anteroposterior view, right - lateral view)

This configuration was assumed to represent a fully healed and remodelled fracture construct (254, 319, 361) (Figure 6-1). Biomechanical tests were performed and stiffness parameters were determined for the healed fracture construct. Subsequently, standardised osteotomies were sequentially performed on each of the femur specimens (with ALFN *in situ*) to simulate common fracture patterns observed in clinical practice namely transverse, comminuted and segmental defect (319, 361). Axial, four-point bending and torsional stiffness were determined for each of the fracture configurations. A flowchart illustrating the sequence of the biomechanical testing for the aforementioned fracture configurations is shown below in Figure 6-2.

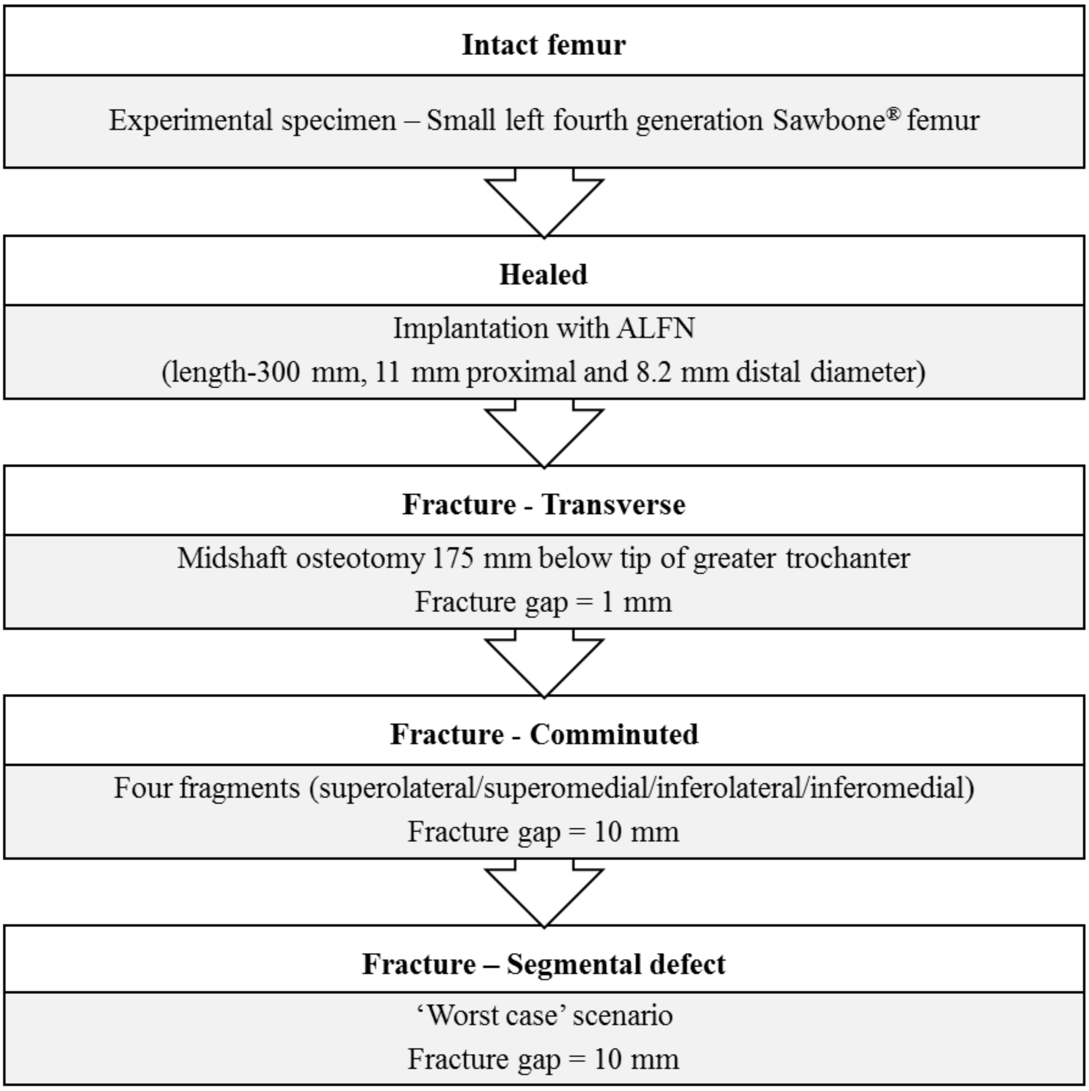

Figure 6-2 Flowchart of biomechanical testing

Biomechanical testing (axial compression / four-point bending) of the healed configuration was performed on the Instron testing machine as described earlier in chapter 4. The remainder of the fracture configurations (transverse / comminuted / segmental defect) were tested for axial compression and four-point bending in a MTS (MTS Systems Corp, Eden Prairie, USA) testing machine with a 500 N load cell. In order to avoid introducing any qualitative error in subsequent comparison of stiffness parameters amongst the different configurations, three additional small composite femur specimens were obtained to serve as a control group (415). These were labelled as Sp4, Sp5 and Sp6 and tested individually in axial compression (up to 300 N) and four-point bending (up to 60 N) in the MTS testing machine. Torsion testing (up to 2 N m) of these femur specimens was performed on the torsion test jig described earlier in chapter 4. The stiffness parameters obtained from these new specimens were pooled and evaluated to obtain the intact femur stiffness values for the control group ($k_{\mathrm{EXP}\ Ctl}$). Subsequently the stiffness parameters of the aforementioned fracture groups were compared with the control group.

6.3 Materials and methods

6.3.1 Implantation of sawbone specimens with ALFN

All the three femur specimens (Sp1, Sp2 and Sp3) were prepared for implantation with ALFN as per the surgical technique described in the manufacturer manual (20). Based on size estimation templates provided by the manufacturer, ALFN (length 300 mm, proximal diameter of 11 mm and distal diameter of 8.2 mm) was selected and inserted into each of the femur specimens. The proximal (120° antegrade) interlocking screw measured 56 mm whereas the first and second distal interlocking screws measured 36 mm and 46 mm respectively. Digital radiographs of the implanted femur specimens confirmed the accuracy of nail and screw size selection (Figure 6-1).

6.3.2 Standardised osteotomy to simulate different fracture types

A midshaft osteotomy (175 mm below the tip of the greater trochanter) was performed on all the sawbones. The femur specimens were aligned by placing the distal end in the PMMA mold. The longitudinal (anatomical) axis of the femoral shaft was marked (416, 417). A Vernier height gauge was used to mark the 175 mm point. An osteotomy perpendicular to the longitudinal axis (gap of 1 mm to simulate a transverse fracture) was performed using a handheld saw. Care was taken not to damage the nail *in situ* whilst performing the osteotomy (361). This technique ensured that the osteotomy was similar across all the test specimens (Figure 6-3).

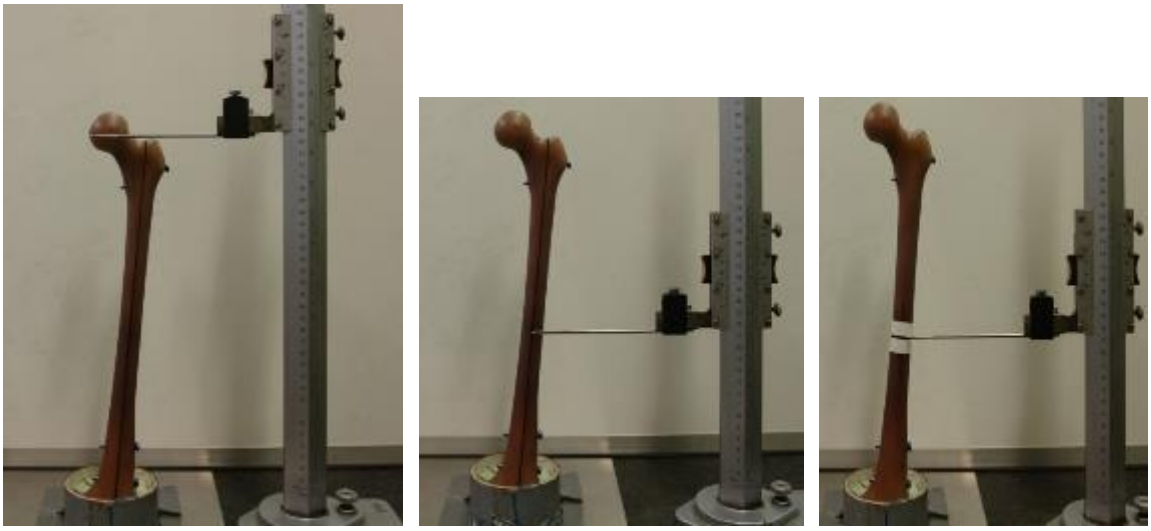

Figure 6-3 Pictures demonstrating transverse fracture osteotomy - Vernier height gauge at tip of greater trochanter (left), 175 mm below tip (middle) and completion of osteotomy (right)

To create a comminuted fracture (with four fragments) two points were marked. The first point was marked at 5.5 mm lateral to the longitudinal axis of the femur. The second point was marked at distance of 17.5 mm from the first point (Figure 6-4). The above points were calculated using arc of a circle principle (371) such that the smaller fragment (minor sector) resulted in an angle of 100° (Figure 6-6). The points were situated 5 mm on either side of the previously created transverse fracture osteotomy. This allowed for creation of a standardised comminuted fracture spanning 10 mm along the longitudinal axis across all the three specimens.

Figure 6-4 Reference points for comminuted fracture osteotomy

Figure 6-5 Reference points on superior aspect of transverse osteotomy to create superolateral and superomedial fragments

At the above points vertical cuts were made towards the transverse fracture resulting in four fragments (superolateral / superomedial / inferolateral / inferomedial) of the comminuted fracture (Figure 6-6).

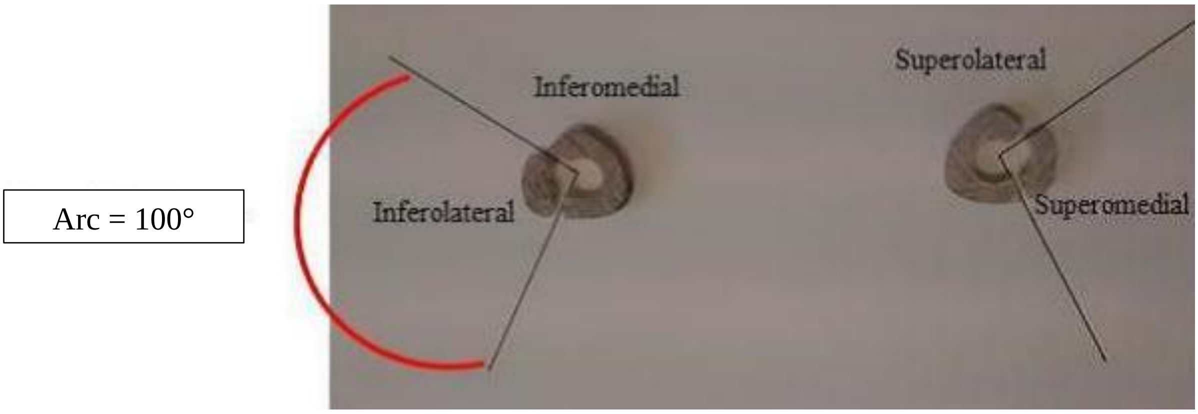

Figure 6-6 Comminuted fracture with four fragments

The comminuted fracture fragments were held together using a single layer of surgical tape (Transpore™; 3M, St Paul, Minnesota, USA) as described in the literature (291, 306) (Figure 6-7).

Figure 6-7 Comminuted fracture fragments held with Transpore™

The last fracture configuration represented the ‘worst-case scenario’ of a segmental defect. All the four fragments described above were removed to create a segmental defect of 10 mm (Figure 6-8).

Figure 6-8 Simulated midshaft segmental defect with a fracture gap of 10 mm

6.3.3 Biomechanical testing

During the immediate postoperative period, patients with intramedullary nail fixation undergo supervised weight bearing and physiotherapy (3, 30). Currently there is a lack of consensus on the optimum weight bearing regimen in the perioperative period (3, 5). In general, an acceptable limit for weight bearing is guided by the severity of the fracture and stability of the intramedullary nail fixation (3, 14, 23, 30, 34, 51, 268). For the purpose of this study an assumption of patient (body weight of 60 kg) mobilising with partial weight bearing (50% of body weight) was made. Additionally, the available parameters from the study by Schneider *et al*. (249) measuring the *in vivo* forces acting on the intramedullary nail were used to estimate the load parameters for the biomechanical testing of femoral specimens with simulated fractures stabilised using the ALFN.

The set up and testing protocol of the three femur and ALFN construct (Sp1/Sp2/Sp3 in healed and fractured configurations) and the control group (Sp4/Sp5/Sp6) was similar to that of the intact sawbones described earlier in chapter 4. However, the maximum load parameters for each test was set appropriately to reflect the perioperative weight bearing status of the patient, as shown in Table 6-1.

Table 6-1 Load parameters used during biomechanical testing. TTJ – torsion test jig

	Group				
	Healed	**Transverse**	**Comminuted**	**Segmental defect**	**Control**
Axial compression					
Maximum Load (N)	600	300	300	300	300
Test setup	Instron	MTS	MTS	MTS	MTS
Four-point bending					
Maximum Load (N)	400	60	60	60	60
Test setup	Instron	MTS	MTS	MTS	MTS
Torsion (internal rotation)					
Maximum Load (N m)	4	2	2	2	2
Test setup	TTJ	TTJ	TTJ	TTJ	TTJ
Torsion (external rotation)					
Maximum Load (N m)	4	2	2	2	2
Test setup	TTJ	TTJ	TTJ	TTJ	TTJ

Following transverse fracture osteotomy, the three femur and ALFN constructs were individually tested to establish stiffness parameters in axial compression, four-point bending and torsion (external/internal rotation). Biomechanical testing of the different groups was undertaken sequentially as illustrated in Figure 6-2.

6.3.3.1 Axial compression

As highlighted in Table 6-1, only the healed group underwent axial compression testing in the Instron testing machine. A compressive load of 600 N was applied at a displacement rate of 0.17 mm/s. The remainder of the groups including the three femurs from the control group underwent axial compression testing using the MTS Criterion® materials testing machine (MTS Systems Corp, Eden Prairie, USA). A compressive force of 300 N was applied along the mechanical axis of the femur at a displacement rate of 0.17 mm/s in the MTS testing machine (Figure 6-9).

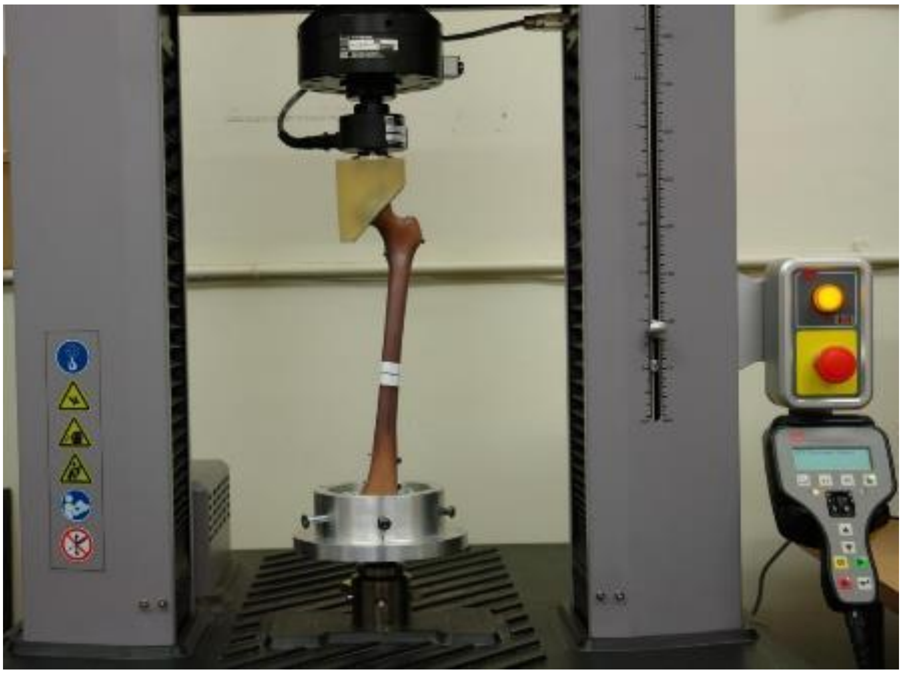

Figure 6-9 Axial compression test setup using the MTS testing machine showing the femur with a transverse fracture and ALFN *in situ*

6.3.3.2 Four-point bending

The healed group underwent four-point bending test using the Instron testing machine. A maximum bending load of 400 N was applied at a displacement rate of 0.17 mm/s. The remainder of the fracture groups including the three femurs from the control group underwent four-point bending tests using the MTS testing machine (Figure 6-10). A maximum bending load of 60 N was applied at a displacement rate of 0.17 mm/s using the MTS testing machine.

Figure 6-10 Four-point bending test set up using the MTS machine with control femur

6.3.3.3 Torsion (internal rotation)

Torsion testing (internal rotation) of all the groups was performed using the torsion test jig with the set up and protocol similar to that described in chapter 4. For the healed group, a maximum torque of 4 N m was applied in 0.2 N m increments whereas a maximum torque of 2 N m was applied in 0.1 N m increments for the remainder of the fracture groups (Table 6-1).

6.3.3.4 Torsion (external rotation)

Torsion testing (external rotation) of all the groups was performed using the torsion test jig with the set up and protocol similar to that described in chapter 4. For the healed group, a maximum torque of 4 N m was applied in 0.2 N m increments whereas a maximum torque of 2 N m was applied in 0.1 N m increments for the remainder of the fracture groups (Table 6-1).

Six tests were performed on each specimen in the above groups with a 10 minute interval in between each loading test to allow the viscoelastic properties of the bone to return to the normal state (286).

6.3.4 Data analysis

Calculation of stiffness parameters in axial compression, four-point bending and torsion (internal/external rotation) was performed as described earlier in chapter 4.

Control group - For each specimen the mean, standard deviation and coefficient of variation was calculated from the six test results. The mean value thus obtained represented the stiffness of the individual specimen (322, 323). As each of the three femur specimens (Sp4, Sp5 and Sp6) underwent six tests, a total of 18 results for each type of stiffness were obtained. These 18 results were further collated to determine the mean stiffness of control femur group ($k_{\mathrm{EXP}\ Ctl}$).

Fracture groups – Similar data analysis was performed on each of the fractured femur and ALFN construct in the transverse, comminuted and segmental defect groups. Each of the FAC underwent six tests generating a total of 18 tests for the group. These 18 results were collated to determine the mean stiffness of the fracture groups namely transverse fracture group ($k_{\mathrm{EXP}\ Tra}$), comminuted fracture group ($k_{\mathrm{EXP}\ Com}$) and segmental defect group ($k_{\mathrm{EXP}\ Seg}$).

Healed group – As above, analysis of the results was performed on the three FAC in the healed group. All the 18 test results were collated to determine the mean stiffness of the healed group ($k_{\text{EXP}\ Hld}$)

Relative construct stiffness - In order to allow comparison and estimate the relative change in the stiffness of the healed and fracture groups, their corresponding stiffness values comprising of the femur and ALFN construct (FAC) were expressed as a percentage of the stiffness of intact and control group as shown below (283, 320, 418).

$$\text{FAC}_{Tra}\ (\%) = \frac{k_{\text{EXP}\ Tra}}{k_{\text{EXP}\ Ctl}} \times 100 \tag{23}$$

where *Tra* = Transverse fracture group, *Ctl* = Control femur group

$$\text{FAC}_{Com}\ (\%) = \frac{k_{\text{EXP}\ Com}}{k_{\text{EXP}\ Ctl}} \times 100 \tag{24}$$

where *Com* = Comminuted fracture group, *Ctl* = Control femur group

$$\text{FAC}_{Seg}\ (\%) = \frac{k_{\text{EXP}\ Seg}}{k_{\text{EXP}\ Ctl}} \times 100 \tag{25}$$

where *Seg* = Segmental defect fracture group, *Ctl* = Control femur group

$$\text{FAC}_{Hld}\ (\%) = \frac{k_{\text{EXP}\ Hld}}{k_{\text{EXP}\ Int}} \times 100 \tag{26}$$

where *Hld* = Healed fracture group, *Int* = Intact femur group

6.4 Results

6.4.1 Axial compression

6.4.1.1 Control group

The results of six tests on the three composite femur specimens (Sp4, Sp5 and Sp6) in the control group are shown in Figure 6-11.

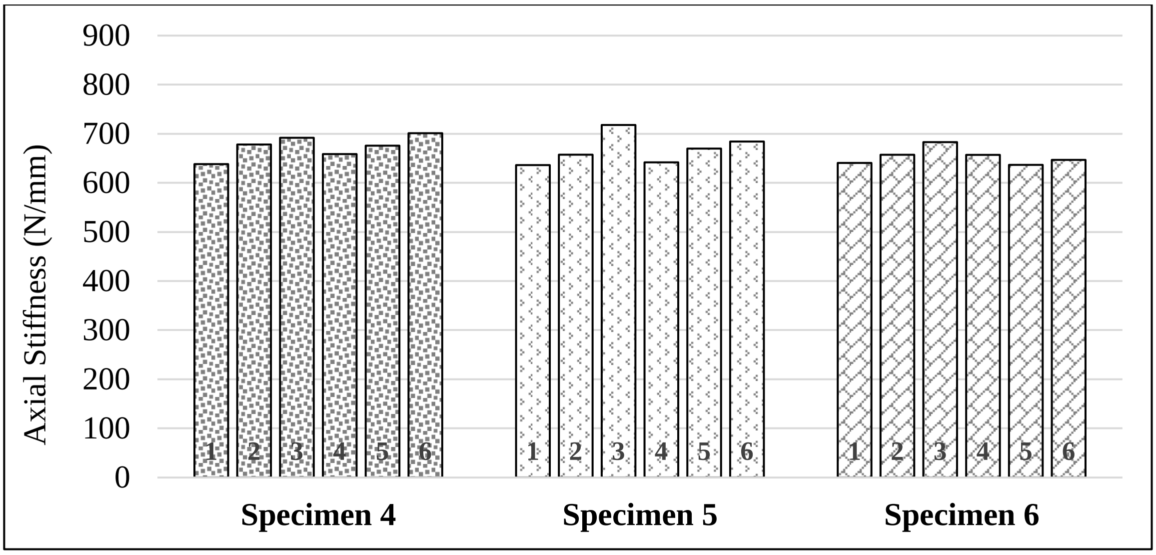

Figure 6-11 Axial stiffness test results of control group

The mean axial stiffness in axial compression of the three femur specimens ranged from 653.58 N/mm – 674.00 N/mm and the standard deviation from 16.67 – 30.20 N/mm. The overall mean axial stiffness of the three femur specimens (control group) ($k_{\mathrm{EXP\ Ax}\ Ctl}$) was 665.17 N/mm with a standard deviation of 24.09 N/mm. (Table 6-2)

Table 6-2 Axial stiffness results of femur specimens in control group

n – number of tests, SD – standard deviation, COV – coefficient of variation

Specimen	n	Mean (N/mm)	SD	COV (%)	Minimum (N/mm)	Median (N/mm)	Maximum (N/mm)
Sp4	6	674.00	22.77	3.38	638.24	677.00	701.19
Sp5	6	667.93	30.20	4.52	636.26	663.66	717.92
Sp6	6	653.58	16.67	2.55	636.70	651.95	683.00
Group							
Control	18	665.17	24.09	3.62	636.26	658.06	717.92

6.4.1.2 Fracture groups

The axial stiffness results of the three fracture groups are shown in Figure 6-12 and Table 6-3.

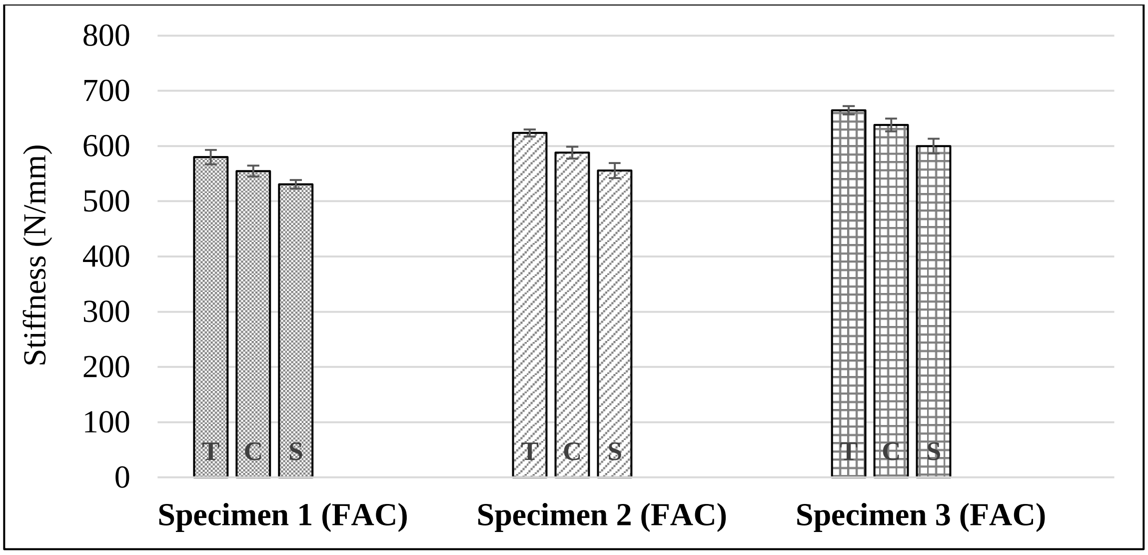

Figure 6-12 Mean axial stiffness with standard deviation (error bars) of three fracture groups

FAC – Femur and ALFN Construct, T – Transverse, C – Comminuted, S – Segmental defect

Table 6-3 Axial stiffness results of the three fracture groups

n – number of tests, SD – standard deviation, COV – coefficient of variation, FAC – Femur and ALFN construct

Specimen	n	Mean (N/mm)	SD	COV (%)	Minimum (N/mm)	Median (N/mm)	Maximum (N/mm)
Sp1 FAC	6	580.03	12.95	2.23	558.41	580.68	595.64
Sp2 FAC	6	623.80	6.51	1.04	611.76	624.35	629.89
Sp3 FAC	6	664.70	7.38	1.11	655.20	663.87	675.90
Group							
Transverse	18	622.84	36.65	5.88	558.41	624.35	675.90
Sp1 FAC	6	554.59	9.72	1.75	541.31	553.07	570.93
Sp2 FAC	6	588.08	10.61	1.80	578.09	586.04	608.51
Sp3 FAC	6	599.82	13.39	2.23	619.89	639.96	649.71
Group							
Comminuted	18	593.62	36.71	6.18	541.31	586.04	649.71
Sp1 FAC	6	530.67	7.94	1.50	522.02	531.65	539.61
Sp2 FAC	6	555.65	13.79	2.48	538.03	553.11	577.19
Sp3 FAC	6	599.82	13.39	2.23	581.10	604.84	612.83
Group							
Segmental defect	18	562.04	31.51	5.61	522.02	553.11	612.83

6.4.1.3 Healed group

Axial stiffness results of the healed group are shown below in Figure 6-13 and Table 6-4.

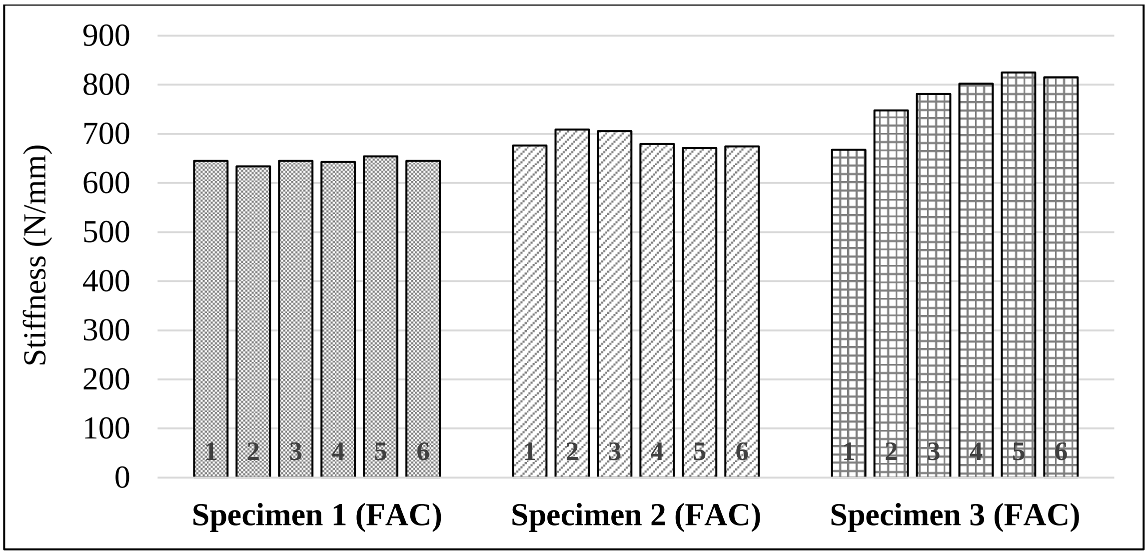

Figure 6-13 Axial stiffness test results of healed group

Table 6-4 Axial stiffness results of healed group

n – number of tests, SD – standard deviation, COV – coefficient of variation, FAC – Femur and ALFN construct

Specimen	n	Mean (N/mm)	SD	COV (%)	Minimum (N/mm)	Median (N/mm)	Maximum (N/mm)
Sp1 FAC	6	644.43	6.49	1.01	633.96	645.11	654.29
Sp2 FAC	6	686.08	16.70	2.43	671.34	677.97	708.89
Sp3 FAC	6	773.29	58.61	7.58	667.63	791.90	825.09
Group							
Healed	18	701.27	64.48	9.19	633.96	675.47	825.09

6.4.2 Four-point bending

6.4.2.1 Control group

The results of six tests on the three control femur specimens (Sp4, Sp5 and Sp6) are illustrated in Figure 6-14.

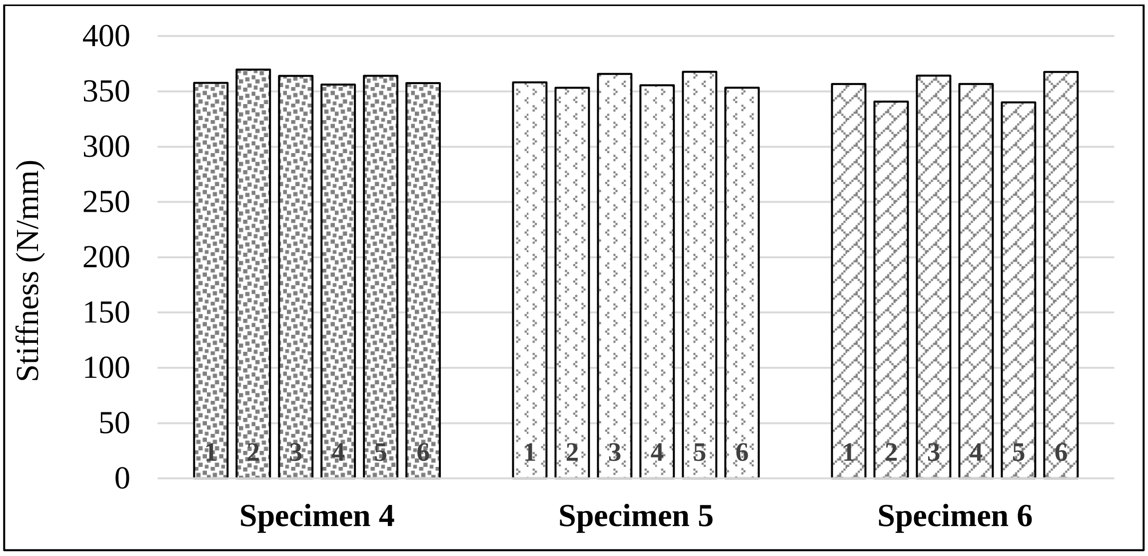

Figure 6-14 Four-point bending stiffness results of control group

The mean four-point bending stiffness of the three femur specimens ranged from 354.34 N/mm – 361.53 N/mm and the standard deviation from 5.28 – 11.60 N/mm. The overall mean four-point bending stiffness of the three femur specimens (control group) ($k_{\mathrm{EXP\ Be}\ Ctl}$) was 358.28 N/mm with a standard deviation of 8.30 N/mm. (Table 6-5)

Table 6-5 Four-point bending stiffness of control femur specimens

n – number of tests, SD – standard deviation, COV – coefficient of variation

Specimen	n	Mean (N/mm)	SD	COV (%)	Minimum (N/mm)	Median (N/mm)	Maximum (N/mm)
Sp4	6	361.53	5.28	1.46	356.17	360.85	369.71
Sp5	6	358.97	6.33	1.76	353.28	356.86	367.72
Sp6	6	354.34	11.60	3.27	340.06	356.69	367.58
Group							
Control	18	358.28	8.30	2.32	340.06	357.60	369.71

6.4.2.2 Fracture groups

The results of the three fracture groups are displayed in Figure 6-15 and Table 6-6.

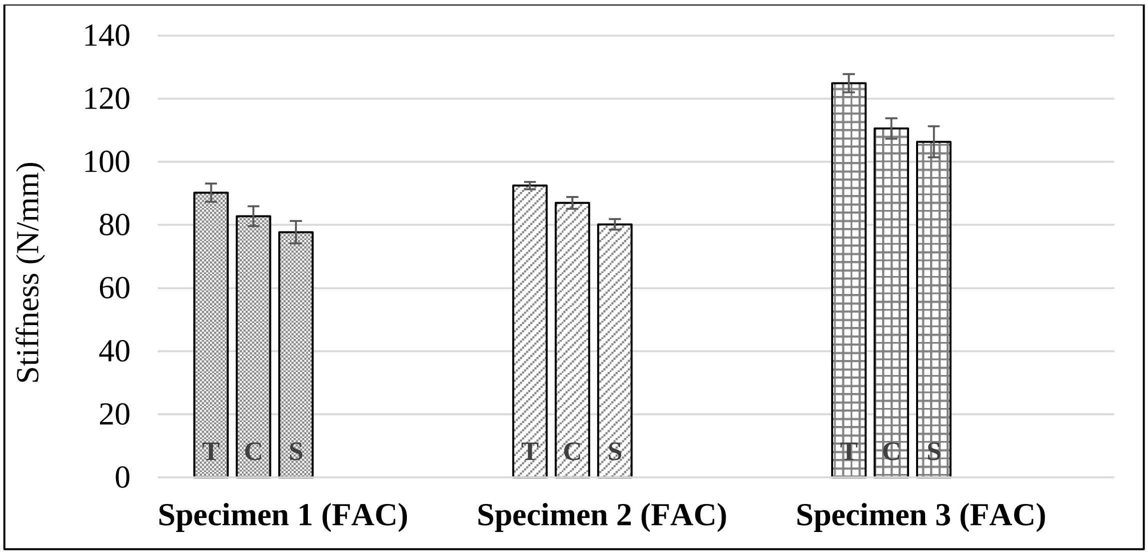

Figure 6-15 Mean four-point bending stiffness with standard deviation (error bars) of three fracture groups

FAC – Femur and ALFN Construct, T – Transverse, C – Comminuted, S – Segmental defect

Table 6-6 Four-point bending stiffness results of the three fracture groups

n – number of tests, SD – standard deviation, COV – coefficient of variation, FAC – Femur and ALFN construct

Specimen	n	Mean (N/mm)	SD	COV (%)	Minimum (N/mm)	Median (N/mm)	Maximum (N/mm)
Sp1 FAC	6	90.21	2.87	3.18	85.83	90.37	93.50
Sp2 FAC	6	92.49	1.19	1.29	90.49	92.96	93.50
Sp3 FAC	6	124.91	2.85	2.28	120.97	125.13	127.99
Group							
Transverse	18	102.53	16.47	16.06	85.83	93.20	127.99
Sp1 FAC	6	82.76	3.12	3.77	79.08	82.61	88.00
Sp2 FAC	6	86.99	1.83	2.11	83.40	87.74	88.29
Sp3 FAC	6	110.58	3.25	2.94	105.96	110.84	114.55
Group							
Comminuted	18	93.44	12.87	13.77	79.08	87.96	114.55
Sp1 FAC	6	77.69	3.54	4.56	73.50	78.04	83.40
Sp2 FAC	6	80.16	1.68	2.10	78.12	80.01	82.59
Sp3 FAC	6	106.32	4.92	4.62	100.84	106.03	112.89
Group							
Segmental defect	18	88.06	13.76	15.63	73.50	80.81	112.89

6.4.2.3 Healed group

Four-point bending stiffness results of the healed group are shown below in Figure 6-16 and

Table 6-7.

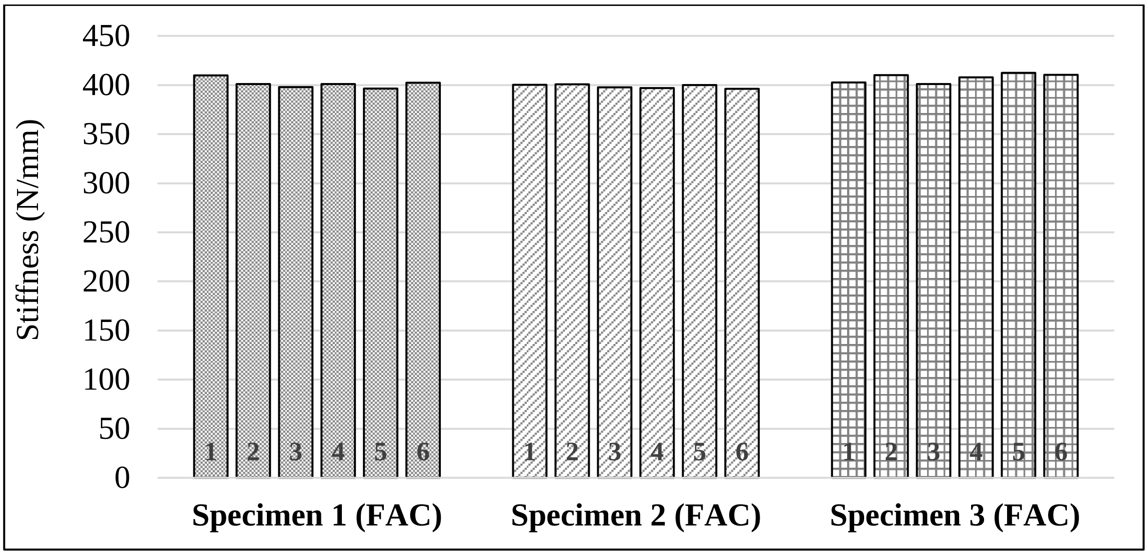

Figure 6-16 Four-point bending stiffness results of the healed group

Table 6-7 Four-point bending stiffness test results of the healed group

n – number of tests, SD – standard deviation, COV – coefficient of variation, FAC – Femur and ALFN construct

Specimen	n	Mean (N/mm)	SD	COV (%)	Minimum (N/mm)	Median (N/mm)	Maximum (N/mm)
Sp1 FAC	6	401.45	4.68	1.16	396.42	401.05	409.85
Sp2 FAC	6	398.64	1.95	0.49	396.18	398.84	400.78
Sp3 FAC	6	407.42	4.58	1.13	401.05	408.99	412.44
Group							
Healed	18	402.50	5.28	1.31	396.18	401.05	412.44

6.4.3 Torsion (internal rotation)

6.4.3.1 Control group

The results of the six tests on the three composite femur specimens are shown in

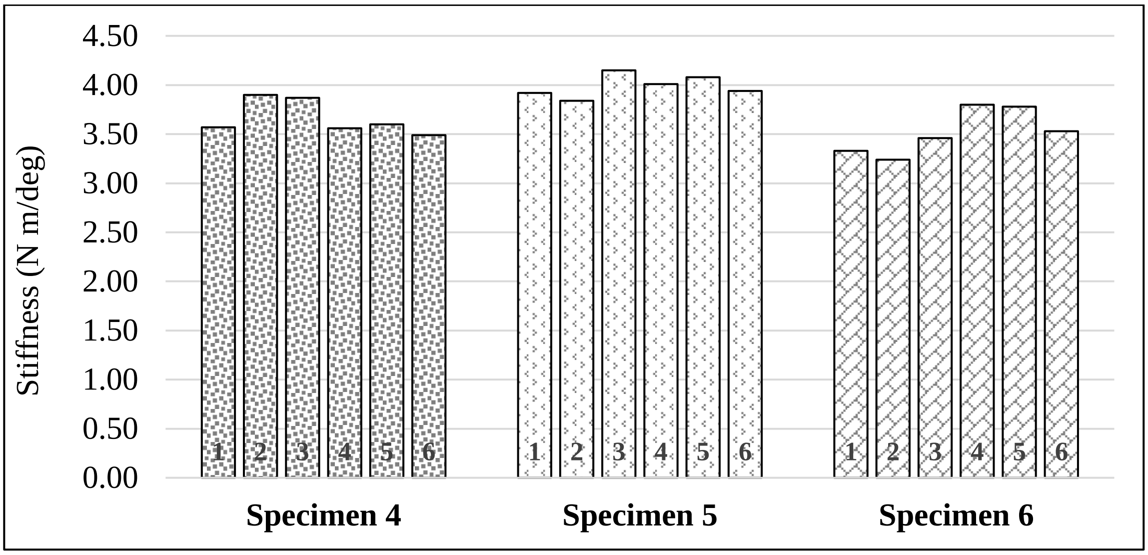

Figure 6-17 Torsional stiffness (internal rotation) results of control group

The mean torsional stiffness of the three femur specimens in internal rotation ranged from 3.52 N m/deg – 3.99 N m/deg and the standard deviation from 0.11 – 0.23 N m/deg. The overall mean torsional stiffness of the three femur specimens (control group) ($k_{\mathrm{EXP\ Ir}\ Ctl}$) in internal rotation was 3.73 N m/deg with a standard deviation of 0.26 N m/deg.

Table 6-8 Torsional stiffness (internal rotation) results of control femur specimens

n – number of tests, SD – standard deviation, COV – coefficient of variation

Specimen	n	Mean (N m/deg)	SD	COV (%)	Minimum (N m/deg)	Median (N m/deg)	Maximum (N m/deg)
Sp4	6	3.67	0.17	4.76	3.49	3.59	3.90
Sp5	6	3.99	0.11	2.84	3.84	3.98	4.15
Sp6	6	3.52	0.23	6.52	3.24	3.50	3.80
Group							
Control	18	3.73	0.26	7.03	3.24	3.79	4.15

6.4.3.2 Fracture groups

The torsion (internal rotation) results of the fracture groups are displayed in Figure 6-18 and Table 6-9.

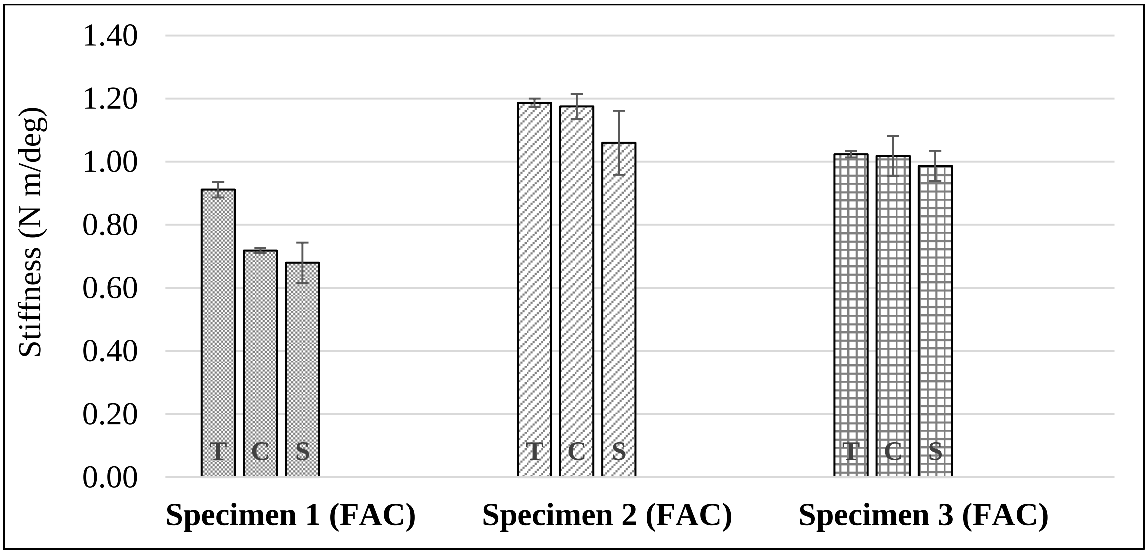

Figure 6-18 Mean torsional stiffness (internal rotation) with standard deviation (error bars) of three fracture groups FAC – Femur and ALFN Construct, T – Transverse, C – Comminuted, S – Segmental defect

Table 6-9 Torsional stiffness (internal rotation) results of the three fracture groups

n – number of tests, SD – standard deviation, COV – coefficient of variation, FAC – Femur and ALFN construct

Specimen	n	Mean (N m/deg)	SD	COV (%)	Minimum (N m/deg)	Median (N m/deg)	Maximum (N m/deg)
Sp1 FAC	6	0.91	0.02	2.72	0.87	0.92	0.94
Sp2 FAC	6	1.19	0.01	1.15	1.17	1.19	1.20
Sp3 FAC	6	1.02	0.01	1.01	1.01	1.02	1.04
Group							
Transverse	18	1.04	0.12	11.28	0.87	1.02	1.20
Sp1 FAC	6	0.72	0.01	1.05	0.71	0.72	0.73
Sp2 FAC	6	1.18	0.04	3.39	1.10	1.20	1.20
Sp3 FAC	6	1.02	0.06	6.22	0.89	1.05	1.05
Group							
Comminuted	18	0.97	0.20	20.52	0.71	1.05	1.20
Sp1 FAC	6	0.68	0.06	9.39	0.57	0.70	0.73
Sp2 FAC	6	1.06	0.10	1.09	0.86	1.09	1.14
Sp3 FAC	6	0.99	0.05	4.91	0.89	1.01	1.02
Group							
Segmental defect	18	0.91	0.18	20.17	0.57	1.00	1.14

6.4.3.3 Healed group

The results of torsion stiffness (internal rotation) for the healed group are shown below in Figure 6-19 and

Table 6-10.

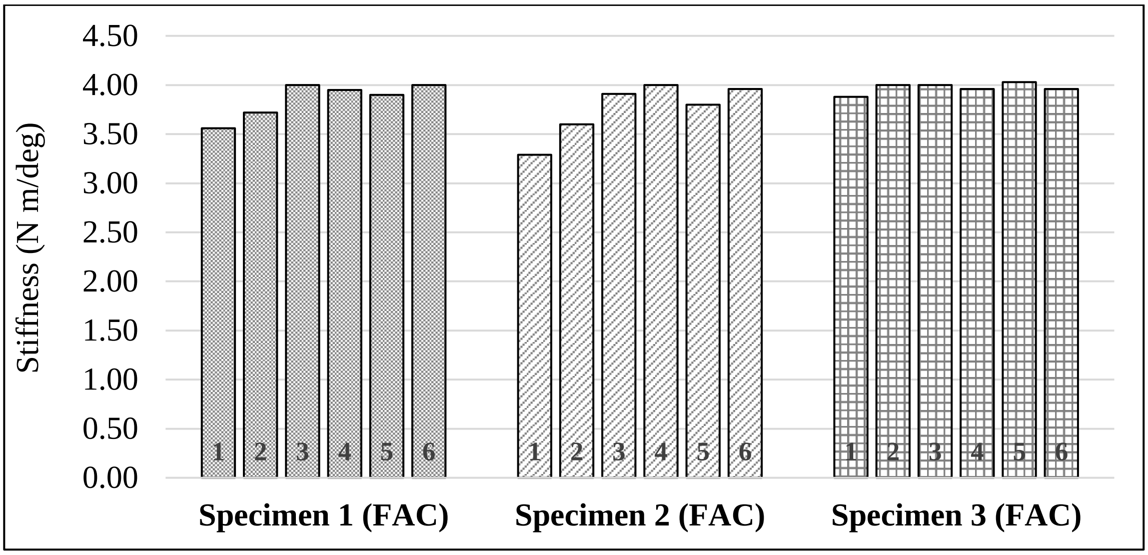

Figure 6-19 Torsion stiffness (internal rotation) results of the healed group

Table 6-10 Torsion stiffness (internal rotation) results of the healed group

n – number of tests, SD – standard deviation, COV – coefficient of variation, FAC – Femur and ALFN construct

Specimen	n	Mean (N m/deg)	SD	COV (%)	Minimum (N m/deg)	Median (N m/deg)	Maximum (N m/deg)
Sp1 FAC	6	3.86	0.18	4.62	3.56	3.93	4.00
Sp2 FAC	6	3.76	0.27	7.22	3.29	3.86	4.00
Sp3 FAC	6	3.97	0.05	1.32	3.88	3.98	4.03
Group							
Healed	18	3.86	0.20	5.16	3.29	3.96	4.03

6.4.4 Torsion (external rotation)

6.4.4.1 Control group

The results of the six tests on the three composite femur specimens are shown in

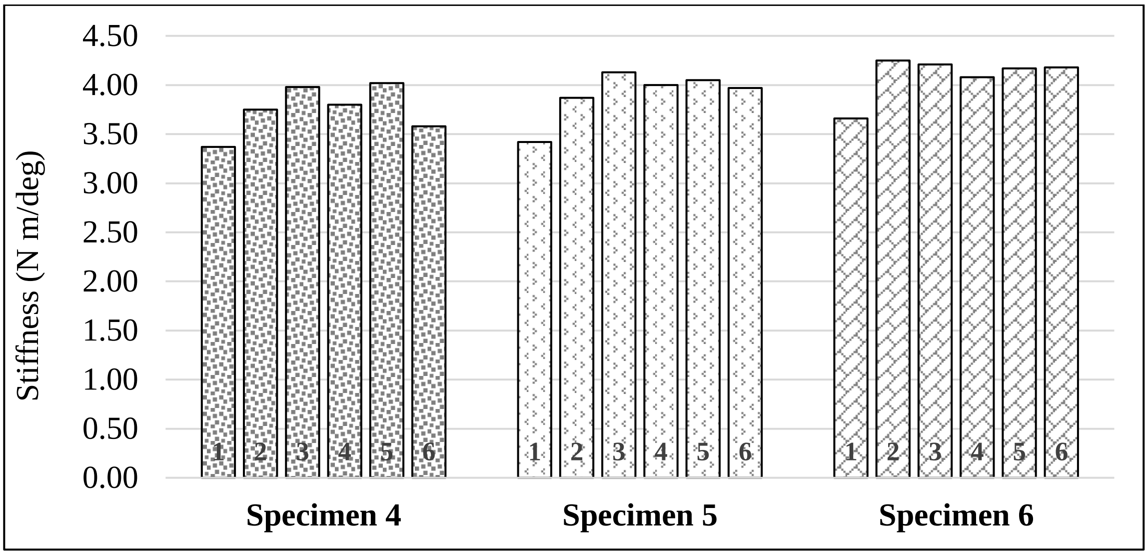

Figure 6-20 Torsional stiffness (external rotation) results of control group

The mean torsional stiffness of the three femur specimens in external rotation ranged from 3.75 N m/deg – 4.09 N m/deg and the standard deviation from 0.22 – 0.25 N m/deg. The overall mean torsional stiffness of the three femur specimens (control group) ($k_{\mathrm{EXP\ Ir}\ Ctl}$) in internal rotation was 3.92 N m/deg with a standard deviation of 0.27 N m/deg.

Table 6-11 Torsional stiffness (external rotation) results of control femur specimens

n – number of tests, SD – standard deviation, COV – coefficient of variation

Specimen	n	Mean (N m/deg)	SD	COV (%)	Minimum (N m/deg)	Median (N m/deg)	Maximum (N m/deg)
Sp4	6	3.75	0.25	6.55	3.37	3.78	4.02
Sp5	6	3.91	0.25	6.49	3.42	3.99	4.13
Sp6	6	4.09	0.22	5.35	3.66	4.18	4.25
Group							
Control	18	3.92	0.27	6.82	3.37	3.99	4.25

6.4.4.2 Fracture groups

The torsion (external rotation) test results are shown in Figure 6-21 and Table 6-12.

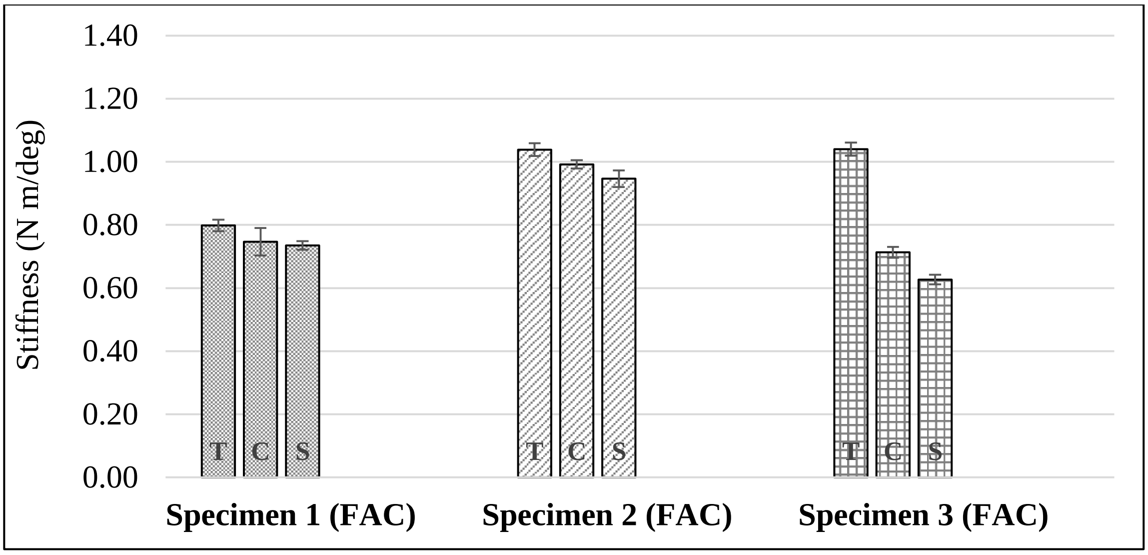

Figure 6-21 Mean torsional stiffness (external rotation) with standard deviation (error bars) of three fracture groups

FAC – Femur and ALFN Construct, T – Transverse, C – Comminuted, S – Segmental defect

Table 6-12 Torsional stiffness (external rotation) results of the three fracture groups

n – number of tests, SD – standard deviation, COV – coefficient of variation, FAC – Femur and ALFN construct

Specimen	n	Mean (N m/deg)	SD	COV (%)	Minimum (N m/deg)	Median (N m/deg)	Maximum (N m/deg)
Sp1 FAC	6	0.80	0.02	2.30	0.78	0.80	0.82
Sp2 FAC	6	1.04	0.02	1.97	1.00	1.04	1.06
Sp3 FAC	6	1.04	0.02	2.02	1.00	1.05	1.06
Group							
Transverse	18	0.96	0.12	12.34	0.78	1.04	1.06
Sp1 FAC	6	0.75	0.04	5.85	0.71	0.73	0.82
Sp2 FAC	6	0.99	0.01	1.34	0.97	1.00	1.00
Sp3 FAC	6	0.71	0.02	2.45	0.68	0.72	0.73
Group							
Comminuted	18	0.82	0.13	15.96	0.68	0.73	1.00
Sp1 FAC	6	0.74	0.01	1.88	0.72	0.74	0.75
Sp2 FAC	6	0.95	0.03	2.81	0.90	0.95	0.97
Sp3 FAC	6	0.63	0.02	2.40	0.60	0.63	0.64
Group							
Segmental defect	18	0.77	0.14	17.93	0.60	0.74	0.97

6.4.4.3 Healed group

The results of torsion stiffness (external rotation) are shown in Figure 6-22 and Table 6-13.

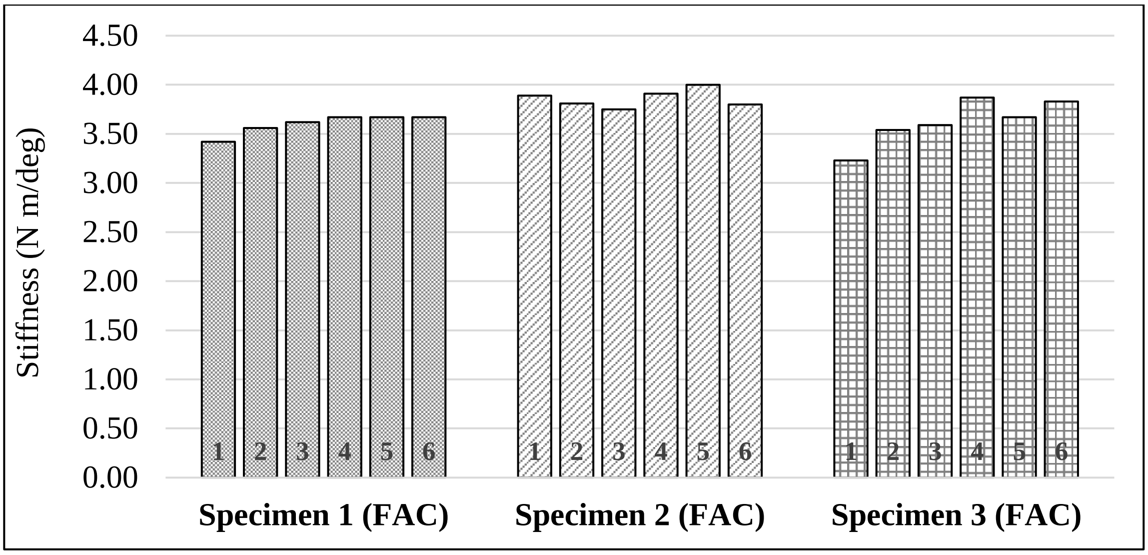

Figure 6-22 Torsion stiffness (external rotation) results of the healed group

Table 6-13 Torsion stiffness (external rotation) results of the healed group

n – number of tests, SD – standard deviation, COV – coefficient of variation, FAC – Femur and ALFN construct

Specimen	n	Mean (N m/deg)	SD	COV (%)	Minimum (N m/deg)	Median (N m/deg)	Maximum (N m/deg)
Sp1 FAC	6	3.60	0.10	2.75	3.42	3.65	3.67
Sp2 FAC	6	3.86	0.09	2.35	3.75	3.85	4.00
Sp3 FAC	6	3.62	0.23	6.40	3.23	3.63	3.87
Group							
Healed	18	3.69	0.19	5.11	3.23	3.67	4.00

6.4.5 Relative Construct Stiffness

The femur and ALFN construct (FAC) stiffness of the healed and fracture groups expressed as a percentage of the stiffness of the intact and control group is displayed below in Figure 6-23

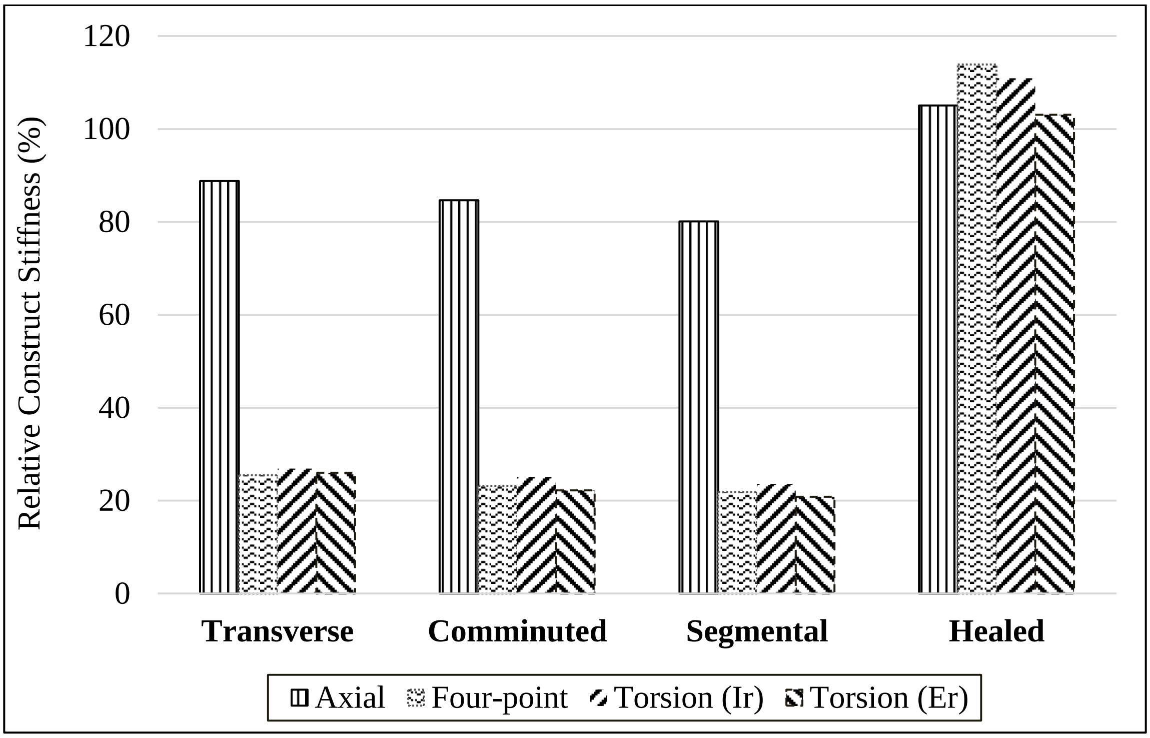

Figure 6-23 Relative construct stiffness of healed and fracture groups

The highest (114% of intact femur) and lowest (21% of intact femur) relative construct stiffness was noted in the healed group during four-point bending test and segmental defect fracture group during torsion (external rotation) respectively. Overall the relative construct stiffness of the FAC in the healed group was more than that of the intact femurs (Figure 6-23).

6.5 Discussion

Several studies in the literature have addressed the biomechanical aspects including the stiffness properties of the different rigid femoral intramedullary nails used in clinical practice (254, 256, 266, 283, 284, 320, 361, 414, 418-424).

Johnson *et al*. (283) evaluated biomechanical properties of three interlocking nails (Brooker-Wills / Klemm-Schellman / Grosse-Kempf) and flexible nail (Ender) using two cadaveric femur fracture models (3 cm subtrochanteric defect and 8 cm midshaft defect). They performed axial loading to failure, bending and torsion tests. The three interlocking nails were 15 mm in diameter and 420 mm in length whereas the Ender nails had a diameter of 4.5 mm. They observed that the distally locked nails (Klemm-Schellman / Grosse-Kempf) resisted significantly higher loads than either the distally bladed (Brooker-Wills) or Ender nails when tested to failure by axial loading. The relative bending stiffness of the three interlocking nails ranged from 55%-70% (3 cm subtrochanteric defect) and 20% (8 cm midshaft defect) of intact femurs. The relative torsional stiffness was reported to be below 3% of that of intact femora.

Bechtold *et al*. (420) compared interlocking (Grosse-Kempf and Brooker-Wills) and non-interlocking (Grosse-Kempf with no cortical transfixation screws) intramedullary nail designs in bending and torsion using 23 cadaveric femora. The Grosse-Kempf nail fixation constructs included a fully interlocked, proximal with first distal, proximal with second distal and only proximal interlocking screw configurations. Additionally, the effect of fracture severity was investigated using three femurs which consisted all three interlocking screws (1 proximal and 2 distal) with 3 cm, 6 cm and 9 cm midshaft segmental defects respectively. The Brooker-Wills nail configurations had one proximal transfixation pin and distal fins. The four-point bending stiffness (mean ± standard deviation) of the Grosse-Kempf nail constructs was 259±111 N /

mm and 235±91 N / mm for the interlocked and non-interlocked configurations respectively. In comparison lower values (207±54 N / mm) were noted for the Brooker-Wills nail. Similar values were reported for interlocking screw configurations (proximal with first distal screw - 262±101 N / mm, proximal with second distal screw - 267±98 N / mm). In the 3 cm, 6 cm and 9 cm midshaft segmental defect models, four-point bending stiffness of 203±70 N / mm, 179±90 N / mm and 158±97 N / mm were reported, respectively. During torsion tests, the mean maximum torque required to produce 10 degree of forced rotation was recorded. For the Brooker-Wills nail, interlocked and non-interlocked configurations of Grosse-Kempf nail mean maximum torque values of 1.22 N m, 2.53 N m and 0.58 N m respectively were noted. Similar values were reported for interlocking screw configurations (proximal with first distal screw – 2.26 N m, proximal with second distal screw – 2.21 N m). In the 3 cm, 6 cm and 9 cm midshaft segmental defect models, they measured a mean maximum torque of 2.21 N m, 2.07 N m and 1.87 N m respectively. The authors concluded that the fully interlocked and partially interlocked Grosse-Kempf nail configurations behaved similarly. However, they hypothesised that although the second distal interlocking screw does not improve static quality of support to the fractured femur, it may improve dynamic performance in a fatigue loading situation (walking).

Alho *et al*. (320) compared the torsional stiffness of slotted (Grosse-Kempf / AO universal) and non-slotted (Grosse-Kempf) locked intramedullary nails using a cadaveric femur model with a 50 mm midshaft defect. All the nails were 14 mm in diameter and 440 mm in length. The relative torsional stiffness of the two slotted nails (8-9%) was lower than that of the non-slotted nail (38%). They attributed this finding to the material properties and the design of the nails. Furthermore they stated that ‘the optimal rotational stiffness of the nail is an unsettled point’. In the same paper, a clinical series of 46 patients treated with slotted nails (24) and non-slotted nails (22) was presented. No significant difference was found in terms of clinical outcomes.

The authors suggested that the main advantage of locked femoral nails was the prevention of rotatory malalignment and shortening.

Bankston *et al*. (45) compared the torsional rigidity and compressive strength of three femoral nail designs (Küntscher / Küntscher interlocking / Brooker-Wills) using 23 cadaveric femora. They created a transverse fracture (gap not stated) and a 30 mm segmental defect distal to the isthmus for specimens undergoing torsion and axial compression tests respectively. During torsion tests, the maximum torque required to produce 15 degree rotation was 0.088 N m, 0.634 N m and 1.08 N m for the Küntscher, Brooker-Wills and Küntscher interlocking nail, respectively. During compression tests they reported that the Küntscher interlocking nail failed at 3000 N load with less than 1 cm shortening. In comparison both the Brooker-Wills and the Küntscher nails failed with 3 cm shortening. They reported that in relative terms the Küntscher and the Brooker-Wills nail provided 3.6 % and 16.3% resistance to compression, respectively in comparison to the Küntscher interlocking nail.

Schandelmaier *et al*. (418) evaluated the influence of nail diameter on the stiffness of the bone implant complex. They compared AO universal femoral nail with a slotted clover leaf design with 11 mm diameter with different solid nail designs (viz. AO 9 mm steel and titanium nails / AO 12 mm titanium nail) in axial compression, four-point bending and torsion using human femora with a 20 mm midshaft segmental defect. The maximum relative stiffness was noted with 12 mm titanium nail under axial compression (65%) and four-point bending (68%) and the 9 mm steel nail under torsion (20%). They reported both groups of nail had significantly less relative stiffness (2-20%) compared to intact femur under torsion. They concluded that the stiffness of bone implant complex in interlocking femoral nails was more dependent on nail profile than on the press fit of nails in the medullary nail.

The standardised osteotomies on composite femurs served three purposes. First, they simulated common fracture patterns noted in clinical practice (425, 426). Second, the similar size and location of osteotomy across all the specimens aimed to minimise variability (58, 72, 291, 294). Third, they provided a reproducible experimental model to evaluate axial and rotational stiffness at the two extremes of fracture patterns i.e. stable (transverse fracture) with significant bone load sharing and completely unstable (segmental defect) with only the ALFN providing axial and rotational stability (419, 427).

Weight-bearing or movement of the limb by the patient generates load resulting in deformation of reamed intramedullary nail due to mechanical bending of the nail within the medullary canal (428). During weight-bearing, the anterior bow of the femur results in a significant bending load on the mid-diaphyseal region of the femur (384). Furthermore, bending of the nail has been postulated to increase the frictional forces at the nail-bone interface thereby enhancing fracture stability (429). Axial compression results demonstrated the relative construct stiffness to remain in a satisfactory range (80%-89% of intact femur) in the fracture groups (Figure 6-23). This may be due to close conformity of the shape of the ALFN with that of the femoral medullary canal.

Bending stiffness results have been demonstrated to vary considerably (283). Sherman *et al.* (429) observed that nails of the same nominal size from different manufacturers varied in their cross-sectional shape (36.85 mm^2 – 63.77 mm^2) and wall thickness (1.00 mm – 2.00 mm). This variation resulted in more than a twofold difference in flexural rigidity in their study. It has been reported that anteroposterior (AP) and medial-lateral bending give comparable results (427). Therefore only AP bending was undertaken in this study. A bending test of a femoral intramedullary nail fixation construct primarily tests the nail (420). The results of four-point bending showed a trend towards decrease in the stiffness across all the three specimens (Figure 6-15). This may be due to the same size of ALFN used in all the three specimens.

Some studies which evaluated paediatric femoral fracture fixation implants used a simultaneous axial load during torsion test (295, 306). However there is a lack of consensus regarding the use of axial load (Table 4-5). Furthermore it has been demonstrated that the rotational stiffness of tubular titanium non-slotted design nail remains unchanged with concomitant low or high axial load (419). Hence to simplify the test setup simultaneous axial load was not applied in the current study.

The test setup and load parameters of the aforementioned studies are varied. Nonetheless certain similar trends and differences can be identified with respect to the results from the current study. Femoral specimens with central segmental defects have been reported to show lower stiffness values across different configurations tested (283). A similar trend was noted in the relative construct stiffness of the comminuted fracture and segmental defect groups (Figure 6-23). The stiffness of intact femur was relatively higher compared to fracture fixation constructs across all modes of testing (axial compression / four-point bending / torsion) (283, 320, 361, 414, 418). Similar findings were noted in the current study (Figure 6-12, Figure 6-15, Figure 6-18 and Figure 6-21). Only the healed group had stiffness values higher than the intact femur specimens (Figure 6-23). Other authors who have evaluated healed configurations have noted similar trend in stiffness parameters (254, 361). The relative stiffness of fracture fixation constructs in an AP bending test has been reported to vary between 55%-70% for subtrochanteric defects (283), 20% for central segment defects (283) and 37%-68% (418). In comparison the relative stiffness of the FAC in the fracture groups varied from 22%-25%. This may be partly due to the fact that the former studies used larger nail sizes (15 mm diameter, 420 mm length – Johnson *et al*. (283), 9-12 mm diameter, length not stated - Schandelmaier *et al*. (418)), whereas the ALFN used in the current study had an outer diameter of 8.2 mm (20) (Figure 3-6). It has been suggested that the profile of the intramedullary nail is the decisive factor for the torsional stiffness of femoral locking nails in the bone implant complex (418). This point is supported by the torsional results and the relative construct stiffness from the current study (Figure 6-18, Figure 6-21 and Figure 6-23). Schandelmaier *et al*. (418) reported the relative torsional stiffness of a 9 mm and 12 mm diameter titanium alloy solid nails to be 12% and 18% of the intact bone respectively. In comparison to the relative torsional stiffness of the ALFN with a 8.2 mm diameter varied from 21% (segmental defect in external rotation) to 27% (transverse fracture in internal rotation) (Figure 6-23). This may be due to the helical profile of the ALFN which permits better transfer of the torsional load across the femur ALFN construct.

6.6 Summary

The stiffness parameters of composite femurs decrease following fracture. The relative construct stiffness of the femur ALFN construct is variable and depends on the type of simulated fracture. The relative construct stiffness of the femur ALFN construct is less than intact femurs across all fracture groups. However, relative construct stiffness of the femur ALFN construct in the healed configuration is higher than intact femurs. Overall femur fracture fixation with ALFN provides adequate stability to the physiological loads experienced in the perioperative period. Biomechanical testing of the FAC provided data for the healed group ($k_{\mathrm{EXP}\ Hld}$) and fracture groups namely transverse fracture group ($k_{\mathrm{EXP}\ Tra}$), comminuted fracture group ($k_{\mathrm{EXP}\ Com}$) and segmental defect group ($k_{\mathrm{EXP}\ Seg}$). This data will be used for comparison and validation of a paediatric femur fracture fixation finite element model which is described in the next chapter (chapter 7).

7 PAEDIATRIC FEMUR FRACTURE FIXATION - FINITE ELEMENT ANALYSIS

7.1 Introduction

This chapter describes the development and validation of the finite element (FE) model of paediatric femur fracture fixation with the ALFN. The development of FE models of ALFN, interlocking screws and the paediatric femur with different fracture configurations in SolidWorks™ is presented in the initial section. Subsequently an overview of the validation methodology with the simulation tests is discussed followed by the results of the FEA. In the last section of the chapter a brief review of the relevant FEA studies is presented along with discussion of the results of the FEA.

7.2 Materials and methods

7.2.1 Development of computer aided design (CAD) models of ALFN in SolidWorks™

A CAD model of the ALFN was developed using orthogonal projection in SolidWorks™ similar to the technique described for the paediatric femur in chapter 5. Anteroposterior (AP) and lateral templates of the ALFN available in the manufacturer's surgical guide were used (273). The templates were appropriately scaled and imported into SolidWorks™ software. The central axis of the nail from the AP and lateral templates were marked using the spline tool (351, 352) (Figure 7-1).

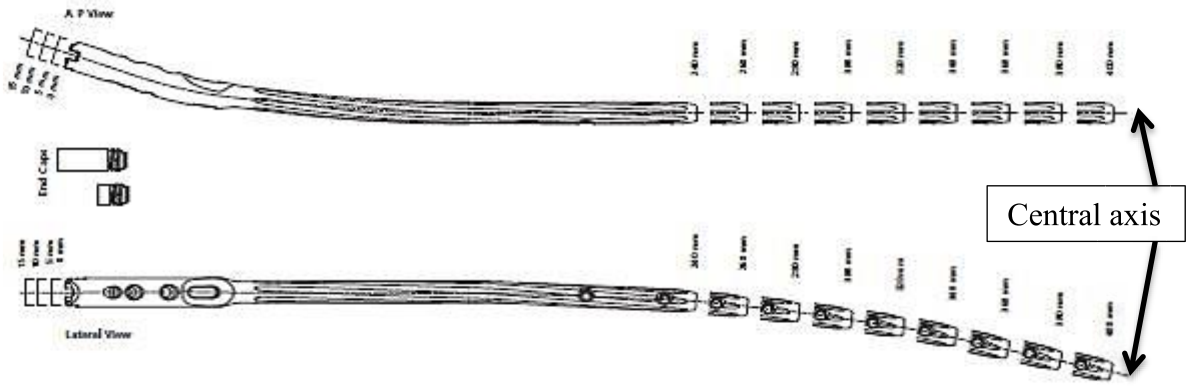

Figure 7-1 Anteroposterior and lateral templates of ALFN

A projection of AP and lateral splines with the 'projected curve - sketch on sketch' tool (430) was used to obtain the three dimensional core helical axis of the ALFN. A proximal sketch (circle with diameter of 11mm) was used to model the proximal section of the ALFN using the sweep function along the helical axis (353). The distal portion of the ALFN with an outer diameter of 8.2 mm was created similarly. The length of ALFN CAD model was 300 mm (same length as the experimental model described in chapter 6) (Figure 7-2).

As the current experimental study addressed femoral shaft fractures, only the 120° antegrade locking and distal interlocking screws were modelled. Particular attention was given to accurately model the 120° antegrade locking hole and the junction between the proximal and distal parts of the ALFN (Figure 7-3). The longitudinal grooves in the distal portion, angular edges at the proximal part and recon holes for the hip screws were not modelled to minimise the computational time (356).

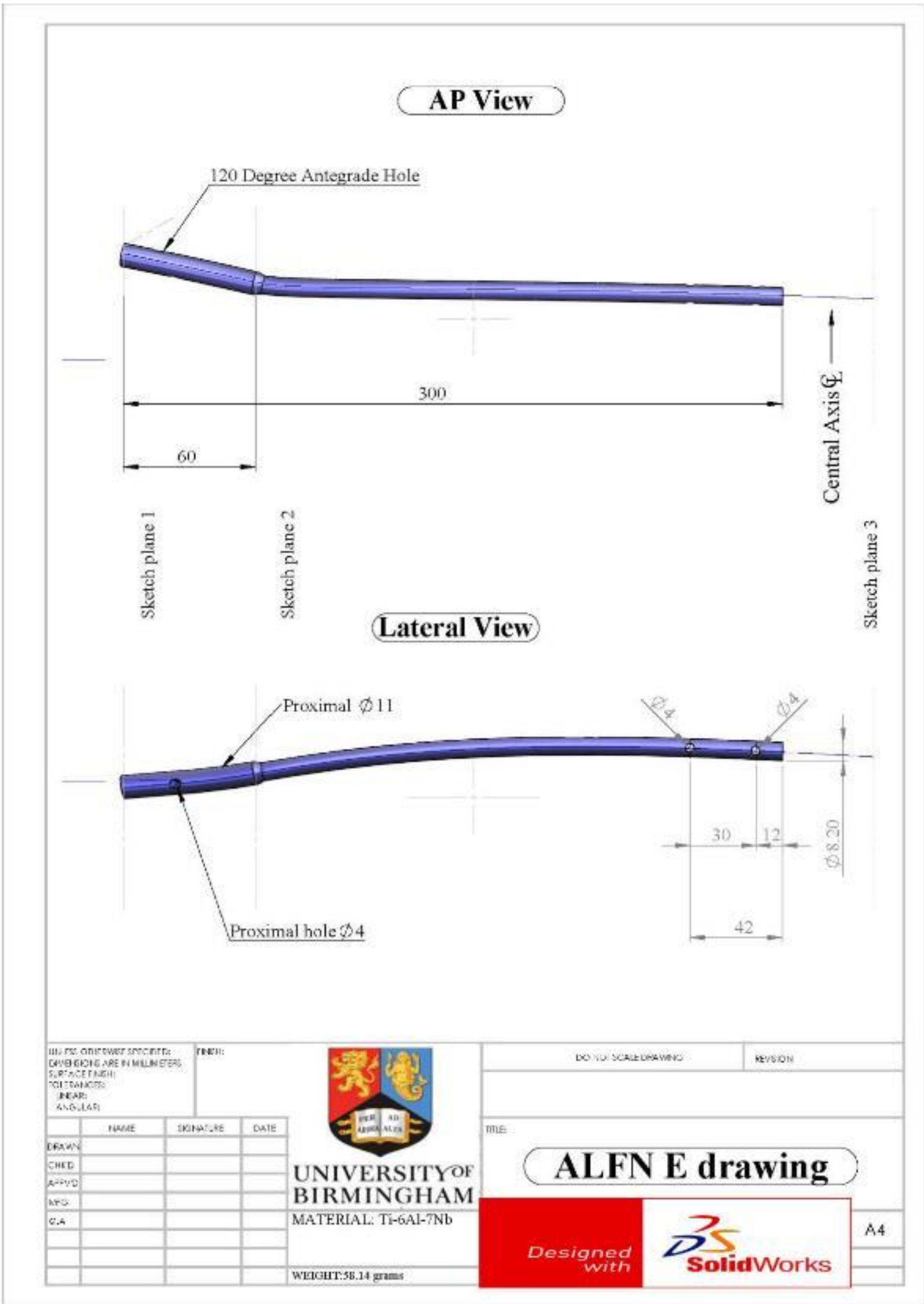

Figure 7-2 Engineering drawing of ALFN in SolidWorks™

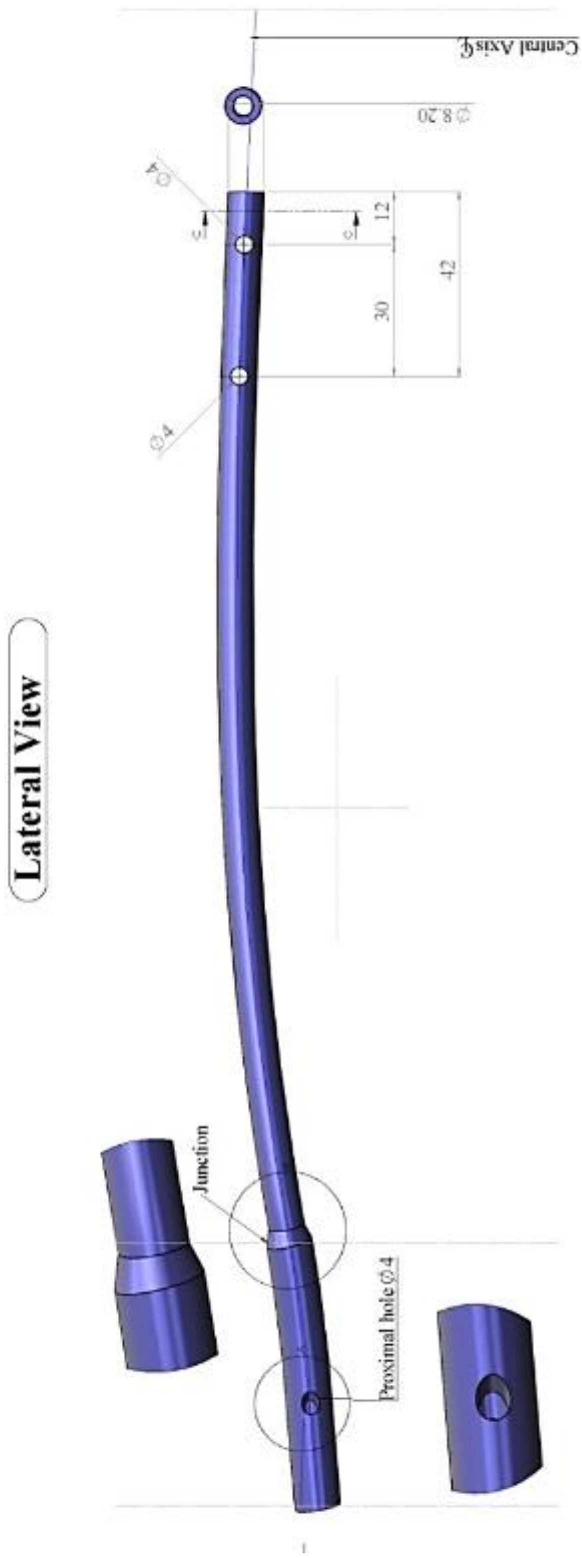

Figure 7-3 Lateral view of ALFN CAD model demonstrating the proximal (120° antegrade) locking screw hole and the junction area

Three interlocking screws (1 proximal + 2 distal) were modeled as solid cylinders with a diameter of 4 mm (348, 355, 414). The length of cylinders measured 56 mm, 36 mm and 46 mm for the proximal and two distal screws respectively (Figure 7-4). The above dimensions were based on the experimental model (described in chapter 6).

Figure 7-4 Isometric view of CAD models of ALFN, proximal and distal interlocking screws

7.2.2 Virtual implantation of the ALFN in the paediatric femur using SolidWorks™

As per the surgical technique, described in the manufacturer's manual, the femoral canal is prepared prior to the insertion and final positioning of the ALFN. The proximal 75 mm is reamed using a reamer with an outer diameter of 13 mm. Distally a reamer with an outer diameter of 9.5 mm is used to prepare the femoral intramedullary canal. Similar steps were undertaken in SolidWorks™ on the femur CAD model using a sketch and 'swept cut' command (352, 431). Subsequently the ALFN and interlocking screws were inserted into the femur using the 'assembly function' in SolidWorks™ (432, 433). Orthogonal digital radiographs of the femur which were used as a template to develop the CAD model of the femur were used as reference to ensure accurate, anatomic positioning of the ALFN and the interlocking screws in the femur (360) (Figure 7-5).

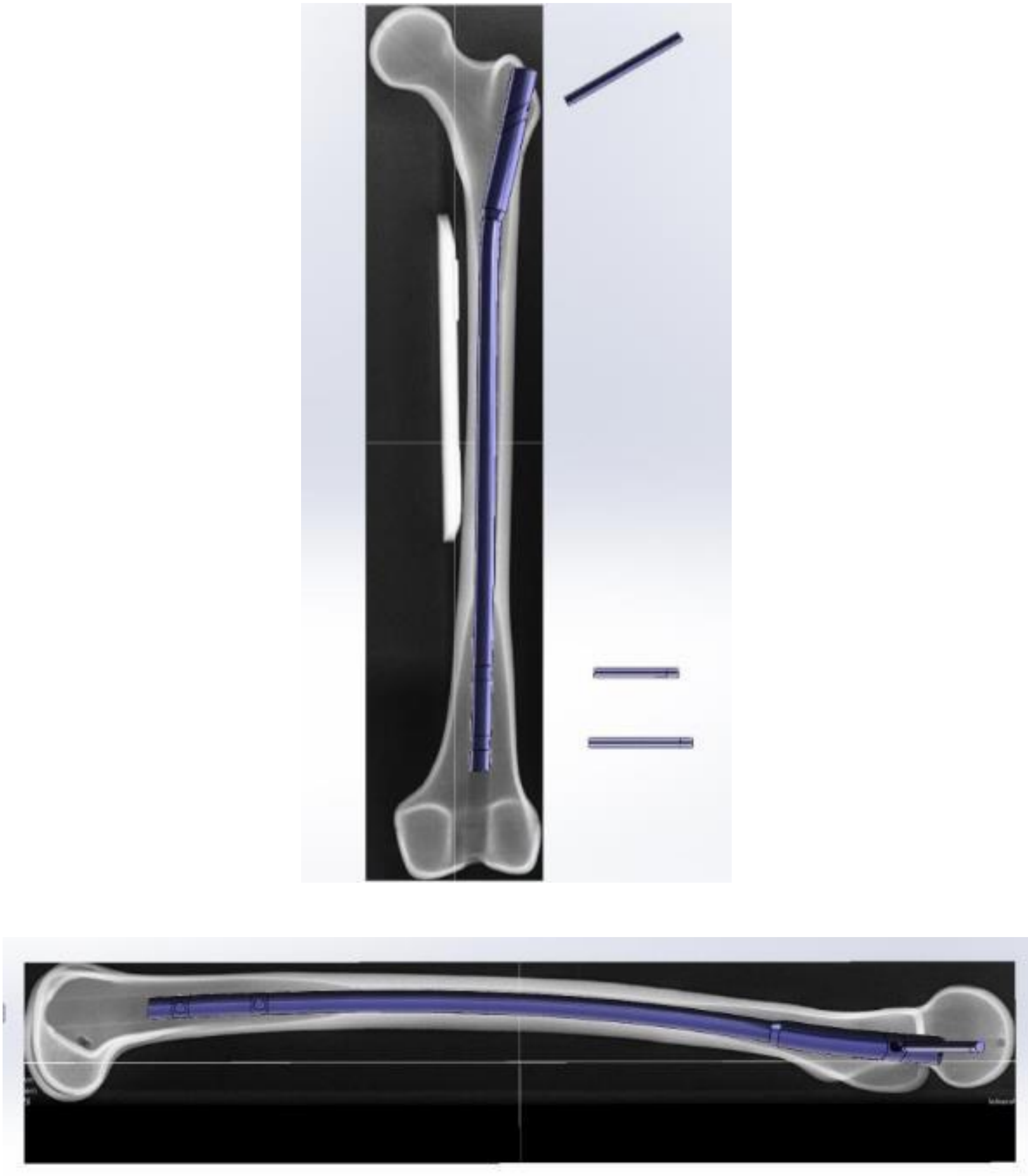

Figure 7-5 Digital radiographs used as a reference to accurately position ALFN and interlocking screws (top- anteroposterior view, below-lateral view)

Following surgery the small gap between the outer surface of intramedullary nail and the reamed medullary canal of the femur consists of a mixture of cancellous bone tissue, marrow contents and haematoma (434, 435). In the FEA model this gap was filled with interpositional material with properties of cancellous bone tissue (elastic modulus = 137 MPa, Poisson’s ratio = 0.30) (300) (Figure 7-6).

Figure 7-6 Interpositional material highlighted in blue overlying the ALFN in the medullary canal

The reamed femur was positioned using the digital radiograph template. The corresponding sites for the interlocking screw holes in the femur were created using a circular sketch and the ‘extruded cut’ command (436) (Figure 7-7).

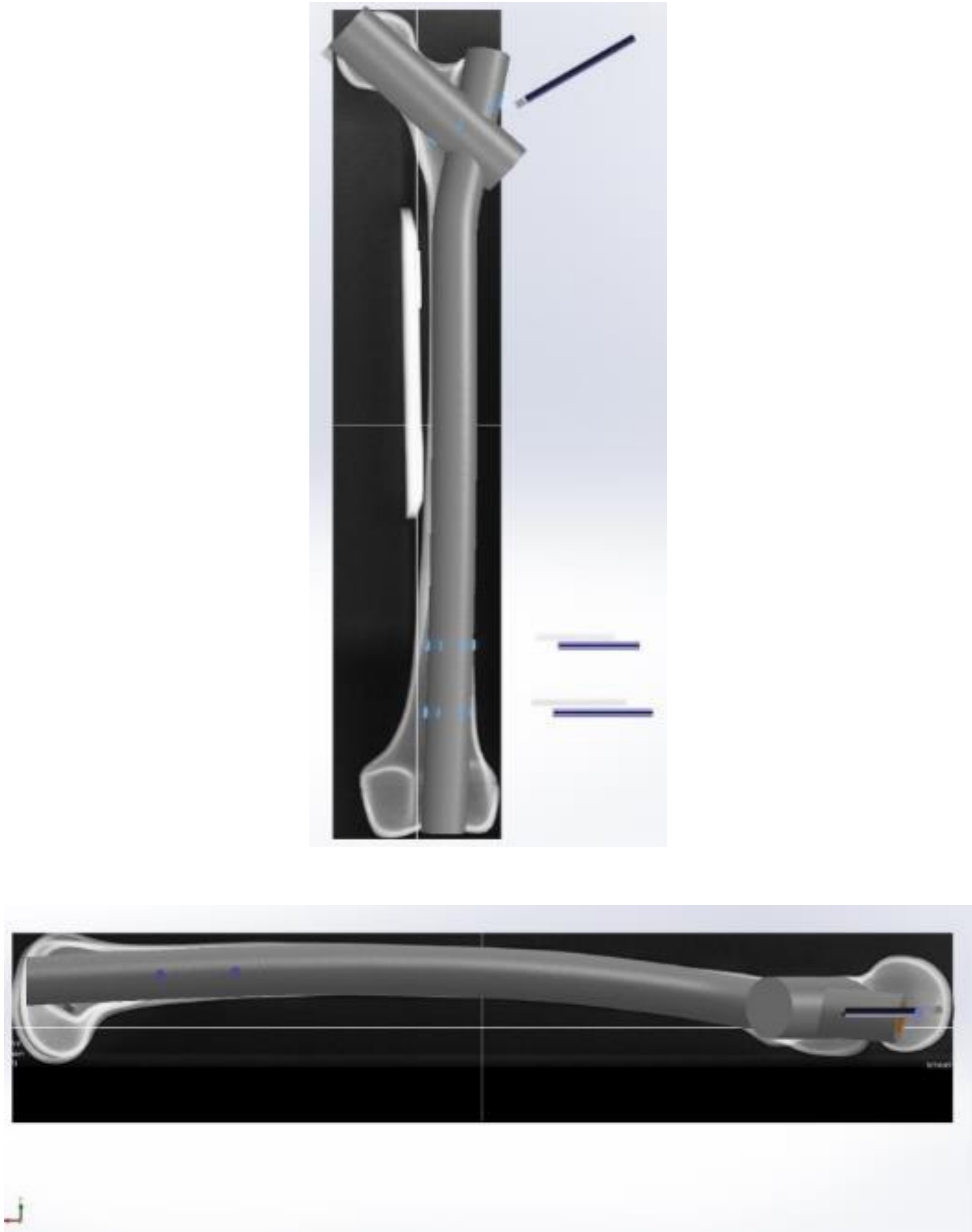

Figure 7-7 Creation of holes in the femur CAD model for the corresponding proximal and distal interlocking screws

The interlocking screws were then accurately positioned using the ‘concentric mate’ command in the SolidWorks^{TM} assembly (437) to match the congruent surfaces of the screw holes with the exterior surfaces of the cylinders representing the interlocking screws. Hence a final assembly of reamed femur, ALFN and interlocking screw CAD models representing paediatric femur fracture fixation was achieved (Figure 7-8).

Figure 7-8 Final assembly of reamed femur, ALFN and interlocking screws representing paediatric femur fracture fixation FEA model

In addition to the assembly, each of the CAD model components from the above assembly (reamed femur, ALFN, interlocking screws) was saved individually. This feature in SolidWorks™ (438) ensured the original reference position of the individual component with respect to the paediatric femur digital radiograph was maintained during subsequent iterations of simulation tests. Furthermore this technique of a modular FEA model consisting of reamed femur, ALFN and interlocking screws allowed for variations in the subsequent iterations of the FEA model to study the effect of fracture level, fracture healing and implant design (described in chapter 8).

7.2.3 Simulated fractures in femur CAD model

7.2.3.1 Transverse fracture FEA model (ALFN and femur with transverse fracture)

A transverse fracture (gap = 1 mm) was created in the reamed femur CAD model at 175 mm below the tip of the greater trochanter using the sketch and 'extruded cut' command (352, 436). This femur CAD model was used in the above assembly to obtain the transverse fracture FEA model.

7.2.3.2 Comminuted fracture FEA model (ALFN and femur with comminuted fracture)

Four comminuted fracture fragments were created in the reamed femur CAD model with dimensions similar to the experimental model using the sketch and 'extruded cut' command (352, 436) (Figure 7-9). This femur CAD model was used in the above assembly to obtain the comminuted fracture FEA model.

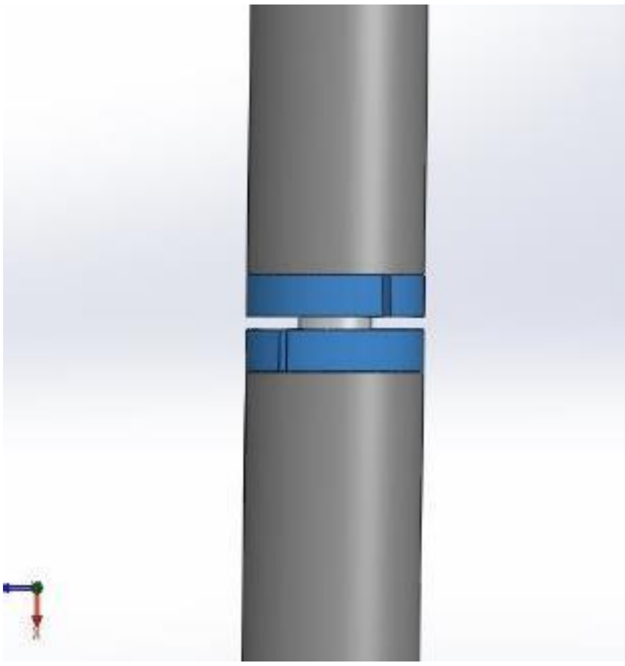

Figure 7-9 Comminuted fracture FEA model with four fracture fragments (highlighted in blue) and ALFN in the medullary canal

7.2.3.3 Segmental defect FEA model (ALFN and femur with segmental defect fracture)

A segmental defect (gap = 10 mm) was created in the reamed femur CAD model using the sketch and 'extruded cut' command (352, 436). This femur CAD model was used in the above assembly to obtain the segmental defect FEA model.

7.2.3.4 Healed fracture FEA model (ALFN and intact reamed femur)

This configuration consisted of an intact reamed femur with ALFN and interlocking screws *in situ* (Figure 7-8).

7.2.4 SolidWorks™ simulation tests

7.2.4.1 Material properties and assumptions

As per the manufacturer's manual, ALFN and the corresponding interlocking screws are manufactured from titanium based alloy (Ti-6Al-7Nb) (273, 439). Hence ALFN and the interlocking screws were assigned the material properties of titanium alloy (Ti-6Al-7Nb) (elastic modulus = 105 GPa, ultimate tensile strength = 900 MPa, yield strength = 800 MPa, Poisson's ratio = 0.30) (439).

Material properties of the composite femur (compressive strength = 157 MPa, compressive modulus = 16.7 GPa, yield strength = 93 MPa, Poisson's ratio = 0.26) (Table 4-1) (300) were assigned to the femur model. The interpositional material between the ALFN and the reamed medullary canal of the femur was assigned with properties of cancellous bone tissue (elastic modulus = 137 MPa, Poisson's ratio = 0.30) (300).

The material properties of the FEA models were assumed to be isotropic and linearly elastic (348, 356, 358, 362, 407, 440).

7.2.4.2 Boundary conditions and simulated load

During simulation tests of the above FEA model assembly representing paediatric femur fracture fixation the boundary conditions of the femur were similar to that described earlier in chapter 5. In addition 'contact set' function was used to define the contact conditions and interactions between the femur, ALFN and the interlocking screws. A 'no penetration' type of contact set (328) was assigned between the outer surface of the proximal and distal interlocking screws and the corresponding holes in the ALFN and femur. Under this condition surface to surface contact formulation is applied by the software. Hence the surfaces of the two selected bodies do not penetrate each other during simulation (441, 442). With respect to the ALFN in the medullary canal no assumption of contact was made (331, 364) (Figure 7-10). Hence the ALFN was allowed to deform and independently come in contact with the medullary canal of the reamed femur depending on the load applied during the various simulation tests (361).

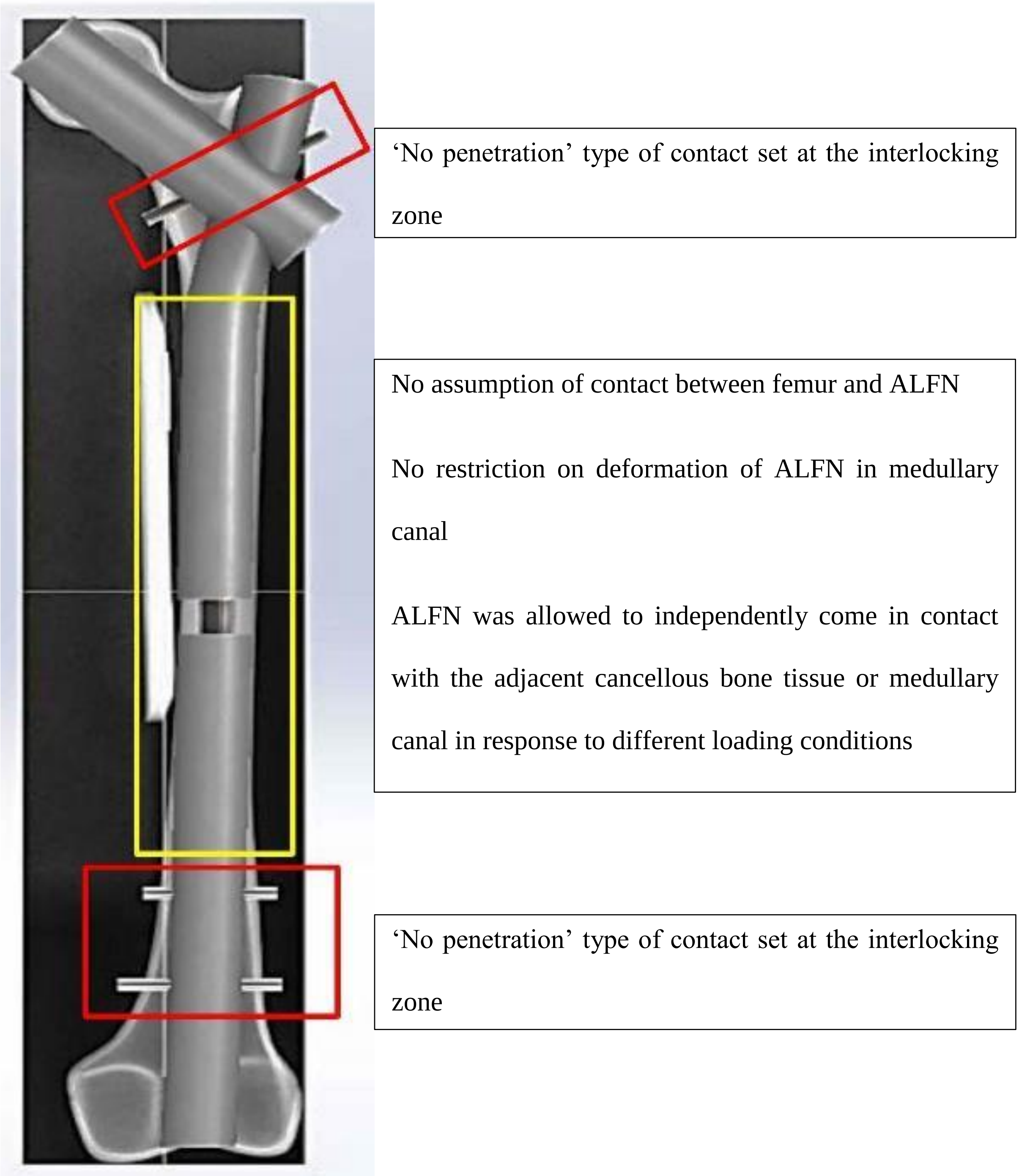

Figure 7-10 Femur and ALFN contact conditions

This approach was adopted mainly to study the behavior of the ALFN in response to the different loading conditions. Furthermore, it also reflected the ‘real world’ scenario wherein the intramedullary nail can deform / displace and contact the medullary canal of the bone during daily activities of the patient. This deformation and subsequent contact in response to the different loads is largely dictated by the material properties and the geometry of the nail (356, 361).

7.2.4.3 Simulated load parameters

For the three fractured femur configurations, simulated load parameters same as the experimental setup (viz. axial compression - maximum 300 N at 30 N increments, four-point bending - maximum 60 N at 10 N increments, torsion - maximum 2 N m at 0.1 N m increments) were used (Table 6-1). For the healed femur configuration, simulated load parameters similar to the experimental setup (viz. axial compression - maximum 600 N at 60 N increments, four-point bending - maximum 400 N at 40 N increments, torsion - maximum 4 N m at 0.2 N m increments) were used (Table 6-1).

7.2.4.4 Mesh selection and convergence

Based on the criteria highlighted in chapter 5, a curvature type mesh with three-dimensional (3D) tetrahedral elements available in Solidworks™ simulation was used. Preliminary simulation tests were conducted on each of the above assembly of the FEA models representing the healed femur and three femur fracture configurations. These tests helped to estimate the default element size, identify the site of maximum displacement and sites of high stress gradient. During axial loading, the maximum displacement (U_X in mm) was predicted in the femoral head region whereas for the four-point bending test the maximum displacement (U_Y in mm) was predicted in the midshaft region adjacent to the simulated fracture. During simulated torsional loading tests (internal and external rotation) the maximum displacement at the point corresponding to the center of the femoral head was noted. Mesh refinement was performed at the regions of interest (viz. interlocking screw holes in femur, ALFN/interlocking screw interface, femoral head and fracture site) by systematically increasing the mesh density in these areas (328, 338) (Figure 7-11). A similar approach to meshing has been used by other investigators in these regions which represent sites of high stress gradient (356, 407, 443). Mesh refinement was undertaken using the mesh control feature in Solidworks™ simulation which allows the user to specify the desired element size and the rate of increase in size of adjacent elements (338).

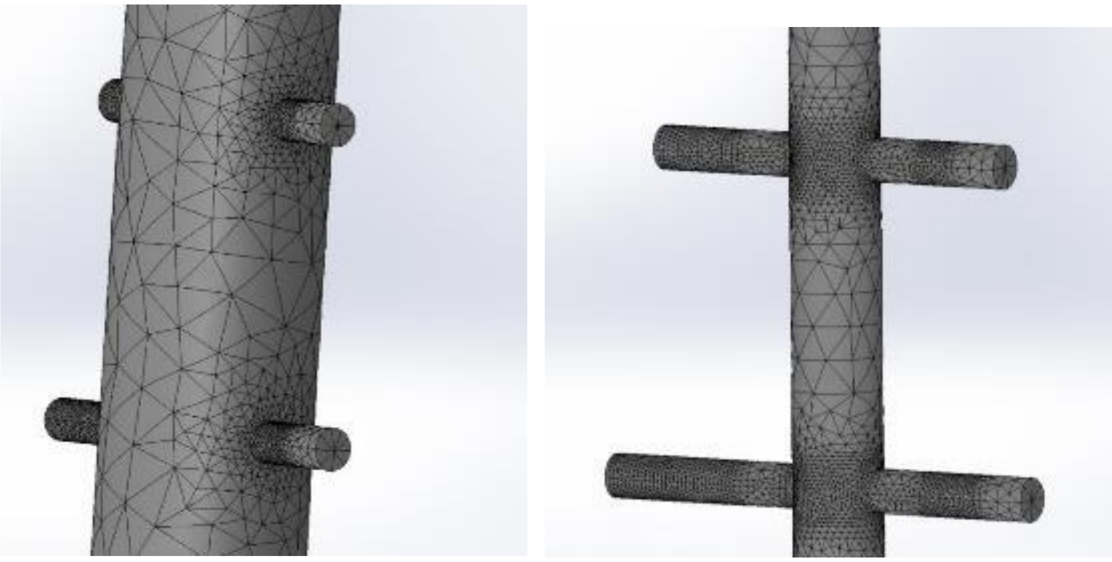

Figure 7-11 Mesh refinement at regions of interest (left-interlocking screw holes in femur, right-ALFN/interlocking screw interface)

Convergence of numerical results (displacement in mm) at the initial simulated load was performed as described earlier in chapter 5 (373). The initial simulated load parameters for the three femur fracture FEA models (viz. axial compression – 30 N, four-point bending – 10 N, torsion - 0.1 N m) and the healed femur FEA model (viz. axial compression - 60 N, four-point bending - 40 N, torsion - 0.2 N m) were used for convergence analysis. Following the preliminary simulation tests, the default element size was provided by the automesher algorithm in Solidworks™ (375). The element size was sequentially decreased from the default size and numerical analysis repeated till the displacement results from the solver demonstrated a plateau effect (337, 338). The iteration at which the displacement result had plateaued was selected to apply further increments of simulated load. Following satisfactory convergence, simulated load increments were applied upto the maximum load as described earlier in chapter 5.

7.2.5 Validation and verification

A comparison of FEA results with experimental results (described in chapter 6) was undertaken to ensure robust validation of the paediatric femur fracture fixation FEA model and its inherent assumptions (327, 330, 331, 334, 344, 345, 356, 360, 376). Validation of the paediatric femur fracture fixation FEA model was performed using the following two methods (361, 368, 376, 378, 379):

a) Linear regression analysis was performed for each of the above FEA model predicted displacement values and the corresponding experimental data to determine the slope, intercept, 95% prediction interval and R^2 value

b) Estimation of the relative error between the experimental stiffness results and the predicted stiffness results from the FEA. The relative error (expressed as percentage) was calculated as below:

$$\text{Relative error} = \frac{(k_{\text{FEA}} - k_{\text{EXP}})}{k_{\text{EXP}}} \times 100 \qquad (27)$$

where k_{FEA} = predicted stiffness of the FEA model and k_{EXP} = mean stiffness value obtained from the corresponding experimental model (three composite femur and ALFN construct described in chapter 6). The above were performed using the data analysis function in Microsoft

Excel 2010. A schematic illustration of the paediatric femur fracture fixation FEA model validation process is presented below in Figure 7-12.

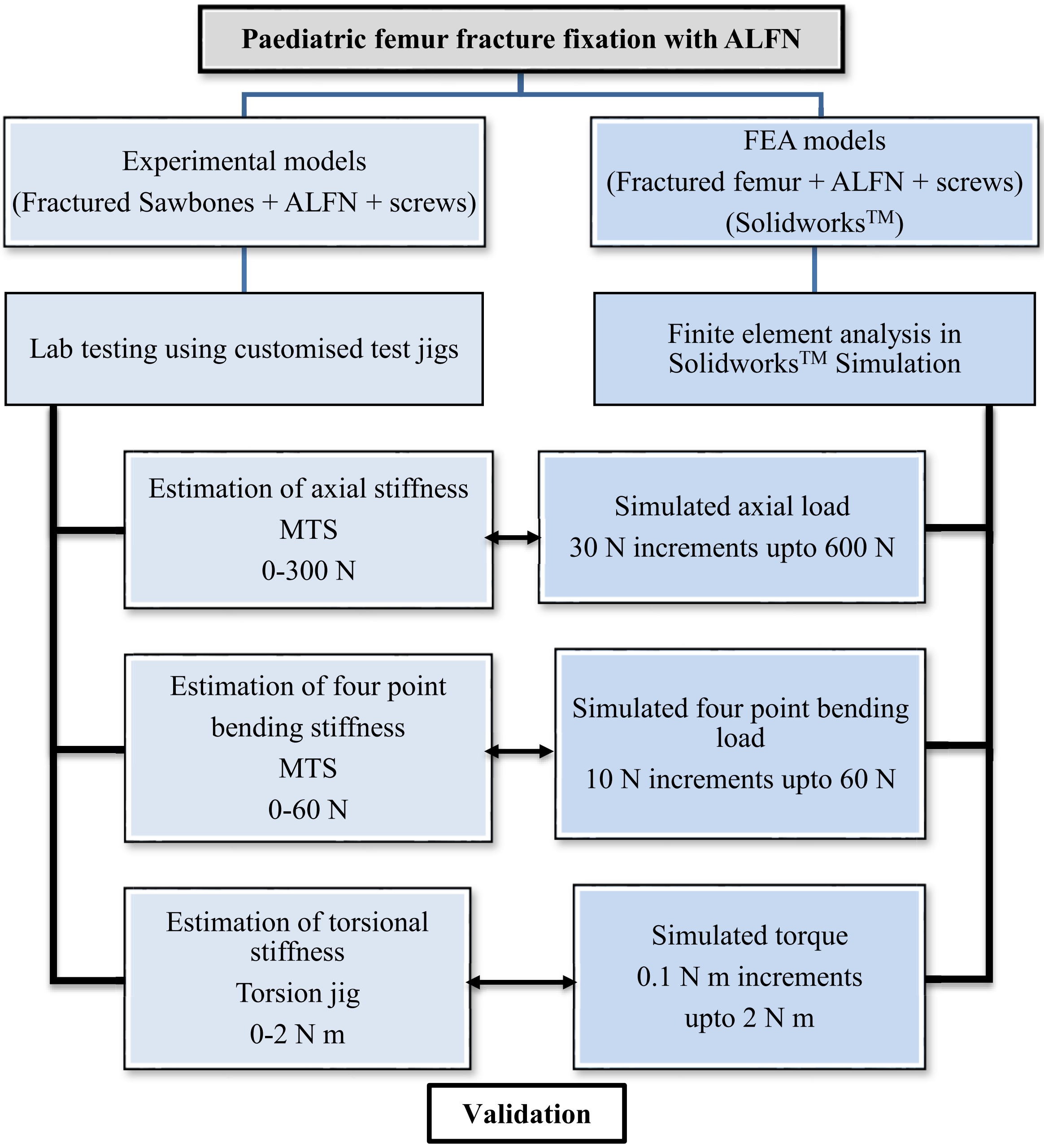

Figure 7-12 Validation of paediatric femur fracture fixation FEA model

7.3 Results

7.3.1 Axial compression

7.3.1.1 Convergence analysis

During convergence analysis, FEA model iterations (transverse – 4 / comminuted – 4 / segmental defect – 5 / healed – 3) demonstrated satisfactory convergence of displacement (U_X) results (Figure 7-13). Details of the different iterations are provided in Table C-1.

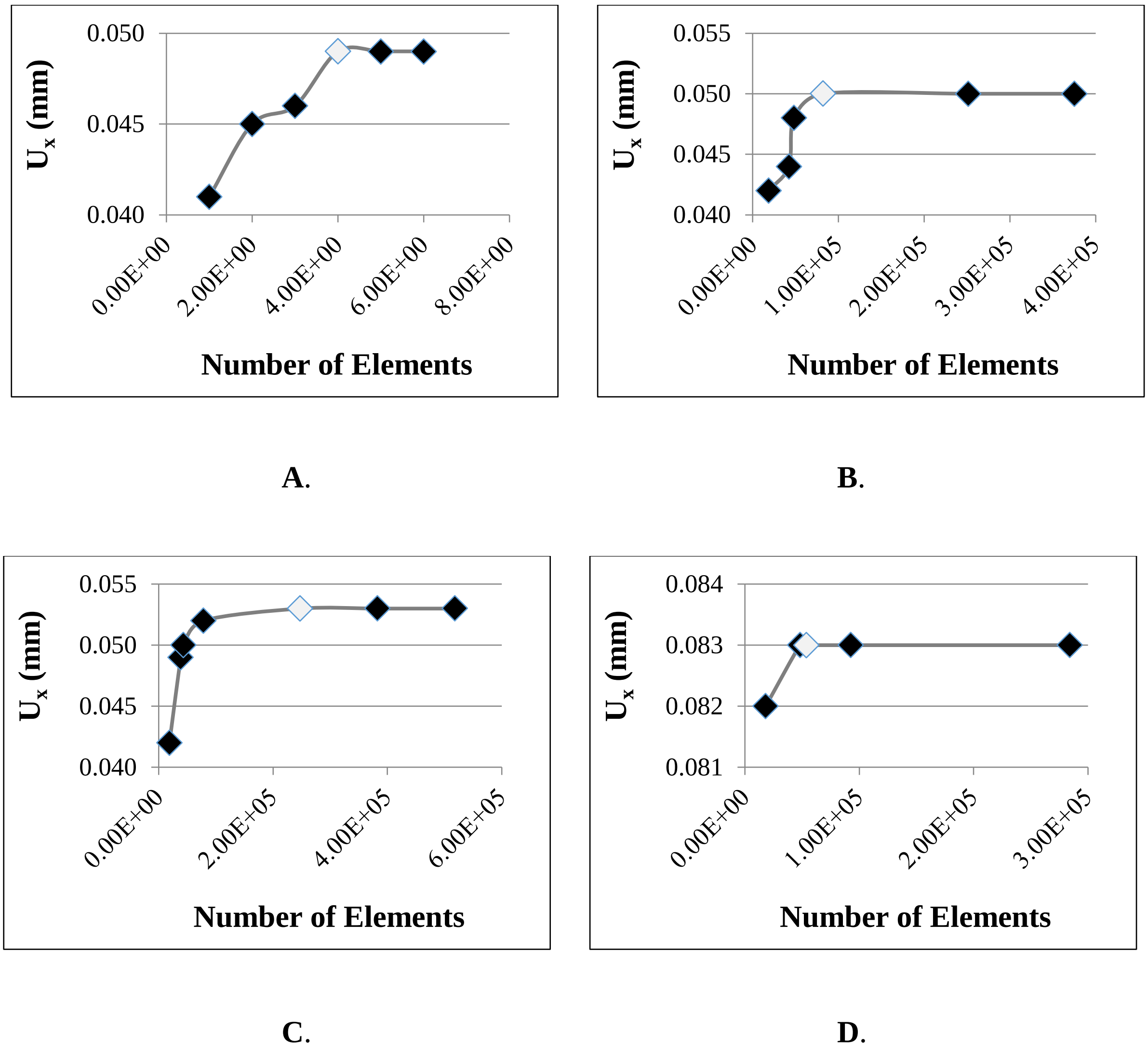

Figure 7-13 Convergence of displacement values in fracture FEA models during simulated axial compression test (A-transverse, B-comminuted, C-segmental defect, D-healed)

7.3.1.2 Predicted axial stiffness ($k_{\text{FEA Ax}}$)

The predicted axial stiffness for the transverse ($k_{\text{FEA Ax } Tra}$) and comminuted ($k_{\text{FEA Ax } Com}$) fracture models was 611.97 N/mm and 602.47 N/mm, respectively (Figure 7-14).

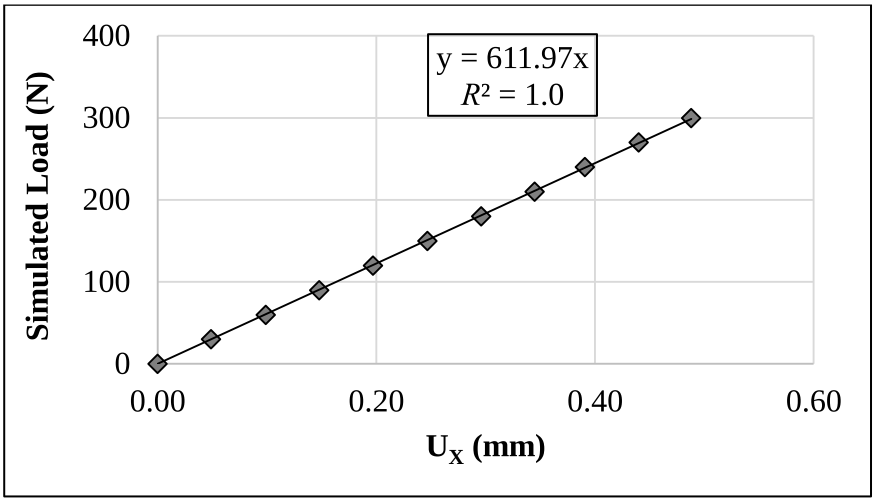

A.

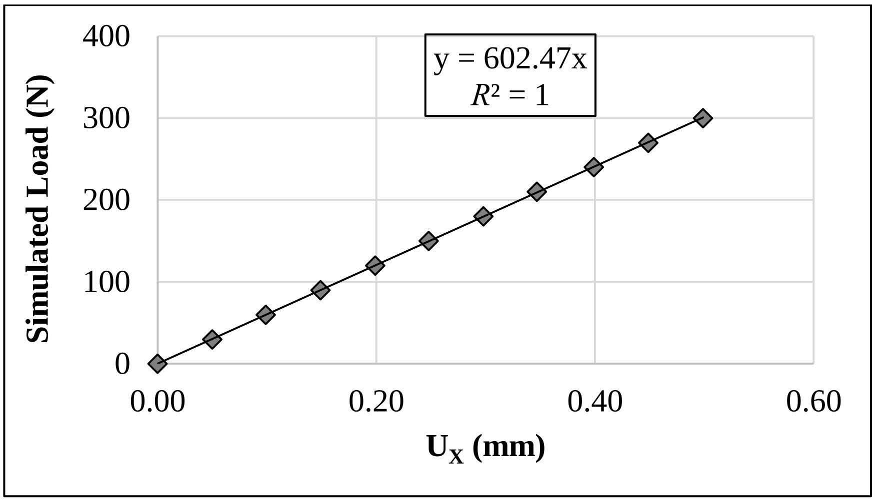

B.

Figure 7-14 Predicted axial stiffness of FEA models (A-transverse fracture, B-comminuted fracture)

The predicted axial stiffness for the segmental defect fracture ($k_{FEA\ Ax\ Seg}$) was 572.09 N/mm whereas the model predicted higher stiffness for a healed fracture ($k_{FEA\ Ax\ Hld}$) at 725.46 N/mm (Figure 7-15).

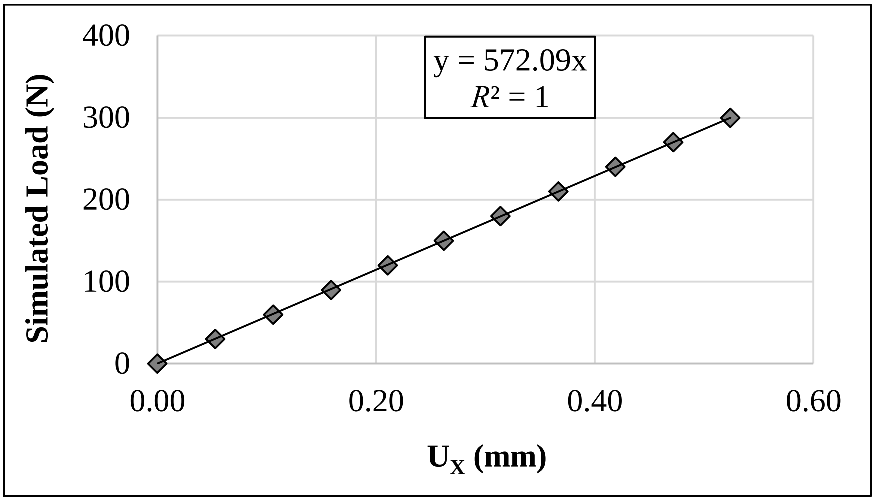

A.

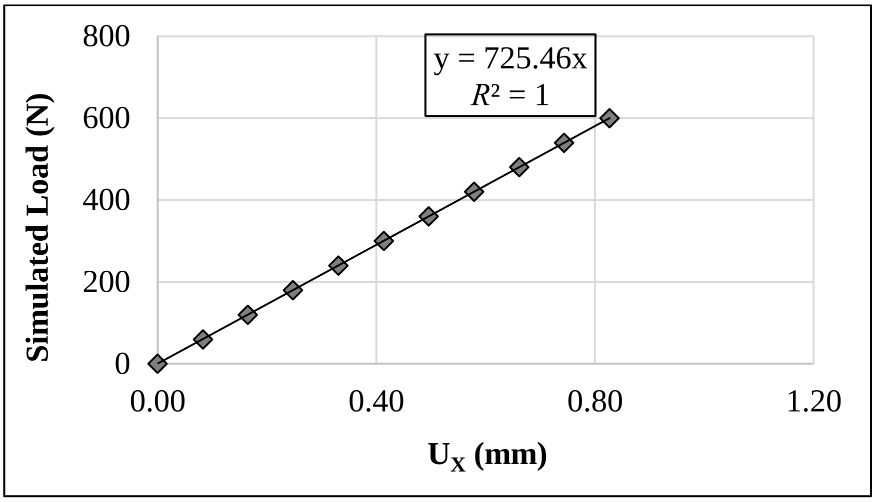

B.

Figure 7-15 Predicted axial stiffness of FEA models (A-segmental defect fracture, B-healed fracture)

7.3.2 Four-point bending

7.3.2.1 Convergence analysis

During convergence analysis, FEA model iterations (transverse – 4 / comminuted – 5 / segmental defect – 5 / healed – 6) demonstrated satisfactory convergence of displacement (U_Y) results (Figure 7-16). Details of the different iterations are provided in Table C-2.

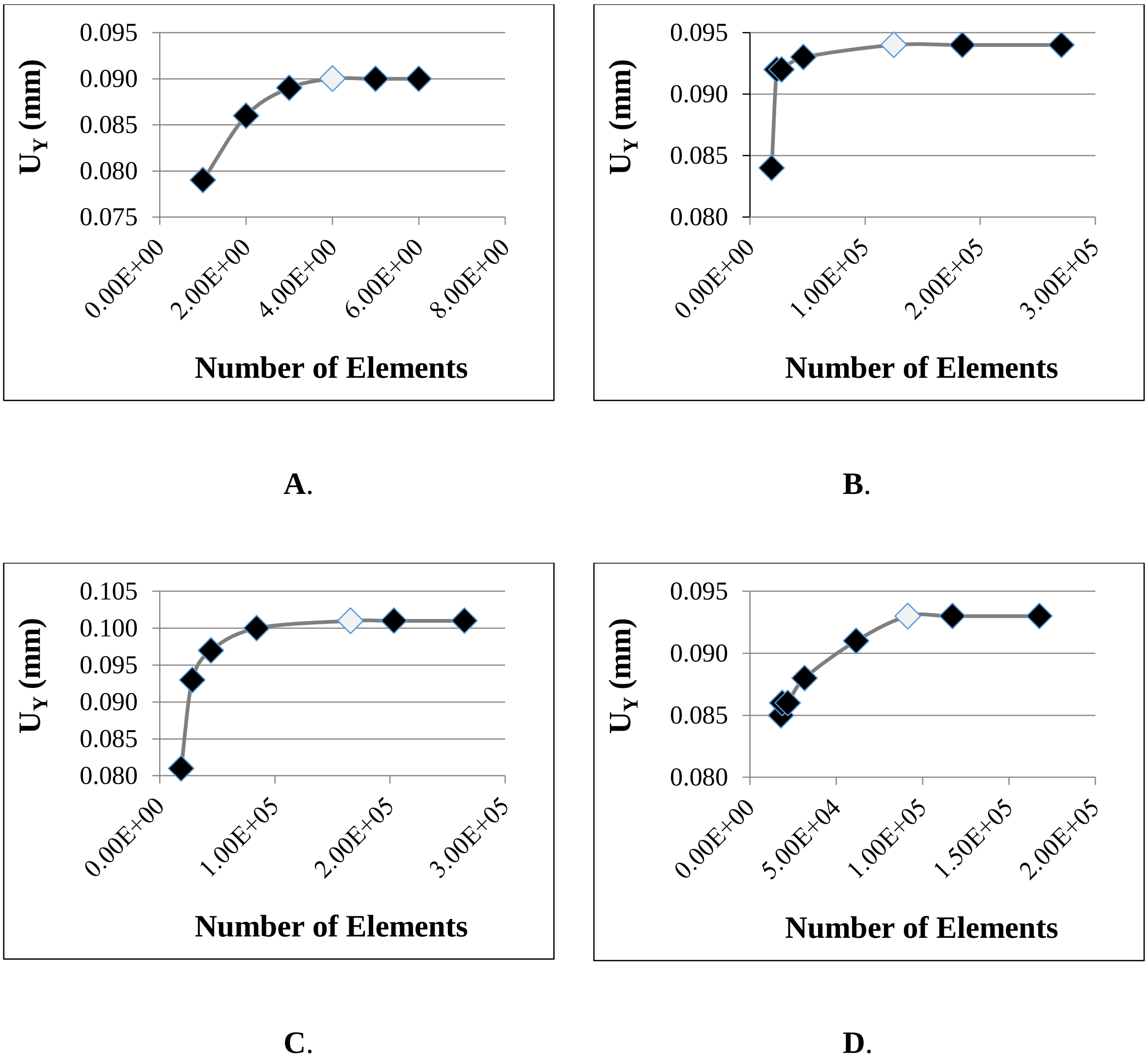

Figure 7-16 Convergence of displacement values in fracture FEA models during simulated four-point bending test (A-transverse, B-comminuted, C-segmental defect, D-healed)

7.3.2.2 Predicted four-point bending stiffness ($k_{\text{FEA Be}}$)

The four-point bending stiffness for the transverse ($k_{\text{FEA Be } Tra}$) and comminuted ($k_{\text{FEA Be } Com}$) fracture models was 111.11 N/mm and 106.71 N/mm, respectively (Figure 7-17).

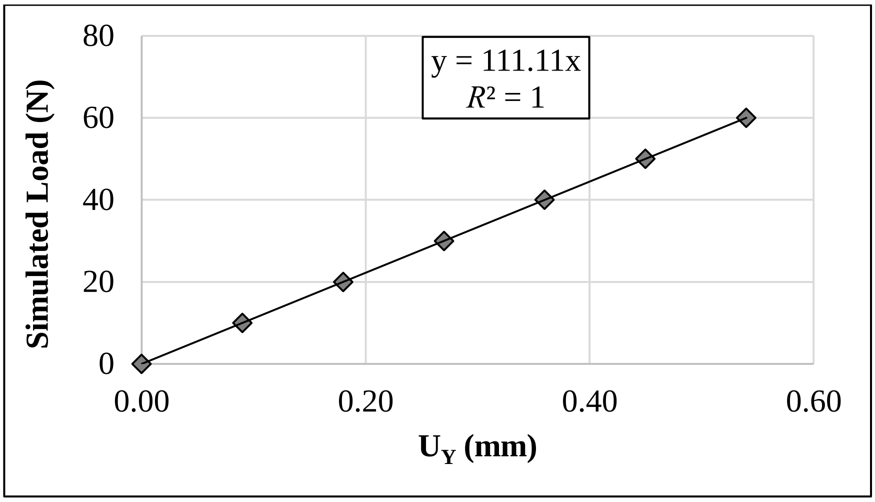

A.

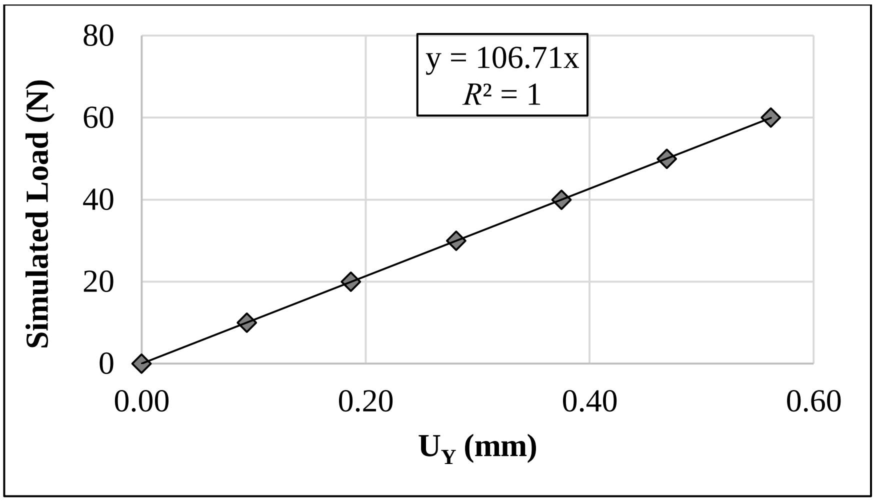

B.

Figure 7-17 Predicted four-point bending stiffness of FEA models (A-transverse fracture, B-comminuted fracture)

The predicted four-point bending stiffness for the segmental defect fracture ($k_{\text{FEA Be } Seg}$) was 99.01 N/mm. In comparison the model predicted higher stiffness for a healed fracture ($k_{\text{FEA Be } Hld}$) at 430.11 N/mm (Figure 7-18).

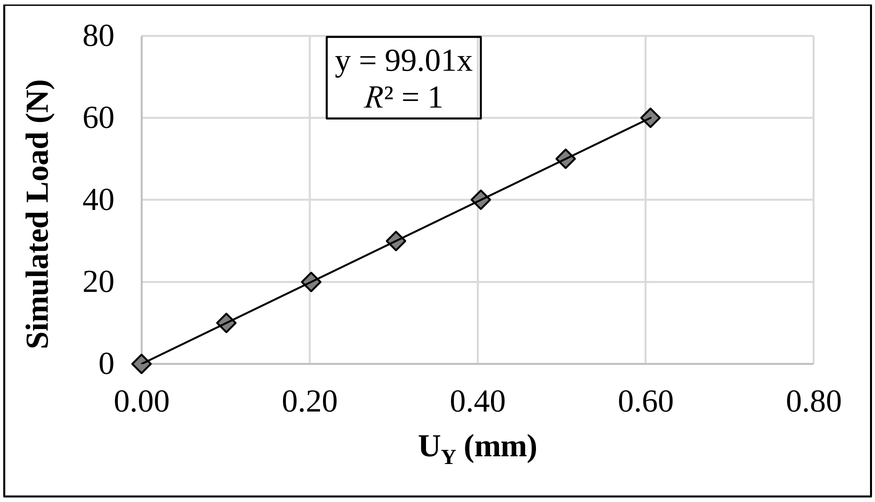

A.

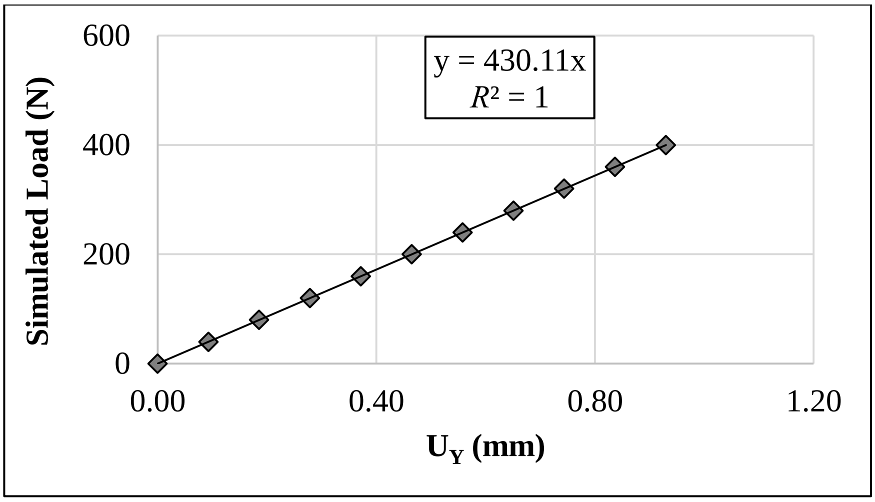

B.

Figure 7-18 Predicted four-point bending stiffness of FEA models (A-segmental defect fracture, B-healed fracture)

7.3.3 Torsion (internal rotation)

7.3.3.1 Convergence analysis

During convergence analysis, FEA model iterations (transverse – 3 / comminuted – 4 / segmental defect – 4 / healed – 3) demonstrated satisfactory convergence of angular rotation (ϕ_{Ir}) results (Figure 7-19). Details of the different iterations are provided in Table C-3.

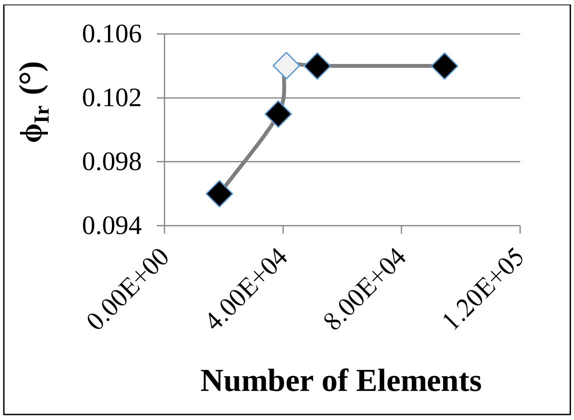

A.

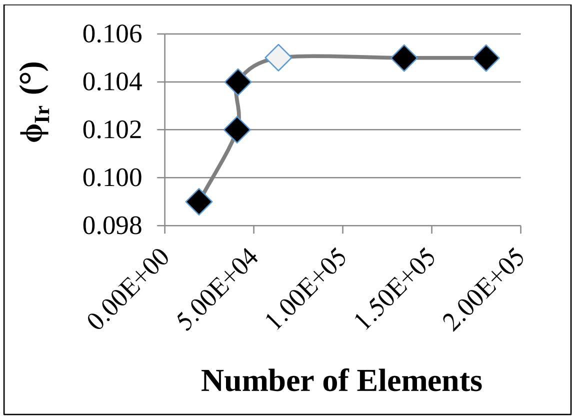

B.

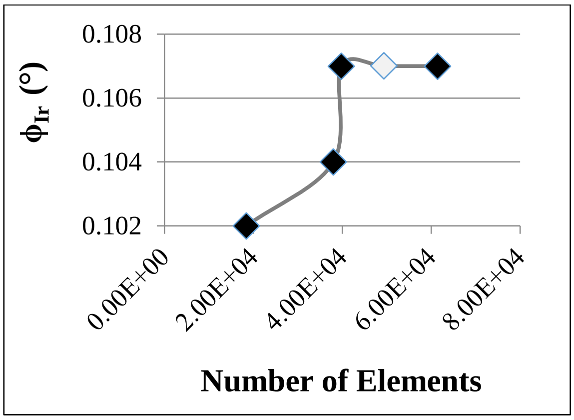

C.

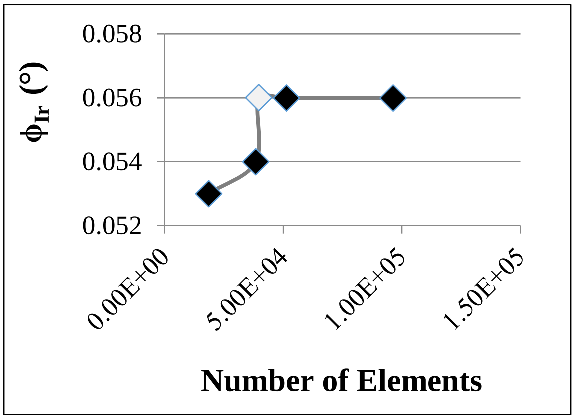

D.

Figure 7-19 Convergence of angular rotation in fracture FEA models during simulated torsion (internal rotation) test (A-transverse, B-comminuted, C-segmental defect, D-healed)

7.3.3.2 Predicted torsional stiffness (internal rotation) ($k_{\text{FEA Ir}}$)

The predicted torsional stiffness for the transverse ($k_{\text{FEA Ir } Tra}$) and comminuted ($k_{\text{FEA Ir } Com}$) fracture models was 0.96 N m / deg and 0.94 N m / deg, respectively (Figure 7-20)

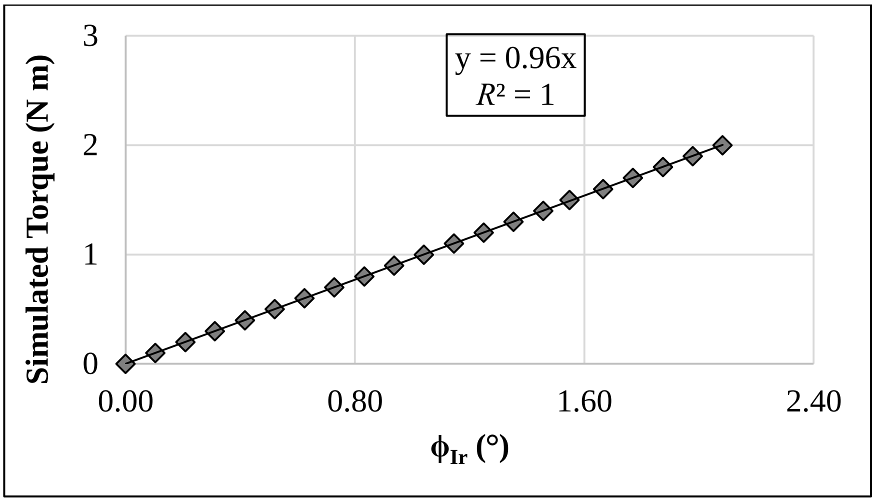

A.

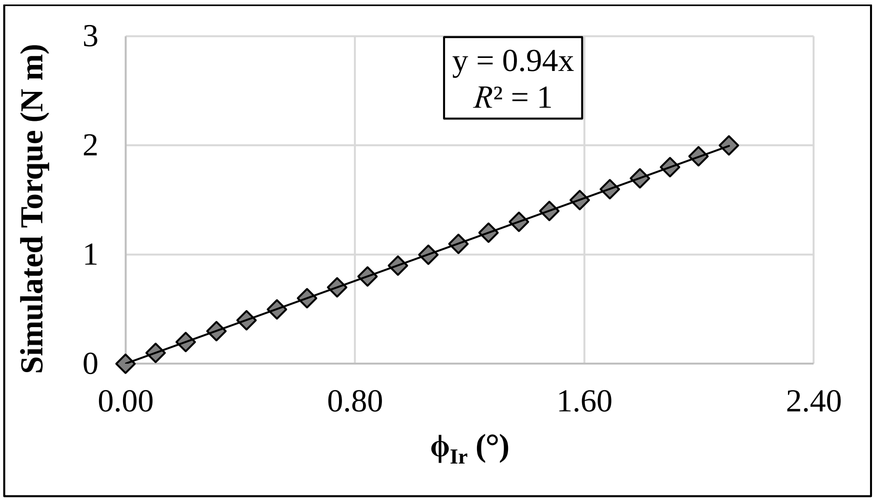

B.

Figure 7-20 Predicted torsional stiffness (internal rotation) of FEA models (A-transverse fracture, B-comminuted fracture)

The predicted torsional stiffness for the segmental defect fracture ($k_{\mathrm{FEA\ Ir}\ Seg}$) was 0.94 N m / deg whereas the model predicted higher stiffness for a healed fracture ($k_{\mathrm{FEA\ Ir}\ Hld}$) was 3.56 N m / deg (Figure 7-21).

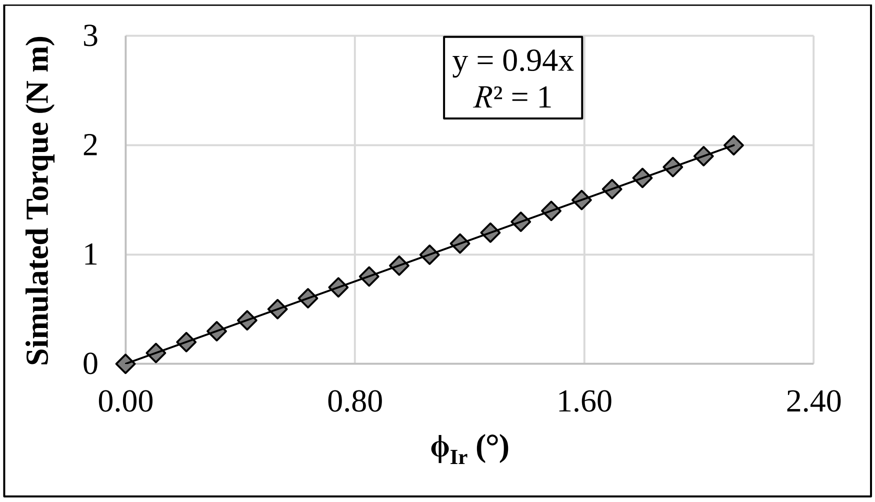

A.

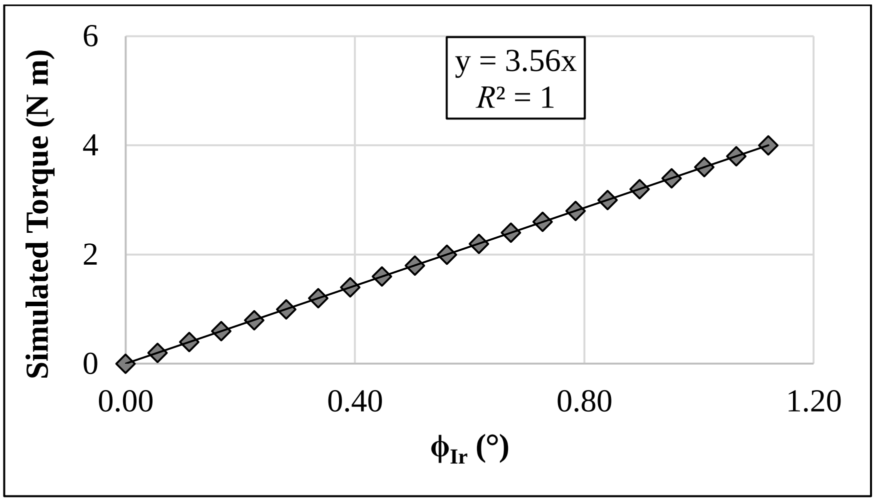

B.

Figure 7-21 Predicted torsional stiffness (internal rotation) of FEA models (A-segmental defect fracture, B-healed fracture)

7.3.4 Torsion (external rotation)

7.3.4.1 Convergence analysis

During convergence analysis, FEA model iterations (transverse – 3 / comminuted – 4 / segmental defect – 4 / healed – 3) demonstrated satisfactory convergence of angular rotation (ϕ_{Er}) results (Figure 7-19). Details of the different iterations are provided in Table C-4.

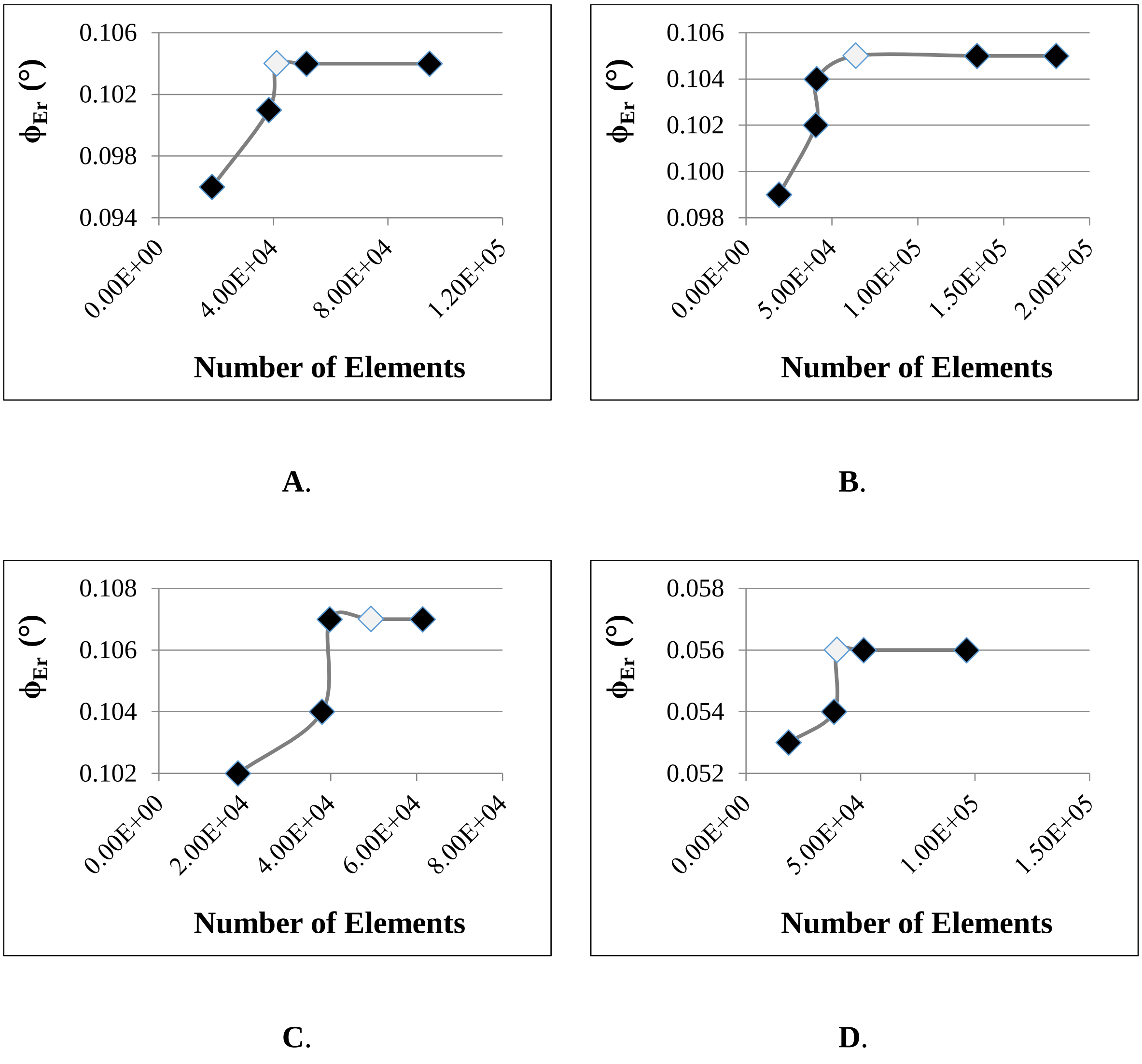

Figure 7-22 Convergence of angular rotation in fracture FEA models during simulated torsion (external rotation) test (A-transverse, B-comminuted, C-segmental defect, D-healed)

7.3.4.2 Predicted torsional stiffness (external rotation) ($k_{\text{FEA Er}}$)

The predicted torsional stiffness for the transverse ($k_{\text{FEA Er } Tra}$) and comminuted ($k_{\text{FEA Er } Com}$) fracture models was 0.96 N m / deg and 0.93 N m / deg, respectively (Figure 7-23).

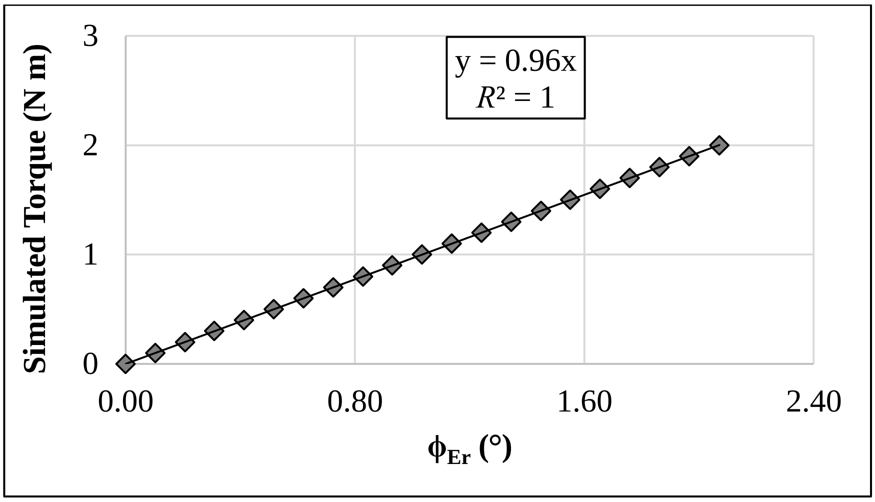

A.

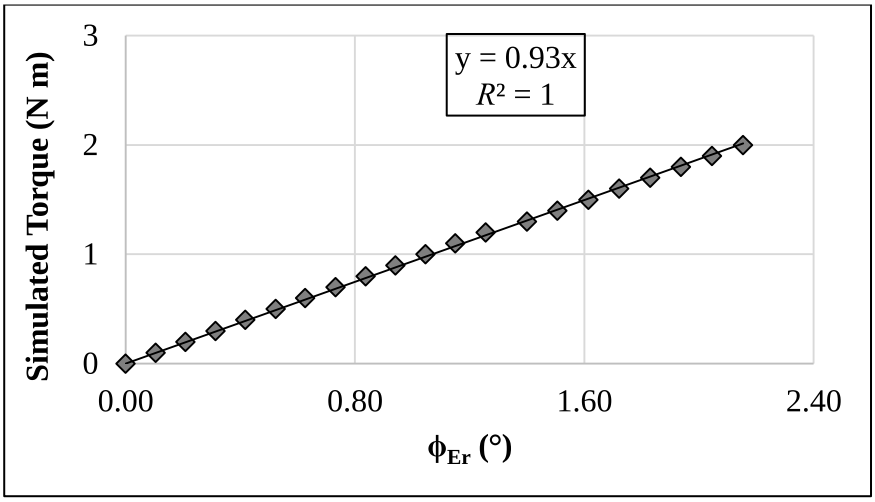

B.

Figure 7-23 Predicted torsional stiffness (external rotation) of FEA models (A-transverse fracture, B-comminuted fracture)

The predicted torsional stiffness for the segmental defect fracture ($k_{\text{FEA Er } Seg}$) was 0.93 N m / deg and 3.55 N m / deg for healed fracture ($k_{\text{FEA Er } Hld}$) (Figure 7-24).

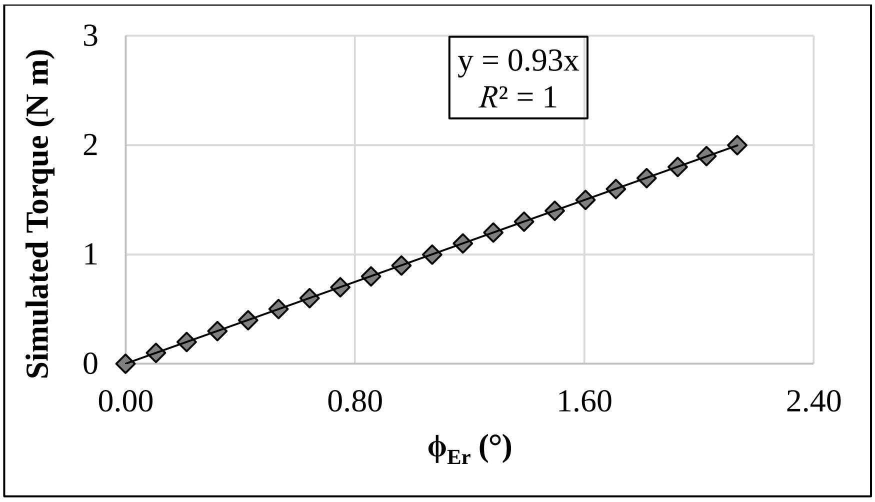

A.

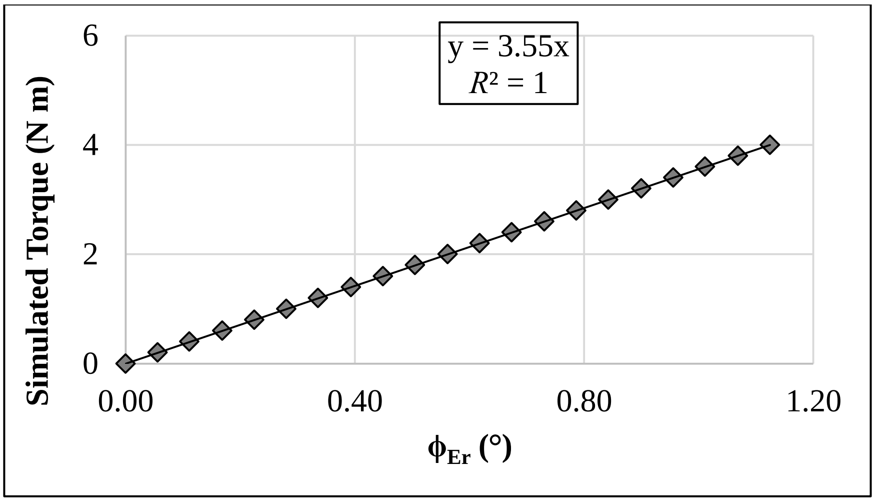

B.

Figure 7-24 Predicted torsional stiffness (external rotation) of FEA models (A-segmental defect fracture, B-healed fracture)

7.3.5 Comparison of FEA and experimental results (linear regression analysis)

7.3.5.1 Axial compression

Comparison of the experimental and the FEA results is presented below (Figure 7-25).

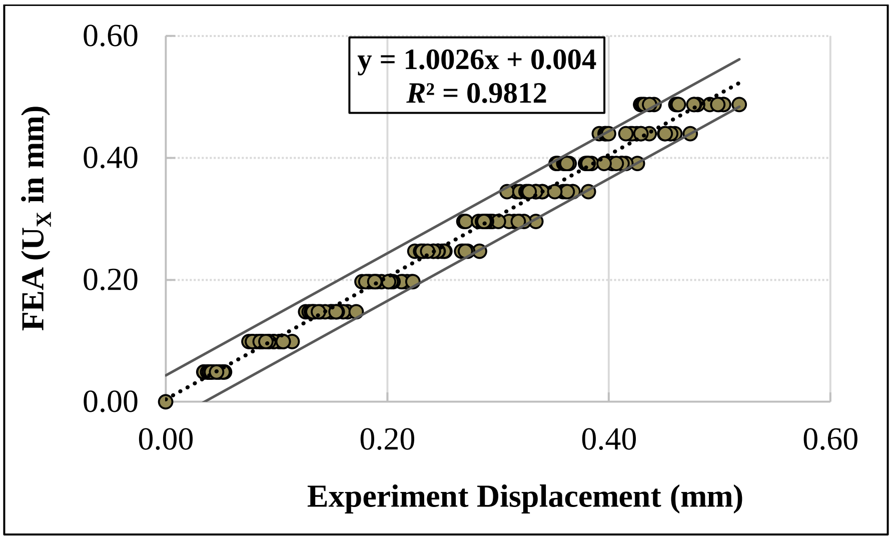

A.

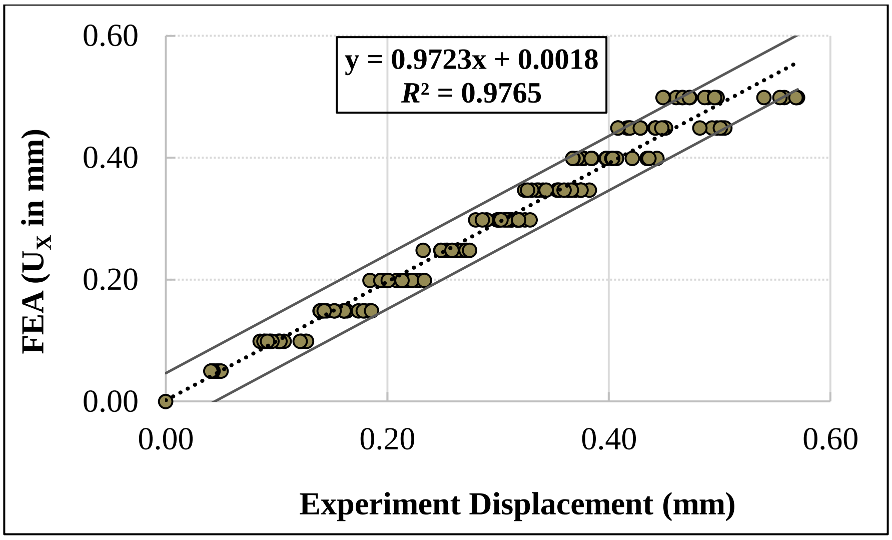

B.

Figure 7-25 Correlation of axial compression results of FEA model and experimental data (dashed line = regression line, solid lines = 95% prediction interval) (A-Transverse fracture, B-Comminuted fracture)

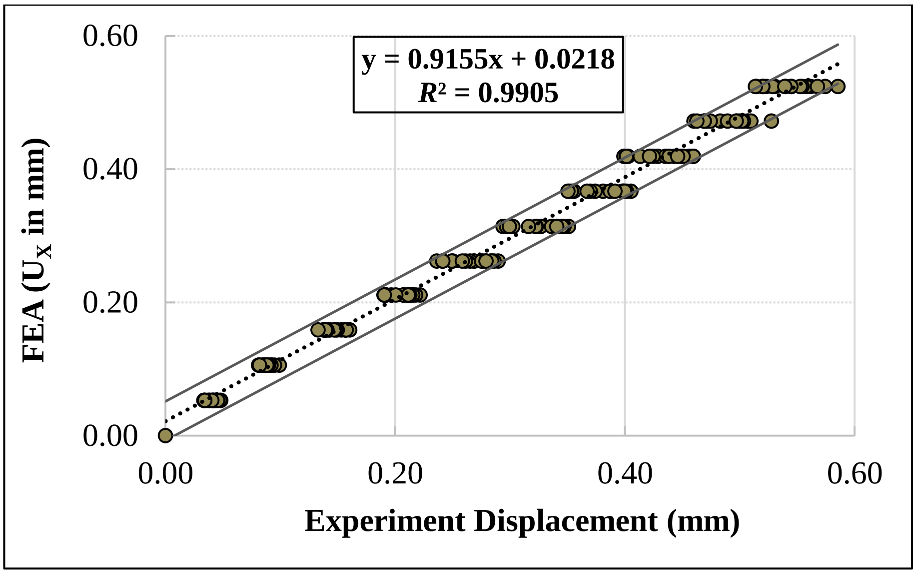

A.

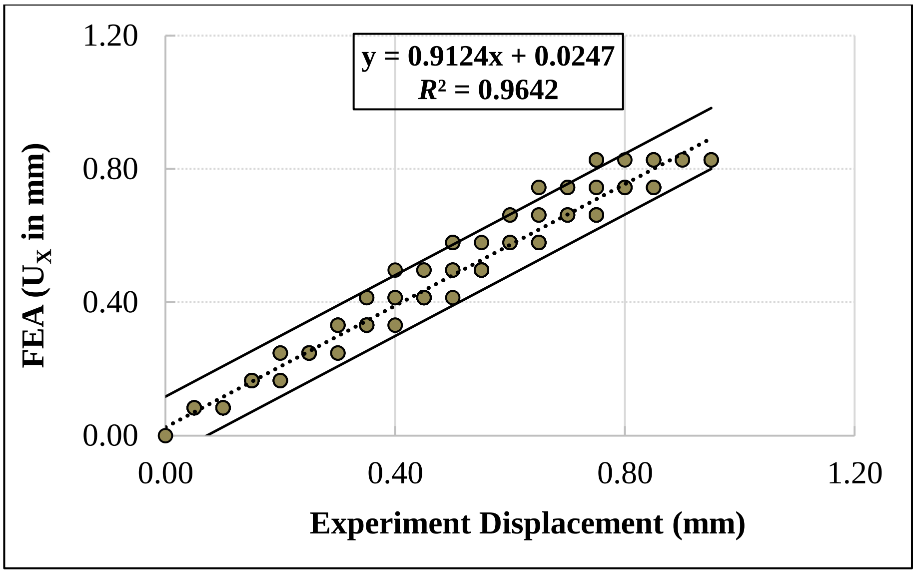

B.

Figure 7-26 Correlation of axial compression results of FEA model and experimental data (dashed line = regression line, solid lines = 95% prediction interval) (A-Segmental defect, B-Healed fracture)

Overall there was a good agreement between the experiment results and the displacement results predicted by the FE models.

7.3.5.2 Four-point bending

The predicted results (U_Y in mm) of the FE models and the experimental results and is shown below.

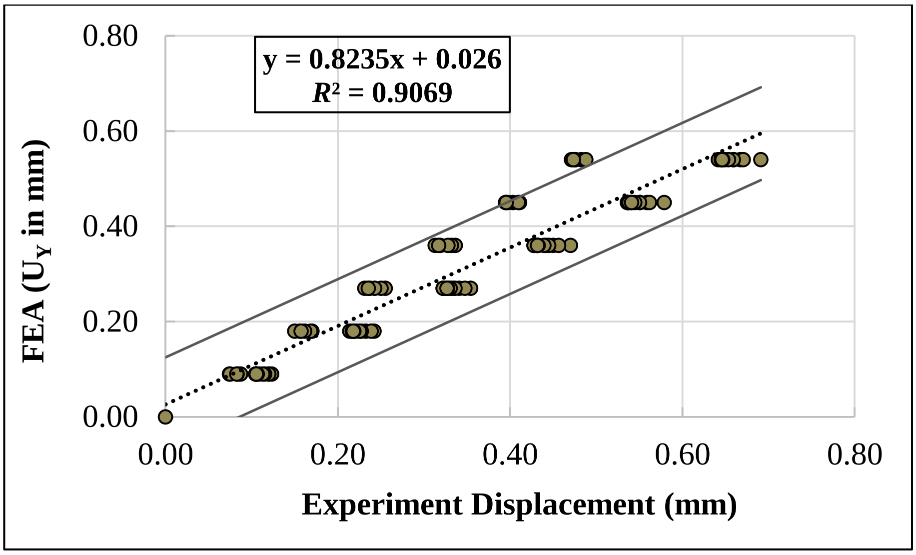

A.

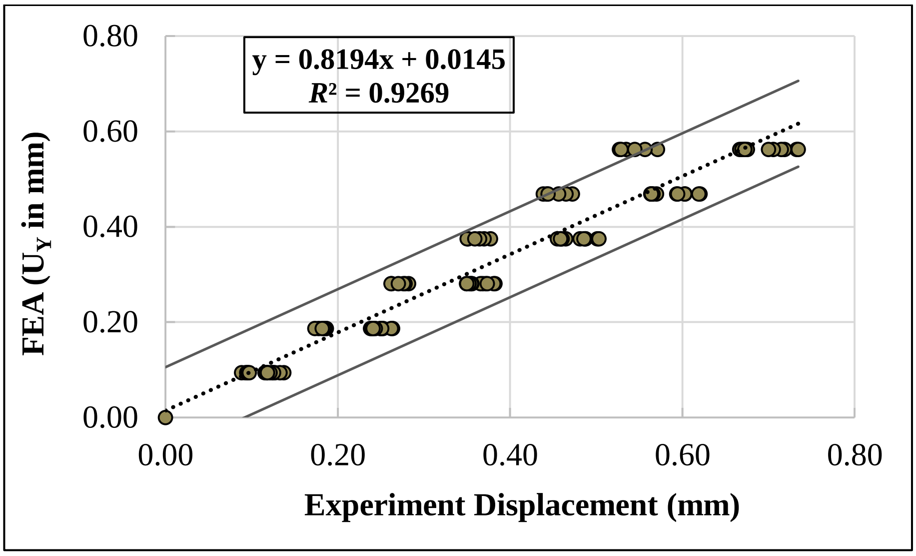

B.

Figure 7-27 Correlation of four-point bending results of transverse fracture FEA model and experimental data (dashed line = regression line, solid lines = 95% prediction interval) (A-Transverse fracture, B-Comminuted fracture)

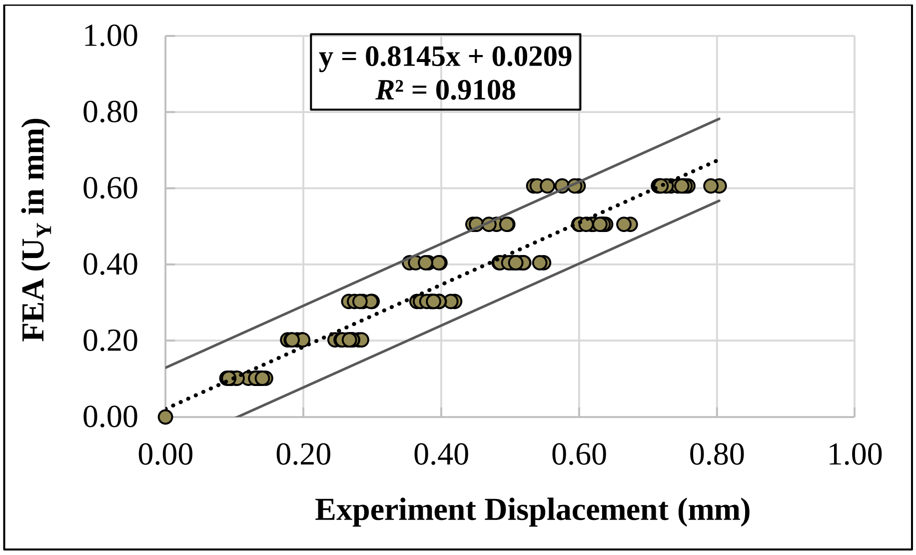

A.

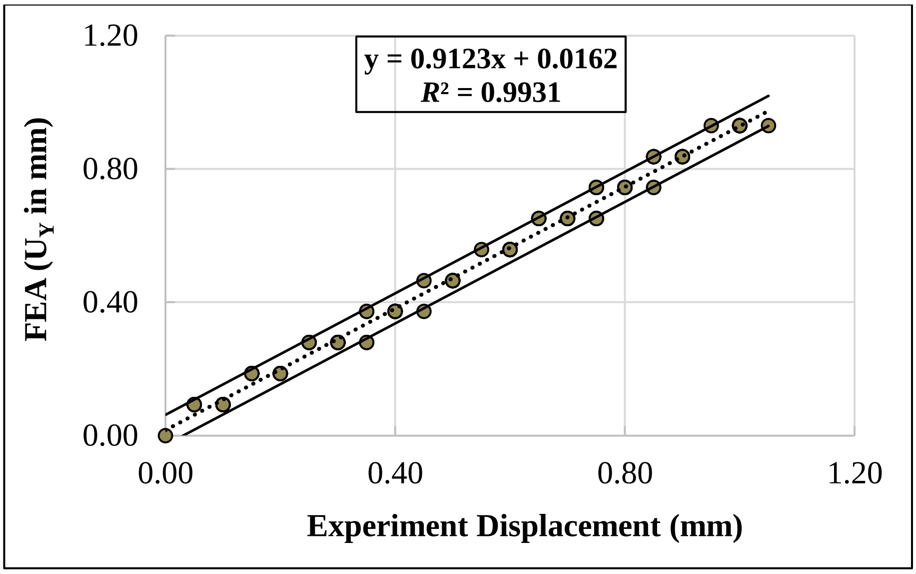

B.

Figure 7-28 Correlation of four-point bending results of comminuted fracture FEA model and experimental data (dashed line = regression line, solid lines = 95% prediction interval) (A-Segmental defect, B-Healed fracture)

Overall there was a good correlation between the displacement results noted during four-point bending experiments and the FE model predictions.

7.3.5.3 Torsion - internal rotation

The comparison of the angular displacement results of experimental testing and the predicted results of the FE models is presented below.

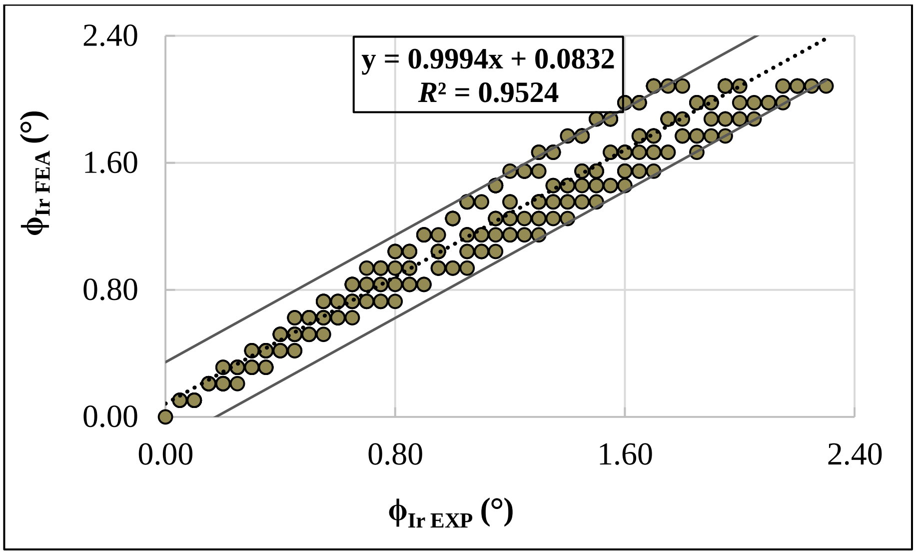

A.

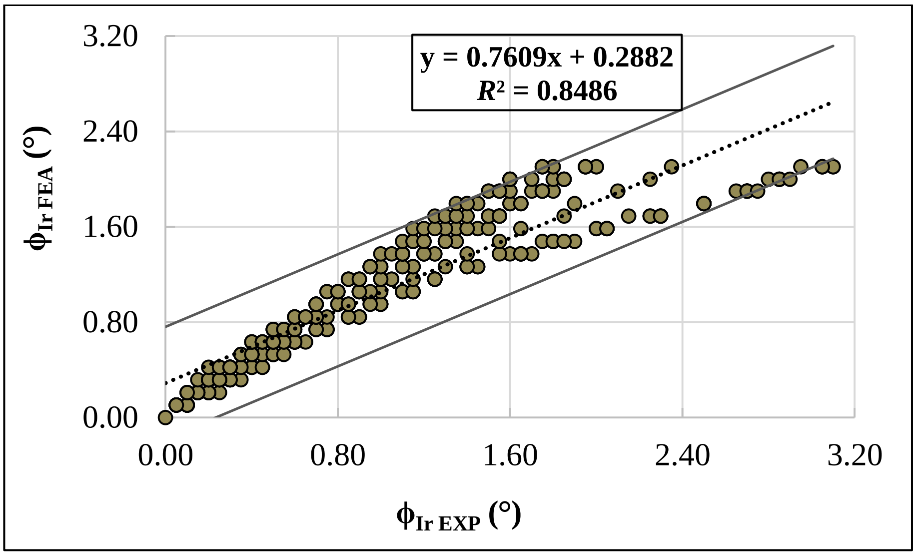

B.

Figure 7-29 Correlation of angular rotation in internal rotation of FEA model and experimental data (dashed line = regression line, solid lines = 95% prediction interval) (A-Transverse fracture, B-Comminuted fracture)

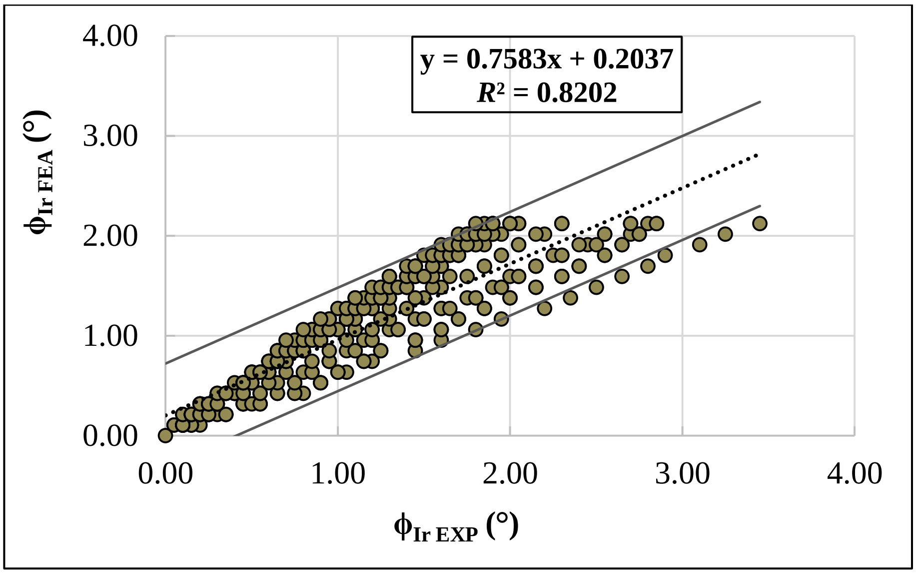

A.

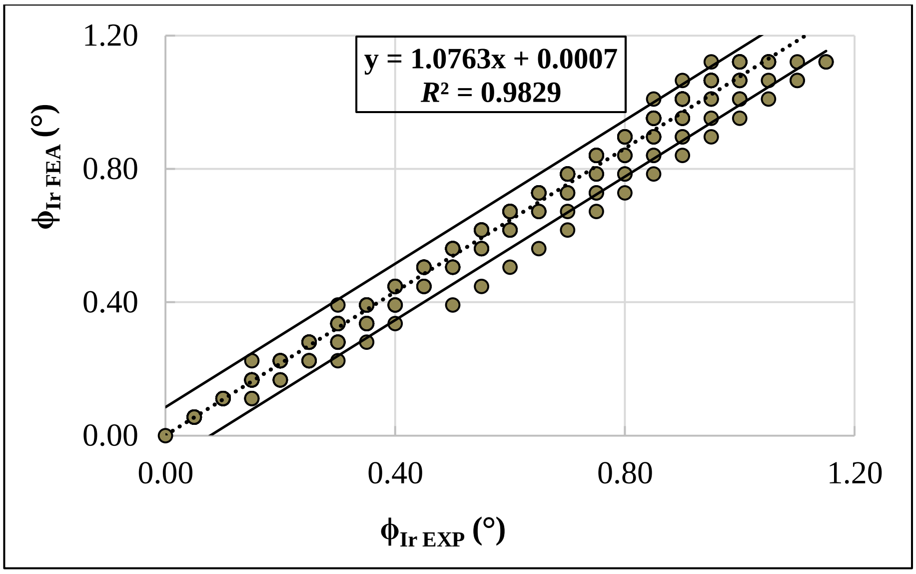

B.

Figure 7-30 Correlation of angular rotation in internal rotation FEA model and experimental data (dashed line = regression line, solid lines = 95% prediction interval) (A-Segmental defect, B-Healed fracture)

In general there was a good agreement between the experimental results and the FE model predictions for the angular rotation during internal rotation.

7.3.5.4 Torsion - external rotation

The comparison of the angular rotation noted in experimental tests and the predicted results of the FE models is shown below.

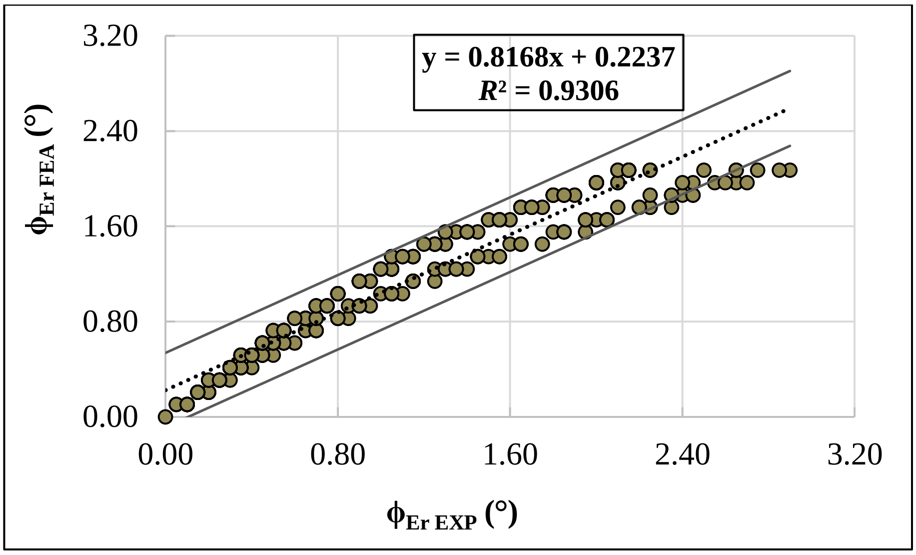

A.

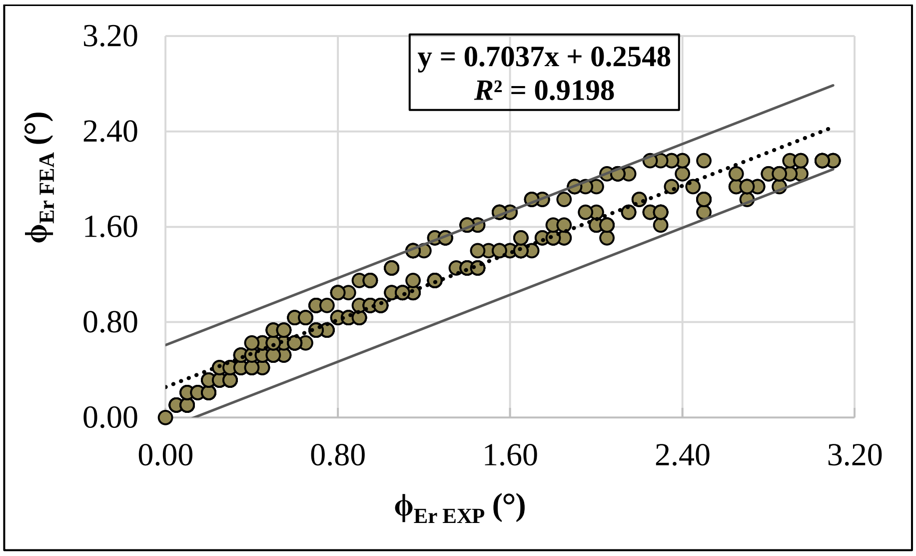

B.

Figure 7-31 Correlation of angular rotation in external rotation of experimental data and FEA model (dashed line = regression line, solid lines = 95% prediction interval) (A-Transverse fracture, B-Comminuted fracture)

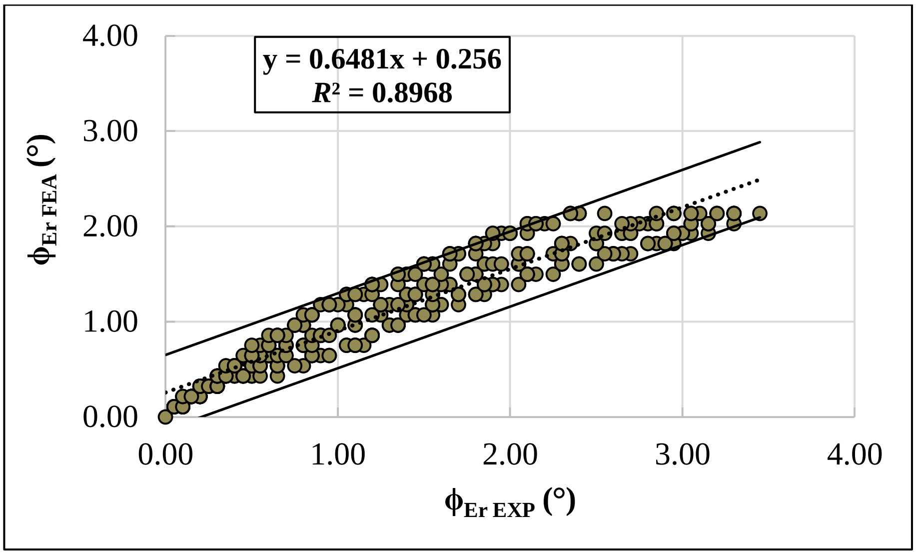

A.

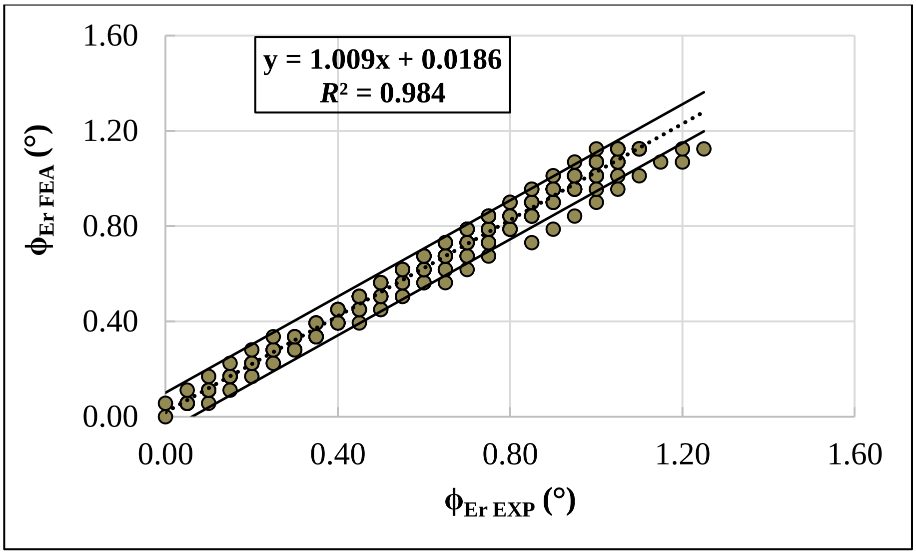

B.

Figure 7-32 Correlation of angular rotation in external rotation of experimental data FEA model (dashed line = regression line, solid lines = 95% prediction interval) (A-Segmental defect, B-Healed fracture)

There was a good agreement between the experimental results and the FE model predictions for the angular rotation during internal rotation.

7.3.6 Relative error between the experimental stiffness and the FEA stiffness

7.3.6.1 Axial compression

The axial stiffness (mean ± standard deviation) of the femur and ALFN construct (Sp1 FAC, Sp2 FAC and Sp3 FAC) during experimental testing was $k_{\mathrm{EXP\ Ax}\ Tra}$ (622.84 ± 36.65 N/mm), $k_{\mathrm{EXP\ Ax}\ Com}$ (593.62 ± 36.71 N/mm), $k_{\mathrm{EXP\ Ax}\ Seg}$ (562.04 ± 31.50 N/mm) and $k_{\mathrm{EXP\ Ax}\ Hld}$ (701.27 ± 64.48 N/mm). In comparison the predicted axial stiffness from the FE models measured $k_{\mathrm{FEA\ Ax}\ Tra}$ (611.97 N/mm), $k_{\mathrm{FEA\ Ax}\ Com}$ (602.47 N/mm), $k_{\mathrm{FEA\ Ax}\ Seg}$ (587.13 N/mm), $k_{\mathrm{FEA\ Ax}\ Hld}$ (725.46 N/mm) representing a relative error of -1.75%, +1.49%, +4.46 and +3.45% respectively (Figure 7-33).

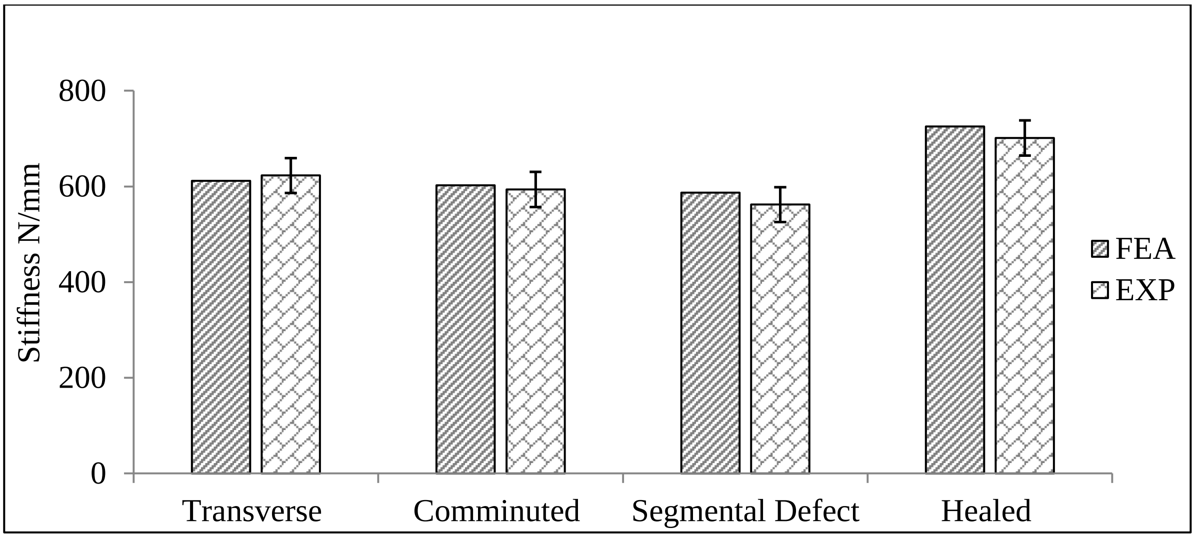

Figure 7-33 Comparison of experimental (EXP) and FEA predicted axial stiffness of different fracture groups

7.3.6.2 Four-point bending

The four-point bending stiffness (mean ± standard deviation) of the three femur and ALFN construct (Sp1 FAC, Sp2 FAC and Sp3 FAC) during experimental testing was $k_{\mathrm{EXP\ Be}\ Tra}$ (102.53 ± 16.47 N/mm), $k_{\mathrm{EXP\ Be}\ Com}$ (93.44 ± 12.86 N/mm), $k_{\mathrm{EXP\ Be}\ Seg}$ (88.06 ± 13.75 N/mm) and $k_{\mathrm{EXP\ Be}\ Hld}$ (402.50 ± 5.28 N/mm). In comparison the predicted axial stiffness from the FE models measured $k_{\mathrm{FEA\ Be}\ Tra}$ (111.11 N/mm), $k_{\mathrm{FEA\ Be}\ Com}$ (106.71 N/mm), $k_{\mathrm{FEA\ Be}\ Seg}$ (99.01 N/mm), $k_{\mathrm{FEA\ Be}\ Hld}$ (430.11 N/mm) representing a relative error of +8.37%, +14.20%, +12.44 and +6.86% respectively (Figure 7-34).

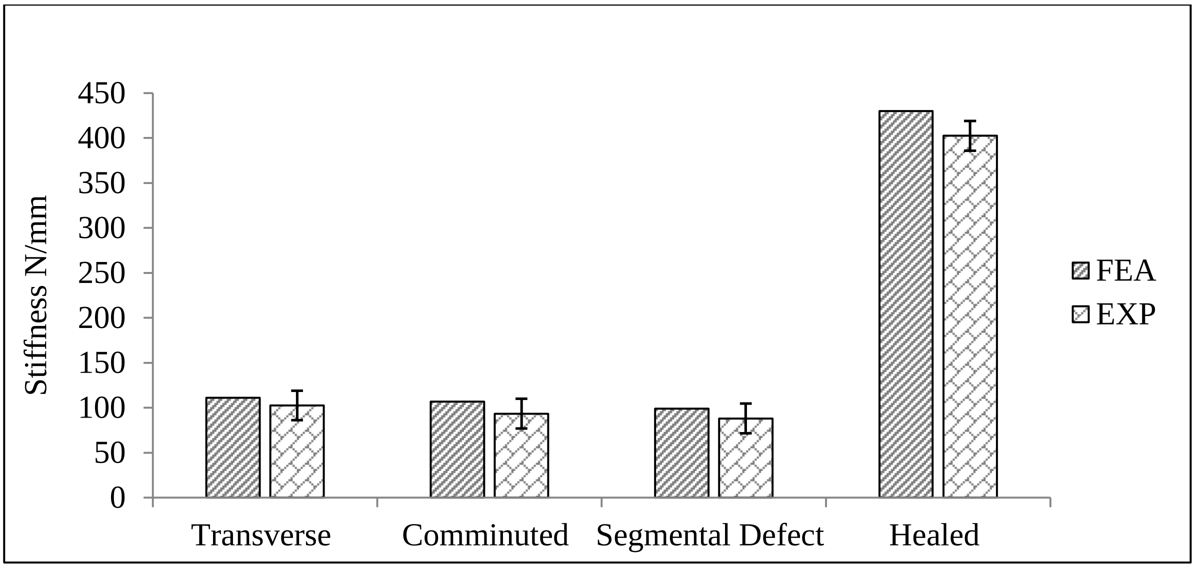

Figure 7-34 Comparison of experimental (EXP) and FEA predicted four-point bending stiffness of different fracture groups

7.3.6.3 Torsion - internal rotation

The torsional stiffness (mean ± standard deviation) of the three femur and ALFN construct (Sp1 FAC, Sp2 FAC and Sp3 FAC) in internal rotation was $k_{\mathrm{EXP\ Ir}\ Tra}$ (1.04 ± 0.12 N m/deg), $k_{\mathrm{EXP\ Ir}\ Com}$ (0.97 ± 0.20 N m/deg), $k_{\mathrm{EXP\ Ir}\ Seg}$ (0.91 ± 0.18 N m/deg) and $k_{\mathrm{EXP\ Ir}\ Hld}$ (3.86 ± 0.20 N m/deg). In comparison the predicted axial stiffness from the FE models measured $k_{\mathrm{FEA\ Ir}\ Tra}$ (0.96 N m/deg), $k_{\mathrm{FEA\ Ir}\ Com}$ (0.94 N m/deg), $k_{\mathrm{FEA\ Ir}\ Seg}$ (0.94 N m/deg), $k_{\mathrm{FEA\ Ir}\ Hld}$ (3.56 N m/deg) representing a relative error of -7.74%, -3.15%, +3.42 and -7.83% respectively (Figure 7-35).

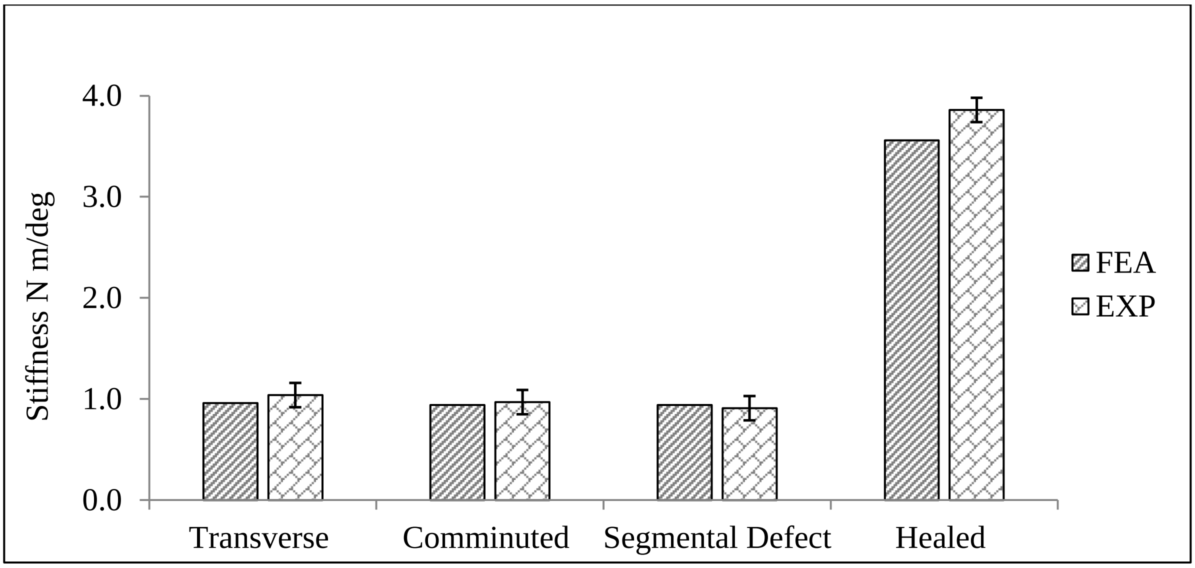

Figure 7-35 Comparison of experimental (EXP) and FEA predicted torsional stiffness (internal rotation) of different fracture groups

7.3.6.4 Torsion - external rotation

The torsional stiffness (mean ± standard deviation) of the three femur and ALFN construct (Sp1 FAC, Sp2 FAC and Sp3 FAC) in external rotation was $k_{\mathrm{EXP\ Er}\ Tra}$ (0.96 ± 0.12 N m/deg), $k_{\mathrm{EXP\ Er}\ Com}$ (0.82 ± 0.13 N m/deg), $k_{\mathrm{EXP\ Er}\ Seg}$ (0.77 ± 0.14 N m/deg) and $k_{\mathrm{EXP\ Er}\ Hld}$ (3.69 ± 0.19 N m/deg). In comparison the predicted torsional stiffness from the FE models measured $k_{\mathrm{FEA\ Er}\ Tra}$ (0.96 N m/deg), $k_{\mathrm{FEA\ Er}\ Com}$ (0.93 N m/deg), $k_{\mathrm{FEA\ Er}\ Seg}$ (0.93 N m/deg), $k_{\mathrm{FEA\ Er}\ Hld}$ (3.55 N m/deg) representing a relative error of 0.12%, +13.80%, +20.87 and -3.91% respectively (Figure 7-36).

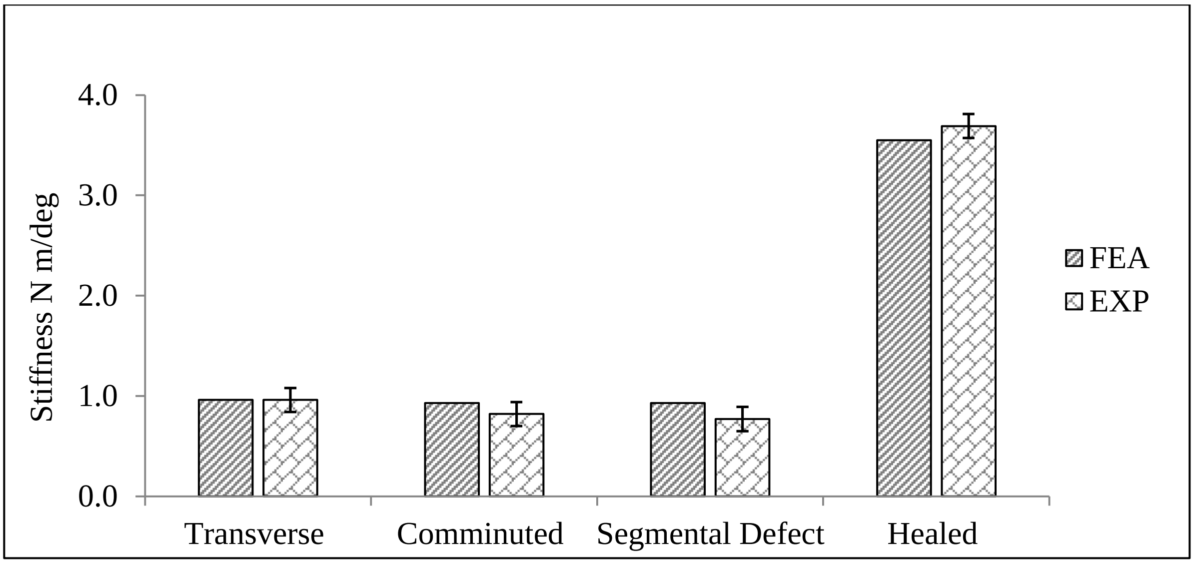

Figure 7-36 Comparison of experimental (EXP) and FEA predicted torsional stiffness (external rotation) of different fracture groups

7.3.7 Other parameters

7.3.7.1 Potential contact area between ALFN and femur

During simulation tests the magnitude and direction of displacement of the ALFN was noted. The proximal portion of the ALFN showed a tendency to displace in the antero-medial direction in response to an axial compression force. (Figure 7-37).

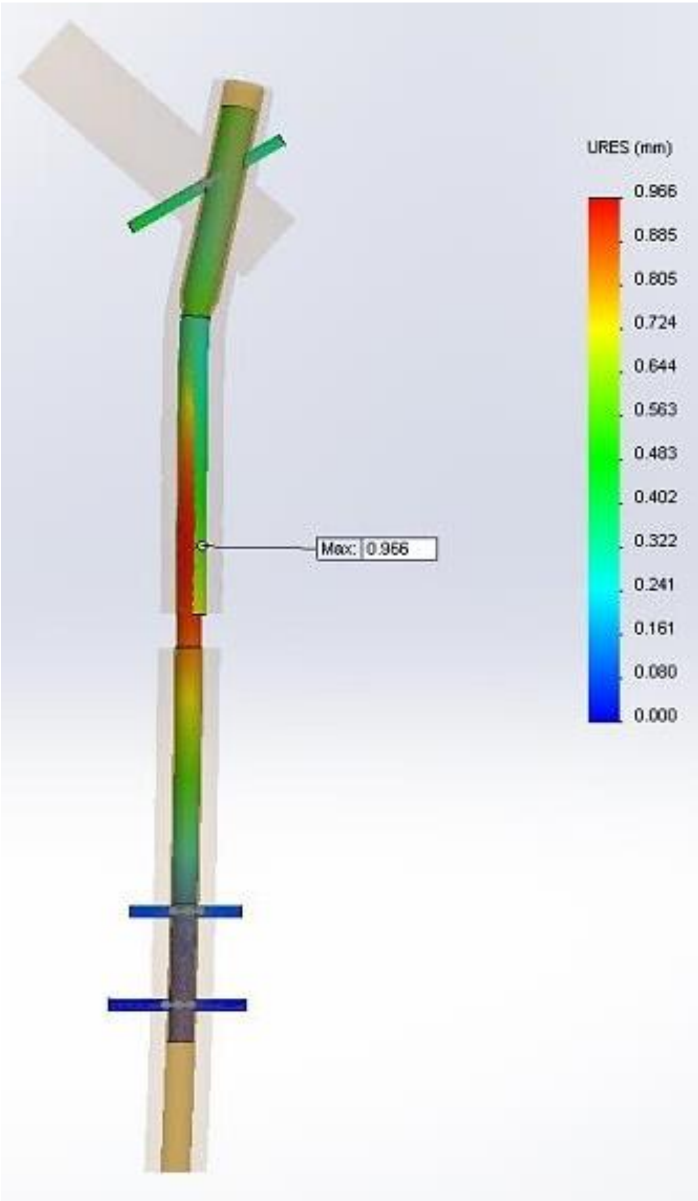

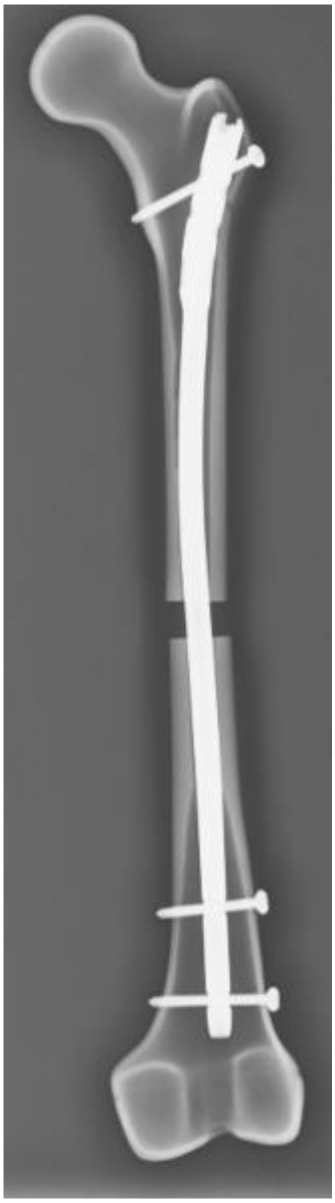

Figure 7-37 Similar region of contact between femur and ALFN (left-FEA model prediction, right-as noted in digital radiograph)

It was noted that in the 'worst case scenario' of a segmental defect at 300 N of compression the maximum displacement of ALFN was 0.966 mm. This resulted in the ALFN contacting the adjacent cancellous bone tissue but not the cortical aspect of the reamed medullary canal (gap between ALFN and reamed medullary canal assumed to be 1.2 mm in FEA model).

Overall the similarity in the displacement behavior of the ALFN during simulation tests and the digital radiographs of the experimental model suggested that the assumptions made in the FEA model were correct. This provided additional validation to the paediatric femur fracture fixation FEA model.

7.3.7.2 Predicted von Mises Stress

The FEA model simulation tests allowed for observation of the site and magnitude of the predicted von Mises stress. The maximum stress ($\sigma_{\upsilon\ \text{Segmental Defect}}$ = 383.6 MPa) was predicted for the segmental defect fracture fixation during axial compression around the proximal interlocking screw (Table 7-1).

Contour plot analysis revealed relatively higher stress in the proximal part of the ALFN in comparison to the distal part (Figure 7-38, Figure 7-39 and Figure 7-40).

Table 7-1 Predicted von Mises stress

T–transverse, C–comminuted, SD–segmental defect, DS1-first distal screw

Simulated Test	**Fracture type**	**Predicted von Mises stress (σ Max)**	
		Site	**MPa**
Axial Compression	T	Proximal interlocking screw	361.50
	C	Proximal interlocking screw	380.30
	SD	Proximal interlocking screw	383.60
Four-point bending	T	DS1 screw hole	37.40
	C	DS1 screw hole	51.39
	SD	DS1 screw hole	64.40
Torsion (internal rotation)	T	DS1 screw hole (posterolateral)	106.79
	C	DS1 screw hole (posterolateral)	115.51
	SD	DS1 screw hole (posterolateral)	115.56
Torsion (external rotation)	T	DS1 screw hole (anterolateral)	122.95
	C	DS1 screw hole (anterolateral)	125.13
	SD	DS1 screw hole (anterolateral)	127.48

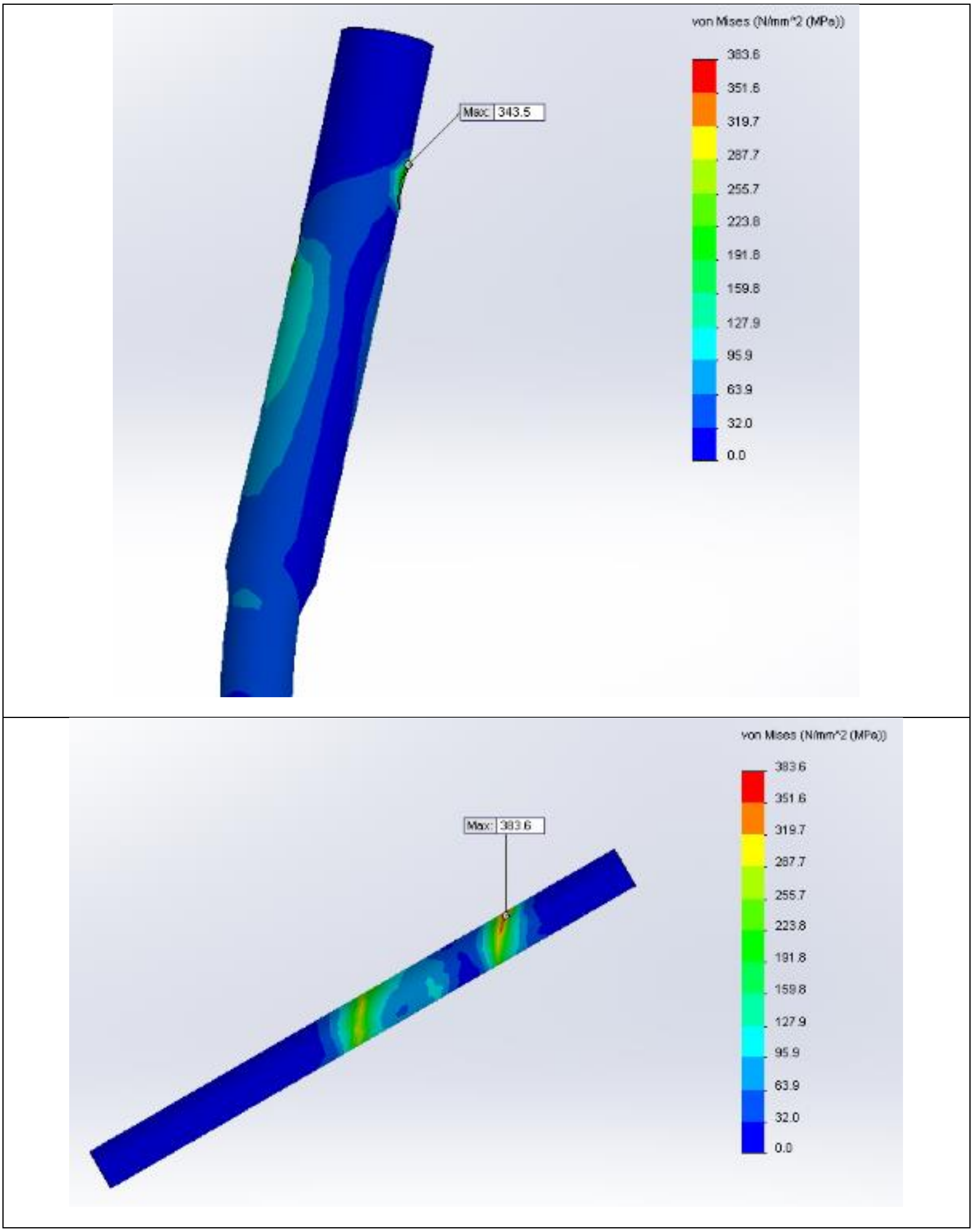

Figure 7-38 Contour plot showing von Mises stress in ALFN for segmental defect fixation (top - proximal interlocking screw hole, bottom - proximal interlocking screw)

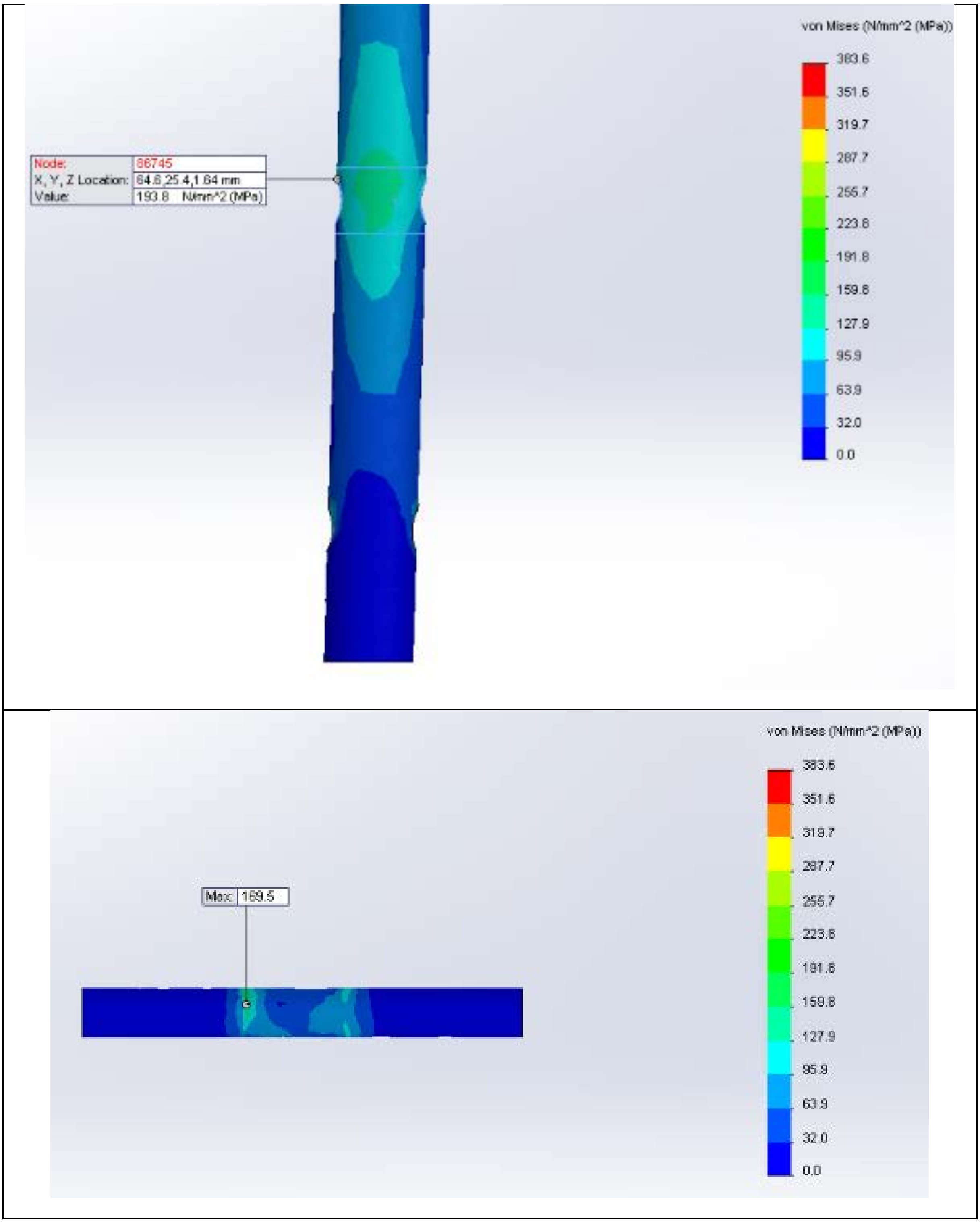

Figure 7-39 Contour plot showing von Mises stress in ALFN for segmental defect fixation (top – first distal interlocking screw hole, bottom – first distal interlocking screw)

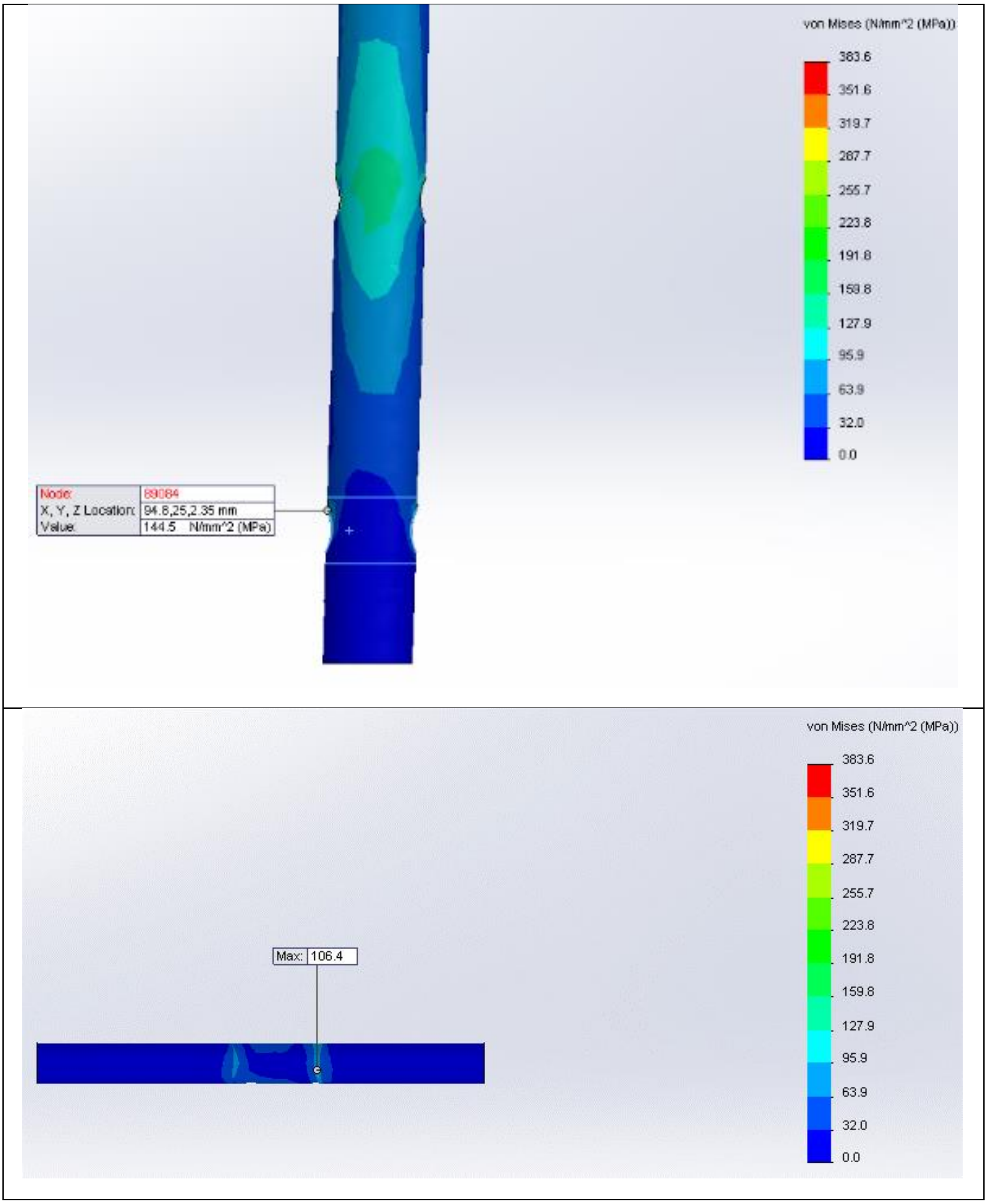

Figure 7-40 Contour plot showing von Mises stress in ALFN for segmental defect fixation (top – second distal interlocking screw hole, bottom – second distal interlocking screw)

7.4 Discussion

Several authors have investigated biomechanical parameters of intramedullary devices used for treating femur fractures using finite element analysis (348, 355, 356, 358, 361, 362, 373, 386, 395, 440, 444-449). However, only a limited number of FEA studies evaluating paediatric femoral fracture fixation exist in the current literature (77, 78). Both the studies evaluated flexible intramedullary nail fixation of paediatric femoral fracture. Perez *et al*. (77) investigated the influence of elastic modulus of two different materials (stainless steel and titanium – type of alloy not reported) on the biomechanical stability of a midshaft transverse fracture having two 3.5 mm flexible nails in a retrograde 'C' pattern. They used gap closure and nail slippage as the outcome measures to assess stability of the construct. They used the femur CAD model available as an open source download (http://www.biomedtown.org) based on the geometry of adult femur (79). Following static analysis, the authors concluded that titanium nails performed better as they slipped less with a gap closure of 0.69 mm in comparison to 1.03 mm noted with stainless steel nails. Additionally they observed that the titanium nails distributed stresses more evenly along the nail axis. Krauze *et al*. (78) compared flexible intramedullary nails of two different materials (316L stainless steel and titanium alloy – Ti-6Al-4V) using a femur FEA model based on a 5-7 year old child. However the details regarding development of the femur FEA model and its dimensions are not provided in the paper. They evaluated oblique fracture at two levels with the fracture located at the midshaft in the first FEA model and in the second model the fracture level was 25 mm proximal. In both these fracture configurations they observed following the FEA that the stresses in both the stainless steel and titanium alloy nails did not exceed the yield point. An important observation in both the aforementioned studies is that the FEA model predictions were not robustly validated against an experimental model. Hence careful interpretation of their results is essential.

Due to proprietary issues specific CAD data was unavailable from the manufacturer for this study. Hence the dimensions from the sample intramedullary nail used in the experimental study and the reference parameters in the manufacturer manual were used whilst creating the CAD model of the ALFN in SolidWorks™. A similar approach has been described by other authors (356, 444, 445). Orthogonal radiographs were used as a template to accurately position the CAD model of the ALFN in the femur. This is vital to accurately replicate laboratory experiments or clinical scenarios (345, 360).

A critical aspect of undertaking FEA of intramedullary nail fixation is to accurately assign the contact / interaction conditions between the nail, interlocking screws and bone (344, 345, 360). Wu *et al*. (372) compared two intramedullary nails for treating subtrochanteric femur fractures using ANSYS software. They assigned special contact elements with a friction factor of 0.3 for the interfaces between the nail and femur. Helwig *et al*. (445) performed FEA of a proximal femur nail (PFN) using ABAQUS software where the threads of neck screw and hip gliding screw were firmly connected with femur by allowing equal displacement for threads and femur. The femur and implant surfaces were defined by gap conditions with no friction allowing relative shifting in the tangential and normal direction with no penetration. In a subsequent study to compare the PFN, Gamma nail and Gliding-Nail a bonded contact was assumed between the distal locking bolt and the nail/femur interfaces (444). Chandrasekaran *et al*. (450) assigned no penetration contact option in ANSYS whilst evaluating a PFN fixation of a subtrochanteric femur fracture. Wang *et al*. (348) investigated the Gamma nail fixation of subtrochanteric femoral fractures using ANSYS software. They used contact elements between screw and Gamma nail and between fracture surfaces whereas the distal locking screws were fully fixed into femoral shaft cortices. On the other hand, Eberle *et al*. (451) investigated Gamma nail fixation with ANSYS software by assuming a bonded contact between screw and femur. They assigned different coefficients of friction (COF) for the screw/nail (COF = 0.38), nail/femur (COF = 0.36) and femur/femur (COF = 0.46) interfaces and contact points. Seral *et al*. (446) compared the PFN with the Gamma nail using ABAQUS software. They assumed that the interface between the femur and the implant was unbonded except medial, lateral and anterior cortex to simulate impingement of the nail. Goffin *et al*. (373) used ABAQUS software to compare the Gamma nail with a sliding hip screw (SHS) for proximal femoral fracture fixation. They assumed the distal screw of the Gamma nail and the screws of the SHS plate to be bonded to the femur. However the interfaces between the bone fragments and the bone and implant were assigned frictional contact with COF ranging from 0.2 (between stainless steel components of SHS) to 0.46 (between bone fragments). Wang *et al*. (447) performed FEA of a proximal femoral nail using ANSYS software to investigate the effect of one and two lag screws in the femoral head. The used 'surface-to-node' contact elements with zero friction to simulate the interaction between the nail and bone, between distal screws and the nail, femoral neck and lag screw.

Cheung *et al*. (356) used ANSYS software to perform FEA of a retrograde intramedullary nail. The retrograde nail screws were coupled to both holes in the femur and constrained for all degrees of freedom. The nail/femur contact condition not stated clearly but it is reported that the nail did not contact the femur during simulation due to 1 mm clearance. Chen *et al*. (414) investigated distal femoral fracture fixation using retrograde intramedullary nail with interlocking screws (3 distal / 2 proximal) using ANSYS software. They assigned bonded contact condition for the screws and no contact condition was simulated between the femur and nail.

Efstathopoulos *et al*. (355) evaluated femur fracture fixation using Fi-Nail by assuming a fully bonded condition between the screws and nail and the nail and femur. However, the software used is not reported. Montanini *et al*. (361) used the Marc software to evaluate the S2 nail (Stryker Trauma GmbH, Germany) using a combination of experimental testing and FEA. The authors state that they 'realistically' modelled the bone/implant interface by assuming a frictionless contact between the nail and reamed canal / between the nail and lag screw. However, it is must be noted that the S2 nail used in their experimental study had no lag screw and the construct consisted of 1 proximal and 2 distal interlocking screws. It is interesting to note that some of the published FEA studies of femoral intramedullary nails have not reported the contact conditions and assumptions used (386, 395, 440). It is evident from the above that there is no clear consensus in the current literature regarding the contact conditions to be used. This may be partly due to the fact that different software have different capabilities and options. Furthermore there is a limited understanding on the precise *in vivo* mechanical behavior at nail/screw, screw/femur and the nail/femur interfaces (249, 345, 452). Hence in the current study the contact conditions were based to simulate the experimental set up.

The type of femur FE model, boundary and loading conditions used during FEA are dictated primarily by the research question(s) of the study (345, 360). The FE model described by Chen *et al*. (414) consisted of the loading fixtures used in the experimental model along with the CAD model of the femur. They performed simulated axial compression and torsion. The femur FE model used by Wu *et al*. (372) was based on 65 year old woman whereas the femur FE model in the study by Helwig *et al*. (445) was based on CT reconstruction but there is no demographic data provided. In both these studies only simulated axial compression was performed. However, they did not undertake any experimental study to validate the femur FE model. Wang *et al*. (348) used a 3D simplified femur model and applied a combination of loads to simulate one-legged stance and stair-climbing. Eberle *et al*. (451) used a digital model of a composite femur to perform axial compression. The femur FE model described by

Efstathopoulos *et al*. (355) consisted of a simplified straight cylinder which was used to perform torsion and bending tests. Seral *et al*. (446) used a surface femur FE model based on a 76 year old woman to simulate the stance phase of gait cycle. Goffin *et al*. (373) used the femur model available from Biomechanics European Laboratory (BEL) repository (www.biomedtown.org) to perform axial compression to simulate walking cycle of a 80 kg person but a corresponding experimental validation was not undertaken. Similarly Chandrasekaran *et al*. (450) used the femur model from the aforementioned website to perform FEA without experimental validation. Wang *et al*. (447) developed a simplified femur FE model to perform simulated bending and torsion tests. Rankovic *et al*. (386) used a straight cylinder femur FE model to undertake axial compression test but without any experimental validation. Cheung *et al*. (356) developed a femur FE model based on the geometry of third generation composite femur to perform simulated loading to represent the late stance and swing phases of gait cycle. They validated the femur FE model with strain values obtained from an experimental model subjected to 600 N axial load. For their study, Montanini *et al*. (361) also used the femur FE model from BEL repository and performed axial compression and simulated walking. This femur FE model was validated using composite femur. In the current study, the femur FE model based on a simplified geometry of a paediatric femur was versatile and allowed all the loading modes (axial compression / bending / torsion) to be evaluated.

It has been reported that the Pearson coefficient of determination (R^2) is a good indicator of correlation between experimental and FEA data (360). There is high correlation if $0.8 < R^2 < 1$. The R^2 value ranged from a low of 0.82 (internal rotation of segmental defect FEA model) to a high of 0.99 (axial compression of segmental defect FEA model and four-point bending of healed fracture FEA model). The relative error between the experimental stiffness (k_{EXP}) and the FEA predicted stiffness (k_{FEA}) ranged from low (internal rotation of healed = -7.83%) to high (external rotation of segmental defect = +20.87%). These results are comparable with the other FEA studies in the literature (361, 368, 378, 413, 414). It is interesting to note that the loading modes with the maximum and minimum relative error also represent the extreme ends of the spectrum in terms of loading mode and fracture configuration. Overall there was good agreement between the experimental data and the FEA model predictions across the different loading modes investigated.

Mesh control was used to refine mesh in areas anticipated to have high stress (356, 360). A direct comparison of the predicted stress values of ALFN cannot be made with the other studies in terms of the absolute values due to the aforementioned reasons. However the location of the maximum predicted von Mises stress in the ALFN is comparable to the FEA studies of femoral intramedullary nails in the literature (360, 361, 444).

7.5 Summary

A paediatric femur fracture fixation FEA model was developed using SolidWorks™ for three different fracture configurations (transverse / comminuted / segmental defect). Successful validation of the FEA models was performed by comparing the simulation test results with the corresponding experimental data using linear regression analysis and relative error estimation. Thus a validated FEA model was produced for each of the fracture configurations from the basic assembly of the CAD models of the ALFN, interlocking screws and the reamed femur.

This validated FEA model was versatile as it allowed simulation tests to be performed across different loading conditions as described earlier. Additionally it provided scope for variation of parameters to investigate the effect of routine clinical factors (fracture level and geometry / fracture healing) and implant design on stiffness. Evaluation of these factors is described in the next chapter.

8 EFFECT OF ROUTINE CLINICAL FACTORS

8.1 Introduction

Femoral fractures in adolescents can present with different patterns and locations (453). Whilst transverse fracture in the midshaft is a common presentation mode, oblique, spiral fractures and fractures of the proximal and distal third regions of the femoral shaft are not uncommon (1, 6, 23, 34, 454). Additionally the orthopaedic surgeon treating patients with these injuries with intramedullary nail fixation has to carefully consider certain implant parameters as they have implications for fracture healing and clinical outcomes (3, 5, 241). This chapter describes the use of the validated FEA model of paediatric femur fracture fixation with ALFN to evaluate some of the commonly encountered clinical factors viz. fracture level and geometry, fracture healing and implant parameters.

8.2 Materials and methods

8.2.1 Fracture level and geometry

In order to study some of the common presentations the sketch used to create the transverse fracture (gap = 1 mm) described above was moved to the proximal and distal third regions of the reamed femur CAD model. Using the 'cut extrude' command femur, CAD models with transverse fracture in the proximal and distal third regions of the femur, respectively, were obtained. The proximal and distal third fractures were created at a distance of 116.66 mm from the tip of the greater trochanter and the distal aspect of the femur respectively (Figure 8-1). This level corresponded to a third of the length of the femoral shaft of the composite femur which measured approximately 350 mm.

The sketch parameters were varied to create an oblique fracture (fracture angle = 45°, gap = 1 mm). The 3D spline sketch feature available in SolidWorks™ (455, 456) was used to create complex fracture geometry like a spiral fracture spanning 20 mm (Figure 8-3). Simulation tests were performed on the above variants of the FEA model similar to those described in chapter 7.

Using the segmental fracture FEA model, the variation in the predicted von Mises stress in the three interlocking screws and the corresponding holes in the ALFN in response to an axial compressive force of 300 N was investigated by varying the distance between the fracture margin and the first distal screw (DS1 screw) from 10 mm to 150 mm.

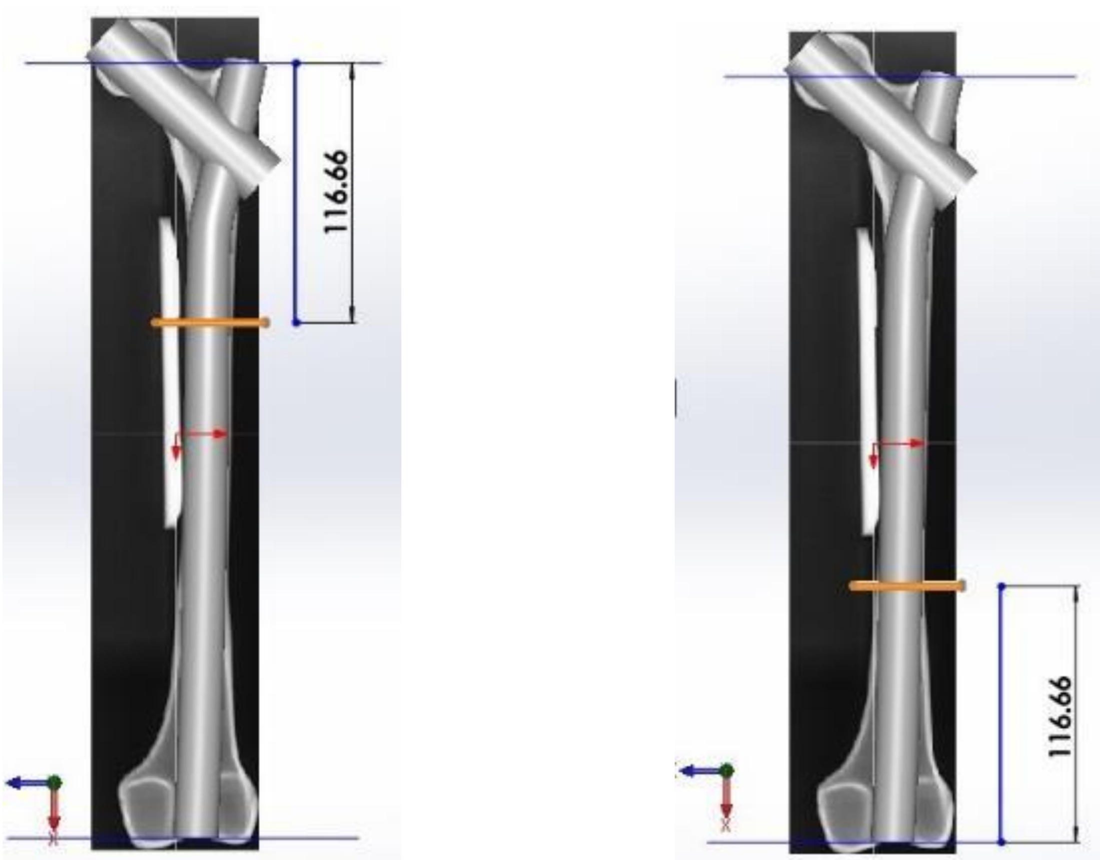

Figure 8-1 Simulated transverse shaft fractures of proximal (left) and distal third (right)

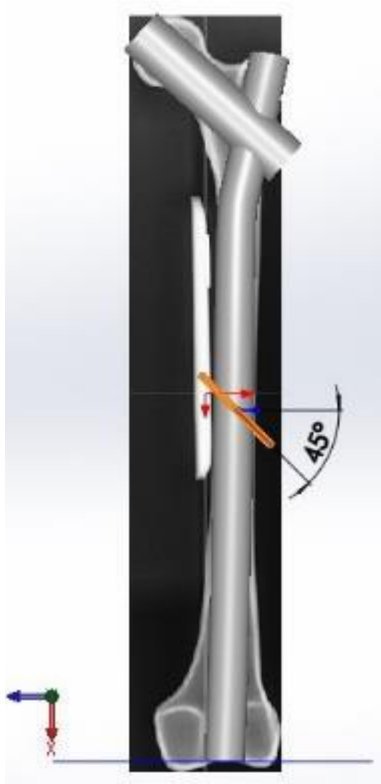

Figure 8-2 Simulated oblique fracture in the midshaft region

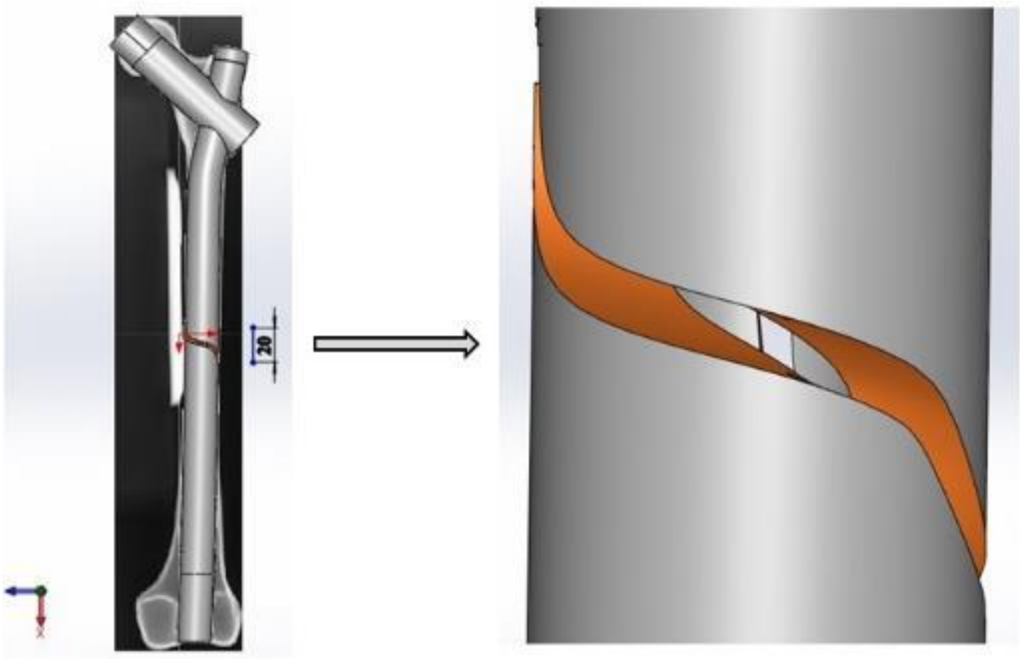

Figure 8-3 Simulated spiral fracture of the midshaft (left) and magnified view (right)

8.2.2 Fracture healing

In the segmental defect FEA model an interpositional section (callus tissue) was introduced at the fracture site using the assembly function (432, 433) (Figure 8-4). Material properties of the elements in this section were then independently varied in relation to the rest of the femur CAD model during simulation tests to study the effect of fracture healing on the overall stiffness parameters and the maximum predicted von Mises stress values (σ_{υ} in MPa) (268).

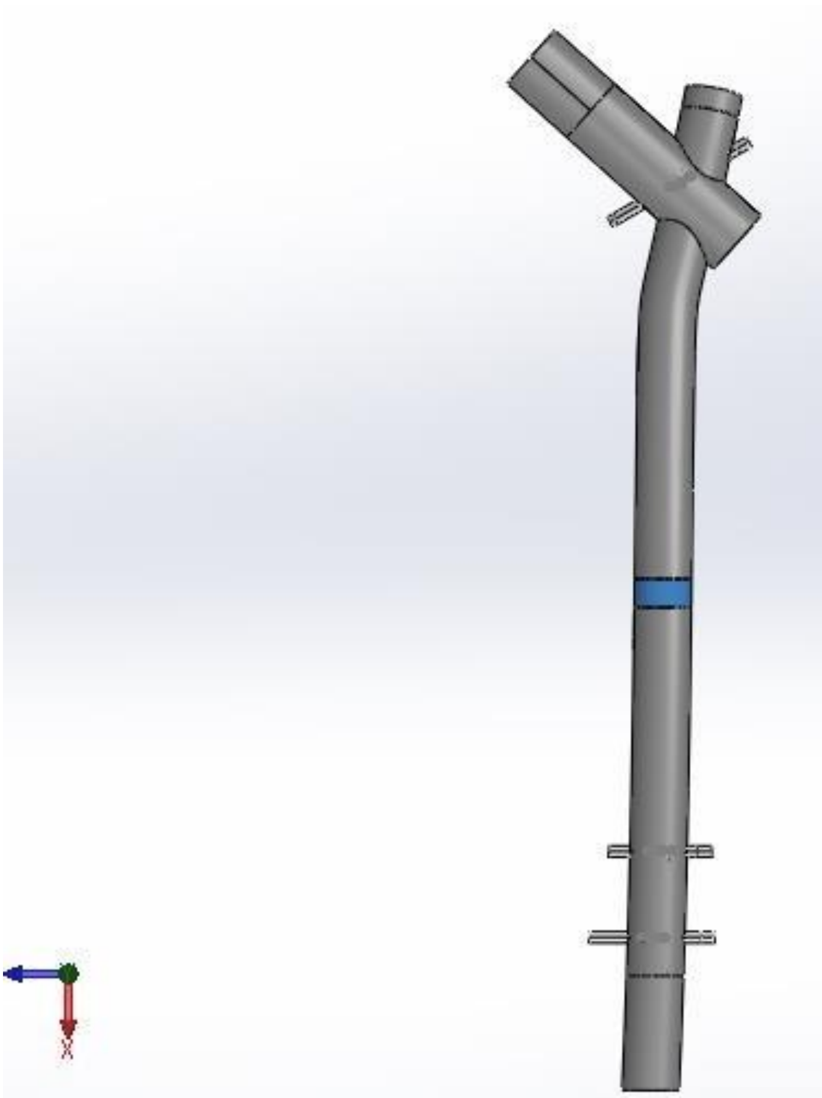

Figure 8-4 Segmental defect FEA model with simulated callus

Simulation of fracture healing was performed over a period of 4-16 weeks post injury. The material properties assigned to the callus tissue at different stages were based on the values available in the current literature (100, 457) and are listed below (Table 8-1).

Table 8-1 Material properties of callus tissue (100, 457)

Callus Tissue	Elastic Modulus (MPa)	Poisson's Ratio
4 weeks	0.19	0.30
8 weeks	28	0.30
12 weeks	30	0.30
16 weeks	75	0.30

A maximum axial compressive force of 300 N (equivalent of a 60 kg patient with 50% partial weight bearing) at 30 N increments was simulated. The resultant displacement and the maximum von Mises stress values were noted for each stage of fracture healing.

8.2.3 Variation in implant parameters

The relative influence of different implant parameters of ALFN on the maximum predicted von Mises stress was studied using the above FEA model. Common design parameters of an intramedullary nail system (viz. material, interlocking screw diameter, relative angle between nail and interlocking screw and nail thickness) were objectively varied based on a Taguchi L9 orthogonal array (458-461). The L9 orthogonal array allowed evaluation of the above four parameters at three levels (460, 462). In total a set of nine simulated experiments were performed with the nine variations of the above FEA model (Table 8-2).

Table 8-2 Variation of implant parameters

Experiment	Proximal Screw / ALFN Relative Angle (°)	Proximal Screw Diameter (mm)	Material	Proximal Wall Thickness (mm)
1	110	3.6	Titanium	2.85
2	110	4.0	Ti-6Al-7Nb	2.95
3	110	4.4	316L Stainless Steel	3.05
4	120	3.6	Ti-6Al-7Nb	3.05
5	120	4.0	316L Stainless Steel	2.85
6	120	4.4	Titanium	2.95
7	130	3.6	316L Stainless Steel	2.95
8	130	4.0	Titanium	3.05
9	130	4.4	Ti-6Al-7Nb	2.85

The material properties used for the different FEA models of the nail and interlocking screws are listed below in Table 8-3.

Table 8-3 Material properties used for intramedullary nail and interlocking screws

Material	Mass Density (kg/m^3)	Elastic Modulus (MPa)	Ultimate Tensile Strength (MPa)	Yield Strength (MPa)	Poisson's Ratio
Titanium	4600	110000	235	140	0.30
Ti-6Al-7Nb	4520	105000	900	800	0.30
316L Stainless Steel	8027	200000	485	170	0.26

The predicted von Mises stress values (σ_υ in MPa) in the proximal portion ALFN and the proximal interlocking screw in response to an axial compression force of 300 N was chosen as the outcome measure. During simulation tests, the σ_υ was noted for each of the nine FEA models. Using the 'smaller is better' type of Taguchi analysis the optimum level for each of the implant parameters (with respect to von Mises stress) was identified (458, 459). Subsequently a final variant of the FEA model was developed for a Ti-6Al-7Nb alloy nail with the optimum implant parameters identified earlier. A final simulation was then performed using this FEA model to test the hypothesis and confirm the reduction in σ_υ (458).

A schematic illustration of the factors evaluated using the validated paediatric femur fracture fixation FEA model is shown below in Figure 8-5.

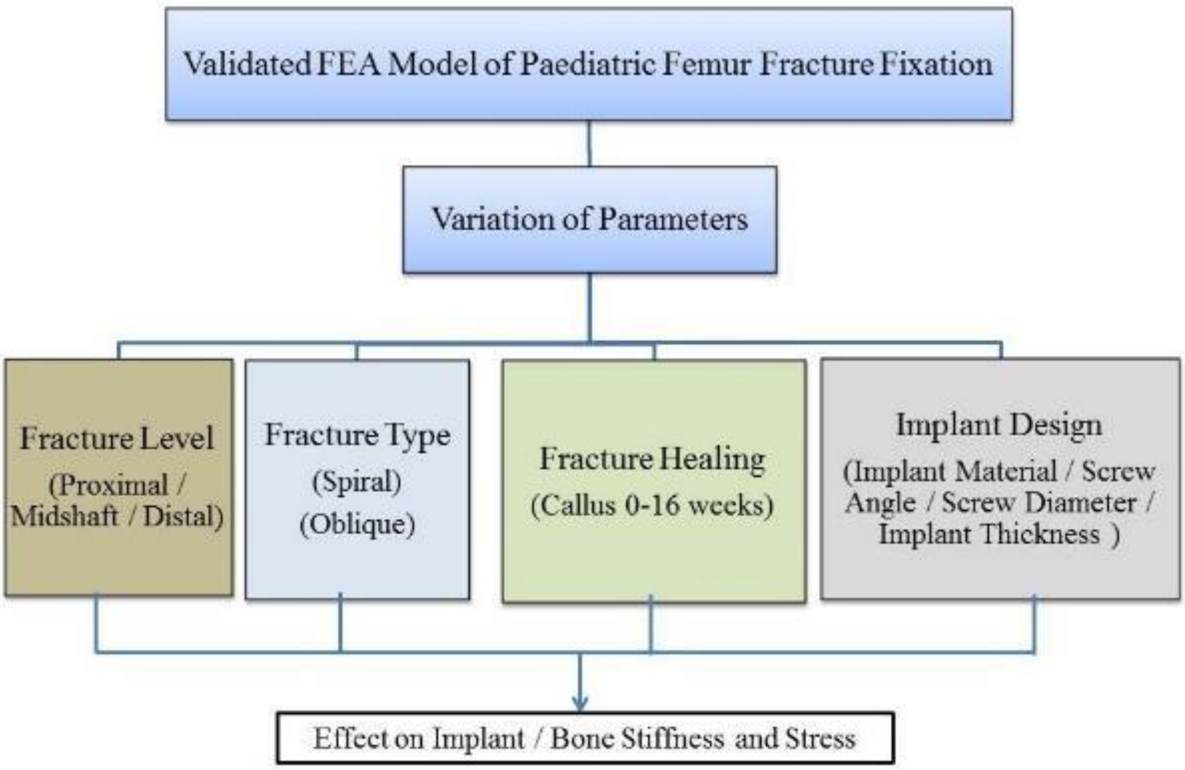

Figure 8-5 Evaluation of factors using validated FEA model

8.2.4 Data Analysis

The simulated load and resultant displacement results were entered into a spreadsheet (Microsoft Excel 2010). Stiffness was determined from the slope of the load-displacement graph, as described earlier in chapter 4. The relative influence of the different implant parameters on the predicted von Mises stress was investigated using the Taguchi method (462, 463). Minitab® statistical software (version 16, Minitab, Inc. Coventry, UK) was used to assign the factors of interest into three levels based on L9 orthogonal array (Table 8-4). The maximum predicted von Mises stress (σ_υ) for each of the nine FEA models described above was noted.

Table 8-4 Investigated implant parameters and Taguchi method levels

Factors	Level 1	Level 2	Level 3
Proximal Screw / ALFN Relative Angle (°)	110	120	130
Proximal Screw Diameter (mm)	3.6	4.0	4.4
Material	Titanium	Ti-6Al-7Nb	316L Stainless Steel
Proximal Wall Thickness (mm)	2.85	2.95	3.05

In the Taguchi method the scatter around the target value is expressed as the signal-to-noise ratio (*S/N*) (463-465). The investigated parameter (viz. predicted von Mises stress) is considered as the signal whereas the noise is due to variations in output or uncontrollable factors (466, 467). The main effects at each level of all investigated parameters on the von Mises stress were computed (459). Analysis was performed in Minitab® using the 'smaller is better' principle (468) with respect to von Mises stress. Subsequently the optimum level of each parameter identified using the Taguchi method was used to develop a novel FEA model and the simulation test was repeated to confirm the actual reduction in the predicted von Mises stress (458, 469).

8.3 Results

The results of variation in fracture level and geometry are presented in Table 8-5.

8.3.1 Effect of fracture level and geometry

Table 8-5 FEA model predicted stiffness for different fracture levels and fracture geometry (axial compression force – 300 N / four-point bending force - 60 N / torque – 2 N m)

	Axial Stiffness (N/mm)	Four point Bending Stiffness (N/mm)	Torsional Stiffness Internal Rotation (N m/deg)	Torsional Stiffness External Rotation (N m/deg)
Fracture Level				
Proximal Third	601.34	93.55	0.95	0.96
Midshaft	611.34	111.11	0.96	0.96
Distal Third	602.34	112.36	0.94	0.94
Fracture Type				
Spiral	576.92	102.04	0.94	0.94
Oblique	623.01	95.74	0.96	0.96

The effect of variation in the distance between the fracture margin and the DS1 screw on the σ_υ in the proximal and distal interlocking zones of the ALFN is shown in Figure 8-6.

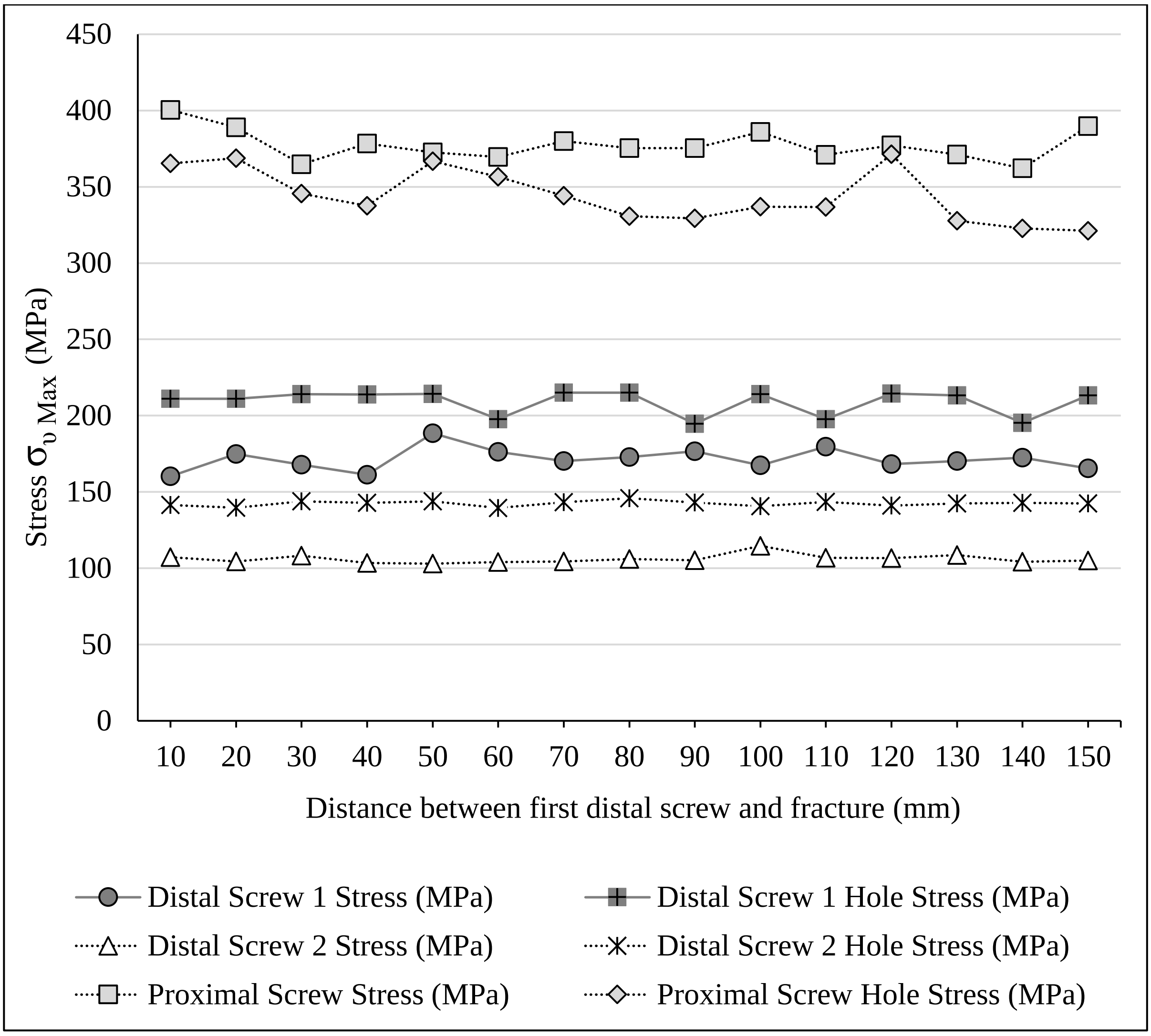

Figure 8-6 Predicted maximum von Mises stress (in response to static axial load of 300 N) with variation in fracture level

Overall the σ_{υ} was noted to remain within a finite range in the three interlocking zones (proximal – 321.20-400.36 MPa / DS1 – 160.25-215.13 MPa / DS2 – 103.00-145.89 MPa).

8.3.2 Effect of fracture healing

The variation in the maximum predicted von Mises stress and the stiffness during fracture healing is presented in Figure 8-7, Figure 8-8, Figure 8-9 and Figure 8-10 below.

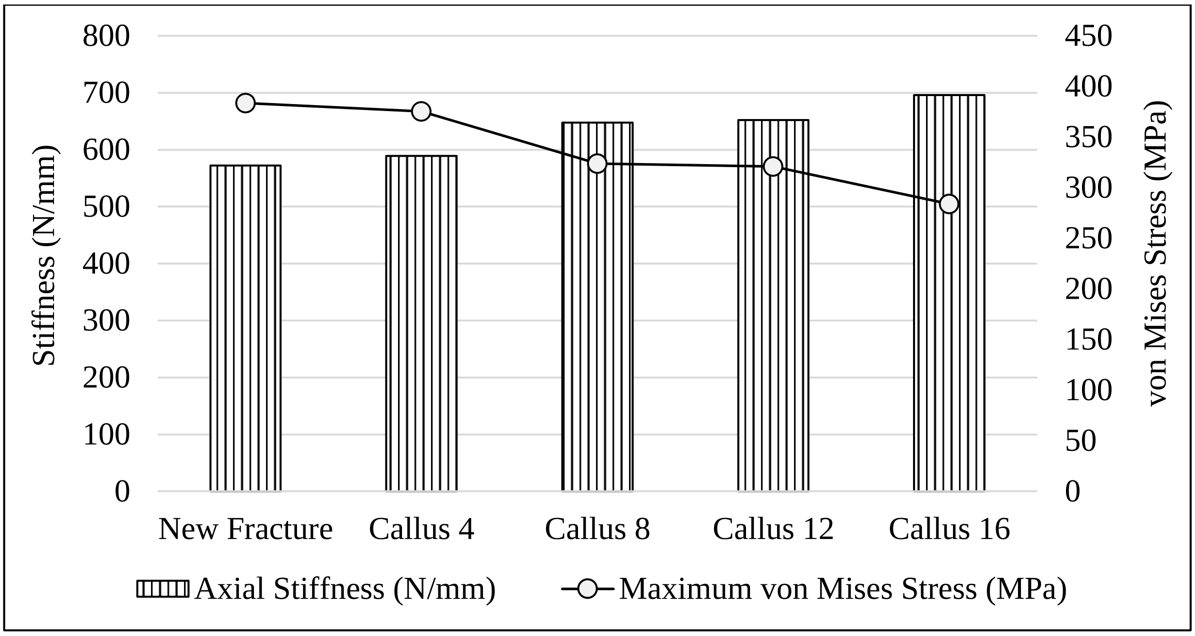

Figure 8-7 Variation of axial stiffness and von Mises stress during fracture healing

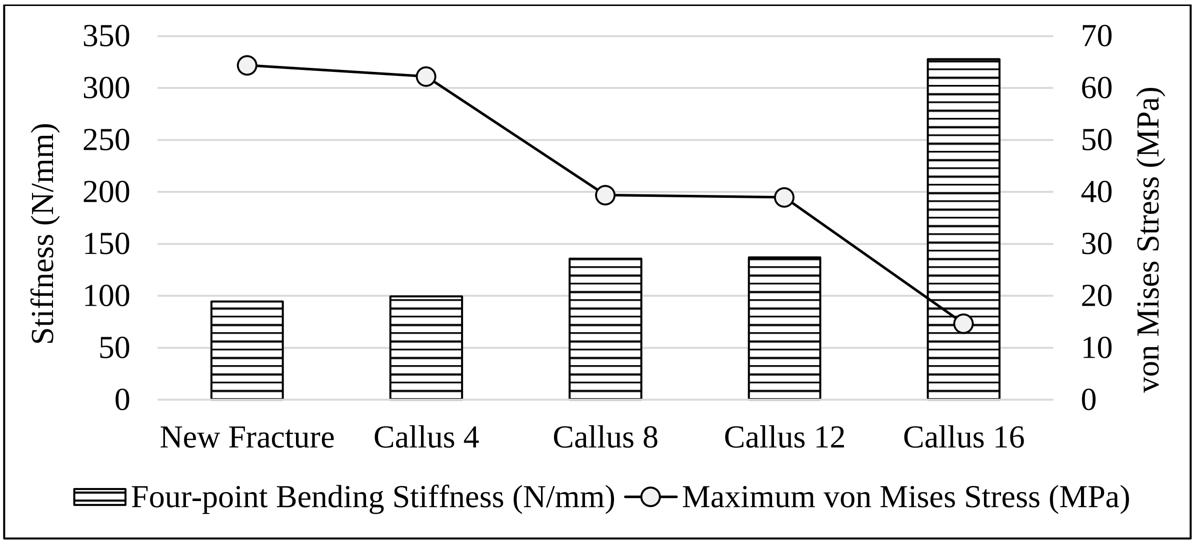

Figure 8-8 Variation of four-point bending stiffness and von Mises stress during fracture healing

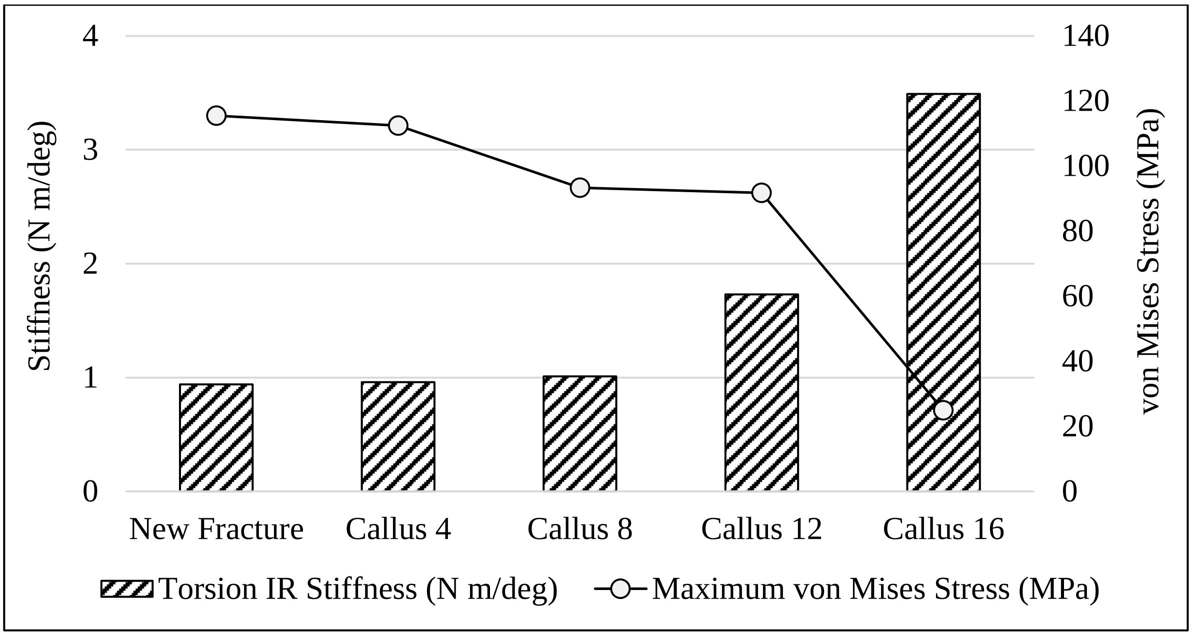

Figure 8-9 Variation of torsional stiffness (internal rotation) and von Mises stress during fracture healing

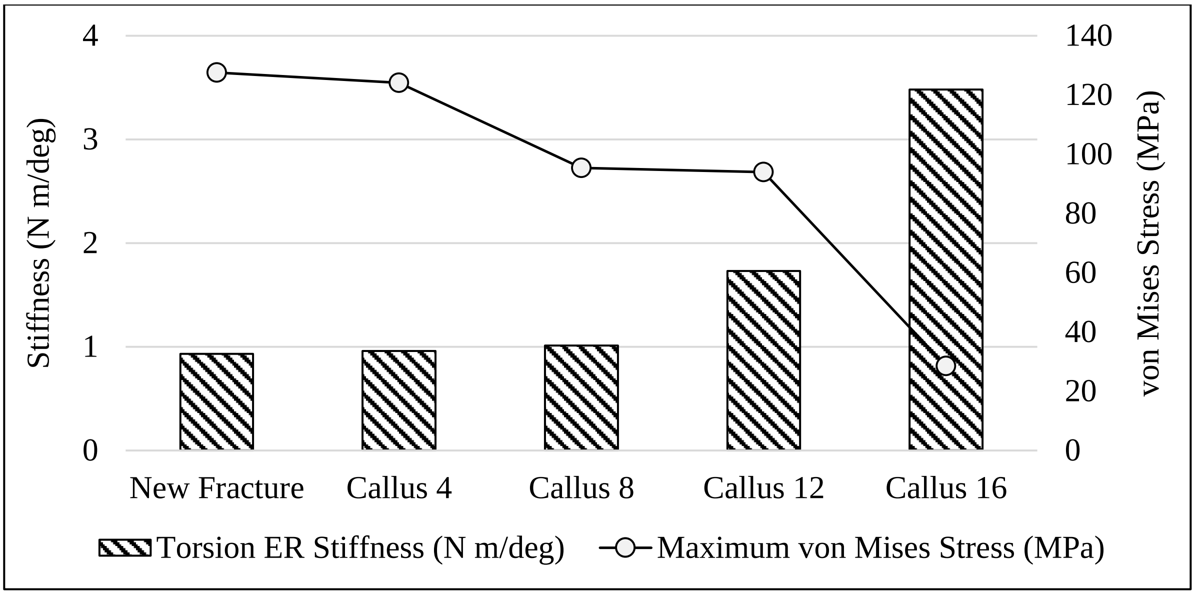

Figure 8-10 Variation of torsional stiffness (external rotation) and von Mises stress during fracture healing

Overall the maximum predicted von Mises stress values in the ALFN showed a downward trend as the fracture consolidated. During early stages of fracture healing, the callus tissue deformed under the simulated axial load of 300 N (Figure 8-11). The FE model predicted a relative decrease in the deformation of the callus tissue as the fracture healing progressed from 4-16 weeks (Figure 8-12 and Figure 8-13). Additionally, the maximum displacement of the ALFN within the medullary canal in response to the simulated load (300 N) reduced as the fracture healed (Figure 8-11, Figure 8-12 and Figure 8-13). This suggested a shift in the load bearing pattern from the ALFN towards the femur as the fracture united.

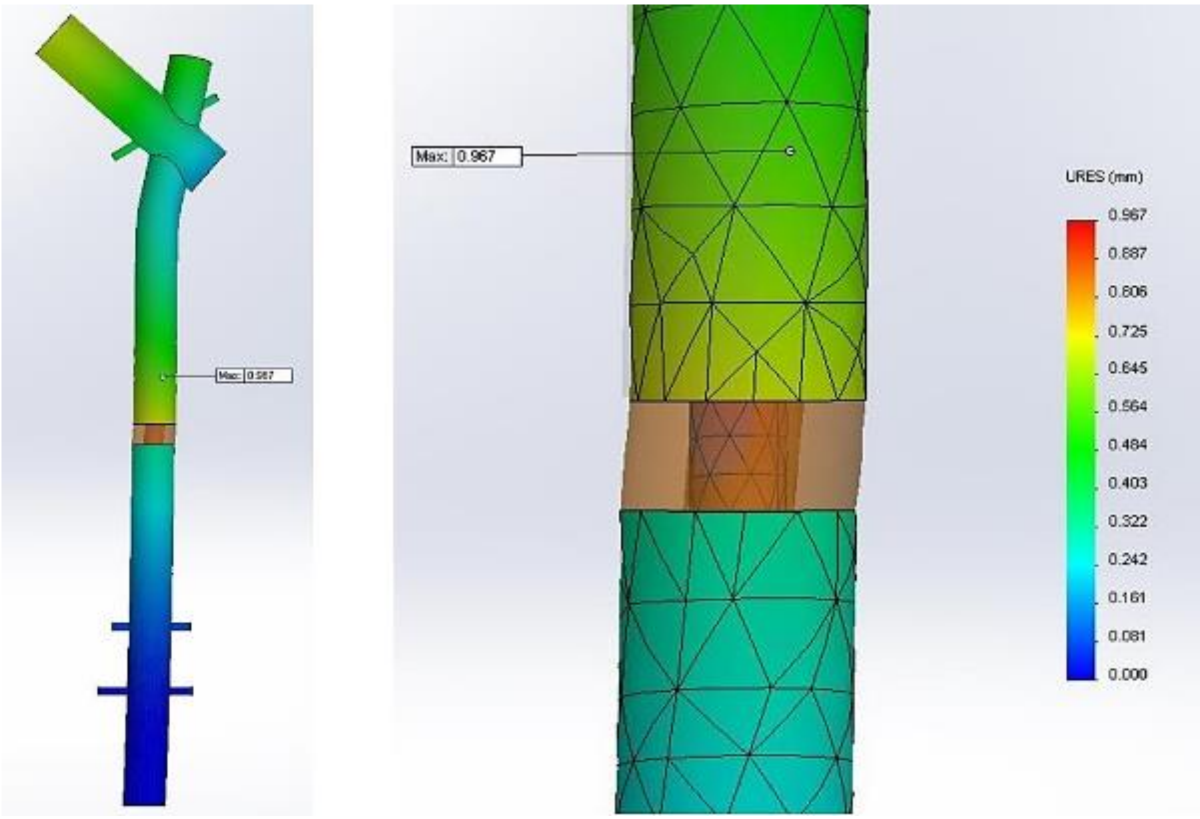

Figure 8-11 Predicted deformation of callus tissue at 4 weeks under axial compression force of 300 N (left - FEA model, right - magnified view showing the outer surface of ALFN coming in contact with callus tissue)

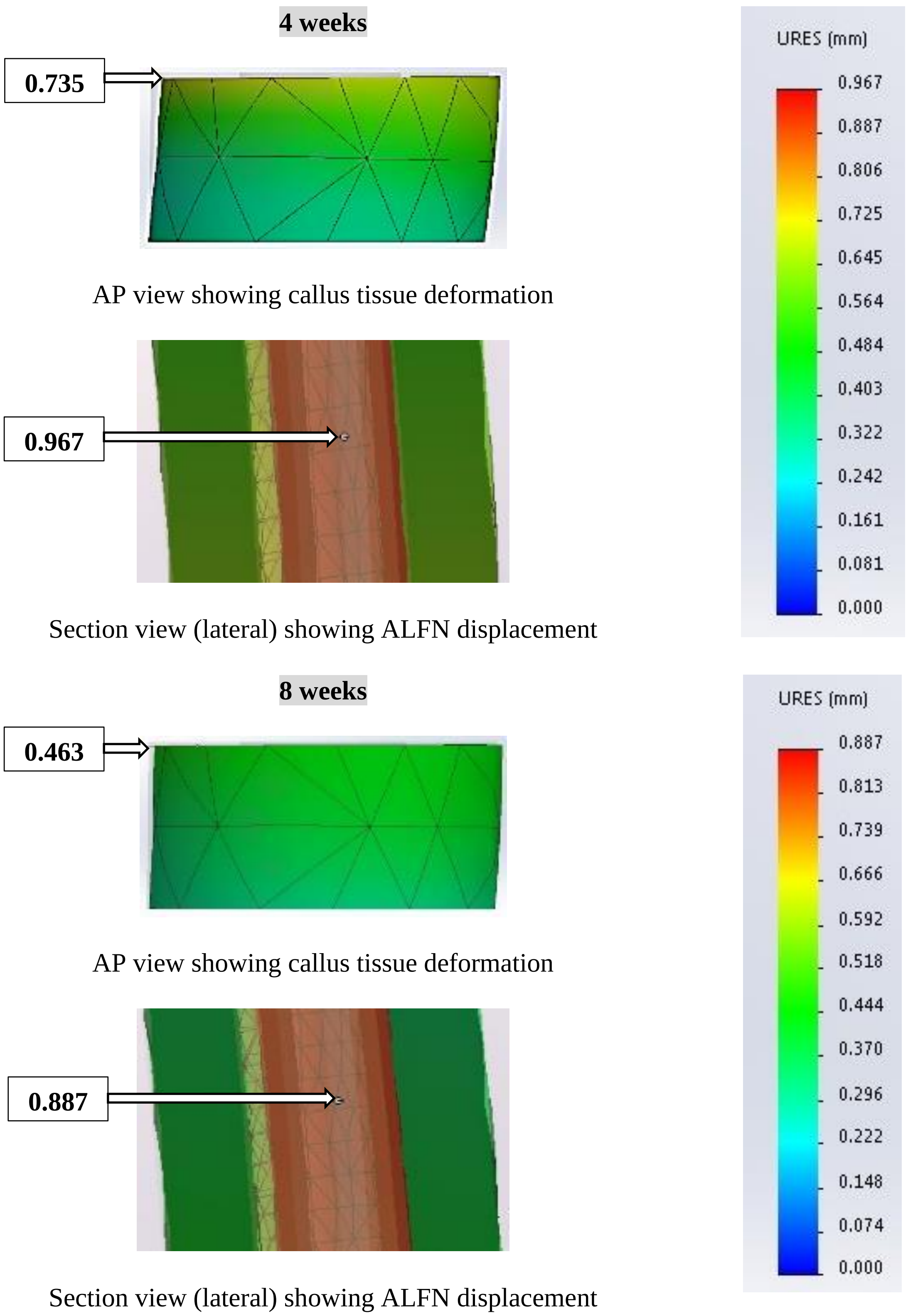

Figure 8-12 Comparison of callus tissue deformation and ALFN displacement during fracture healing (AP-anteroposterior)

12 weeks

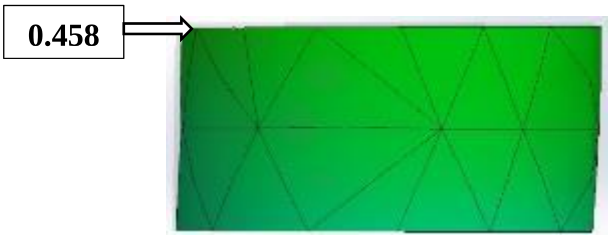

AP view showing callus tissue deformation

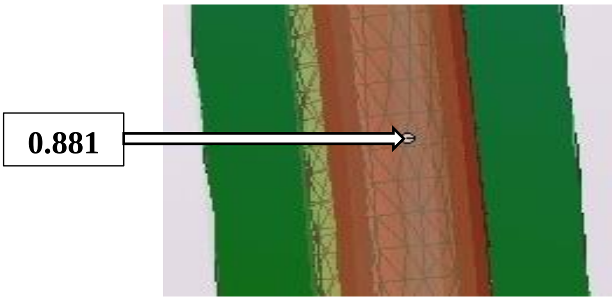

Section view (lateral) showing ALFN displacement

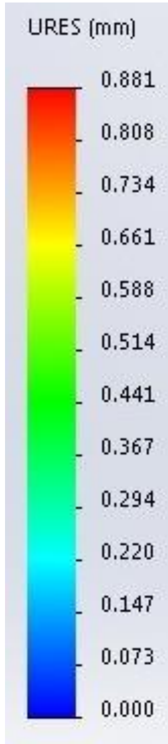

16 weeks

AP view showing callus tissue deformation

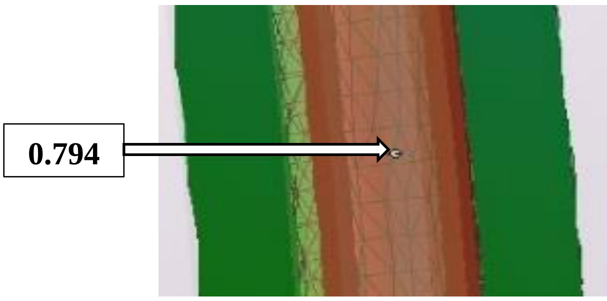

Section view (lateral) showing ALFN displacement

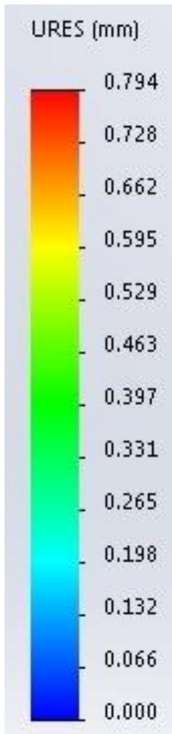

Figure 8-13 Comparison of callus tissue deformation and ALFN displacement during fracture healing (AP-anteroposterior)

8.3.3 Effect of implant parameters

The predicted von Mises stress in the proximal interlocking zone for the nine FEA models based on L9 Taguchi orthogonal array is displayed below in Figure 8-14.

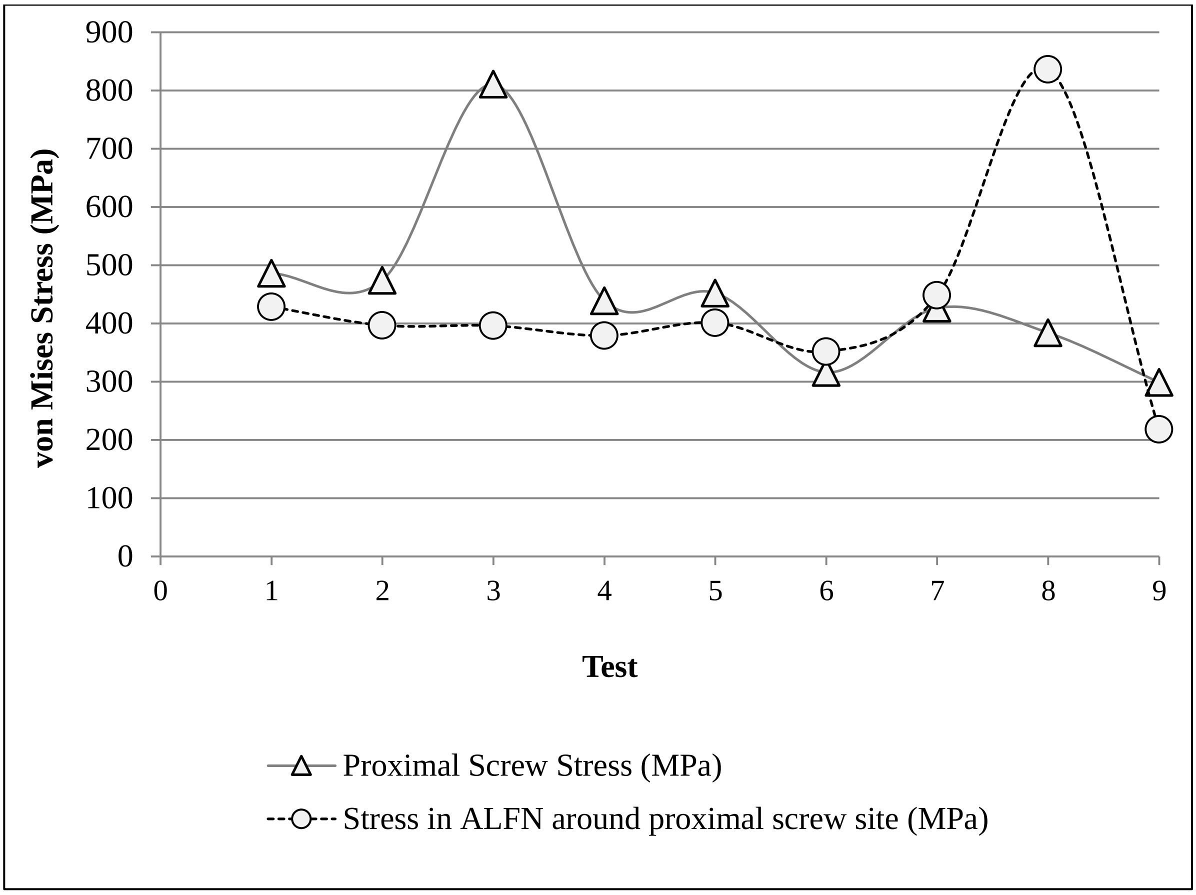

Figure 8-14 Predicted stress values of the nine FEA models

The results of 'smaller-is-better' analysis are shown in Figure 8-15 and Table 8-6. The relative angle between the ALFN and the proximal interlocking screw contributed the most with a delta value of 3.88. Amongst these the highest *S/N* ratio (-51.27) was noted at 130° with 120° being fairly close with *S/N* ratio (-51.99). The nail material was noted to be second most important factor (delta = 2.82) with both titanium and Ti-6Al-7Nb having similar *S/N* ratio at -51.81 and -51.96 respectively. Contour plot analysis comparing predicted von Mises stress in the ALFN and Ti-6Al-7Nb nail with optimum parameters identified with Taguchi method are shown in Figure 8-16, Figure 8-17, Figure 8-18, Figure 8-19, Figure 8-20 and Figure 8-21.

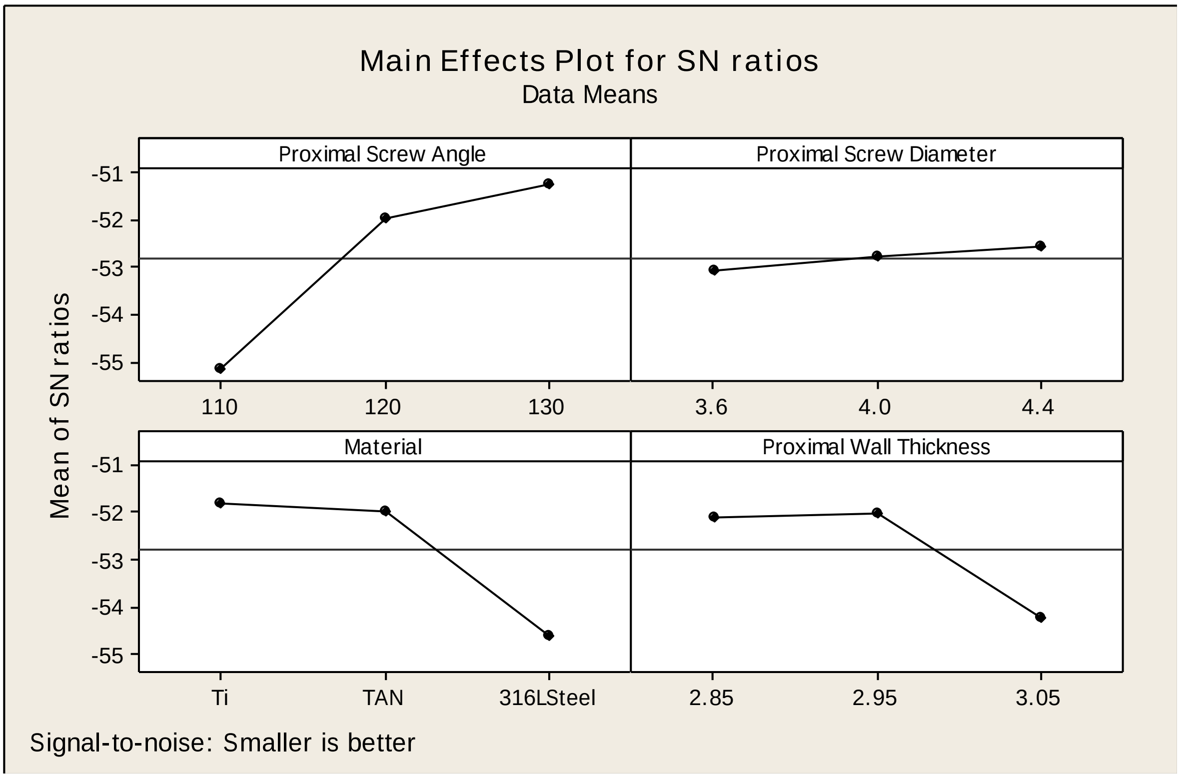

Figure 8-15 Taguchi analysis (smaller is better) based on predicted von Mises stress

Table 8-6 Taguchi analysis showing effect of each implant parameter on the maximum predicted von Mises stress

Level	Relative Angle Between ALFN and Proximal Screw	Proximal Screw Diameter	Material	Proximal Wall Thickness
1	-55.15	-53.06	-51.81	-52.12
2	-51.99	-52.77	-51.96	-52.04
3	-51.27	-52.56	-54.63	-54.24
Delta	3.88	0.50	2.82	2.20
Rank	1	4	2	3

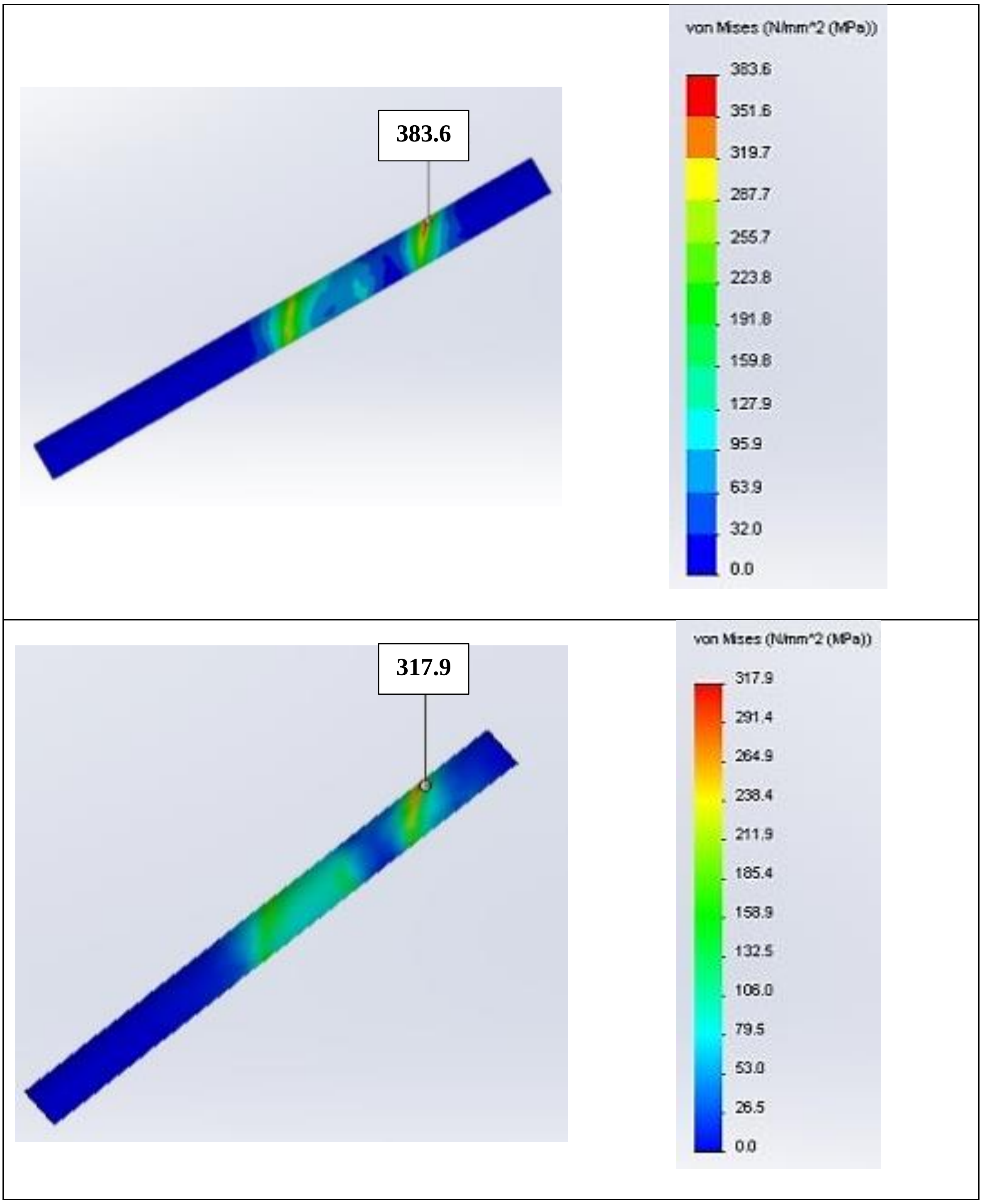

Figure 8-16 Contour plot showing maximum von Mises stress in proximal screw (top – ALFN, bottom – Ti-6Al-7Nb nail with optimum parameters identified with Taguchi method

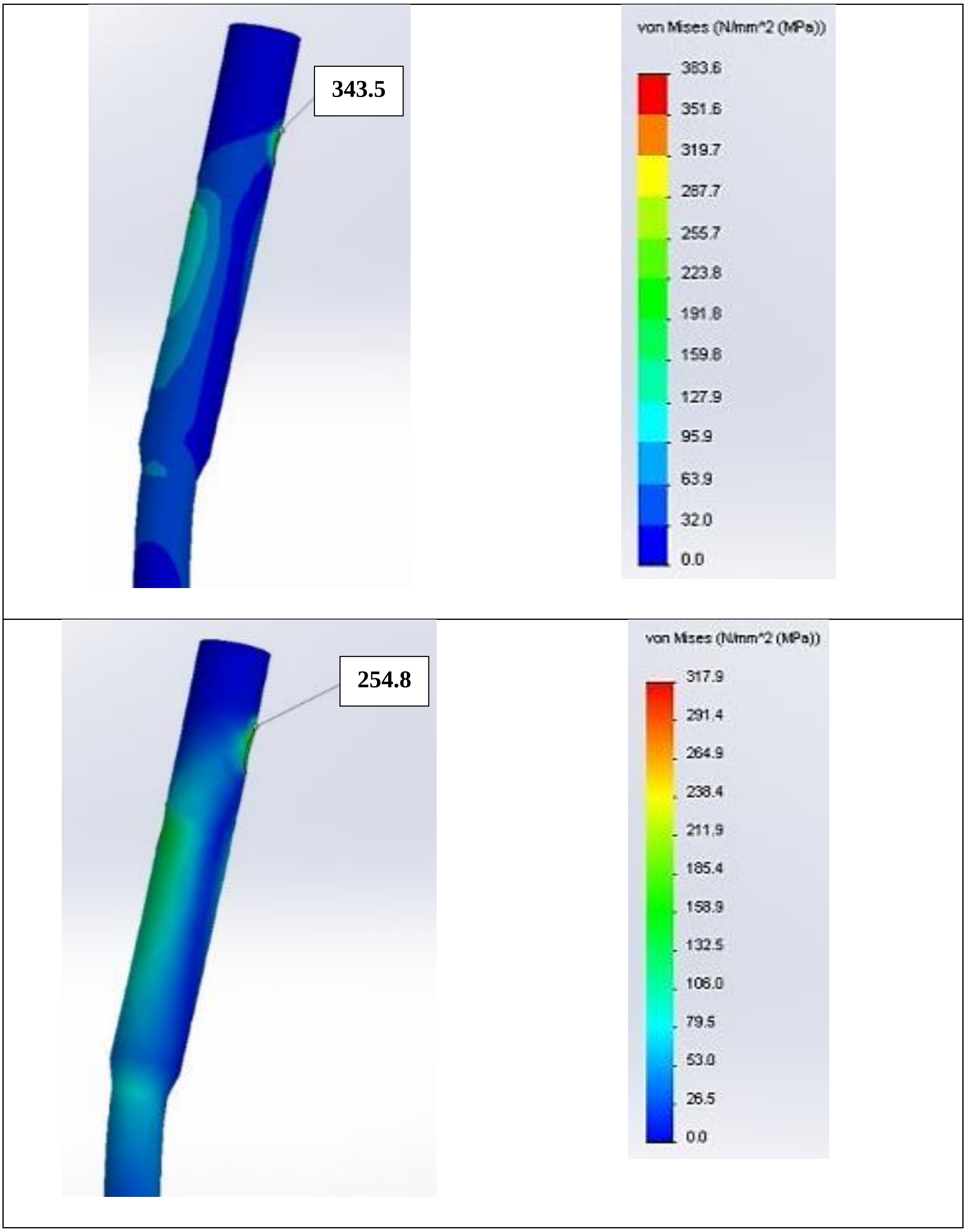

Figure 8-17 Contour plot showing maximum von Mises stress in proximal interlocking screw hole (top – ALFN, bottom – Ti-6Al-7Nb nail with optimum parameters identified with Taguchi method

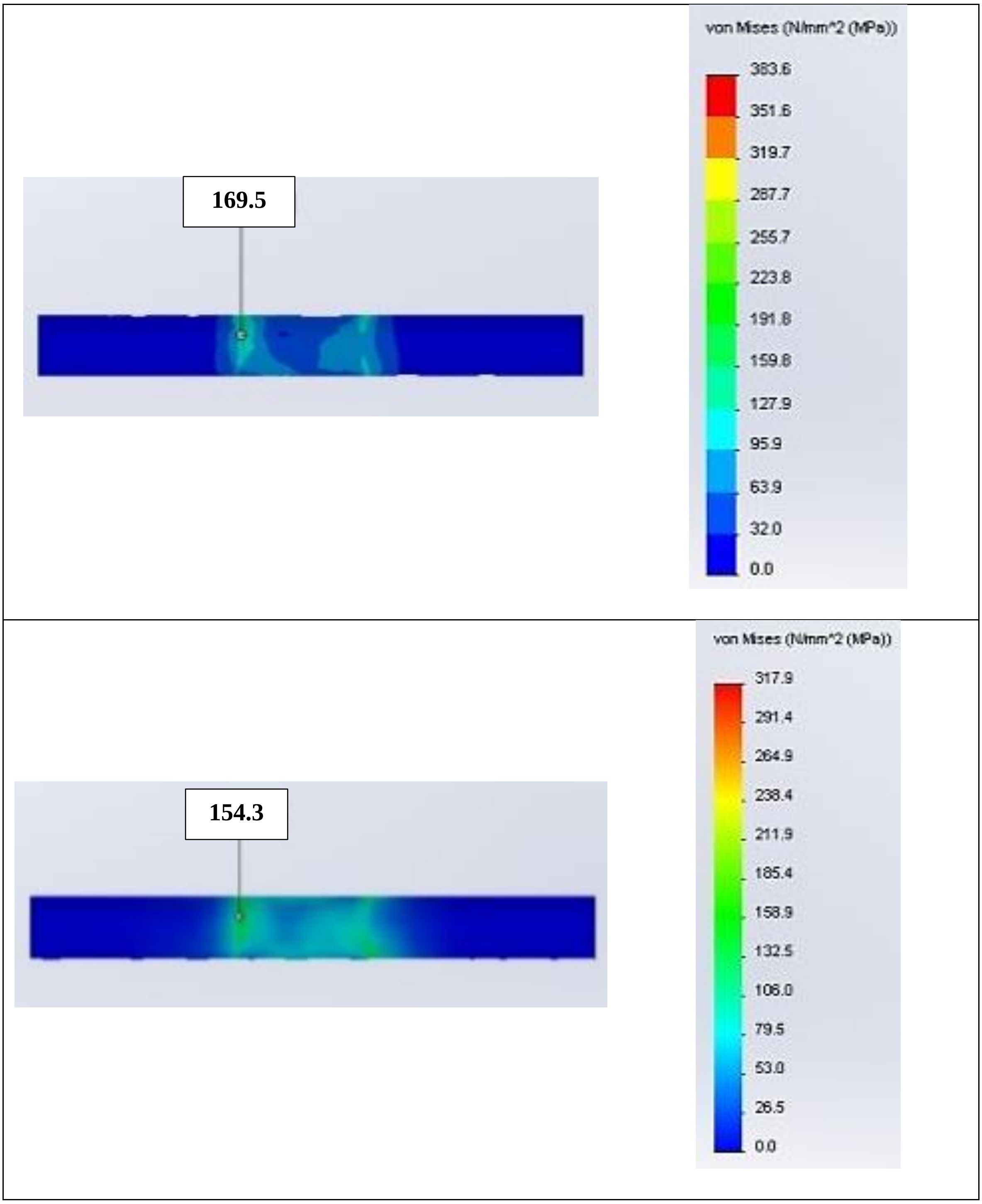

Figure 8-18 Contour plot showing maximum von Mises stress in first distal screw (top – ALFN, bottom – Ti-6Al-7Nb nail with optimum parameters identified with Taguchi method

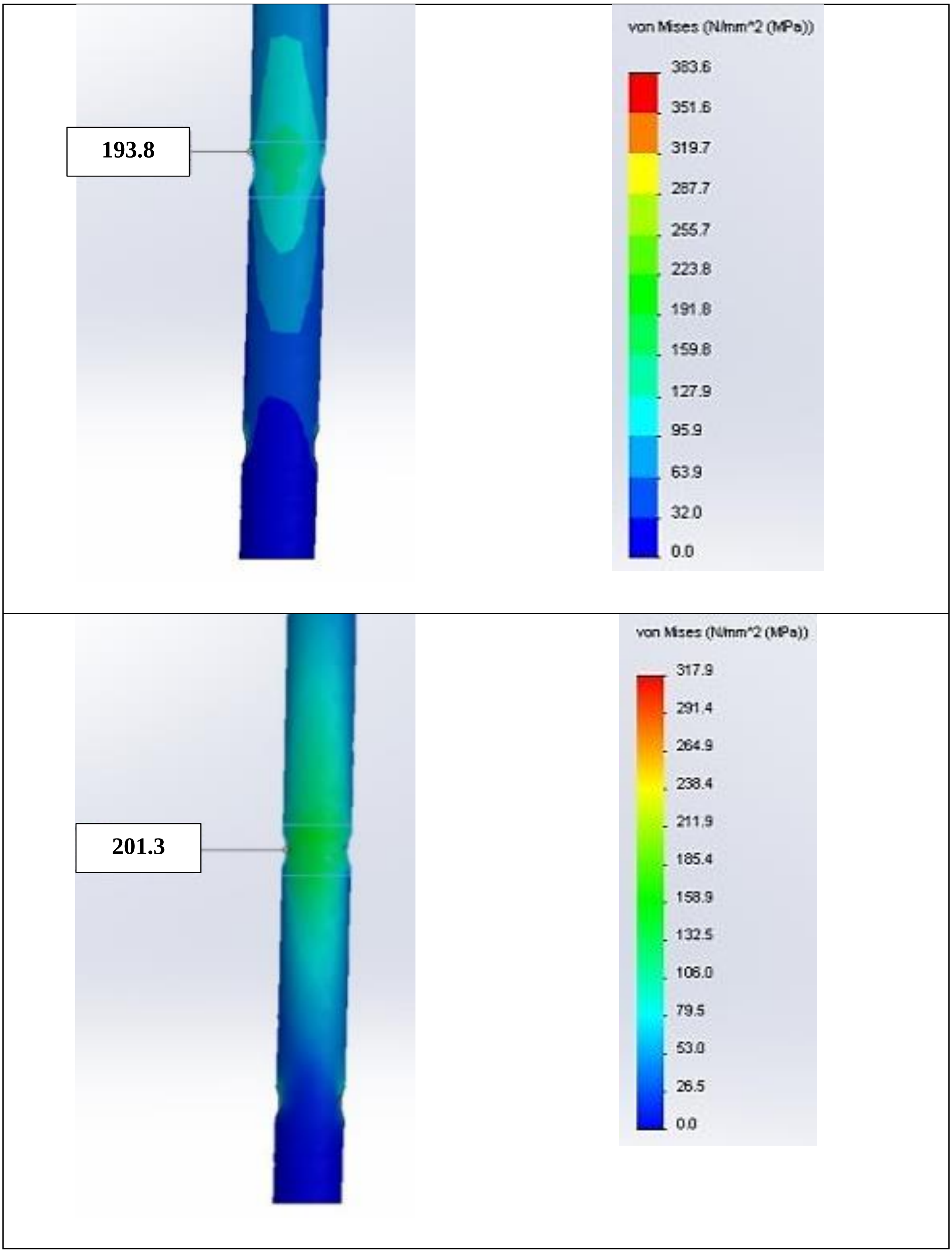

Figure 8-19 Contour plot showing maximum von Mises stress in first distal screw hole (top – ALFN, bottom – Ti-6Al-7Nb nail with optimum parameters identified with Taguchi method

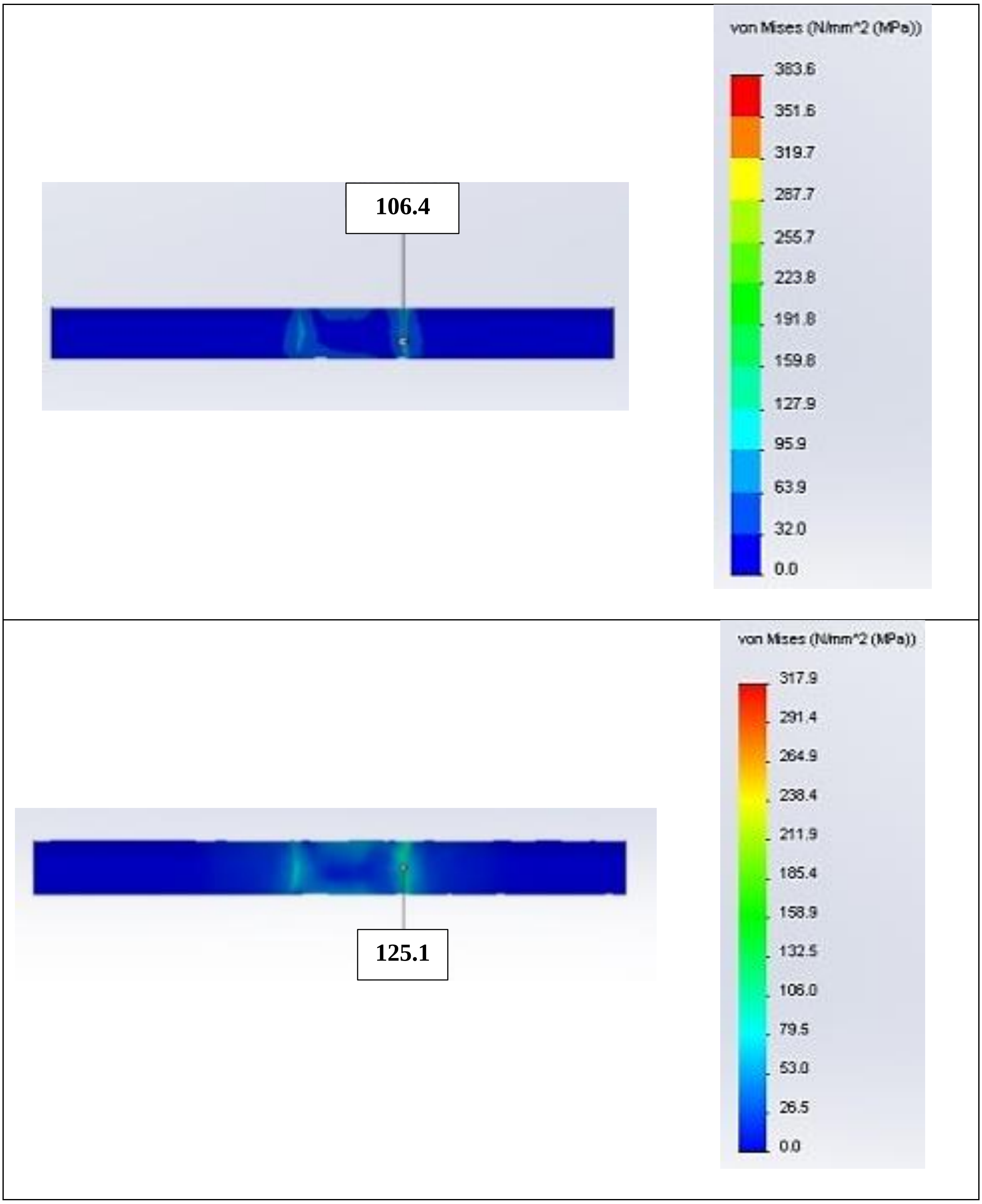

Figure 8-20 Contour plot showing maximum von Mises stress in second distal screw (top – ALFN, bottom – Ti-6Al-7Nb nail with optimum parameters identified with Taguchi method

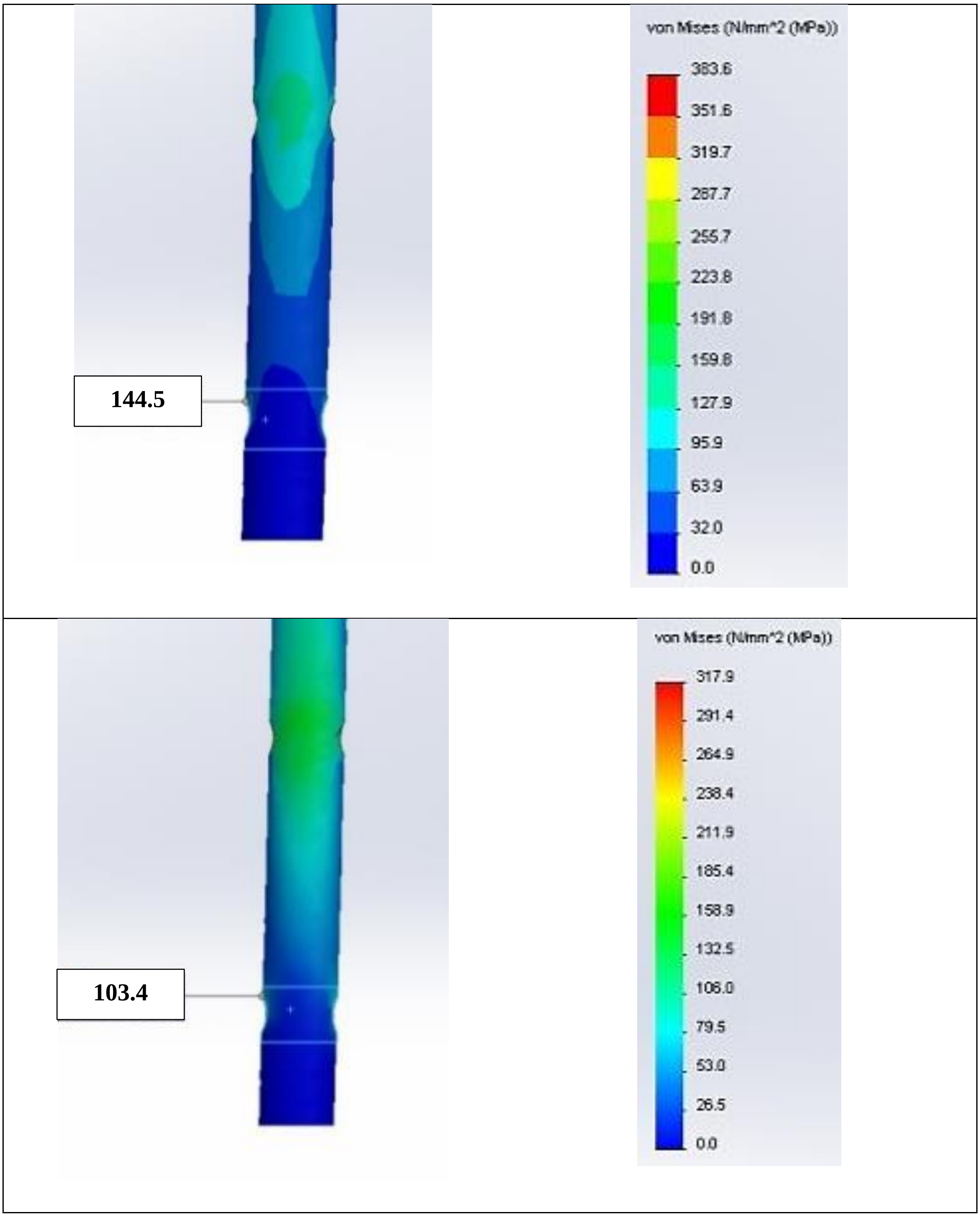

Figure 8-21 Contour plot showing maximum von Mises stress in second distal screw hole (top – ALFN, bottom – Ti-6Al-7Nb nail with optimum parameters identified with Taguchi method

The final simulation test with Ti-6Al-7Nb nail with optimum implant parameters identified using Taguchi analysis confirmed overall reduction in σ_υ (Table 8-7).

Table 8-7 Comparison of predicted von Mises stress values for ALFN and TAN* = Ti-6Al-7Nb nail with optimum implant parameters identified using Taguchi analysis

IM Nail	von Mises Stress (MPa)						
	Proximal Screw	Proximal Screw Hole	Distal Screw 1	Distal Screw 1 Hole	Distal Screw 2	Distal Screw 2 Hole	Average Stress
ALFN	383.6	343.5	169.5	193.8	106.4	144.5	223.6
TAN*	317.9	254.8	154.3	201.3	125.1	103.4	192.8

8.4 Discussion

A robust FEA model with generic and modular features provides the scope for investing a range of factors (331, 345, 360). This aspect of FEA was used in the current part of the study wherein a validated model allowed evaluation of some of the factors relevant to femoral fracture treatment using the ALFN. It has been reported that the torque along the nail/femur assembly remains fairly constant (470). Furthermore it has been experimentally demonstrated that rotational stiffness of an intramedullary nail/femur construct is largely determined by the inherent torsional stiffness of the nail (419). The simulated torsional stiffness results of the different fracture geometry and level which showed similar values (Table 8-5) compare favorably with this finding.

In comparison to the clinical studies (7, 8, 12, 23, 29, 38, 40, 41, 471-497) relatively fewer biomechanical studies in the current literature have addressed fracture healing following intramedullary nail fixation (249, 254, 498-502). This includes a combination of human (249), animal (499, 501-503), composite bone based experimental (254, 500) and finite element studies (268, 504, 505).

Schneider *et al*. (249) performed a unique study in which they investigated the forces experienced *in vivo* by a stainless steel intramedullary nail used to treat a comminuted femoral shaft fracture in an adult male. With the patient partial weight bearing (250 N), they noted a mean axial force component of 300 N and 205 N at an early (<7 weeks) and late (>12 weeks) postoperative period, respectively. In the early postoperative period they observed a bending force of 62 N with a corresponding bending moment of 16 N m whilst the torsional moment varied between 3-7 N m. In contrast when patient's weight bearing status was 'touch ground' the axial, bending and torsional force components reduced by approximately one sixth, one sixtieth and one tenth of the previous values, respectively. Furthermore, similar load components were noted in both one and two leg stance. Interestingly, even after fracture consolidation they noted that approximately 50% of the load was transmitted through the nail. The authors also suggested that data from other *in vivo* studies measuring hip joint reaction forces (506-509) should not be used in isolation to predict the loads acting along the femur as the muscle forces contribute significantly towards the strains noted on the cortical bone (510).

Henry *et al*. (503) compared bending stiffness in three groups of rabbit radii. Following osteotomy the first group had no implant and served as a control whereas the second and third group had fracture stabilisation with vitallium intramedullary nails and plate/screws, respectively. They reported that as the fracture healed stiffness returned more rapidly than strength. Additionally they suggested that the stiffness of the healing bone regulated fracture union. Using a sheep metatarsal, Sedel *et al*. (501) reported significantly higher mechanical properties (ultimate bending strength, stiffness, moment of inertia, energy to failure, tensile strength) of fracture callus at three months following intramedullary nail treatment compared to plating. Molster *et al*. (502) used a rat tibia model to compare fracture callus after intramedullary nailing with rigid stainless steel rods and flexible nitinol (titanium-nickel alloy) rods. They reported that bones with flexible nailing showed hypertrophic callus whereas only scanty callus was noted in the bones with rigid nailing. Wilson *et al*. (499) used a telemetric intramedullary nail for *in vivo* measurement of fracture healing in sheep femora. However, due to a combination of factors (viz. poor study design, implant design, surgical technique, animal model, single-channel telemetry system) they were unable to obtain any conclusive findings.

Miles *et al*. (254) simulated fracture healing in a composite femur model using glass fibre cloth and epoxy resin to study the load transfer in interlocking intramedullary nails (AO Universal / Russell-Taylor). They reported the Russell-Taylor nail to have more stiffness both in bending and torsion. In consequence it contributed more to the stiffness of the femur/nail construct. In their study Nemchand *et al*. (511) simulated fracture callus using composite materials and noted a gradual decrease in the load measured by telemeterised intramedullary nail compared to the composite tibia during axial compression and four point bending.

Bucholz *et al*. (268) used an axisymmetric FEA model with a simplified set of loads in ANSYS software to investigate femoral fractures treated with 316L stainless steel intramedullary nails. Fracture healing was simulated by varying the modulus of elasticity of the elements in the fracture site. Their model predicted that early weight bearing before the fracture regained 50% of its original stiffness and resulted in high stress in the nail beyond the endurance limit with a risk of fatigue fracture. However, this finding is in contrast to clinical studies wherein early weight bearing regimen had uneventful recovery (471, 492, 512).

Wehner *et al*. (498) investigated the influence of nail diameter on the healing of tibial shaft fractures using an idealized transverse fracture FEA model. They concluded that the healing time was not significantly affected by the nail diameter but a stiffer material (viz. stainless steel as opposed to titanium) could potentially reduce healing time. However, this conclusion is not substantiated by reported outcomes from clinical studies wherein titanium alloy (Ti-6Al-4V) tibial nails were used (513, 514)

Mehboob *et al*. (505) evaluated healing of a tibial shaft fracture stabilised with composite intramedullary nail using a simplified FEA model and mechano-regulation algorithm with deviatoric strain. They reported that the healing of a tibial fracture was improved by the relatively low modulus of the composite intramedullary nail. To date only limited clinical use of these nails has been reported (515) with some authors questioning the advantage offered by their low modulus of elasticity (516)

Complex FEA models and algorithms have been described to simulate fracture healing (517-527). However, these were beyond the scope of the current study where the focus of the investigation was to evaluate the variation in the stiffness of the construct and stress in the ALFN during fracture healing. Hence only a simplified callus tissue model was used. Nonetheless the current FEA model predicted an increase in the stiffness of the femur/ALFN construct and a corresponding decrease in the von Mises stress in the ALFN over a period of 0-16 weeks (Figure 8-7, Figure 8-8, Figure 8-9 and Figure 8-10). This observation, coupled with the relative decrease in deformation of the callus tissue (Figure 8-11, Figure 8-12 and Figure 8-13), suggested a shift in load sharing pattern from the ALFN to the femur as the fracture healing progressed. This finding compares favorably with the clinical (249) and FEA (268, 361) studies in the literature.

Bucholz *et al*. (268) investigated the fatigue failure of the first distal interlocking screw hole of three 316L stainless steel nail designs (Klemm-Schellman / Grosse-Kempf / Küntscher) used for fixation of the distal third femoral fractures using an axisymmetric FEA model of the Grosse-Kempf nail with simplified muscle loads. They reported that the distance between the fracture and the DS1 hole was a critical factor in the amount of stress generated. In particular if this distance was less than 50 mm it resulted in stress values in excess of the endurance limit of the nail material (316L stainless steel). They validated their FEA model experimentally using an unpreserved human cadaveric femur. The difference in stress values between the experimental and FEA model was reported to range from 0.9 – 23.3%. On closer inspection certain limitations are apparent with the FEA model used in this study. The femoral head, femoral curvature including the anterior bow was ignored whereas muscle based loads were applied without specifying the location/area of application of such loads. The nail/bone interface was fully constrained. Additionally the location of DS1 screw was not reported. A combination of these factors may have contributed to their conclusions which are different to the evidence from other numerical (528, 529), biomechanical (270) and clinical studies (258, 471, 512, 530, 531).

In a subsequent study, Antekeier *et al*. (270) performed fatigue testing of Grosse-Kempf and titanium alloy (Ti-6Al-4V, Trigen™, Smith & Nephew, Memphis, TN) nails by reproducing the experimental conditions similar to that described by Bucholz *et al*. (268). They reported a critical distance of 30 mm (between the fracture and DS1 screw) below which the risk of fatigue failure increased in the Trigen™ nails. Shih *et al*. (407) studied the influence of muscular contractions on the stress at the distal interlocking zone using a FEA model. They simulated a 316L stainless steel intramedullary nail with 13 mm diameter, 1.5 mm wall thickness and anterior radius of curvature of 1500 mm. However, the length of nail and the interlocking screws were not provided. The femur model consisted of a 10 mm wide fracture in the distal third of the shaft. They evaluated three fracture variants with the distance between the fracture and the DS1 screw ranging from 10-30 mm. They reported that the stress in both the distal interlocking screws was highest with a 30 mm gap and lowest with a 10 mm gap. Apart from the fact that this paper reported the results of a FEA model without experimental validation, other limitations have to be considered. Shih *et al*. (407) based their vectorial components of muscle forces on a study (366) which used cables and screws to simulate the pull of the muscles on a synthetic femur. Furthermore, the authors of this study (366) themselves concluded that the *in vivo* data in the literature contradicted the validity of their experimental set up. As highlighted earlier muscle forces contribute significantly towards the strains noted on the cortical bone (510) and may not be an accurate representation of the *in vivo* loads acting on the intramedullary nail (249).

It is evident from the above that conflicting evidence exists in the current literature in terms of influence of fracture level on the stress in the DS1 screw hole. In the current study a simplified axial compression load (300 N) was applied to the FEA model corresponding to the femoral head along the mechanical axis, similar to the experimental model and to that described by Antekeier *et al*. (270). The influence of the distance between the fracture site and the DS1 screw hole was investigated by varying this distance from 10-150 mm. The resultant effect was measured by noting the maximum predicted von Mises stress values at the interlocking zones corresponding to the proximal and two distal screws of the ALFN. Unlike the steep rise in stress values at less than 50 mm as reported by Bucholz *et al*. (268), it was observed that the predicted von Mises stress values in the interlocking zones of the ALFN remained within an acceptable range regardless of the distance (Figure 8-6). Furthermore, the maximum predicted von Mises stress in the interlocking zones (proximal – 321.20-400.36 MPa / DS1 – 160.25-215.13 MPa /

DS2 – 103.00-145.89 MPa) were well below the endurance limit of Ti-6Al-7Nb, reported to range from 540 MPa (439) to 750 MPa (532).

It has been demonstrated that the cyclical bending motion can result in eccentric compression of the reamed medullary canal leading to dynamic toggle of the distal bone fragment (270). ALFN closely matches the shape of the medullary canal of the femur. This feature may allow a more conforming deformation of the ALFN along with the femur leading to better stress distribution (429). This may represent a potential biomechanical advantage of the helical geometry.

Hajek *et al*. (256) used matched cadaveric femurs to investigate the modes of failure in a Klemm-Schellman nail with one or two distal interlocking screws. Under axial compression they observed that in specimens with two distal interlocking screws the nail failed. Furthermore the DS1 screw failed on the medial aspect either through cutout or by bending in the region between the nail and the medial cortex. The maximum predicted von Mises stress for the DS1 screw (169.5 MPa) (Figure 8-18) in the current study was on the medial aspect whereas relatively higher stress (193.8 MPa) (Figure 8-19) was predicted in the corresponding region of nail. This prediction of the current FEA model compares favorably with the findings of Hajek *et al*. (256).

The Taguchi method originally described by Dr. Genichi Taguchi (462-464, 467) has been extensively used in various disciplines like genetics, orthopaedics and pharmaceuticals (461, 533-535). It has been demonstrated that axial force is of one order magnitude greater than shear forces in a femur/intramedullary nail assembly (470). The segmental defect FEA model was predicted to have the highest von Mises stress around the proximal interlocking screw during axial compression (chapter 7). This model which represented the 'worst case scenario' was selected to study the common implant parameters on the stress. Implant parameters such as material, nail / interlocking screw diameter, nail design, relative angle between nail and interlocking screws, number and location of interlocking screws play a critical role in the stress noted in the interlocking zone (356, 361, 447, 528). Hence four implant factors (viz. material, interlocking screw diameter, relative angle between nail and interlocking screw and nail thickness) were chosen to assess their influence on the maximum predicted von Mises stress at the proximal interlocking zone. Each of these factors was assigned three levels (Table 8-4). Hence a subset of nine FEA models were derived from the initial validated model and nine simulated experiments were systematically performed as per Taguchi L9 orthogonal array to assess the maximum predicted von Mises stress for each model (458-461). It was noted that the relative angle between the ALFN and the proximal interlocking screw contributed the most with a delta of value 3.88 (Figure 8-15 and Table 8-6). Amongst these the highest *S/N* ratio (-51.27) was noted at 130° with 120° being fairly close with *S/N* ratio (-51.99). The nail material was noted to be second most important factor (delta = 2.82) with both titanium and Ti-6Al-7Nb having similar *S/N* ratios at -51.81 and -51.96, respectively. Proximal wall thickness and proximal screw diameter had delta values of 2.20 and 0.50, respectively. Based on the above, the optimum level for each of the aforementioned implant factors was identified and an idealized FEA model of a Ti-6Al-7Nb nail was developed. A final simulation test on this model confirmed the hypothesis as the maximum predicted von Mises stress at the proximal interlocking screw was lower at 317.9 MPa compared to the 383.6 MPa noted with ALFN (Figure 8-16). Furthermore, the average stress in the intramedullary nail system was also lower at 192.8 MPa compared to the 223.6 MPa noted with ALFN (Table 8-7). The current study is the first to investigate the biomechanical parameters of femoral intramedullary nail by applying the Taguchi method to perform simulation tests on FEA models.

8.5 Summary

The FEA model predicted some variation in the axial and four point bending stiffness parameters based on fracture level and geometry. However, similar torsional stiffness values were predicted for the different fracture levels and patterns evaluated. The predicted von Mises stress in the distal interlocking zones remains in a finite range irrespective of the proximity of the fracture margin to the first distal interlocking screw. The helical geometry of the ALFN may play a role in the above two findings.

As fracture healing progresses over a duration of 16 weeks there is a relative increase in stiffness parameters with a corresponding decrease in the von Mises stress in the ALFN and interlocking screws. Simulation tests based on the Taguchi method demonstrated that the relative angle between the ALFN/intramedullary nail and the proximal interlocking screw and the nail material play a critical role in determining the stress values in the proximal interlocking zone.

The next/final chapter discusses the salient findings of the current study with relevant clinical implications.

9 DISCUSSION AND CONCLUSIONS

This chapter includes a brief discussion regarding the findings from the work presented in the earlier chapters. The salient findings, addressing the primary research objectives and questions, is presented in the next section. Subsequently the limitations of the current work and the potential areas for future research are discussed. Finally, the main conclusions of this study are presented.

9.1 Discussion

Femoral fractures in adolescents are severe injuries with a risk of associated morbidity (3-5). Surgical treatment options such as flexible intramedullary nails, plate and screw fixation, rigid intramedullary nails and external fixators have been described in the literature. Flexible intramedullary nails used initially had poor outcome in heavier, older children with unstable fractures due to loss of length and rotation at the fracture site (6). Rigid intramedullary interlocking nails help overcome the limitations of the flexible nails with different types of rigid intramedullary nails described in the literature to fix adolescent femoral fractures (7-14). Rigid intramedullary fixation with helical nail design viz. Expert adolescent lateral femoral nail (ALFN) has been suggested as a treatment option due to the perceived advantages of stable fixation and avoiding iatrogenic damage to the growth plate (29). However there is no biomechanical study available in the literature on this nail design. Hence the current research work, representing the first *in vitro* biomechanical study of the ALFN was undertaken wherein the biomechanical parameters of paediatric femur fracture fixation with ALFN were investigated using a combination of study modalities (viz. sawbone based experimental model testing and finite element analysis) (345, 356, 360, 361, 414, 470).

In the initial part of the study (chapter 4), stiffness parameters of intact sawbones under axial compression, four-point bending and torsion were established. Customised test jigs were designed and fabricated to allow multiple tests of the small sized sawbone specimens. A survey of the biomechanical literature showed considerable variation in the test set up including load magnitude, loading rate and number of tests performed (Table 4-3, Table 4-4 and Table 4-5). A rigid intramedullary nail, like the ALFN, is clinically indicated in children weighing more than 45 kg with femoral shaft fractures (29). Hence for the purpose of biomechanical testing the load parameters were derived based on this clinical scenario of a hypothetical adolescent with a body weight of 60 kg. Data from the only study available in the literature (249) which reported loads acting on a femoral intramedullary nail *in vivo* was also used as a guide to estimate clinically relevant load parameters for the biomechanical tests. Stiffness parameters of intact sawbones served as a baseline for comparative analysis in the subsequent investigations. Additionally this data was used to validate the FEA model of paediatric femur.

FEA of the femur has been extensively used as a research tool in orthopaedic biomechanical studies (79, 268, 308, 327, 330, 331, 334, 336, 344-346, 348, 355, 356, 359-361, 373, 378, 379, 381). However, the majority of the described FEA models pertain to the adult femur (330, 346, 382). There is very limited information available regarding FEA using a paediatric size femur with only two studies in the current literature (77, 78) describing a FEA model to investigate flexible intramedullary nail fixation. Perez *et al.* (77) used the bone model available for download from the internet (www.biomedtown.org). This model based on a synthetic femur measured 420 mm in length with a canal diameter of 9 mm. However, it must be noted that the authors did not experimentally validate their FEA model which is a primary requisite for any FEA (327, 330, 331, 334, 344, 345, 356, 360, 376). Furthermore, it has been reported that a change in the synthetic femur geometry from a large to small dimension can result in axial and torsional rigidity differences of 1.5 and 2.2 times, respectively, despite having the same Young's modulus for the cortical bone (347). It will be of interest to note the accuracy of predictions from their model if the overall dimensions were scaled down to be representative of a child's small femur. Krauze *et al.* (404) performed biomechanical analysis comparing flexible intramedullary nails of two different materials. The femur FEA model in this study is reported to be based on a 5-7 year old child. However, the details regarding development of the femur FEA model and its dimensions are not provided in the paper. As with the earlier study there was no experimental validation of the FEA model.

Hence in the second part of the study (chapter 5), a FEA model based on simplified geometry of the paediatric femur was developed using orthogonal digital radiographs as a template in SolidWorks™ (350). Previous studies in this field (402, 403) have used specialised algorithms to develop three dimensional bone models from radiographs. However, the lack of widespread availability of such algorithms limits their applicability. Enhanced processing capability of computers has enabled development of bone FEA models with good visual similarity through accurate geometric representation. However, this approach does not necessarily guarantee the numerical accuracy of the results predicted by such models (381). Following validation it was demonstrated that digital radiographs enable development of a FEA model in SolidWorks™ that is simple yet representative of the overall dimensions and critical features such as radius of curvature of the paediatric femur. This is an important requisite for a femur FEA model used to assess the biomechanical parameters of intramedullary implants (18). It has been demonstrated that omission of cancellous bone in the femur FEA model does not significantly alter the overall stiffness results (356, 361). Therefore, in the paediatric FEA model cancellous bone tissue was not modelled separately to optimise computational time (395). Results from simulation tests using the FEA model to estimate axial, four-point bending and torsional stiffness were similar to the experimental sawbone model. This validated FEA model of a paediatric femur was subsequently used for evaluation of fracture fixation using ALFN. Simulation data obtained using the paediatric femur FEA model can be useful in estimation of the range of loads that can be safely applied to a fracture fixation construct. This information can be helpful in planning and establishing parameters for an experimental setup (360).

In the subsequent part of the study (chapter 6) biomechanical testing of paediatric femur fracture fixation with ALFN was performed. The three intact femur specimens were prepared and implanted with ALFN as per the surgical technique (273) following which biomechanical testing allowed assessment of stiffness parameters of a healed and remodelled fracture (361). The standardised osteotomies on composite femurs served three purposes. First, they simulated common fracture patterns noted in clinical practice (425, 426). Second, the similar size and location of osteotomy across all the specimens aimed to minimise variability (58, 72, 291, 294). Third, they provided a reproducible experimental model to evaluate axial and rotational stiffness at the two extremes of fracture patterns i.e. stable (transverse fracture) with significant bone load sharing and completely unstable (segmental defect) with only the ALFN providing axial and rotational stability (419, 427). Axial compression results demonstrated the relative construct stiffness to remain in a satisfactory range (80%-89% of intact femur) in the fracture groups (Figure 6-23). This may be due to close conformity of the shape of the ALFN with that of the femoral medullary canal. It has been reported that anteroposterior (AP) and medial-lateral bending give comparable results (427). Therefore only AP bending was undertaken in this study. A bending test of a femoral intramedullary nail fixation construct primarily tests the nail (420). The results of four-point bending showed a trend towards decrease in the stiffness across all three specimens (Figure 6-15). This may be due to the same size of ALFN used in all three specimens. It has been suggested that the profile of the intramedullary nail is the decisive factor for the torsional stiffness of femoral locking nails in the bone implant complex (418). This point is supported by the torsional results and the relative construct stiffness from the current study (Figure 6-18, Figure 6-21 and Figure 6-23).

The focus of the fourth part of the study (chapter 7) was to develop a FEA model of paediatric femur fracture fixation with ALFN. Development of a reliable CAD model of the ALFN with its complex helical geometry posed unique challenges. Due to proprietary reasons, detailed information regarding the ALFN was not available from the manufacturer. Under such circumstances some authors have used the technique of reverse engineering to obtain the geometric information of the implant (306, 439). However, this method requires additional resources in terms of scanning equipment and software to process the data obtained from the scan (344). Hence a novel approach to develop the CAD model for ALFN using the surgical template available in the manufacturer manual was used. This technique allowed the CAD model to accurately represent the helical axis of the ALFN which is one of the key design features. Furthermore, development in SolidWorks™ using sketches with dimensions based on measurements from the actual implant allowed for variations during simulation testing to evaluate different implant parameters (Taguchi analysis described in chapter 8). A parametric type of FEA model was used in the current study for the aforementioned reasons. It has been suggested that results from FEA studies should be verified using an experimental model in at least one load case (356). However, in the current study validation of the paediatric femur fracture fixation FEA model data was undertaken for each type of femur fracture tested in the laboratory. This ensured robustness of the FEA model and allowed subsequent simulation tests with variations of factors like fracture geometry, fracture healing and design parameters.

Stiffness parameters of three different types of fractures (transverse / comminuted / segmental defect) were evaluated in addition to a fully healed configuration. In general it was noted that there was trend towards decrease in stiffness with an increase in severity of the fracture type. Mean axial stiffness for transverse fracture fixation with ALFN measured 622.84 (± 36.65) N/mm in comparison to 562.04 (± 31.50) N/mm measured for the segmental defect. Correspondingly the maximum predicted von Mises stress from the simulation tests was $\sigma_{Transverse}$ = 361.5 MPa and $\sigma_{Segmental}$ = 383.6 MPa for the transverse and segmental defect fractures, respectively, suggesting an increased load sharing by the ALFN in the relatively unstable segmental defect type of fracture. The inverse relationship between the predicted stiffness and maximum von Mises stress values was further evident during the course of fracture consolidation (Figure 8-7, Figure 8-8, Figure 8-9 and Figure 8-10). This finding compares favorably with the clinical (249) and FEA (268, 361) studies in the literature.

A robust FEA model with generic and modular features provides the scope for investing a range of factors (331, 345, 360). This aspect of FEA was used in the final part of the study (chapter 8) wherein the validated model allowed evaluation of some of the factors relevant to femoral fracture treatment using the ALFN. To evaluate the process of fracture healing the 'worst case scenario' of segmental defect was selected. Apart from being technically easier to model the callus tissue for a segmental defect, it was assumed that this model would help identify any trend / variation in stiffness at the different temporal points of fracture healing. In the current literature several authors have adopted different approaches to model the callus tissue (356, 457, 517, 536). Three distinct histological types of calluses (central / peripheral / adjacent) are formed at the fracture site during the process of healing (457, 537). Amongst these it is central callus that contributes towards endochondral calcification and subsequent bone formation. Hence for the purpose of this study only the central callus tissue was modelled during simulation tests (273). In general the FEA model predicted a global increase in stiffness across all the three loading conditions as the fractured healed. It was observed that this trend continued till 16 weeks with the stiffness results approaching that of an intact femur (Figure 8-7, Figure 8-8, Figure 8-9 and Figure 8-10). Clinical studies of patients who underwent intramedullary nail fixation have also reported similar observations (538). Additionally, the FEA model predicted a decrease in the maximum displacement of the ALFN within the medullary canal as the fracture healed (Figure 8-12 and Figure 8-13).

The effect of the fracture level on the maximum von Mises stress in the first distal interlocking screw (DS1) was studied using a simulated axial compressive force applied to the femoral head area along the mechanical axis of the femur. The distance between the fracture margin and the interlocking screw was varied from 10 mm to 150 mm. The FEA results suggested that there was only a small variation in the predicted axial stiffness and the maximum von Mises stress (Figure 8-6). Analysis of the resultant displacement of the ALFN showed a similar feature. This finding is different from that reported by Bucholz *et al.* (268) who evaluated stress in the distal interlocking screw of a Grosse-Kempf nail using an axisymmetric type of FEA model. Unlike that study it was noted that the maximum predicted von Mises stress in the interlocking screws of the ALFN remained within a finite range. Furthermore, the stress values did not significantly increase at a critical distance as was noted in their axisymmetric model. ALFN closely matches the shape of the medullary canal of the femur. This feature may allow compliant deformation of the ALFN along with the femur leading to better stress distribution. This may represent a potential biomechanical advantage of the helical geometry. Amongst the three different loading conditions (axial / four-point bending / torsion) studied in the paediatric femur fracture fixation FEA model, the maximum displacement of the ALFN was in response to the axial compressive load of 300 N. It was noted that the proximal portion of the ALFN displaced in an anteromedial direction (Figure 7-37). Dynamic analysis with animation plots (539) showed that as the ALFN displaced it compressed the adjacent contents of the medullary canal but did not contact the inner wall of the medullary canal. This pattern of displacement was observed across all the fracture types studied. It was observed that at higher loads the degree of displacement increased. This may have an implication in terms of the stability of fractures located in the anteromedial part of the proximal femur.

Simulation tests on all the paediatric femur fracture fixation FEA models showed the von Mises stress to be relatively higher in the proximal portion of the ALFN (120° proximal interlocking screw, screw hole and their common interface) (Figure 7-38). Amongst the three loading conditions studied stress was higher under axial loading. This prompted a theoretical evaluation of the common intramedullary nail design parameters using the Taguchi method. Minimisation of the stress in the proximal part of the ALFN in response to an axial compressive force of 300 N was selected as the outcome measure. As demonstrated from the results (Table 8-6) (Figure 8-15) the relative angle between the ALFN/proximal interlocking screw was the most significant factor (delta = 3.88) followed by nail material (delta = 2.82). Previous FEA studies have reported that stainless steel can significantly increase stress in the interlocking screws when compared to Ti-6Al-7Nb (356, 470). Similar findings were predicted by the FEA models in the current study. The diameter of the proximal interlocking screw contributed least towards the stress (delta = 0.50). Based on this information a FEA model variant of the ALFN with the optimum parameters was developed to test the hypothesis. Simulation test on this variant showed the stress values to be lower (317.9 MPa compared to the 383.6 MPa noted with ALFN) (Figure 8-16) thereby confirming the hypothesis and validating the assumptions made during the analysis. The current study is the first to investigate the biomechanical parameters of a femoral intramedullary nail by applying the Taguchi method to perform simulation tests on FEA models.

9.2 Salient findings with respect to the research questions

9.2.1 Biomechanical stability of paediatric femur fracture fixation with ALFN

The stiffness parameters established during experimental testing confirmed that the biomechanical stability of paediatric femur fracture fixation with ALFN is comparable to the data on the other intramedullary nails available in the literature (Table 9-1, Table 9-2 and Table 9-3).

Table 9-1 Relative construct stiffness under axial compression test

T–transverse, C–comminuted, SD–segmental defect, SS–stainless steel, TAN-Ti-6Al-7Nb, AO-Arbeitsgemeinschaft für Osteosynthesefragen, ALFN-adolescent lateral femoral nail

Study	Femur Specimen / Fracture Type	Nail	Nail dimensions (mm) (Length/Diameter)	Material	Relative construct stiffness (%)
Schandelmaier *et al.* (418)	Cadaver / 20 mm midshaft SD	AO solid	NR / 9	SS	62
		AO solid	NR / 9	TAN	50
		AO slotted	NR / 11	SS	49
		AO solid	NR / 12	TAN	65
Current	Sawbone® / 1 mm T	ALFN	300 / 8.2	TAN	89
	Sawbone® / 10 mm C	ALFN	300 / 8.2	TAN	85
	Sawbone® / 10 mm SD	ALFN	300 / 8.2	TAN	80

Axial compression results demonstrated the relative construct stiffness to remain in a satisfactory range (80%-89% of intact femur) in the fracture groups (Figure 6-23). Furthermore, the FEA model predicted similar axial stiffness parameters for the midshaft, proximal, and distal third level transverse fractures (Table 8-5). This may be due to close conformity of the shape of the ALFN with that of the femoral medullary canal permitting better distribution of the axial load along the ALFN/femur construct.

The relative stiffness of fracture fixation constructs in AP bending test has been reported to vary between 20% (283) and 37%-68% (418) for central segment defects. However for subtrochanteric defects it can vary between 55%-70% (283). In comparison the relative stiffness of the FAC in the fracture groups varied from 22%-25% (Table 9-2). This may be partly due to the fact that the former studies (283, 418) used larger nail sizes whereas the ALFN used in the current study had an outer diameter of 8.2 mm (20) (Figure 3-6).

A bending test of a femoral intramedullary nail fixation construct primarily tests the nail (420). The results of four-point bending showed a similar trend towards decrease in the stiffness across all the three specimens as the fracture severity increased (Figure 6-15). This may be due to the same size of ALFN used across all the three specimens.

Table 9-2 Relative construct stiffness under bending test

T–transverse, C–comminuted, SD–segmental defect, SS–stainless steel, TAN-Ti-6Al-7Nb, AO-Arbeitsgemeinschaft für Osteosynthesefragen, ALFN-adolescent lateral femoral nail, BW-Brooker Wills, KS-Klemm-Schellman, GK- Grosse-Kempf

Study	Femur Specimen / Fracture Type	Nail	Nail dimensions (mm) (Length/Diameter)	Material	Relative construct stiffness (%)
Schandelmaier *et al.* (418)	Cadaver / 20 mm midshaft SD	AO solid	NR / 9	SS	43
		AO solid	NR / 9	TAN	45
		AO slotted	NR / 11	SS	37
		AO solid	NR / 12	TAN	68
Johnson *et al.* (340)	Cadaver / 30 mm subtrochanteric SD	BW	420 / 15	SS	55
		KS		SS	65
		GK		SS	70
Johnson *et al.* (283)	Cadaver / 80 mm midshaft SD	BW	420 / 15	SS	20
		KS		SS	20
		GK		SS	20

Table 9-2 continued					
Study	**Femur Specimen / Fracture Type**	**Nail**	**Nail dimensions (mm) (Length/Diameter)**	**Material**	**Relative construct stiffness (%)**
Current	Sawbone® / 1 mm T	ALFN	300 / 8.2	TAN	25
	Sawbone® / 10 mm C	ALFN	300 / 8.2	TAN	23
	Sawbone® / 10 mm SD	ALFN	300 / 8.2	TAN	22

It has been suggested that the profile of the intramedullary nail is the decisive factor for the torsional stiffness of femoral locking nails in the bone implant complex (418). This point is supported by the torsional results and the relative construct stiffness from the current study (Figure 6-18, Figure 6-21 and Figure 6-23).

Johnson *et al.* (283)reported the relative torsional stiffness of femur / different nail (BW/ KS/ GK) constructs to be below 3% of that of intact femora. Schandelmaier *et al.* (418) reported the relative torsional stiffness of a 9 mm and 12 mm diameter titanium alloy solid nails to be 12% and 18% of the intact bone, respectively. In comparison to the relative torsional stiffness of ALFN with a 8.2 mm diameter varied from 21% (segmental defect in external rotation) to 27% (transverse fracture in internal rotation) (Figure 6-23). This may be due to the helical profile of the ALFN which permits better transfer of the torsional load across the femur ALFN construct.

Table 9-3 Relative construct stiffness under torsion test

T–transverse, C–comminuted, SD–segmental defect, SS–stainless steel, TAN-Ti-6Al-7Nb, AO-Arbeitsgemeinschaft für Osteosynthesefragen, ALFN-adolescent lateral femoral nail, BW-Brooker Wills, KS-Klemm-Schellman, GK- Grosse-Kempf, IR-internal rotation, ER-external rotation

Study	Femur specimen / Fracture type	Nail	Nail dimensions (mm) (Length /Diameter)	Material	Relative construct stiffness (%)
Schandelmaier *et al.* (418)	Cadaver / 20mm midshaft SD	AO solid	NR / 9	SS	20
		AO solid	NR / 9	TAN	12
		AO slotted	NR / 11	SS	2
		AO solid	NR / 12	TAN	18
Johnson *et al.* (283)	Cadaver / 30 mm subtrochanteric SD	BW	420 / 15	SS	2.5
		KS	420 / 15	SS	2.4
		GK	420 / 15	SS	2.5
Johnson *et al.* (283)	Cadaver / 80 mm midshaft SD	BW	420 / 15	SS	2.2
		KS	420 / 15	SS	2.3
		GK	420 / 15	SS	2.8

Table 9-3 continued					
Study	**Femur specimen / Fracture type**	**Nail**	**Nail dimensions (mm) (Length /Diameter)**	**Material**	**Relative construct stiffness (%)**
Alho *et al.* (320)	Cadaver / 50 mm midshaft SD	GK slotted	440 / 14	SS	9
		GK, non-slotted	440 / 14	SS	38
		AO/ASIF	440 / 14	SS	8
Current	Sawbone® / 1 mm T	ALFN	300 / 8.2	TAN	IR-27 ER-26
Current	Sawbone® / 10 mm C	ALFN	300 / 8.2	TAN	IR-25 ER-22
Current	Sawbone® / 10 mm SD	ALFN	300 / 8.2	TAN	IR-24 ER-21

9.2.2 Comparison with data on other implants

A brief survey comparing the ALFN with the biomechanical studies of other implants used for paediatric femur fracture fixation such as flexible intramedullary nails, external fixator and plate/screws is presented below in Table 9-4, Table 9-5 and Table 9-6.

Although the test set up in these studies is varied, certain general observations can be made with respect to the ALFN. In general, higher stiffness parameters of the femur/ALFN construct under higher magnitude of axial and torsional loading conditions in comparison to the other implants. Under bending conditions similar if not higher stiffness parameters were noted

Table 9-4 Axial compression data from literature for different implants used in paediatric femur fracture fixation

T–transverse, C–comminuted, SD–segmental defect, SS–stainless steel, Ti-titanium, Fl-flexible, N-newton, Ex-fix – external fixator

Study	Femur specimen / Length (mm) / Canal diameter (mm)	Fracture Type	Implants	Max Load (N)	Mean axial stiffness (N/mm)
Volpon *et al.* (56)	Sawbone® / 350 / 9.5	SD	Fl nail (Ti) 3.5 mm x 2	85	145.23
			Fl nail (Ti) 3.5 mm x 2 + End cap	85	157.94
Mani *et al.* (291)	Sawbone® / 450 / 9.0	T	Fl nail (SS) 3.5 mm x 2	400	580.00
			Fl nail (SS) 3.5 mm x 2 + End cap	400	620.00
			Fl nail (Ti) 3.5 mm x 2	400	780.00
			Fl nail (Ti) 4.0 mm x 2	400	600.00
			Ex-fix	400	610.00
			Double Ex-fix	400	600.00
Mahar *et al.* (292)	Sawbone® / 380 / 9.0	T	Fl nail (Ti) 3.5 mm x 2	50	892.00
			Fl nail (SS) 3.5 mm x 2	50	463.00

Table 9-4 continued					
Study	**Femur specimen / Length (mm) / Canal diameter (mm)**	**Fracture Type**	**Implants**	**Max Load (N)**	**Mean axial stiffness (N/mm)**
Mani *et al.* (291)	Sawbone® / 450 / 9.0	C	Fl nail (SS) 3.5 mm x 2	400	590.00
			Fl nail (SS) 3.5 mm x 2 + End cap	400	420.00
			Fl nail (Ti) 3.5 mm x 2	400	410.00
			Fl nail (Ti) 4.0 mm x 2	400	500.00
			Ex-fix	400	700.00
			Double Ex-fix	400	680.00
Green *et al.* (293)	Sawbone® / 280 / 8.0	T	Fl nail (Ti) 2.0 mm x 2	85	620.00
			Fl nail (Ti) 2.0 mm + 3.0 mm	85	700.00
			Fl nail (Ti) 3.0 mm x 2	85	640.00
			Fl nail (Ti) 3.0 mm + 4.0 mm	85	790.00
			Fl nail (Ti) 2.0 mm + 3.0 mm + 4.0 mm	85	620.00
			Fl nail (Ti) 4.0 mm x 2	85	610.00

Table 9-4 continued					
Study	**Femur specimen / Length (mm) / Canal diameter (mm)**	**Fracture Type**	**Implants**	**Max Load (N)**	**Mean axial stiffness (N/mm)**
Mahar *et al.* (292)	Sawbone® / 380 / 9.0	C	Fl nail (Ti) 3.5 mm x 2	50	792.00
			Fl nail (SS) 3.5 mm x 2	50	447.00
Lee *et al.* (75)	Sawbone® / 380 / 9.0	T	Fl nail (SS) 3.5 mm x 2	50	547.00
Lee *et al.* (75)	Sawbone® / 380 / 9.0	C	Fl nail (SS) 3.5 mm x 2	50	532.00
Current	Sawbone® / 375 / 9.5	T	ALFN	300	622.84
Current	Sawbone® / 375 / 9.5	C	ALFN	300	593.62
Current	Sawbone® / 375 / 9.5	SD	ALFN	300	562.04

It is evident from the above that the ALFN provides good stability under higher axial load compared to the flexible nails. Mani *et al.* (291) used a total of eight composite femurs to assess six different modes of fixation. Furthermore, the same specimen used to assess external fixation (with multiple drill holes in the shaft) of a comminuted fracture was also used to assess titanium flexible nails. Hence the possibility of methodological discrepancy and the subsequent effect on their data needs to be considered.

Table 9-5 Bending test data from literature of different implants used in paediatric femur fracture fixation

T–transverse, C–comminuted, SD–segmental defect, SS–stainless steel, Ti-titanium, Fl-flexible, N-newton, Ex-fix – external fixator, NR-not reported

Study	Femur specimen / Length (mm) / Canal diameter (mm)	Fracture Type	Implants	Max Load (N)	Mean bending stiffness (N/mm)
Volpon *et al.* (56)	Sawbone® / 350 / 9.5	SD	Fl nail (Ti) 3.5 mm x 2	67	66.27
			Fl nail (Ti) 3.5 mm x 2 + End cap	67	66.99
Mani *et al.* (291)	Sawbone® / 450 / 9.0	T	Fl nail (SS) 3.5 mm x 2	400	55.00
			Fl nail (SS) 3.5 mm x 2 + End cap	400	50.00
			Fl nail (Ti) 3.5 mm x 2	400	40.00
			Fl nail (Ti) 4.0 mm x 2	400	55.00
			Ex-fix	400	180.00
			Double Ex-fix	400	240.00
Mani *et al.* (291)	Sawbone® / 450 / 9.0	C	Fl nail (SS) 3.5 mm x 2	400	45.00
			Fl nail (SS) 3.5 mm x 2 + End cap	400	50.00
			Fl nail (Ti) 3.5 mm x 2	400	45.00

Table 9-5 continued

Study	Femur specimen / Length (mm) / Canal diameter (mm)	Fracture Type	Implants	Max Load (N)	Mean bending stiffness (N/mm)
Mani *et al.* (291)	Sawbone® / 450 / 9.0	C	Fl nail (Ti) 4.0 mm x 2	400	40.00
			Ex-fix	400	145.00
			Double Ex-fix	400	160.00
Green *et al.* (293)	Sawbone® / 280 / 8.0	T	Fl nail (Ti) 2.0 mm x 2	67	4.00
			Fl nail (Ti) 2.0 mm + 3.0 mm	67	12.00
			Fl nail (Ti) 3.0 mm x 2	67	14.00
			Fl nail (Ti) 3.0 mm + 4.0 mm	67	29.00
			Fl nail (Ti) 2.0 mm + 3.0 mm + 4.0 mm	67	20.00
			Fl nail (Ti) 4.0 mm x 2	67	55.00
Li *et al.* (294)	Sawbone® / 350 / 9.5	T	Fl nail (Ti) 4.0 mm x 2	628	42.00
Doser *et al.* (58)	Sawbone® / 455 / 13.0	T	Fl nail (Ti) 4.0 mm x 2 Prebent 0°	NR	17.03

Table 9-5 continued					
Study	**Femur specimen / Length (mm) / Canal diameter (mm)**	**Fracture Type**	**Implants**	**Max Load (N)**	**Mean bending stiffness (N/mm)**
Doser *et al.* (58)	Sawbone® / 455 / 13.0	T	Fl nail (Ti) 4.0 mm x 2 Prebent 30°	NR	15.04
			Fl nail (Ti) 4.0 mm x 2 Prebent 45°		14.80
			Fl nail (Ti) 4.0 mm x 2 Prebent 60°		12.20
Current	Sawbone® / 375 / 9.5	T	ALFN	60	102.53
Current	Sawbone® / 375 / 9.5	C	ALFN	60	93.44
Current	Sawbone® / 375 / 9.5	SD	ALFN	60	88.06

It can be observed that of the above studies only Mani *et al.* used higher load (400 N) whilst performing four-point bending tests on flexible intramedullary nails. However, as highlighted before the apparent methodological discrepancy introduced by using the same specimen to test multiple fixation modalities limits the robustness of their data.

Table 9-6 Torsion test data from literature of different implants used in paediatric femur fracture fixation

LO-long oblique, S-spiral, B-butterfly, T–transverse, C–comminuted, SD–segmental defect, SS–stainless steel, Ti-titanium, Fl-flexible, LCP-locking compression plate, Ex-fix – external fixator, NR-not reported

Study	Femur specimen / Length (mm) / Canal diameter (mm)	Fracture Type	Implants	Max torque (N m) / Failure point (degree)	Mean torsional stiffness (N m/deg)
Porter *et al.* (306)	Sawbone® / 445 / 10.0	LO	Fl nail (Ti) 4.0 mm x 2	NR	2.52
			4.5 mm LCP (Ti) 16 hole	NR	4.92
Porter *et al.* (306)	Sawbone® / 445 / 10.0	C	Fl nail (Ti) 4.0 mm x 2	NR	0.34
			4.5 mm LCP (Ti) 16 hole	NR	1.20
Mani *et al.* (291)	Sawbone® / 450 / 9.0	T	Fl nail (SS) 3.5 mm x 2	2 / 10°	0.70
			Fl nail (SS) 3.5 mm x 2 + End cap	2 /10°	0.50
			Fl nail (Ti) 3.5 mm x 2	2 / 10°	0.70
			Fl nail (Ti) 4.0 mm x 2	2 / 10°	0.50
			Ex-fix	2 / 10°	0.10
			Double Ex-fix	2 / 10°	0.10

Table 9-6 continued					
Study	**Femur specimen / Length (mm) / Canal diameter (mm)**	**Fracture Type**	**Implants**	**Max torque (N m) / Failure point (degree)**	**Mean torsional stiffness (N m/deg)**
Mani *et al.* (291)	Sawbone® / 450 / 9.0	C	Fl nail (SS) 3.5 mm x 2	2 / 10°	0.90
			Fl nail (SS) 3.5 mm x 2 + End cap	2 / 10°	0.90
			Fl nail (Ti) 3.5 mm x 2	2 / 10°	1.10
			Fl nail (Ti) 4.0 mm x 2	2 / 10°	0.60
			Ex-fix	2 / 10°	0.10
			Double Ex-fix	2 / 10°	0.10
Green *et al.* (293)	Sawbone® / 280 / 8.0	T	Fl nail (Ti) 2.0 mm x 2	2 / NR	ER – 0.006 IR – 0.005
			Fl nail (Ti) 2.0 mm + 3.0 mm	2 / NR	ER – 0.014 IR – 0.013
			Fl nail (Ti) 3.0 mm x 2	2 / NR	ER – 0.008 IR – 0.005
			Fl nail (Ti) 3.0 mm + 4.0 mm	2 / NR	ER – 0.011 IR – 0.009
			Fl nail (Ti) 2.0 mm + 3.0 mm + 4.0 mm	2 / NR	ER – 0.015 IR – 0.017
			Fl nail (Ti) 4.0 mm x 2	2 / NR	ER – 0.026 IR – 0.025

Table 9-6 continued					
Study	**Femur specimen / Length (mm) / Canal diameter (mm)**	**Fracture Type**	**Implants**	**Max torque (N m) / Failure point (degree)**	**Mean torsional stiffness (N m/deg)**
Lee *et al.* (75)	Sawbone® / 380 / 9.0	T	Fl nail (SS) 3.5 mm x 2	1 / NR	0.09
Lee *et al.* (75)	Sawbone® / 380 / 9.0	C	Fl nail (SS) 3.5 mm x 2	1 / NR	0.08
Gwyn *et al.* (72)	Sawbone® / NR / 9.0	T	Fl nail (Ti) 4.0 mm x 2	NR / 15°	ER – 0.12 IR – 0.11
		O	Fl nail (Ti) 4.0 mm x 2		ER – 0.19 IR – 0.24
		S	Fl nail (Ti) 4.0 mm x 2		ER – 0.45 IR – 0.19
		B	Fl nail (Ti) 4.0 mm x 2		ER – 0.18 IR – 0.14
		C	Fl nail (Ti) 4.0 mm x 2		ER – 0.14 IR – 0.12
Fricka *et al.* (295)	Sawbone® / 380 / 9.0	T	Fl nail (Ti) 3.5 mm x 2 Antegrade	1 / NR	0.07
			Fl nail (Ti) 3.5 mm x 2 Retrograde		0.10
Fricka *et al.* (295)	Sawbone® / 380 / 9.0	C	Fl nail (Ti) 3.5 mm x 2 Antegrade	1 / NR	0.06
					9

Table 9-6 continued					
Study	**Femur specimen / Length (mm) / Canal diameter (mm)**	**Fracture Type**	**Implants**	**Max torque (N m) / Failure point (°)**	**Mean torsional stiffness (N m/deg)**
Fricka *et al.* (295)	Sawbone® / 380 / 9.0	C	Fl nail (Ti) 3.5 mm x 2 Retrograde	1 / NR	0.11
Kaiser *et al.* (57)	Sawbone® / 450 / 10.0	S	Fl nail (SS) 3.5 mm x 2 Prebent 0°	NR / 10°	ER – 0.20 IR – 0.14
			Fl nail (SS) 3.5 mm x 2 Prebent 30°		ER – 0.15 IR – 0.18
			Fl nail (SS) 3.5 mm x 2 Prebent 60°		ER – 0.32 IR – 0.14
Current study	Sawbone® / 375 / 9.5	T	ALFN	2 / 10°	ER – 0.96 IR – 1.04
Current study	Sawbone® / 375 / 9.5	C	ALFN	2 / 10°	ER – 0.82 IR – 0.97
Current study	Sawbone® / 375 / 9.5	SD	ALFN	2 / 10°	ER – 0.77 IR – 0.91

As per the criteria proposed by Flynn *et al.* (24) to evaluate paediatric femur fixation malunion > 10° leads to poor clinical outcomes. A major advantage of rigid interlocking intramedullary nail fixation is the rotational stability (241, 473, 493, 540, 541). Hence, a comparison of the angular displacement during torsion tests of ALFN is presented in Table 9-7.

Table 9-7 Comparison of angular rotation of different fixation methods

T–transverse, C–comminuted, SD–segmental defect, SS–stainless steel, Ti-titanium, Fl-flexible, LCP-locking compression plate, Ex-fix – external fixator, NR-not reported

Study	Femur specimen / Length (mm) / Canal diameter (mm)	Fracture Type	Implants	Torque (N m)	Angular rotation (degree) (Mean±SD)
Volpon *et al.* (56)	Sawbone® / 350 / 9.5	SD	Fl nail (Ti) 3.5 mm x 2	1.26	20.0±NR
			Fl nail (Ti) 3.5 mm x 2 + End cap	1.44	20.0±NR
Mahar *et al.* (292)	Sawbone® / 380 / 9.0	T	Fl nail (Ti) 3.5 mm x 2	1.00	18.4±3.7
			Fl nail (SS) 3.5 mm x 2	1.00	22.7±4.0
Mahar *et al.* (292)	Sawbone® / 380 / 9.0	C	Fl nail (Ti) 3.5 mm x 2	1.00	18.5±3.2
			Fl nail (SS) 3.5 mm x 2	1.00	24.3±4.8
Goodwin *et al.* (66)	Sawbone® / NR / 9.0	SD midshaft	Fl nail (Ti) 3.5 mm x 2 Antegrade	1.00	32.0±8.0
		SD midshaft	Fl nail (Ti) 3.5 mm x 2 Retrograde	1.00	37.0±7.0
		SD distal third	Fl nail (Ti) 3.5 mm x 2 Antegrade	1.00	41.0±3.0

Table 9-7 continued					
Study	**Femur specimen / Length (mm) / Canal diameter (mm)**	**Fracture Type**	**Implants**	**Torque (N m)**	**Angular rotation (degree) (Mean±SD)**
Goodwin *et al.* (66)	Sawbone® / NR / 9.0	SD distal third	Fl nail (Ti) 3.5 mm x 2 Retrograde	1.00	41.0±15.0
Mahar *et al.* (296)	Sawbone® / 380 / 9.0	SD midshaft	Fl nail (Ti) 3.0 mm x 2	2.00	163.0±5.0
			Fl nail (Ti) 3.5 mm x 2	2.00	46.0±6.0
			Fl nail (Ti) 4.0 mm x 2	2.00	21.0±4.0
Fricka *et al.* (295)	Sawbone® / 380 / 9.0	T	Fl nail (Ti) 3.5 mm x 2 Antegrade	1.00	30.9±8.3
			Fl nail (Ti) 3.5 mm x 2 Retrograde	1.00	18.4±3.7
Fricka *et al.* (295)	Sawbone® / 380 / 9.0	C	Fl nail (Ti) 3.5 mm x 2 Antegrade	1.00	32.1±7.6
			Fl nail (Ti) 3.5 mm x 2 Retrograde	1.00	18.5±3.2
Lee *et al.* (75)	Sawbone® / 380 / 9.0	T	Fl nail (SS) 3.5 mm x 2	1.00	22.2±1.9

Table 9-7 continued					
Study	**Femur specimen / Length (mm) / Canal diameter (mm)**	**Fracture Type**	**Implants**	**Torque (N m)**	**Angular rotation (degree) (Mean±SD)**
Lee *et al.* (75)	Sawbone® / 380 / 9.0	C	Fl nail (SS) 3.5 mm x 2	1.00	24.1±2.4
Current study	Sawbone® / 375 / 9.5	T	ALFN	2.00	ER- 2.3±0.3 IR- 2.0±0.2
Current study	Sawbone® / 375 / 9.5	C	ALFN	2.00	ER- 2.8±0.3 IR- 2.3±0.5
Current study	Sawbone® / 375 / 9.5	SD	ALFN	2.00	ER- 2.9±0.3 IR- 2.3±0.5

It can be noted that the angular rotation for paediatric femur fracture fixation with ALFN is less than other modalities by a factor ranging from ten to forty. This compares favorably with the only clinical study on ALFN (29) in which no malunion was reported.

9.2.3 Simplified FEA model of paediatric femur

It was demonstrated that orthogonal digital radiographs can be used as a template to develop a FEA model of the paediatric femur that is simple yet representative of the overall dimensions and features viz. radius of curvature (350). Simplified FEA models of paediatric femur and paediatric femur fracture fixation with ALFN were developed in SolidWorks^{TM} and successfully validated with experimental data for axial compression, four-point bending and torsion tests in external/internal rotation.

9.2.4 Fracture and implant factors

Overall only a small variation in stiffness parameters was noted due to a change in the fracture level and geometry. However, the tendency of the proximal portion of the ALFN to displace in an anteromedial direction under axial load may have implications for fractures in this region.

Fracture healing over a duration of 16 weeks results in a decrease in von Mises stress noted in the ALFN. Correspondingly simulation tests predicted the stiffness of the femur/ALFN construct to approach that of the intact femur around 16 weeks.

It was demonstrated using the Taguchi method and FEA that implant parameters such as the relative angle between the ALFN and proximal interlocking screw along with the type of material used in the nail manufacture can have a major influence on stress in the proximal portion of the ALFN.

9.2.5 Clinical implications - partial weight-bearing is safe

Using a combination of biomechanical testing and FEA it was demonstrated that the paediatric femur/AFLN construct provides adequate stability as evident with the stiffness parameters. Additionally the maximum predicted von Mises stress in the ALFN appear to be within an acceptable range.

Hence in a paediatric patient (weighing upto 60 kg) with a femoral shaft fracture fixation with the ALFN, partial weight-bearing (up to 50%) can be safely undertaken in the perioperative period. Following operative fixation the stiffness improves with fracture healing and approaches that of the intact femur around 16 weeks.

9.3 Limitations and scope for future work

The paediatric femur has a complex shape and microarchitecture both of which contribute towards load transmission during weight-bearing and activity. The simulation model in the current study was an attempt to simplify the femur anatomy using a basic geometric entity like a cylinder. Hence the results from this model can be used only as a general guide to predict the behavior of the paediatric femur under different loading conditions. Furthermore, the forces experienced by the paediatric and intramedullary nail *in vivo* are of a complex nature and have not been clearly defined. Information available from the adult literature in this research area (249) has provided some insight. Accurate assessment using simulation models comes at the cost of significant computational resources (344, 542). However, this was not the main objective of the current study. In general simulation studies are based on a set of assumptions which are the inherent limitations and the current study is no exception to this rule.

In the current study due to the aforementioned reasons a simplified experimental setup and FEA model were used whereas the paediatric femur has complex architecture and with multiple *in vivo* loads. Telemetric nail technology (499, 543-545), three-dimensional gait analysis (398, 546, 547) and electromyography (548-552) have rapidly evolved in the recent past. A combination of these technologies and devices can be used in future clinical studies. This would enable access to very useful data regarding *in vivo* loads thereby allowing a considerable improvement in our understanding in this field.

Subsequent to the commencement of this study, the manufacturer of ALFN has introduced two other variants with 9 mm and 10 mm outer diameter in the distal portion (275). Furthermore, different multiplanar rigid (553-555) and semi-rigid (556) nails from other manufacturers have also been released for clinical use in the paediatric population. A comparative biomechanical study of these nails will be useful to evaluate the relative strengths and weaknesses of each design. This would enable the operating surgeon to make an appropriate implant selection whilst treating different types of fractures.

9.4 Conclusions

The current study has contributed novel biomechanical data regarding the ALFN. As demonstrated from the above biomechanical and simulation test results, ALFN provides adequate stability when used for fixation of common patterns (transverse, comminuted or segmental defect) of femoral shaft fractures noted in the adolescent population.

Adolescents undergoing femoral fracture fixation with ALFN can safely weight bear upto 50% of the body weight in the postoperative period. Following operative fixation the stiffness improves with fracture healing and approaches that of the intact femur around 16 weeks.

References

1. Bridgman S, Wilson R. Epidemiology of femoral fractures in children in the West Midlands region of England 1991 to 2001. J Bone Joint Surg Br. 2004;86(8):1152-7.

2. Hinton RY, Lincoln A, Crockett MM, Sponseller P*, et al.* Fractures of the femoral shaft in children. Incidence, mechanisms, and sociodemographic risk factors. J Bone Joint Surg Am. 1999;81(4):500-9.

3. Hosalkar HS, Pandya NK, Cho RH, Glaser DA*, et al.* Intramedullary nailing of pediatric femoral shaft fracture. The Journal of the American Academy of Orthopaedic Surgeons. 2011;19(8):472-81.

4. Hunter JB. Femoral shaft fractures in children. Injury. 2005;36 Suppl 1:A86-93.

5. Kocher MS, Sink EL, Blasier RD, Luhmann SJ*, et al.* American Academy of Orthopaedic Surgeons clinical practice guideline on treatment of pediatric diaphyseal femur fracture. J Bone Joint Surg Am. 2010;92(8):1790-2.

6. Leet AI, Pichard CP, Ain MC. Surgical treatment of femoral fractures in obese children: does excessive body weight increase the rate of complications? J Bone Joint Surg Am. 2005;87(12):2609-13.

7. Ziv I, Blackburn N, Rang M. Femoral intramedullary nailing in the growing child. J Trauma. 1984;24(5):432-4.

8. Galpin RD, Willis RB, Sabano N. Intramedullary nailing of pediatric femoral fractures. J Pediatr Orthop. 1994;14(2):184-9.

9. Herndon WA, Mahnken RF, Yngve DA, Sullivan JA. Management of femoral shaft fractures in the adolescent. J Pediatr Orthop. 1989;9(1):29-32.

10. Valdiserri L, Marchiodi L, Rubbini L. Kuntscher nailing in the treatment of femoral fractures in children. Is it completely contraindicated? Ital J Orthop Traumatol. 1983;9(3):293-6.

11. Stans AA, Morrissy RT, Renwick SE. Femoral shaft fracture treatment in patients age 6 to 16 years. J Pediatr Orthop. 1999;19(2):222-8.

12. Buford D, Christensen K, Weatherall P. Intramedullary nailing of femoral fractures in adolescents. Clin Orthop Relat Res. 1998(350):85-9.

13. Gonzalez-Herranz P, Burgos-Flores J, Rapariz JM, Lopez-Mondejar JA*, et al.* Intramedullary nailing of the femur in children. Effects on its proximal end. J Bone Joint Surg Br. 1995;77(2):262-6.

14. Gordon JE, Khanna N, Luhmann SJ, Dobbs MB*, et al.* Intramedullary nailing of femoral fractures in children through the lateral aspect of the greater trochanter using a modified rigid humeral intramedullary nail: preliminary results of a new technique in 15 children. J Orthop Trauma. 2004;18(7):416-22.

15. Fernandez Dell'Oca AA. The principle of helical implants. Unusual ideas worth considering. Injury. 2002;33 Suppl 1:SA1-27.

16. Ehmke LW, Polzin BM, Madey SM, Bottlang M. Femoral nailing through the trochanter: the reamer pathway indicates a helical nail shape. J Orthop Trauma. 2006;20(10):668-74.

17. Harper MC, Carson WL. Curvature of the femur and the proximal entry point for an intramedullary rod. Clin Orthop Relat Res. 1987(220):155-61.

18. Egol KA, Chang EY, Cvitkovic J, Kummer FJ*, et al.* Mismatch of current intramedullary nails with the anterior bow of the femur. J Orthop Trauma. 2004;18(7):410-5.

19. Reynolds RA, Legakis JE, Thomas R, Slongo TF*, et al.* Intramedullary nails for pediatric diaphyseal femur fractures in older, heavier children: early results. Journal of children's orthopaedics. 2012;6(3):181-8.

20. Synthes. Expert ALFN. Adolescent Lateral Femoral Nail 2014. Available from: http://www.synthes.com/MediaBin/International%20DATA/036.000.648.pdf.

21. Gregory P, Sullivan JA, Herndon WA. Adolescent femoral shaft fractures: rigid versus flexible nails. Orthopedics. 1995;18(7):645-9.

22. Kanellopoulos AD, Yiannakopoulos CK, Soucacos PN. Closed, locked intramedullary nailing of pediatric femoral shaft fractures through the tip of the greater trochanter. J Trauma. 2006;60(1):217-22; discussion 22-3.

23. Keeler KA, Dart B, Luhmann SJ, Schoenecker PL*, et al.* Antegrade intramedullary nailing of pediatric femoral fractures using an interlocking pediatric femoral nail and a lateral trochanteric entry point. J Pediatr Orthop. 2009;29(4):345-51.

24. Flynn JM, Hresko T, Reynolds RA, Blasier RD*, et al.* Titanium elastic nails for pediatric femur fractures: a multicenter study of early results with analysis of complications. J Pediatr Orthop. 2001;21(1):4-8.

25. Maruenda-Paulino JI, Sanchis-Alfonso V, Gomar-Sancho F, Darder-Prats A*, et al.* Kuntscher nailing of femoral shaft fractures in children and adolescents. International orthopaedics. 1993;17(3):158-61.

26. Edgren W. Coxa plana. A clinical and radiological investigation with particular reference to the importance of the metaphyseal changes for the final shape of the proximal part of the femur. Acta orthopaedica Scandinavica Supplementum. 1965:Suppl 84:1-129.

27. Townsend DR, Hoffinger S. Intramedullary nailing of femoral shaft fractures in children via the trochanter tip. Clin Orthop Relat Res. 2000(376):113-8.

28. The Oxford 2011 Levels of Evidence. Available from: http://www.cebm.net/index.aspx?o=5653.

29. Reynolds R, Legakis J, Thomas R, Slongo T*, et al.* Intramedullary nails for pediatric diaphyseal femur fractures in older, heavier children: early results. J Child Orthop. 2012(6):181-8.

30. Park H, Kim HW. Treatment of femoral shaft fracture with an interlocking humeral nail in older children and adolescents. Yonsei medical journal. 2012;53(2):408-15.

31. Park KC, Oh CW, Byun YS, Oh JK*, et al.* Intramedullary nailing versus submuscular plating in adolescent femoral fracture. Injury. 2012;43(6):870-5.

32. Garner MR, Bhat SB, Khujanazarov I, Flynn JM*, et al.* Fixation of length-stable femoral shaft fractures in heavier children: flexible nails vs rigid locked nails. J Pediatr Orthop. 2011;31(1):11-6.

33. Ramseier LE, Janicki JA, Weir S, Narayanan UG. Femoral fractures in adolescents: a comparison of four methods of fixation. J Bone Joint Surg Am. 2010;92(5):1122-9.

34. Jencikova-Celerin L, Phillips JH, Werk LN, Wiltrout SA*, et al.* Flexible interlocked nailing of pediatric femoral fractures: experience with a new flexible interlocking intramedullary nail compared with other fixation procedures. J Pediatr Orthop. 2008;28(8):864-73.

35. Mehlman CT, Bishai SK. Tibial nails for femoral shaft fractures in large adolescents with open femoral physes. Journal of Trauma and Acute Care Surgery. 2007;63(2):424-8.

36. Letts M, Jarvis J, Lawton L, Davidson D. Complications of rigid intramedullary rodding of femoral shaft fractures in children. J Trauma. 2002;52(3):504-16.

37. Tortolani PJ, Ain MC, Miller NH, Brumback RJ*, et al.* Tibial nails for femoral shaft fractures in adolescents: "off-label" usage. Orthopedics. 2001;24(6):553-7.

38. Momberger N, Stevens P, Smith J, Santora S*, et al.* Intramedullary nailing of femoral fractures in adolescents. J Pediatr Orthop. 2000;20(4):482-4.

39. Skak SV, Overgaard S, Nielsen JD, Andersen A*, et al.* Internal fixation of femoral shaft fractures in children and adolescents: a ten- to twenty-one-year follow-up of 52 fractures. J Pediatr Orthop B. 1996;5(3):195-9.

40. Beaty JH, Austin SM, Warner WC, Canale ST*, et al.* Interlocking intramedullary nailing of femoral-shaft fractures in adolescents: preliminary results and complications. J Pediatr Orthop. 1994;14(2):178-83.

41. Timmerman LA, Rab GT. Intramedullary nailing of femoral shaft fractures in adolescents. J Orthop Trauma. 1993;7(4):331-7.

42. Reeves RB, Ballard RI, Hughes JL. Internal fixation versus traction and casting of adolescent femoral shaft fractures. J Pediatr Orthop. 1990;10(5):592-5.

43. Kirby RM, Winquist RA, Hansen ST, Jr. Femoral shaft fractures in adolescents: a comparison between traction plus cast treatment and closed intramedullary nailing. J Pediatr Orthop. 1981;1(2):193-7.

44. Wu C, Tai C. A biomechanical comparison of unlocked or locked reamed intramedullary nails in the treatment of mid-third simple transverse femoral shaft fractures. Chang Gung medical journal. 2006;29(3):275-82.

45. Bankston AB, Keating EM, Saha S. The biomechanical evaluation of intramedullary nails in distal femoral shaft fractures. Clin Orthop Relat Res. 1992(276):277-82.

46. Rabenseifner L, Hirasawa Y. A comparative study of biomechanical property of Kuntscher nail and Otte-Plansee nail. Nihon geka hokan Archiv fur japanische Chirurgie. 1987;56(3):304-12.

47. Mileski RA, Garvin KL, Crosby LA. Avascular necrosis of the femoral head in an adolescent following intramedullary nailing of the femur. A case report. J Bone Joint Surg Am. 1994;76(11):1706-8.

48. Astion DJ, Wilber JH, Scoles PV. Avascular necrosis of the capital femoral epiphysis after intramedullary nailing for a fracture of the femoral shaft. A case report. J Bone Joint Surg Am. 1995;77(7):1092-4.

49. Prasarn ML, Cattaneo MD, Achor T, Ahn J*, et al.* The effect of entry point on malalignment and iatrogenic fracture with the Synthes lateral entry femoral nail. J Orthop Trauma. 2010;24(4):224-9.

50. MacNeil JA, Francis A, El-Hawary R. A systematic review of rigid, locked, intramedullary nail insertion sites and avascular necrosis of the femoral head in the skeletally immature. J Pediatr Orthop. 2011;31(4):377-80.

51. Blasier RD. Surgical Technique for Adolescent Femur Fractures: The Trochanteric Entry Intramedullary Nail. Operative Techniques in Orthopaedics. 2009;19(1):24-30.

52. Moroz LA, Launay F, Kocher MS, Newton PO*, et al.* Titanium elastic nailing of fractures of the femur in children. Predictors of complications and poor outcome. J Bone Joint Surg Br. 2006;88(10):1361-6.

53. Angadi DS, Shepherd DE, Vadivelu R, Barrett T. Rigid intramedullary nail fixation of femoral fractures in adolescents: what evidence is available? Journal of orthopaedics and traumatology : official journal of the Italian Society of Orthopaedics and Traumatology. 2013.

54. Dogan Ö, Minareci E, Vural CA, Daglar B*, et al.* Sa4.10 Retrograde versus retrograde combined with antegrade titanium elastic nail fixation of pediatric femoral-shaft fractures: a biomechanical study. Injury.44:S25.

55. Porter SE, Booker GR, Parsell DE, Weber MD*, et al.* Biomechanical analysis comparing titanium elastic nails with locked plating in two simulated pediatric femur fracture models. Journal of Pediatric Orthopaedics. 2012;32(6):587-93.

56. Volpon JB, Perina MM, Okubo R, Maranho DAC. Biomechanical performance of flexible intramedullary nails with end caps tested in distal segmental defects of pediatric femur models. Journal of Pediatric Orthopaedics. 2012;32(5):461-6.

57. Kaiser M, Zachert G, Wendlandt R, Eggert R*, et al.* Increasing stability by pre-bending the nails in elastic stable intramedullary nailing A biomechanical analysis of a synthetic femoral spiral fracture model. Journal of Bone & Joint Surgery, British Volume. 2012;94(5):713-8.

58. Doser A, Helwig P, Konstantinidis L, Kuminack KF*, et al.* Does the extent of prebending affect the stability of femoral shaft fractures stabilized by titanium elastic nails? A biomechanical investigation on an adolescent femur model. Journal of Pediatric Orthopaedics. 2011;31(8):834-8.

59. Kaiser MM, Zachert G, Wendlandt R, Rapp M*, et al.* Biomechanical analysis of a synthetic femoral spiral fracture model: do end caps improve retrograde flexible intramedullary nail fixation. J Orthop Surg Res. 2011;6:46.

60. Kaiser M, Wessel L, Zachert G, Stratmann C*, et al.* Biomechanical analysis of a synthetic femur spiral fracture model: Influence of different materials on the stiffness in flexible intramedullary nailing. Clinical Biomechanics. 2011;26(6):592-7.

61. Sagan ML, Datta JC, Olney BW, Lansford TJ*, et al.* Residual deformity after treatment of pediatric femur fractures with flexible titanium nails. Journal of Pediatric Orthopaedics. 2010;30(7):638-43.

62. Abosala AW, D; Cunningham, J. A Biomechanical Study of the Stability of Titanium Elastic Nails in the Treatment of Oblique Segmental Fracture of the Femur in Children. The

Internet Journal of Orthopedic Surgery [Internet]. 2010; 19(1). Available from: https://ispub.com/IJOS/19/1/11579.

63. Li Y, Stabile KJ, Shilt JS. Biomechanical analysis of titanium elastic nail fixation in a pediatric femur fracture model. Journal of Pediatric Orthopaedics. 2008;28(8):874-8.

64. Perez A, Mahar A, Negus C, Newton P*, et al.* A computational evaluation of the effect of intramedullary nail material properties on the stabilization of simulated femoral shaft fractures. Medical engineering & physics. 2008;30(6):755-60.

65. Mahar A, Sink E, Faro F, Oka R*, et al.* Differences in biomechanical stability of femur fracture fixation when using titanium nails of increasing diameter. Journal of children's orthopaedics. 2007;1(3):211-5.

66. Goodwin R, Mahar AT, Oka R, Steinman S*, et al.* Biomechanical evaluation of retrograde intramedullary stabilization for femoral fractures: the effect of fracture level. Journal of Pediatric Orthopaedics. 2007;27(8):873-6.

67. Mehlman CT, Nemeth NM, Glos DL. Antegrade versus retrograde titanium elastic nail fixation of pediatric distal-third femoral-shaft fractures: a mechanical study. Journal of orthopaedic trauma. 2006;20(9):608-12.

68. Mani US, Sabatino CT, Sabharwal S, Svach DJ*, et al.* Biomechanical comparison of flexible stainless steel and titanium nails with external fixation using a femur fracture model. Journal of Pediatric Orthopaedics. 2006;26(2):182-7.

69. Crist BD, Dart BR, Czuwala PJ, Olney BW*, et al.* Using flexible nails to improve stabilization of proximal femur fractures in adolescents. American journal of orthopedics (Belle Mead, NJ). 2006;35(1):37-41.

70. Green JK, Werner FW, Dhawan R, Evans PJ*, et al.* A biomechanical study on flexible intramedullary nails used to treat pediatric femoral fractures. Journal of Orthopaedic Research. 2005;23(6):1315-20.

71. Mahar AT, Lee SS, Lalonde FD, Impelluso T*, et al.* Biomechanical comparison of stainless steel and titanium nails for fixation of simulated femoral fractures. Journal of Pediatric Orthopaedics. 2004;24(6):638-41.

72. Gwyn DT, Olney BW, Dart BR, Czuwala PJ. Rotational control of various pediatric femur fractures stabilized with titanium elastic intramedullary nails. Journal of Pediatric Orthopaedics. 2004;24(2):172-7.

73. Fricka KB, Mahar AT, Lee SS, Newton PO. Biomechanical analysis of antegrade and retrograde flexible intramedullary nail fixation of pediatric femoral fractures using a synthetic bone model. Journal of Pediatric Orthopaedics. 2004;24(2):167-71.

74. Kiely N. Mechanical properties of different combinations of flexible nails in a model of a pediatric femoral fracture. Journal of Pediatric Orthopaedics. 2002;22(4):424-7.

75. Lee SS, Mahar AT, Newton PO. Ender nail fixation of pediatric femur fractures: a biomechanical analysis. Journal of Pediatric Orthopaedics. 2001;21(4):442-5.

76. Greis P, Ward WT, Rodosky M, Rudert MJ*, et al.* A Clinical And Comparative Biomechanical Evaluation Of Proximal Femoral Osteotomy Fixation In Children. Orthopedics. 1993;16(3):273-9.

77. Perez A, Mahar A, Negus C, Newton P*, et al.* A computational evaluation of the effect of intramedullary nail material properties on the stabilization of simulated femoral shaft fractures. Med Eng Phys. 2008;30(6):755-60.

78. Krauze A, Marciniak J. Numerical method in biomechanical analysis of intramedullary osteosynthesis in children. Journal of Achievements in Materials and Manufacturing Engineering. 2006;15(1-2):120-6.

79. Viceconti M, Casali M, Massari B, Cristofolini L, *et al.* The 'standardized femur program' proposal for a reference geometry to be used for the creation of finite element models of the femur. J Biomech. 1996;29(9):1241.

80. Thanos K. Bones of the Lower Limb 2015. Available from: https://courses.candelalearning.com/anatomyphysiology/chapter/chapter-8-the-appendicular-skeleton-2/#m46364-fs-id2661070.

81. Gray H. The Femur. Available from: http://www.bartleby.com/107/59.html.

82. Thanos K. Bone Tissue and the Skeletal System 2015. Available from: https://courses.candelalearning.com/anatomyphysiology/chapter/chapter-6-bone-tissue-and-the-skeletal-system-2/.

83. Leeson CRL, T.S. Human Structure: A Companion to Anatomical Studies1972.

84. Gray H. Anatomy of the Human Body. Available from: http://www.bartleby.com/107/1.html.

85. Recker RR. Embryology anatomy and microstructure of bone. Disorders of Bone and Mineral Metaholism. New York: Raven Press; 1992. p. 219-40.

86. Buckwalter J, Glimcher M, Cooper R, Recker R. Bone biology. J Bone Joint Surg Am. 1995;77(8):1256-75.

87. Buckwalter JA, Cruess, R. Healing of musculoskeletal tissues. Rockwood and Green's Fractures in Adults1991. p. 181-222.

88. Chiras D. Human Biology: Jones & Bartlett Learning; 2011.

89. Starr C. Biology: A Human Emphasis: Cengage Learning; 2005.

90. Arnett T. Regulation of bone cell function by acid–base balance. Proceedings of the Nutrition Society. 2003;62(02):511-20.

91. Green J, Kleeman CR. Role of bone in regulation of systemic acid-base balance. Kidney Int. 1991;39(1):9-26.

92. New SA. Nutrition Society Medal Lecture: The role of the skeleton in acid—base homeostasis. Proceedings of the Nutrition Society. 2002;61(02):151-64.

93. Burr DB, Akkus O. Chapter 1 - Bone Morphology and Organization. Basic and Applied Bone Biology2014. p. 3-25.

94. Morrison SJ, Scadden DT. The bone marrow niche for haematopoietic stem cells. Nature. 2014;505(7483):327-34.

95. Anthony BA, Link DC. Regulation of hematopoietic stem cells by bone marrow stromal cells. Trends in immunology. 2014;35(1):32-7.

96. Keaveny TM, Morgan EF, Yeh OC. Bone mechanics. Standard handbook of biomedical engineering and design. 2004:1-24.

97. Ram RR. Hierarchy Of Bone Structure Report. 2006.

98. Dobson J. Pioneers of osteogeny. Bone & Joint Journal. 1952;34(4):702-7.

99. Cowin SC, Doty SB. Tissue Mechanics: Springer; 2007.

100. Kim S-H, Chang S-H, Jung H-J. The finite element analysis of a fractured tibia applied by composite bone plates considering contact conditions and time-varying properties of curing tissues. Composite Structures. 2010;92(9):2109-18.

101. Triffit JT. The organic matrix of bone tissue. In: Urist MR, editor. Fundamental and Clinical Bone Physiology. Philadelphia: J.B.Lippincott; 1980. p. 45-82.

102. Bellido T, Plotkin LI, Bruzzaniti A. Chapter 2 - Bone Cells. Basic and Applied Bone Biology2014. p. 27-45.

103. Glimcher MJ. Composition, structure, and organization of bone and other mineralized tissues and the mechanism of calcification. Handbook of Physiology: Endocrinology1976. p. 25.

104. Abdelgawad A, Naga O. Introduction to Orthopedic Nomenclature. Pediatric Orthopedics: Springer New York; 2014. p. 1-14.

105. Dietz FR, Morcuende, J.A. Embryology and Development of the Musculoskeletal System. Lovell and Winter's Pediatric Orthopaedics2006. p. 27.

106. Arkader A, Skaggs DL. Chapter 2 - Physeal Injuries. Green's Skeletal Trauma in Children 2015. p. 16-35.

107. Langenskiold A. Role of the ossification groove of Ranvier in normal and pathologic bone growth: a review. J Pediatr Orthop. 1998;18(2):173-7.

108. Fenichel I, Evron Z, Nevo Z. The perichondrial ring as a reservoir for precartilaginous cells. In vivo model in young chicks' epiphysis. International orthopaedics. 2006;30(5):353-6.

109. Van der Eerden B, Karperien M, Wit J. Systemic and local regulation of the growth plate. Endocrine reviews. 2003;24(6):782-801.

110. Scheuer L, Black S, Cunningham C, Christie A. Developmental Juvenile Osteology: Elsevier Science; 2000.

111. Lee MC, Eberson CP. Growth and development of the child's hip. Orthop Clin North Am. 2006;37(2):119-32, v.

112. O'Rahilly R, Gardner E. The timing and sequence of events in the development of the limbs in the human embryo. Anatomy and embryology. 1975;148(1):1-23.

113. Siffert RS. Patterns of deformity of the developing hip. Clin Orthop Relat Res. 1981(160):14-29.

114. Anderson M, Green WT, Messner MB. Growth and predictions of growth in the lower extremities. J Bone Joint Surg Am. 1963;45-A:1-14.

115. Chung SM. The arterial supply of the developing proximal end of the human femur. J Bone Joint Surg Am. 1976;58(7):961-70.

116. Currey J. The structure and mechanics of bone. J Mater Sci. 2012;47(1):41-54.

117. Landis W. The strength of a calcified tissue depends in part on the molecular structure and organization of its constituent mineral crystals in their organic matrix. Bone. 1995;16(5):533-44.

118. Keller TS. Predicting the compressive mechanical behavior of bone. J Biomech. 1994;27(9):1159-68.

119. Ducheyne P, Heymans L, Martens M, Aernoudt E*, et al.* The mechanical behaviour of intracondylar cancellous bone of the femur at different loading rates. J Biomech. 1977;10(11/12):747-62.

120. Martin RB. Determinants of the mechanical properties of bones. J Biomech. 1991;24 Suppl 1:79-88.

121. Martens M, Van Audekercke R, Delport P, De Meester P*, et al.* The mechanical characteristics of cancellous bone at the upper femoral region. J Biomech. 1983;16(12):971-83.

122. Goldstein SA, Wilson DL, Sonstegard DA, Matthews LS. The mechanical properties of human tibial trabecular bone as a function of metaphyseal location. J Biomech. 1983;16(12):965-9.

123. Reilly DT, Burstein AH. The elastic and ultimate properties of compact bone tissue. J Biomech. 1975;8(6):393-405.

124. Reilly DT, Burstein AH, Frankel VH. The elastic modulus for bone. J Biomech. 1974;7(3):271-5.

125. Burstein AH, Currey JD, Frankel VH, Reilly DT. The ultimate properties of bone tissue: the effects of yielding. J Biomech. 1972;5(1):35-44.

126. Rho JY, Kuhn-Spearing L, Zioupos P. Mechanical properties and the hierarchical structure of bone. Med Eng Phys. 1998;20(2):92-102.

127. Zioupos P, Currey JD. Changes in the stiffness, strength, and toughness of human cortical bone with age. Bone. 1998;22(1):57-66.

128. Landis W. The strength of a calcified tissue depends in part on the molecular structure and organization of its constituent mineral crystals in their organic matrix. Bone. 1995;16(5):533-44.

129. van der Linden JC, Birkenhager-Frenkel DH, Verhaar JA, Weinans H. Trabecular bone's mechanical properties are affected by its non-uniform mineral distribution. J Biomech. 2001;34(12):1573-80.

130. Goldstein SA. The mechanical properties of trabecular bone: dependence on anatomic location and function. J Biomech. 1987;20(11-12):1055-61.

131. Carter DR, Hayes WC. Bone compressive strength: the influence of density and strain rate. Science. 1976;194(4270):1174-6.

132. Ding M, Danielsen CC, Hvid I, Overgaard S. Three-dimensional microarchitecture of adolescent cancellous bone. Bone. 2012;51(5):953-60.

133. Ohman C, Baleani M, Pani C, Taddei F*, et al.* Compressive behaviour of child and adult cortical bone. Bone. 2011;49(4):769-76.

134. Hirsch C, Evans FG. Studies on Some Physical Properties of Infant Compact Bone. Acta Orthop Scand. 1965;35:300-13.

135. Thomas AE, Adele LB, Caren MG, Vincent JV*, et al.* The mineral and mechanical properties of bone in chronic experimental diabetes. Journal of Orthopaedic Research. 1988;6(3):317-23.

136. Reilly DT, Burstein AH. Review article. The mechanical properties of cortical bone. J Bone Joint Surg Am. 1974;56(5):1001-22.

137. Brear K, Currey JD, Raines S, Smith KJ. Density and temperature effects on some mechanical properties of cancellous bone. Engineering in medicine. 1988;17(4):163-7.

138. Bonfield W, Li CH. The temperature dependence of the deformation of bone. J Biomech. 1968;1(4):323-9.

139. An YH, Draughn RA. Mechanical Testing of Bone and the Bone-Implant Interface: CRC Press; 1999.

140. Burstein AH, Reilly DT, Martens M. Aging of bone tissue: mechanical properties. J Bone Joint Surg Am. 1976;58(1):82-6.

141. Cezayirlioglu H, Bahniuk E, Davy DT, Heiple KG. Anisotropic yield behavior of bone under combined axial force and torque. J Biomech. 1985;18(1):61-9.

142. Evans FG, Lebow M. Regional differences in some of the physical properties of the human femur. Journal of applied physiology. 1951;3(9):563-72.

143. Yamada H, Evans FG. Strength of biological materials: Williams & Wilkins; 1970.

144. Sedlin ED, Hirsch C. Factors affecting the determination of the physical properties of femoral cortical bone. Acta Orthop Scand. 1966;37(1):29-48.

145. Keller TS, Mao Z, Spengler DM. Young's modulus, bending strength, and tissue physical properties of human compact bone. J Orthop Res. 1990;8(4):592-603.

146. Lotz JC, Gerhart TN, Hayes WC. Mechanical properties of metaphyseal bone in the proximal femur. J Biomech. 1991;24(5):317-29.

147. Currey JD, Foreman J, Laketic I, Mitchell J*, et al.* Effects of ionizing radiation on the mechanical properties of human bone. J Orthop Res. 1997;15(1):111-7.

148. Hirsch C, da Silva O. The effect of orientation on some mechanical properties of femoral cortical specimens. Acta Orthop Scand. 1967;38(1):45-56.

149. Bonfield W, Grynpas MD. Anisotropy of the Young's modulus of bone. Nature. 1977;270(5636):453-4.

150. Katz JL. Anisotropy of Young's modulus of bone. Nature. 1980;283(5742):106-7.

151. Martin RB, Boardman DL. The effects of collagen fiber orientation, porosity, density, and mineralization on bovine cortical bone bending properties. J Biomech. 1993;26(9):1047-54.

152. Sasaki N, Matsushima N, Ikawa T, Yamamura H*, et al.* Orientation of bone mineral and its role in the anisotropic mechanical properties of bone--transverse anisotropy. J Biomech. 1989;22(2):157-64.

153. Kuhn JL, Goldstein SA, Ciarelli MJ, Matthews LS. The limitations of canine trabecular bone as a model for human: a biomechanical study. J Biomech. 1989;22(2):95-107.

154. Carter DR, Hayes WC. The compressive behavior of bone as a two-phase porous structure. J Bone Joint Surg Am. 1977;59(7):954-62.

155. Odgaard A, Hvid I, Linde F. Compressive axial strain distributions in cancellous bone specimens. J Biomech. 1989;22(8-9):829-35.

156. Linde F, Hvid I, Pongsoipetch B. Energy absorptive properties of human trabecular bone specimens during axial compression. J Orthop Res. 1989;7(3):432-9.

157. Keaveny TM, Pinilla TP, Crawford RP, Kopperdahl DL*, et al.* Systematic and random errors in compression testing of trabecular bone. J Orthop Res. 1997;15(1):101-10.

158. Ethier CR, Simmons CA. Introductory Biomechanics: From Cells to Organisms: Cambridge University Press; 2007.

159. Spatz HC, O'Leary EJ, Vincent JF. Young's moduli and shear moduli in cortical bone. Proceedings Biological sciences / The Royal Society. 1996;263(1368):287-94.

160. Gong JK, Arnold JS, Cohn SH. Composition of Trabecular and Cortical Bone. The Anatomical record. 1964;149:325-31.

161. Norrdin RW, Phemister RD, Jaenke RS, Lo Presti CA. Density and composition of trabecular and cortical bone in perinatally irradiated beagles with chronic renal failure. Calcified tissue research. 1977;24(1):99-104.

162. Mow VC, Huiskes R. Basic Orthopaedic Biomechanics & Mechano-biology: Lippincott Williams & Wilkins; 2005.

163. Gibson LJ. The mechanical behaviour of cancellous bone. J Biomech. 1985;18(5):317-28.

164. Hayes W, Gerhart T. Biomechanics of bone: applications for assessment of bone strength. Bone and mineral research1985. p. 259-94.

165. Hayes WC, Piazza SJ, Zysset PK. Biomechanics of fracture risk prediction of the hip and spine by quantitative computed tomography. Radiologic clinics of North America. 1991;29(1):1-18.

166. Hayes W, Bouxsein M. Biomechanics of cortical and trabecular bone: implications for assessment of fracture risk. Basic Orthopaedic Biomechanics1997.

167. Nordin M, Frankel VH. Basic Biomechanics of the Musculoskeletal System: Lippincott Williams and Wilkins; 2012.

168. Sammarco GJ, Burstein AH, Davis WL, Frankel VH. The biomechanics of torsional fractures: The effect of loading on ultimate properties. Journal of Biomechanics. 1971;4(2):113-7.

169. Natali AN, Meroi EA. A review of the biomechanical properties of bone as a material. Journal of Biomedical Engineering. 1989;11(4):266-76.

170. McElhaney JH. Dynamic response of bone and muscle tissue. Journal of applied physiology. 1966;21(4):1231-6.

171. Lakes RS, Katz JL. Viscoelastic properties of wet cortical bone II. Relaxation mechanisms. Journal of Biomechanics. 1979;12(9):679-87.

172. Schmitt KU, Cronin DS, Muser MH, Walz F. Trauma Biomechanics: An Introduction to Injury Biomechanics2014.

173. Marsell R, Einhorn TA. The biology of fracture healing. Injury. 2011;42(6):551-5.

174. Mckibbin B, editor The biology of fracture healing in long bones. J Bone Joint Surg Br; 1978.

175. Perren S. Physical and biological aspects of fracture healing with special reference to internal fixation. Clinical orthopaedics and related research. 1979;138:175-96.

176. Frick SL. Chapter 1 - Skeletal Growth, Development, and Healing as Related to Pediatric Trauma. Green's Skeletal Trauma in Children (Fifth Edition)2015. p. 1-15.

177. Sfeir C, Ho L, Doll BA, Azari K*, et al.* Fracture repair. Bone Regeneration and Repair: Springer; 2005. p. 21-44.

178. Ito K, Perren SM. Biology of fracture healing. AO Principles of Fracture Management (Ruedi TP, Buckley RE, Moran CG, eds), AO Foundation Publishing, Davos. 2013.

179. Beaty JH, Rockwood CA, Kasser JR. Rockwood and Wilkins' Fractures in Children: Wolters Kluwer/Lippincott, Williams & Wilkins; 2010.

180. Calmar EA, Vinci RJ. The anatomy and physiology of bone fracture and healing. Clinical Pediatric Emergency Medicine. 2002;3(2):85-93.

181. Ramachandran M. Basic Orthopaedic Sciences: The Stanmore Guide: CRC Press; 2006.

182. Shapiro F. Bone development and its relation to fracture repair. The role of mesenchymal osteoblasts and surface osteoblasts. Eur Cell Mater. 2008;15(53):e76.

183. Willy C, Schneider P, Engelhardt M, Hargens A*, et al.* Richard von Volkmann. Clinical orthopaedics and related research. 2008;466(2):500-6.

184. Forriol F, Shapiro F. Bone development: interaction of molecular components and biophysical forces. Clinical orthopaedics and related research. 2005;432:14-33.

185. Wallace ME, Hoffman EB. Remodelling of angular deformity after femoral shaft fractures in children. Journal of Bone & Joint Surgery, British Volume. 1992;74(5):765-9.

186. Schatzker J, Tile M. The Rationale of Operative Fracture Care: Springer; 1996.

187. Poolman RW, Kocher MS, Bhandari M. Pediatric femoral fractures: a systematic review of 2422 cases. J Orthop Trauma. 2006;20(9):648-54.

188. Shilt J, Li Y. Chapter 14 - Fractures of the Femoral Shaft. In: Swiontkowski GAMF, editor. Green's Skeletal Trauma in Children (Fifth Edition)2015. p. 365-89.

189. Abdelgawad AA, Sieg RN, Laughlin MD, Shunia J*, et al.* Submuscular bridge plating for complex pediatric femur fractures is reliable. Clin Orthop Relat Res. 2013;471(9):2797-807.

190. May C, Yen YM, Nasreddine AY, Hedequist D*, et al.* Complications of plate fixation of femoral shaft fractures in children and adolescents. J Child Orthop. 2013;7(3):235-43.

191. Anastasopoulos J, Petratos D, Konstantoulakis C, Plakogiannis C*, et al.* Flexible intramedullary nailing in paediatric femoral shaft fractures. Injury. 2010;41(6):578-82.

192. Salem KH, Lindemann I, Keppler P. Flexible intramedullary nailing in pediatric lower limb fractures. J Pediatr Orthop. 2006;26(4):505-9.

193. Chitgopkar SD. Flexible nailing of fractures in children using stainless steel Kirschner wires. J Pediatr Orthop B. 2008;17(5):251-5.

194. Salonen A, Lahdes-Vasama T, Mattila VM, Välipakka J*, et al.* Pitfalls of femoral Titanium Elastic Nailing. Scandinavian Journal of Surgery. 2015;104(2):121-6.

195. Ligier JN, Metaizeau JP, Prevot J, Lascombes P. Elastic stable intramedullary nailing of femoral shaft fractures in children. J Bone Joint Surg Br. 1988;70(1):74-7.

196. Metaizeau JP. Stable elastic intramedullary nailing for fractures of the femur in children. J Bone Joint Surg Br. 2004;86(7):954-7.

197. Thakur AJ. Elements of Fracture Fixation: Elsevier Health Sciences APAC; 2012.

198. Hunter JB. The principles of elastic stable intramedullary nailing in children. Injury. 2005;36(1, Supplement):S20-S4.

199. Luhmann SJ, Schootman M, Schoenecker PL, Dobbs MB*, et al.* Complications of titanium elastic nails for pediatric femoral shaft fractures. J Pediatr Orthop. 2003;23:443-7.

200. Sink EL, Gralla J, Repine M. Complications of pediatric femur fractures treated with titanium elastic nails: a comparison of fracture types. Journal of Pediatric Orthopaedics. 2005;25(5):577-80.

201. Eidelman M, Ghrayeb N, Katzman A, Keren Y. Submuscular plating of femoral fractures in children: the importance of anatomic plate precontouring. J Pediatr Orthop B. 2010;19(5):424-7.

202. Perren SM. Evolution of the internal fixation of long bone fractures. The scientific basis of biological internal fixation: choosing a new balance between stability and biology. J Bone Joint Surg Br. 2002;84(8):1093-110.

203. Kanlic EM, Anglen JO, Smith DG, Morgan SJ*, et al.* Advantages of submuscular bridge plating for complex pediatric femur fractures. Clinical orthopaedics and related research. 2004;426:244-51.

204. Sink EL, Hedequist D, Morgan SJ, Hresko T. Results and technique of unstable pediatric femoral fractures treated with submuscular bridge plating. Journal of Pediatric Orthopaedics. 2006;26(2):177-81.

205. Hedequist DJ, Sink E. Technical aspects of bridge plating for pediatric femur fractures. Journal of orthopaedic trauma. 2005;19(4):276-9.

206. Agus H, Kalenderer Ö, Eryanilmaz G, Ömeroglu H. Biological internal fixation of comminuted femur shaft fractures by bridge plating in children. Journal of Pediatric Orthopaedics. 2003;23(2):184-9.

207. Loder RT, Feinberg JR. Orthopaedic implants in children: survey results regarding routine removal by the pediatric and nonpediatric specialists. Journal of Pediatric Orthopaedics. 2006;26(4):510-9.

208. Lovell M, Galasko C, Wright N. Removal of orthopedic implants in children: morbidity and postoperative radiologic changes. Journal of Pediatric Orthopaedics B. 1999;8(2):144-6.

209. Kahle WK. The case against routine metal removal. Journal of Pediatric Orthopaedics. 1994;14(2):229-37.

210. Pate O, Hedequist D, Leong N, Hresko T. Implant removal after submuscular plating for pediatric femur fractures. Journal of Pediatric Orthopaedics. 2009;29(7):709-12.

211. Bae J, Oh J, Oh C, Hur C. Technical difficulties of removal of locking screw after locking compression plating. Archives of orthopaedic and trauma surgery. 2009;129(1):91-5.

212. Ehlinger M, Adam P, Simon P, Bonnomet F. Technical difficulties in hardware removal in titanium compression plates with locking screws. Orthopaedics & Traumatology: Surgery & Research. 2009;95(5):373-6.

213. Kumar G, Dunlop C. Case Report: A Technique to Remove a Jammed Locking Screw from a Locking Plate. Clinical Orthopaedics and Related Research®. 2011;469(2):613-6.

214. Ramseier LE, Janicki JA, Weir S, Narayanan UG. Femoral fractures in adolescents: a comparison of four methods of fixation. The Journal of Bone & Joint Surgery. 2010;92(5):1122-9.

215. Aronson J, Tursky EA. External Fixation of Femur Fractures in Children. Journal of Pediatric Orthopaedics. 1992;12(2):157-63.

216. Blasier RD, Aronson J, Tursky EA. External Fixation of Pediatric Femur Fractures. Journal of Pediatric Orthopaedics. 1997;17(3):342-6.

217. Sola J, Schoenecker PL, Gordon JE. External Fixation of Femoral Shaft Fractures in Children: Enhanced Stability with the Use of an Auxiliary Pin. Journal of Pediatric Orthopaedics. 1999;19(5):587.

218. Gregory P, Pevny T, Teague D. Early Complications with External Fixation of Pediatric Femoral Shaft Fractures. Journal of orthopaedic trauma. 1996;10(3):191-8.

219. Domb BG, Sponseller PD, Ain M, Miller NH. Comparison of Dynamic Versus Static External Fixation for Pediatric Femur Fractures. Journal of Pediatric Orthopaedics. 2002;22(4):428-30.

220. Bar-On E, Sagiv S, Porat S. External fixation or flexible intramedullary nailing for femoral shaft fractures in children. J Bone Joint Surg Br. 1997;79(6):975-8.

221. Flynn J, Skaggs D. Femoral Shaft Fractures. In: Beaty JHK, J.R., editor. Rockwood and Wilkins Fractures in Children. 7 ed: Lippincott Williams & Wilkins; 2010. p. 798-841.

222. Skaggs DL, Leet AI, Money MD, Shaw BA*, et al.* Secondary fractures associated with external fixation in pediatric femur fractures. Journal of Pediatric Orthopaedics. 1999;19(5):582.

223. Beaty JH. Operative Treatment of Femoral Shaft Fractures in Children and Adolescents. Clinical orthopaedics and related research. 2005;434:114-22.

224. Bong MR, Koval KJ, Egol KA. The history of intramedullary nailing. Bulletin of the NYU hospital for joint diseases. 2006;64(3-4):94-7.

225. Farill J. Orthopedics in Mexic. J Bone Joint Surg Am. 1952;24-A-3:506-12.

226. Bircher H. Eine neue Methode unmittelbarer Retention bei Frakturen der Röhrenknochen. Arch Klin Chir. 1886;34:410.

227. Gluck T. Autoplastic transplantation. Implantation von Fremdkörpern. Berl Klin Wochenschr. 1890:19.

228. Senn N. A new method of direct fixation of the fragments in compound and ununited fractures. Annals of surgery. 1893;XVIII.:125-51.

229. Nicolaysen J. Lidt on Diagnosen og Behandlungen av. Fr.colli femoris. Nord Med Ark. 1897;8:1.

230. Lilienthal H. Fracture of the femur: open operation with introduction of intramedullary splint. Ann Surg. 1911;53:541-2.

231. Schöne G. Zur Behandlung von Vorderarmfrakturen mit Bolzung. Münch Med Wschr. 1913;60:2327-8.

232. Burghard F. A System of Operative Surgery: London; 1914.

233. Hoglund E. New intramedullary bone implant. Surg Gynecol Obstet. 1917;24:243.

234. HeyGroves E. Ununited fractures with special reference to gunshot injuries and the use of bone grafting. Br J Surg. 1918;6:203.

235. Smith-Petersen M. Intracapsular fractures of the neck of the femur. Treatment by internal fixation. Arch Surg. 1931;23:715-59.

236. Küntscher G. Die Marknalung von Knochenbruchen. Langenbecks. Arch Klin Chir. 1940;200:443-55.

237. Vecsei V, Hajdu S, Negrin LL. Intramedullary nailing in fracture treatment: history, science and Kuntscher's revolutionary influence in Vienna, Austria. Injury. 2011;42 Suppl 4:S1-5.

238. Bohler L, Bohler J. Kutscher's medullary nailing. J Bone Joint Surg Am. 1949;31A(2):295-305.

239. Fischer AW MR. Weitere Erfahrungen mit der Marknagelung nach Küntscher. Arch Klin Chir. 1942;203:531.

240. Modny MT, Bambara J. The perforated cruciate intramedullary nail: preliminary report of its use in geriatric patients. Journal of the American Geriatrics Society. 1953;1(8):579-88.

241. Bong MR, Kummer FJ, Koval KJ, Egol KA. Intramedullary nailing of the lower extremity: biomechanics and biology. The Journal of the American Academy of Orthopaedic Surgeons. 2007;15(2):97-106.

242. Kempf I, Grosse A, Beck G. Closed locked intramedullary nailing. Its application to comminuted fractures of the femur. J Bone Joint Surg Am. 1985;67(5):709-20.

243. Russell TA. Intramedullary nailing: evolutions of femoral intramedullary nailing: first to fourth generations. J Orthop Trauma. 2011;25 Suppl 3:S135-8.

244. Kuntscher GB. The Kuntscher method of intramedullary fixation. J Bone Joint Surg Am. 1958;40-A(1):17-26.

245. Taylor JC, Russell, T.A, LaVelle, D,G and Calandruccio, R.A. Clinical Results of 100 Femoral Shaft Fractures Treated with the Russell-Taylor Interlocking Nail System. Annual Meeting of The American Academy of Orthopaedic Surgeons; Jan 26; San Francisco1987.

246. Stapert JW, Geesing CL, Jacobs PB, de Wit RJ*, et al.* First experience and complications with the long Gamma nail. J Trauma. 1993;34(3):394-400.

247. Horn J, Linke B, Hontzsch D, Gueorguiev B*, et al.* Angle stable interlocking screws improve construct stability of intramedullary nailing of distal tibia fractures: a biomechanical study. Injury. 2009;40(7):767-71.

248. Trigen Sureshot: Smith and Nephew Inc; 2010 [cited 2015]. Available from: http://www.smith-nephew.com/professional/products/all-products/trigen-sureshot/.

249. Schneider E, Michel MC, Genge M, Zuber K*, et al.* Loads acting in an intramedullary nail during fracture healing in the human femur. J Biomech. 2001;34(7):849-57.

250. Rommens P, Hessmann M. Intramedullary Nailing: A Comprehensive Guide: Springer; 2015.

251. Kempf I, Leung KS, Grosse A. Practice of Intramedullary Locked Nails: Scientific Basis and Standard Techniques: Springer Berlin Heidelberg; 2002.

252. Tencer AF, Sherman MC, Johnson KD. Biomechanical factors affecting fracture stability and femoral bursting in closed intramedullary rod fixation of femur fractures. Journal of biomechanical engineering. 1985;107(2):104-11.

253. Russell TA, Taylor JC, LaVelle DG, Beals NB*, et al.* Mechanical characterization of femoral interlocking intramedullary nailing systems. Journal of orthopaedic trauma. 1991;5(3):332-40.

254. Miles A, Eveleigh R, Wight B, Goodwin M. An investigation into the load transfer in interlocking intramedullary nails during simulated healing of a femoral fracture. Proceedings of the Institution of Mechanical Engineers, Part H: Journal of Engineering in Medicine. 1994;208(1):19-26.

255. Kyle R. Biomechanics of intramedullary fracture fixation. Orthopedics. 1985;8(11):1356-9.

256. Hajek P, Bicknell H, Bronson W, Albright J*, et al.* The use of one compared with two distal screws in the treatment of femoral shaft fractures with interlocking intramedullary nailing. A clinical and biomechanical analysis. The Journal of Bone & Joint Surgery. 1993;75(4):519-25.

257. Procter P, von Oldenburg G, von Wieding H, Speitling A. Materials Used for Intramedullary Devices. In: Kwok-Sui Leung IK, Volker Alt, Gilbert Taglang, H.J.T.M. Haarman, Hartmut Seidel, Reinhard Schnettler, editor. Practice of Intramedullary Locked Nails: New Developments in Techniques and Applications: Springer; 2006 p. 67-84.

258. Brumback R, Ellison T, Poka A, Bathon G*, et al.* Intramedullary nailing of femoral shaft fractures. Part III: Long-term effects of static interlocking fixation. The Journal of Bone & Joint Surgery. 1992;74(1):106-12.

259. Williams W, Parker B. Complications associated with the use of the Gamma nail. Injury. 1992;23(5):291-2.

260. Mazzocca A, DeAngelis J, Caputo A, Browner B*, et al.* Metallurgy. In: Browner BD, editor. Skeletal Trauma: Basic Science, Management, and Reconstruction: Saunders/Elsevier; 2009. p. 88.

261. ASTM F67-13, Standard Specification for Unalloyed Titanium, for Surgical Implant Applications (UNS R50250, UNS R50400, UNS R50550, UNS R50700). West Conshohocken, PA: ASTM International; 2013.

262. ASTM F136-13, Standard Specification for Wrought Titanium-6Aluminum-4Vanadium ELI (Extra Low Interstitial) Alloy for Surgical Implant Applications (UNS R56401). West Conshohocken, PA: ASTM International; 2013.

263. ASTM F1295-11, Standard Specification for Wrought Titanium-6Aluminum-7Niobium Alloy for Surgical Implant Applications (UNS R56700). West Conshohocken, PA: ASTM International; 2011.

264. Lin S, Lo C, Cheng S, Kuo M*, et al.* Use of reconstruction nails to manage ipsilateral displaced femoral neck-shaft fractures: assessment of a new approach. Journal of Orthopaedic Surgery. 2002;10(2).

265. Karachalios T, Atkins R, Sarangi P, Crichlow T*, et al.* Reconstruction nailing for pathological subtrochanteric fractures with coexisting femoral shaft metastases. Journal of Bone & Joint Surgery, British Volume. 1993;75(1):119-22.

266. Roberts CS, Nawab A, Wang M, Voor MJ*, et al.* Second generation intramedullary nailing of subtrochanteric femur fractures: a biomechanical study of fracture site motion. Journal of orthopaedic trauma. 2002;16(4):231-8.

267. Ricci W, Devinney S, Haidukewych G, Herscovici D*, et al.* Trochanteric nail insertion for the treatment of femoral shaft fractures. Journal of orthopaedic trauma. 2008;22(3):S2.

268. Bucholz RW, Ross SE, Lawrence KL. Fatigue fracture of the interlocking nail in the treatment of fractures of the distal part of the femoral shaft. J Bone Joint Surg Am. 1987;69(9):1391-9.

269. Tencer AF. Biomechanics of Fractures and Fracture Fixation. In: Bucholz RWH, J.D.; Court-Brown, C.M.; Tornetta, P., editor. Rockwood and Green's Fractures in Adults. 7 ed: Lippincott Williams & Wilkins; 2012. p. 3-38.

270. Antekeier SB, Burden Jr RL, Voor MJ, Roberts CS. Mechanical study of the safe distance between distal femoral fracture site and distal locking screws in antegrade intramedullary nailing. Journal of orthopaedic trauma. 2005;19(10):693-7.

271. Giannoudis P, Schneider E. Principles of fixation of osteoporotic fractures. Journal of Bone & Joint Surgery, British Volume. 2006;88(10):1272-8.

272. Wähnert D, Hoffmeier KL, von Oldenburg G, Fröber R*, et al.* Internal Fixation of Type-C Distal Femoral Fractures in Osteoporotic Bone2010 2010-06-01 00:00:00. 1442-52 p.

273. Synthes. Expert Adolescent Lateral Femoral Nail 2014. Available from: http://www.synthes.com/MediaBin/International%20DATA/036.000.648.pdf.

274. Reynolds R. New Pediatric Products. In: Pohlemann T, editor. TK News Trauma 2009: AO Foundation; 2009. p. 27-8.

275. Reynolds R, Slongo T. Trauma Pediatric. In: Pohlemann T, editor. TK System Innovations: AO Foundation; 2010. p. 50.

276. Yuehuei H. An WRB, and Robert A. Draughn. Basic Concepts of Mechanical Property Measurement and Bone Biomechanics. In: Yuehuei H. An RAD, editor. Mechanical Testing of Bone and the Bone-Implant Interface: CRC Press; 1999. p. 23-39.

277. Miles AW, Gheduzzi S. Basic biomechanics and biomaterials. Surgery - Oxford International Edition.30(2):86-91.

278. Golish SR, Mihalko WM. Principles of biomechanics and biomaterials in orthopaedic surgery. J Bone Joint Surg Am. 2011;93(2):207-12.

279. Currey JD. The Shapes of Bones. Bones: Structure and Mechanics: Princeton University Press; 2013. p. 194-244.

280. Bauchau OA, Craig JI. Euler-Bernoulli beam theory. In: Bauchau OA, Craig JI, editors. Structural Analysis. Dordrecht: Springer Netherlands; 2009. p. 173-221.

281. Malik SS, Malik SS. Orthopaedic Biomechanics Made Easy: Cambridge University Press; 2015.

282. Hipp J, Hayes W. Biomechanics of Fractures. In: Browner BD, editor. Skeletal Trauma: Basic Science, Management, and Reconstruction: Saunders/Elsevier; 2009. p. 51-81.

283. Johnson K, Tencer A, Blumenthal S, August A*, et al.* Biomechanical performance of locked intramedullary nail systems in comminuted femoral shaft fractures. Clinical orthopaedics and related research. 1986;206:151-61.

284. Bankston AB, Keating EM, Saha S. The biomechanical evaluation of intramedullary nails in distal femoral shaft fractures. Clinical orthopaedics and related research. 1992;276:277-82.

285. Butts MK, Bechtold JE, Hoeltzel DA, Kyle RF*, et al.* Testing method for evaluating bending stiffness and torsional stability of femurs implanted with intramedullary nails. Intramedullary Rods: Clinical Performance and Related Laboratory Testing. 1989;1008:20.

286. Cristofolini L, Viceconti M, Cappello A, Toni A. Mechanical validation of whole bone composite femur models. J Biomech. 1996;29(4):525-35.

287. Guidance for professionals: Human Tissue Authority; 2015. Available from: https://www.hta.gov.uk/policies/relevant-material-under-human-tissue-act-2004.

288. Heiner AD, Brown TD. Structural properties of a new design of composite replicate femurs and tibias. J Biomech. 2001;34(6):773-81.

289. Heiner AD. Structural properties of fourth-generation composite femurs and tibias. J Biomech. 2008;41(15):3282-4.

290. Gardner MP, Chong AC, Pollock AG, Wooley PH. Mechanical evaluation of large-size fourth-generation composite femur and tibia models. Annals of biomedical engineering. 2010;38(3):613-20.

291. Mani US, Sabatino CT, Sabharwal S, Svach DJ*, et al.* Biomechanical comparison of flexible stainless steel and titanium nails with external fixation using a femur fracture model. J Pediatr Orthop. 2006;26(2):182-7.

292. Mahar AT, Lee SS, Lalonde FD, Impelluso T*, et al.* Biomechanical comparison of stainless steel and titanium nails for fixation of simulated femoral fractures. J Pediatr Orthop. 2004;24(6):638-41.

293. Green JK, Werner FW, Dhawan R, Evans PJ*, et al.* A biomechanical study on flexible intramedullary nails used to treat pediatric femoral fractures. J Orthop Res. 2005;23(6):1315-20.

294. Li Y, Stabile KJ, Shilt JS. Biomechanical analysis of titanium elastic nail fixation in a pediatric femur fracture model. J Pediatr Orthop. 2008;28(8):874-8.

295. Fricka KB, Mahar AT, Lee SS, Newton PO. Biomechanical analysis of antegrade and retrograde flexible intramedullary nail fixation of pediatric femoral fractures using a synthetic bone model. J Pediatr Orthop. 2004;24(2):167-71.

296. Mahar A, Sink E, Faro F, Oka R*, et al.* Differences in biomechanical stability of femur fracture fixation when using titanium nails of increasing diameter. J Child Orthop. 2007;1(3):211-5.

297. Mehlman CT, Nemeth NM, Glos DL. Antegrade versus retrograde titanium elastic nail fixation of pediatric distal-third femoral-shaft fractures: a mechanical study. J Orthop Trauma. 2006;20(9):608-12.

298. Abosala A, Westacott D, Cunningham J. A Biomechanical Study of the Stability of Titanium Elastic Nails in the Treatment of Oblique Segmental Fracture of the Femur in Children. The Internet Journal of Orthopedic Surgery. 2010;19(1).

299. Flinck M, von Heideken J, Janarv P-M, Wåtz V*, et al.* Biomechanical comparison of semi-rigid pediatric locking nail versus titanium elastic nails in a femur fracture model. Journal of children's orthopaedics. 2015;9(1):77-84.

300. Sawbones. Biomechanical Test Materials. Pacific Research Laboratories, Inc; 2015. p. 4.

301. ASTM. Standard Specification and Test Methods for Intramedullary Fixation Devices. 2012.

302. Gilbert JL. Complexity in modeling of residual stresses and strains during polymerization of bone cement: effects of conversion, constraint, heat transfer, and viscoelastic property changes. Journal of biomedical materials research Part A. 2006;79(4):999-1014.

303. Lee AJ, Ling RS, Gheduzzi S, Simon JP*, et al.* Factors affecting the mechanical and viscoelastic properties of acrylic bone cement. Journal of materials science Materials in medicine. 2002;13(8):723-33.

304. Jaeblon T. Polymethylmethacrylate: properties and contemporary uses in orthopaedics. Journal of the American Academy of Orthopaedic Surgeons. 2010;18(5):297-305.

305. Magnan B, Bondi M, Maluta T, Samaila E*, et al.* Acrylic bone cement: current concept review. Musculoskeletal surgery. 2013;97(2):93-100.

306. Porter SE, Booker GR, Parsell DE, Weber MD*, et al.* Biomechanical analysis comparing titanium elastic nails with locked plating in two simulated pediatric femur fracture models. J Pediatr Orthop. 2012;32(6):587-93.

307. Kaiser MM, Wessel LM, Zachert G, Stratmann C*, et al.* Biomechanical analysis of a synthetic femur spiral fracture model: Influence of different materials on the stiffness in flexible intramedullary nailing. Clin Biomech (Bristol, Avon). 2011.

308. Taddei F, Cristofolini L, Martelli S, Gill HS*, et al.* Subject-specific finite element models of long bones: An in vitro evaluation of the overall accuracy. Journal of Biomechanics. 2006;39(13):2457-67.

309. Cristofolini L. Non-Destructive Testing: Biomed Town; 2010. Available from: https://www.biomedtown.org/biomed_town/LHDL/Reception/collection/NonDestructiveTesting.

310. Damm P, Schwachmeyer V, Dymke J, Bender A*, et al.* In vivo hip joint loads during three methods of walking with forearm crutches. Clinical Biomechanics. 2013;28(5):530-5.

311. Bergmann G, Deuretzbacher G, Heller M, Graichen F*, et al.* Hip contact forces and gait patterns from routine activities. Journal of Biomechanics. 2001;34(7):859-71.

312. Stansfield BW, Nicol AC, Paul JP, Kelly IG*, et al.* Direct comparison of calculated hip joint contact forces with those measured using instrumented implants. An evaluation of a three-dimensional mathematical model of the lower limb. Journal of Biomechanics. 2003;36(7):929-36.

313. Heller MO, Bergmann G, Deuretzbacher G, Claes L*, et al.* Influence of femoral anteversion on proximal femoral loading: measurement and simulation in four patients. Clinical Biomechanics. 2001;16(8):644-9.

314. Duda GN, Schneider E, Chao EYS. Internal forces and moments in the femur during walking. Journal of Biomechanics. 1997;30(9):933-41.

315. Schwachmeyer V, Damm P, Bender A, Dymke J*, et al.* In vivo hip joint loading during post-operative physiotherapeutic exercises. 2013.

316. Heller MO, Bergmann G, Deuretzbacher G, Dürselen L*, et al.* Musculo-skeletal loading conditions at the hip during walking and stair climbing. Journal of Biomechanics. 2001;34(7):883-93.

317. Heller MO, Bergmann G, Kassi JP, Claes L*, et al.* Determination of muscle loading at the hip joint for use in pre-clinical testing. Journal of Biomechanics. 2005;38(5):1155-63.

318. Dailey HL, Daly CJ, Galbraith JG, Cronin M*, et al.* The Flexible Axial Stimulation (FAST) intramedullary nail provides interfragmentary micromotion and enhanced torsional stability. Clinical Biomechanics (Bristol, Avon). 2013;28(5):579-85.

319. Bear L, Hamilton J, Sukere A, Lynch G*, et al.* Testing of Intramedullary Nails Using Physiological Loading. In: Harvey JP, Daniels A, Games RF, editors. Intramedullary Rods: Clinical Performance and Related Laboratory Testing. 1008. Philadelphia: ASTM International; 1989. p. 26-33.

320. Alho A, Moen O, Husby T, Ronningen H*, et al.* Slotted versus non-slotted locked intramedullary nailing for femoral shaft fractures. Arch Orthop Trauma Surg. 1992;111(2):91-5.

321. Rogers M. Biomechanical Testing of Salter-Harris Fractures Type I and II in the Distal Femur and Proximal Tibia. 2013.

322. Keller T, Liebschner AK. Tensile and Compression Testing of Bone. In: Yuehuei H. An RAD, editor. Mechanical Testing of Bone and the Bone-Implant Interface: CRC Press; 1999. p. 175-205.

323. Zdero R, Shah S, Mosli M, Schemitsch E. The effect of load application rate on the biomechanics of synthetic femurs. Proceedings of the Institution of Mechanical Engineers, Part H: Journal of Engineering in Medicine. 2010;224(4):599-605.

324. Chotel F, Braillon P, Sailhan F, Gadeyne S*, et al.* Bone stiffness in children: part I. In vivo assessment of the stiffness of femur and tibia in children. J Pediatr Orthop. 2008;28(5):534-7.

325. Chotel F, Braillon P, Sailhan F, Gadeyne S*, et al.* Bone stiffness in children: part II. Objectives criteria for children to assess healing during leg lengthening. J Pediatr Orthop. 2008;28(5):538-43.

326. Kurowski PM. Engineering Analysis with SolidWorks Simulation 2012: SDC Publications; 2012.

327. Roberts GL, Pallister I. Finite element analysis in trauma & orthopaedics–an introduction to clinically relevant simulation & its limitations. Orthopaedics and Trauma. 2012;26(6):410-6.

328. Weber M, Verma G. SolidWorks Simulation 2015 Black Book: CreateSpace Independent Publishing Platform; 2015.

329. Hart RT, Thongpreda N, Van Buskirk WC. Supercomputer use in orthopaedic biomechanics research: focus on functional adaptation of bone. Engineering in Medicine and Biology Magazine, IEEE. 1988;7(4):39-43.

330. Huiskes R, Chao E. A survey of finite element analysis in orthopedic biomechanics: the first decade. Journal of biomechanics. 1983;16(6):385-409.

331. Simpson DJ. A finite element strategy applied to intramedullary nailing of the proximal femur: Brunel University School of Engineering and Design PhD Theses; 2005.

332. Koivumäki J. Modeling Of Proximal Femur: University of Oulu; 2013.

333. Mehta J. Redesign of the total wrist prosthesis to address wrist rotation: University of Texas; 2013.

334. Bell CG. A finite element and experimental investigation of the femoral component mechanics in a total hip arthroplasty: Queensland University of Technology; 2006.

335. Haase K. Finite Element Analysis of Orthopaedic Plates and Screws to Reduce the Effects of Stress Shielding: University of Ottawa; 2009.

336. Lai W. Prediction of pathological fracture risk due to metastatic bone defectusing finite element method: The University of Hong Kong (Pokfulam, Hong Kong); 2006.

337. Shih RH. Introduction to Finite Element Analysis Using SolidWorks Simulation 2012: SDC Publ.; 2012.

338. Akin JE. Finite Element Analysis Concepts: Via SolidWorks: World Scientific; 2010.

339. Liebling TM, Pournin L. Voronoi Diagrams and Delaunay Triangulations: Ubiquitous Siamese Twins. Journal of Documenta Mathematica–Optimization Stories. 2012:419-31.

340. Chang K. Chapter 7 - Structural Analysis. In: Chang K-H, editor. e-Design. Boston: Academic Press; 2015. p. 325-90.

341. Mesh Quality Checks: Dassault Systèmes; 2012. Available from: http://help.solidworks.com/2016/english/SolidWorks/cworks/c_Mesh_Quality_Checks.htm.

342. Running Studies: Dassault Systèmes; 2012. Available from: http://help.solidworks.com/2012/English/SolidWorks/cworks/Running_Analysis.htm.

343. Patel S. Choosing a solver: GoEngineer; 2015 [cited 2015]. Available from: http://kb.goengineer.com/go/Default.aspx?typeID=7&Keyword=%22Simulation%22&theType=Postsales&ResultCount=16.

344. Herrera A. Finite element simulation. Applications in Orthopaedics and Traumatology. 2010. In: Finite Element Analysis [Internet]. InTech; [121-50]. Available from: http://www.intechopen.com/books/finite-element-analysis/finite-element-simulation-applications-in-orthopaedics-and-traumatology-.

345. Cristofolini L, Schileo E, Juszczyk M, Taddei F*, et al.* Mechanical testing of bones: the positive synergy of finite-element models and in vitro experiments. Philosophical transactions Series A, Mathematical, physical, and engineering sciences. 2010;368(1920):2725-63.

346. Nareliya R, Kumar V. Finite Element Application To Femur Bone: A Review. 2012.

347. Papini M, Zdero R, Schemitsch EH, Zalzal P. The biomechanics of human femurs in axial and torsional loading: comparison of finite element analysis, human cadaveric femurs, and synthetic femurs. Journal of biomechanical engineering. 2007;129(1):12-9.

348. Wang CJ, Yettram AL, Yao MS, Procter P. Finite element analysis of a Gamma nail within a fractured femur. Med Eng Phys. 1998;20(9):677-83.

349. Zienkiewicz OC, Taylor RL, Zhu JZ. The Finite Element Method: Its Basis and Fundamentals: Its Basis and Fundamentals: Elsevier Science; 2013.

350. Angadi D, Shepherd D, Vadivelu R, Barrett T, editors. Orthogonal Digital Radiographs-A Novel Template for a Paediatric Femur Finite Element Model Development. 5th International Conference on Biomedical Engineering in Vietnam; 2015: Springer.

351. Creating 2D Splines: Dassault Systèmes; 2012. Available from: http://help.solidworks.com/2012/english/SolidWorks/sldworks/sketched_spline.htm?format=P.

352. Bethune JD. Engineering Design and Graphics with SolidWorks: Pearson Education; 2011.

353. Sweep Overview: Dassault Systèmes; 2012. Available from: http://help.solidworks.com/2012/English/SolidWorks/sldworks/Sweep_Overview.htm?format=P.

354. Strauss EJ, Kummer FJ, Koval KJ, Egol KA. The "Z-effect" phenomenon defined: A laboratory study. Journal of Orthopaedic Research. 2007;25(12):1568-73.

355. Efstathopoulos N, Nikolaou VS, Xypnitos FN, Korres D*, et al.* Investigation on the distal screw of a trochanteric intramedullary implant (Fi-nail) using a simplified finite element model. Injury. 2010;41(3):259-65.

356. Cheung G, Zalzal P, Bhandari M, Spelt JK*, et al.* Finite element analysis of a femoral retrograde intramedullary nail subject to gait loading. Med Eng Phys. 2004;26(2):93-108.

357. Juszczyk MM, Cristofolini L, Viceconti M. The human proximal femur behaves linearly elastic up to failure under physiological loading conditions. J Biomech. 2011;44(12):2259-66.

358. Pomsuk P, Aroonjarattham P, Saktaveekulkit N, Riansuwan K*, et al.* Biomechanical Effect of Nail Length to Thai Femoral Shaft Fracture.

359. Trabelsi N, Yosibash Z, Wutte C, Augat P*, et al.* Patient-specific finite element analysis of the human femur—a double-blinded biomechanical validation. Journal of biomechanics. 2011;44(9):1666-72.

360. Zdero R, Bougherara H. Orthopaedic biomechanics: a practical approach to combining mechanical testing and finite element analysis. Finite Element Analysis David Moratal. 2010:171-94.

361. Montanini R, Filardi V. In vitro biomechanical evaluation of antegrade femoral nailing at early and late postoperative stages. Med Eng Phys. 2010;32(8):889-97.

362. Filardi V, Montanini R. Measurement of local strains induced into the femur by trochanteric Gamma nail implants with one or two distal screws. Medical engineering & physics. 2007;29(1):38-47.

363. Wieding J, Souffrant R, Fritsche A, Mittelmeier W*, et al.* Finite element analysis of osteosynthesis screw fixation in the bone stock: an appropriate method for automatic screw modelling. PloS one. 2012;7(3):e33776.

364. Simpson D, Brown C, Yettram A, Procter P*, et al.* Finite element analysis of intramedullary devices: the effect of the gap between the implant and the bone. Proceedings of the Institution of Mechanical Engineers, Part H: Journal of Engineering in Medicine. 2008;222(3):333-45.

365. Fox MJ, Scarvell JM, Smith PN, Kalyanasundaram S*, et al.* Lateral drill holes decrease strength of the femur: an observational study using finite element and experimental analyses. Journal of Orthopaedic Surgery and Research. 2013;8(1):1-8.

366. Simoes J, Vaz M, Blatcher S, Taylor M. Influence of head constraint and muscle forces on the strain distribution within the intact femur. Medical Engineering & Physics. 2000;22(7):453-9.

367. Besdo S, Kruger AK, Rossig C, Helmecke P*, et al.* Finite Element Study of Degradable Intramedullary Nails out of Magnesium Alloy for Ovine Tibiae. Biomed Tech (Berl). 2013.

368. Gray HA, Taddei F, Zavatsky AB, Cristofolini L*, et al.* Experimental validation of a finite element model of a human cadaveric tibia. Journal of biomechanical engineering. 2008;130(3):031016.

369. Cherian JJ, Kapadia BH, Banerjee S, Jauregui JJ*, et al.* Mechanical, anatomical, and kinematic axis in TKA: concepts and practical applications. Current reviews in musculoskeletal medicine. 2014;7(2):89-95.

370. Lecerf G, Fessy MH, Philippot R, Massin P*, et al.* Femoral offset: Anatomical concept, definition, assessment, implications for preoperative templating and hip arthroplasty. Orthopaedics & Traumatology: Surgery & Research. 2009;95(3):210-9.

371. Bird J. Arc length and area of circles and sectors. Understanding Engineering Mathematics: Taylor & Francis; 2013. p. 278.

372. Wu X, Yang M, Wu L, Niu W. A Biomechanical Comparison of Two Intramedullary Implants for Subtrochanteric Fracture in Two Healing Stages: A Finite Element Analysis. Applied Bionics and Biomechanics. 2015;2015.

373. Goffin JM, Pankaj P, Simpson AH. A computational study on the effect of fracture intrusion distance in three-and four-part trochanteric fractures treated with Gamma nail and sliding hip screw. Journal of Orthopaedic Research. 2014;32(1):39-45.

374. Yousif A, Aziz M. Biomechanical Analysis of the human femur bone during normal walking and standing up. IOSR Journal of Engineering (IOSRJEN). 2012;2(8):13-9.

375. Background on Meshing: Dassault Systèmes; 2012. Available from: http://help.solidworks.com/2012/English/SolidWorks/cworks/step5_mesh_the_part.htm?id=0daed76596f64817ad6522c593372e7c#Pg0.

376. Anderson AE, Ellis BJ, Weiss JA. Verification, validation and sensitivity studies in computational biomechanics. Computer methods in biomechanics and biomedical engineering. 2007;10(3):171-84.

377. Oberkampf WL, Roy C. Verification and validation in computational simulation. AIAA Professional Development Short-course. 2004:6-7.

378. Yosibash Z, Katz A, Milgrom C. Toward verified and validated FE simulations of a femur with a cemented hip prosthesis. Medical engineering & physics. 2013;35(7):978-87.

379. Pettersen SH, Wik TS, Skallerud B. Subject specific finite element analysis of stress shielding around a cementless femoral stem. Clinical Biomechanics. 2009;24(2):196-202.

380. Analysis Solvers: Dassault Systèmes; 2012. Available from: http://help.solidworks.com/2014/English/SolidWorks/cworks/c_Analysis_Solvers.htm.

381. Viceconti M, McNamara BP, Toni A, Giunti A, editors. FEM analysis of the static stresses induced in a THR femoral component during a standardized fatigue test. Second International Symposium on Computer Methods in Biomechanics and Biomedical Engineering, London; 1996.

382. Prendergast P. Finite element models in tissue mechanics and orthopaedic implant design. Clinical Biomechanics. 1997;12(6):343-66.

383. Brekelmans W, Poort H, Slooff T. A new method to analyse the mechanical behaviour of skeletal parts. Acta Orthop Scand. 1972;43(5):301-17.

384. Rybicki EF, Simonen FA, Weis Jr EB. On the mathematical analysis of stress in the human femur. Journal of Biomechanics. 1972;5(2):203-15.

385. Kluess D, Wieding J, Souffrant R, Mittelmeier W*, et al.* Finite Element Analysis in Orthopaedic Biomechanics: INTECH Open Access Publisher; 2010.

386. Rankovic V, Ristic B, Kojic M. Internal Fixation of Femoral Bone Comminuted Fracture-FE Analysis. Journal of the Serbian Society for Computational Mechanics. 2007;1(1):120-8.

387. Jade S. Finite Element Analysis of a Femur to Deconstruct the Design Paradox of Bone Curvature. 2012.

388. Jade S, Tamvada KH, Strait DS, Grosse IR. Finite element analysis of a femur to deconstruct the paradox of bone curvature. Journal of Theoretical Biology. 2014;341:53-63.

389. Huiskes H. Stress analyses of intramedullary fixated joint prosthesis. International conference on finite elements in biomechanics / Ed. 1980.

390. Mittlmeier T, Mattheck C, Dietrich F. Effects of mechanical loading on the profile of human femoral diaphyseal geometry. Medical engineering & physics. 1994;16(1):75-81.

391. Completo A, Fonseca F, Simoes J. Experimental validation of intact and implanted distal femur finite element models. Journal of biomechanics. 2007;40(11):2467-76.

392. Taddei F, Viceconti M, Manfrini M, Toni A. Mechanical strength of a femoral reconstruction in paediatric oncology: a finite element study. Proceedings of the Institution of Mechanical Engineers, Part H: Journal of Engineering in Medicine. 2003;217(2):111-9.

393. Greer B, Wang E, Jiang Y. On the appropriateness of using the standardized femur for FEA in the proximal region.

394. Augat P, Göttlinger M, Henschel J, Eberle S. Lack of universal bone material laws limits accuracy in subject specific FE models. 11th World Congress on Computational Mechanics July 20 - 25, 2014; Barcelona, Spain: International Association for Computational Mechanics (IACM); 2014.

395. Liu C, Xing W, Zhang Y, Pan Z*, et al.* Three-Dimensional Finite Element Analysis and Comparison of a New Intramedullary Fixation with Interlocking Intramedullary Nail. Cell Biochem Biophys. 2015;71(2):717-24.

396. Taylor M, Tanner K, Freeman M, Yettram A. Stress and strain distribution within the intact femur: compression or bending? Medical engineering & physics. 1996;18(2):122-31.

397. Bain GI, Zacest AC, Paterson DC, Middleton J*, et al.* Abduction Strength Following Intramedullary Nailing of the Femur. Journal of Orthopaedic Trauma February/March. 1997;11(2):93-7.

398. Archdeacon M, Ford K, Wyrick J, Paterno M*, et al.* A Prospective Functional Outcome and Motion Analysis Evaluation of the Hip Abductors After Femur Fracture and Antegrade Nailing. Journal of Orthopaedic Trauma. 2008;22(1):3-9.

399. Kapp W, Lindsey R, Noble P, Rudersdorf T*, et al.* Long-Term Residual Musculoskeletal Deficits after Femoral Shaft Fractures Treated with Intramedullary Nailing. Journal of Trauma-Injury Infection & Critical Care. 2000;49(3):446-9.

400. Biyani A, Jones DA, Daniel CL, Bishay M. Assessment of hip abductor function in relation to peritrochanteric heterotopic ossification after closed femoral nailing. Injury.24(2):97-100.

401. Ferguson ES. Engineering and the Mind's Eye: MIT Press; 1994.

402. Baudoin A, Skalli W, de Guise JA, Mitton D. Parametric subject-specific model for in vivo 3D reconstruction using bi-planar X-rays: application to the upper femoral extremity. Medical & biological engineering & computing. 2008;46(8):799-805.

403. Mitton D, Landry C, Veron S, Skalli W*, et al.* 3D reconstruction method from biplanar radiography using non-stereocorresponding points and elastic deformable meshes. Medical & biological engineering & computing. 2000;38(2):133-9.

404. Krauze A, Marciniak J. Numerical method in biomechanical analysis of intramedullary osteosynthesis in children.

405. Bagi I. Finite element study of some parameters of bone fractures fixed with screws. Mechanical Engineering. 2012;55(1):57-61.

406. Bagi I, Olasz S. Study of Screws for Femoral Neck Fixing, Using Finite Element Calculation and In-Vitro Testing. Periodica Polytechnica Engineering Mechanical Engineering. 2015;59(1):43.

407. Shih KS. Influence of muscular contractions on the stress analysis of distal femoral interlocking nailing. Clinical Biomechanics. 2008;23(1):38-44.

408. Greco GD, Jansen WC, Landre Junior J, Seraidarian PI. Biomechanical analysis of the stresses generated by different disocclusion patterns in an implant-supported mandibular complete denture. Journal of Applied Oral Science. 2009;17:515-20.

409. Takahashi H, Moriyama S, Furuta H, Matsunaga H*, et al.* Three lateral osteotomy designs for bilateral sagittal split osteotomy: biomechanical evaluation with three-dimensional finite element analysis. Head & face medicine. 2010;6(1):4.

410. Eraslan O, İnan Ö. The effect of thread design on stress distribution in a solid screw implant: a 3D finite element analysis. Clinical oral investigations. 2010;14(4):411-6.

411. Liang S, Wang W, Wang Z, Liu Y. Mechanics Analysis of the Human Ankle Based on SolidWorks Simulation. Mechanical & Electrical Engineering Technology. 2013;8:010.

412. Sharma P, Sharma S, Vidhya S, Mathur M. Comparative Finite Element Analysis of Jaipur Foot and Polyurethane Foot. Engineering. 2013;5(10):518.

413. Ariza O, Gilchrist S, Widmer R, Guy P*, et al.* Comparison of explicit finite element and mechanical simulation of the proximal femur during dynamic drop-tower testing. Journal of biomechanics. 2015;48(2):224-32.

414. Chen SH, Yu TC, Chang CH, Lu YC. Biomechanical analysis of retrograde intramedullary nail fixation in distal femoral fractures. Knee. 2008;15(5):384-9.

415. Daniels A, Hofmann A, West H, Morgan J. Initial Mechanical Stability of Three Distally Locked Intramedullary Nail Systems. In: J. P. Harvey J, A. U. Daniels, and R. F.

Games, editor. Intramedullary Rods: Clinical Performance and Related Laboratory Testing. Philadelphia: American Society for Testing and Materials; 1989. p. 80-6.

416. Simpson D, Monk A, Murray D, Gill H. Biomechanics in orthopaedics: considerations of the hip and knee. Surgery (Oxford). 2010;28(10):478-82.

417. Malik SS, Malik SS. Axes of the lower limbs. Orthopaedic Biomechanics Made Easy: Cambridge University Press; 2015. p. 96-7.

418. Schandelmaier P, Farouk O, Krettek C, Reimers N*, et al.* Biomechanics of femoral interlocking nails. Injury. 2000;31(6):437-43.

419. McKellop H, Ebramzadeh, E., Fortune, l., and Sarmiento, A.,. Stability of Subtrochanteric Femoral Fractures Fixed with Interlocking Intramedullary Rods. In: J. P. Harvey J, A. U. Daniels, and R. F. Games, editor. Intramedullary Rods: Clinical Performance and Related Laboratory Testing. Philadelphia: American Society for Testing and Materials; 1989. p. 65-79.

420. Bechtold J, Schaffhausen I, Kyle R, Gustilo R. Comparison of Interlocking and Noninterlocking Intramedullary Nails in Bending and Torsion. Intramedullary Rods: Clinical Performance and Related Laboratory Testing. Philadelphia: American Society for Testing and Materials; 1989. p. 60-4.

421. Kyle RF, Schaffhausen JM, Bechtold JE. Biomechanical characteristics of interlocking femoral nails in the treatment of complex femoral fractures. Clin Orthop Relat Res. 1991(267):169-73.

422. Huang SC, Lin CC, Lin J. Increasing nail-cortical contact to increase fixation stability and decrease implant strain in antegrade locked nailing of distal femoral fractures: a biomechanical study. J Trauma. 2009;66(2):436-42.

423. Meyer RW, Plaxton NA, Postak PD, Gilmore A*, et al.* Mechanical comparison of a distal femoral side plate and a retrograde intramedullary nail. J Orthop Trauma. 2000;14(6):398-404.

424. Hoffmann S, Gerber C, von Oldenburg G, Kessler M*, et al.* Effect of angular stability and other locking parameters on the mechanical performance of intramedullary nails. Biomedizinische Technik Biomedical Engineering. 2015;60(2):157-64.

425. Wright JG, Wang EE, Owen JL, Stephens D*, et al.* Treatments for paediatric femoral fractures: a randomised trial. The Lancet. 2005;365(9465):1153-8.

426. Sanders J, Browne R, Mooney J, Raney E*, et al.* Treatment of femoral fractures in children by pediatric orthopedists: results of a 1998 survey. Journal of Pediatric Orthopaedics. 2001;21(4):436-41.

427. Tencer A, Johnson K, Johnston D, Gill K. A biomechanical comparison of various methods of stabilization of subtrochanteric fractures of the femur. Journal of orthopaedic research. 1984;2(3):297-305.

428. Hunter SG. Deformation of Femoral Intramedullary Nails. Clinical Orthopaedics and Related Research. 1982;171:83-6.

429. Sherman MC, Tencer, A. F., and Johnson, K. D. Biomechanical Variables Affeetlng Stability and Stresses in the Fractured Femur During Intramedullary Nailing. In: J. P. Harvey J, A. U. Daniels, and R. F. Games, editor. lntramedullary Rods: Clinical Performance and

Related Laboratory Testing. Philadelphia: American Society for Testing and Materials; 1989. p. 87-107.

430. Projecting Sketched Curves: Dassault Systèmes; 2012. Available from: http://help.solidworks.com/2012/English/SolidWorks/sldworks/hidd_dve_proj_sketch.htm?format=P.

431. Shih RH. Create the swept feature. Introduction to Finite Element Analysis Using SolidWorks Simulation 2012: SDC Publ.; 2012. p. 11-2.

432. Adding Components to an Assembly: Dassault Systèmes; 2012. Available from: http://help.solidworks.com/2012/English/SolidWorks/sldworks/Adding_Components_to_an_Assembly.htm?format=P.

433. Assemblies: Dassault Systèmes; 2012

Available from: http://help.solidworks.com/2012/English/SolidWorks/sldworks/Assemblies.htm?id=e4b1d05b6e3a4ad681a2881b6f9b53f6#Pg0.

434. Wenisch S, Trinkaus K, Hild A, Hose D*, et al.* Human reaming debris: a source of multipotent stem cells. Bone. 2005;36(1):74-83.

435. Hoegel FW, Abdulazim AN, Buehren V, Augat P. Quantification of reaming debris at the fracture gap of diaphyseal A3 femur fractures after reamed intramedullary nailing and using an intramedullary application system. J Trauma. 2010;69(6):E98-101.

436. Extrude Features: Dassault Systèmes; 2012. Available from: http://help.solidworks.com/2012/English/SolidWorks/sldworks/Hidd_dve_end_spec_dlg.htm?format=P.

437. Mates Overview 2012. Available from: http://help.solidworks.com/2012/English/SolidWorks/sldworks/aha1317932497838.htm?format=P.

438. Fixing the Position of a Component: Dassault Systèmes; 2012. Available from: http://help.solidworks.com/2012/English/SolidWorks/sldworks/Fixing_the_Position_of_a_Component.htm?format=P.

439. Synthes. Implant Materials - Titanium 6% Aluminium - 7% Niobium. 2014 [cited 2014]. Available from: http://www.synthes.com/sites/NA/NAContent/Docs/Product%20Support%20Materials/Materials%20Booklets/Implant%20Materials%20-%20Titanium--6_%20Aluminum--7_%20Niobium.pdf.

440. Mahaisavariya B, Sitthiseripratip K, Suwanprateeb J. Finite element study of the proximal femur with retained trochanteric gamma nail and after removal of nail. Injury. 2006;37(8):778-85.

441. Petrova RV. Introduction to Static Analysis Using SolidWorks Simulation: CRC Press; 2014.

442. Component Contact: Dassault Systèmes; 2012. Available from: http://help.solidworks.com/2012/English/SolidWorks/cworks/ID_HELP_WELDS_CONTACT.htm?format=P.

443. Saidpour SH. Assessment of carbon fibre composite fracture fixation plate using finite element analysis. Annals of biomedical engineering. 2006;34(7):1157-63.

444. Helwig P, Faust G, Hindenlang U, Hirschmuller A*, et al.* Finite element analysis of four different implants inserted in different positions to stabilize an idealized trochanteric femoral fracture. Injury. 2009;40(3):288-95.

445. Helwig P, Faust G, Hindenlang U, Kroplin B*, et al.* Finite element analysis of a bone-implant system with the proximal femur nail. Technol Health Care. 2006;14(4-5):411-9.

446. Seral B, Garcia JM, Cegonino J, Doblare M*, et al.* Finite element study of intramedullary osteosynthesis in the treatment of trochanteric fractures of the hip: Gamma and PFN. Injury. 2004;35(2):130-5.

447. Wang CJ, Brown CJ, Yettram AL, Procter P. Intramedullary femoral nails: one or two lag screws? A preliminary study. Med Eng Phys. 2000;22(9):613-24.

448. Samiezadeh S, Tavakkoli Avval P, Fawaz Z, Bougherara H. Biomechanical assessment of composite versus metallic intramedullary nailing system in femoral shaft fractures: A finite element study. Clin Biomech (Bristol, Avon). 2014.

449. Bayoglu R, Okyar A, editors. A physiologically accurate mechanical representation of the bone-implant construct under gait loads. Proceedings of the sixth national biomechanics congress, Sakarya University; 2012.

450. Chandrasekaran A, Krishnakumar R. Finite Element Analysis of Proximal Femur Nail for Subtrochanteric Fractured Femur.

451. Eberle S, Augat P. Preventing Contact Convergence Problems in Bone-Implant Contact Models.

452. Eveleigh RJ. A review of biomechanical studies of intramedullary nails. Med Eng Phys. 1995;17(5):323-31.

453. Parikh SN, Wells L, Mehlman CT, Scherl SA. Management of fractures in adolescents. The Journal of Bone & Joint Surgery. 2010;92(18):2947-58.

454. Dameron TB, Jr., Thompson HA. Femoral-shaft fractures in children. Treatment by closed reduction and double spica cast immobilization. J Bone Joint Surg Am. 1959;41-A:1201-12.

455. Creating 3D Splines: Dassault Systèmes; 2012. Available from: http://help.solidworks.com/2012/English/SolidWorks/sldworks/Sketched_3D_Spline.htm?format=P.

456. Spline on Surface: Dassault Systèmes; 2012. Available from: http://help.solidworks.com/2012/English/SolidWorks/sldworks/Spline_on_Surface.htm?format=P.

457. Gardner TN, Stoll T, Marks L, Mishra S*, et al.* The influence of mechanical stimulus on the pattern of tissue differentiation in a long bone fracture--an FEM study. J Biomech. 2000;33(4):415-25.

458. Yang K, Teo EC, Fuss FK. Application of Taguchi method in optimization of cervical ring cage. J Biomech. 2007;40(14):3251-6.

459. Dar FH, Meakin JR, Aspden RM. Statistical methods in finite element analysis. J Biomech. 2002;35(9):1155-61.

460. Lin CL, Chang SH, Chang WJ, Kuo YC. Factorial analysis of variables influencing mechanical characteristics of a single tooth implant placed in the maxilla using finite element analysis and the statistics-based Taguchi method. European journal of oral sciences. 2007;115(5):408-16.

461. Chen AC, Lin YH, Kuo HN, Yu TC*, et al.* Design optimisation and experimental evaluation of dorsal double plating fixation for distal radius fracture. Injury. 2013;44(4):527-34.

462. Taguchi G, Konishi S, Konishi S, Institute AS. Orthogonal Arrays and Linear Graphs: Tools for Quality Engineering: American Supplier Institute; 1987.

463. Taguchi G, Yokoyama Y. Taguchi methods: design of experiments: ASI Press; 1993.

464. Taguchi G, Clausing D. Robust quality. Harvard Business Review. 1990;68(1):65-75.

465. Taguchi G, Phadke MS. Quality engineering through design optimization. Quality Control, Robust Design, and the Taguchi Method: Springer; 1989. p. 77-96.

466. Roy RK. A Primer on the Taguchi Method: Society of Manufacturing Engineers; 1990.

467. Taguchi G. Taguchi on Robust Technology Development: Bringing Quality Engineering Upstream: ASME Press; 1993.

468. Montgomery DC. Design and Analysis of Experiments, 8th Edition: John Wiley & Sons, Incorporated; 2012.

469. Hsu W, Chao C, Hsu H, Lin J*, et al.* Parametric study on the interface pullout strength of the vertebral body replacement cage using FEM-based Taguchi methods. Medical engineering & physics. 2009;31(3):287-94.

470. Cheung GH. Finite element analysis of an implanted femoral retrograde intramedullary nail. Ottawa: National Library of Canada = Bibliothèque nationale du Canada; 2004.

471. Arazi M, Ögün TC, Oktar MN, Memik R*, et al.* Early weight-bearing after statically locked reamed intramedullary nailing of comminuted femoral fractures: is it a safe procedure? Journal of Trauma and Acute Care Surgery. 2001;50(4):711-6.

472. Kempf I, Grosse A, Rigaut P. The treatment of noninfected pseudarthrosis of the femur and tibia with locked intramedullary nailing. Clinical orthopaedics and related research. 1986;212:142-54.

473. Klemm K, Borner M. Interlocking nailing of complex fractures of the femur and tibia. Clinical orthopaedics and related research. 1986;212:89-100.

474. Henderson CE, Lujan T, Bottlang M, Fitzpatrick DC*, et al.* Stabilization of distal femur fractures with intramedullary nails and locking plates: differences in callus formation. The Iowa orthopaedic journal. 2010;30:61.

475. Webb L, Winquist R, Hansen S. Intramedullary Nailing and Reaming for Delayed Union or Nonunion of the Femoral Shaft: A Report of 105 Consecutive Cases. Clinical orthopaedics and related research. 1986;212:133-41.

476. Wu C, Chen W. Treatment of femoral shaft aseptic nonunions: comparison between closed and open bone-grafting techniques. Journal of Trauma and Acute Care Surgery. 1997;43(1):112-6.

477. Christensen NO. Küntscher intramedullary reaming and nail fixation for non-union of fracture of the femur and the tibia. Journal of Bone & Joint Surgery, British Volume. 1973;55(2):312-8.

478. Hak DJ, Lee SS, Goulet JA. Success of exchange reamed intramedullary nailing for femoral shaft nonunion or delayed union. Journal of orthopaedic trauma. 2000;14(3):178-82.

479. Wu C. The effect of dynamization on slowing the healing of femur shaft fractures after interlocking nailing. Journal of Trauma and Acute Care Surgery. 1997;43(2):263-7.

480. Wu C, Shih C. Distal femoral nonunion treated with interlocking nailing. Journal of Trauma and Acute Care Surgery. 1991;31(12):1659-62.

481. Wu C, Shih C. Effect of dynamization of a static interlocking nail on fracture healing. Canadian journal of surgery Journal canadien de chirurgie. 1993;36(4):302-6.

482. Kessler S, Hallfeldt K, Perren S, Schweiberer L. The effects of reaming and intramedullary nailing on fracture healing. Clinical orthopaedics and related research. 1986;212:18-25.

483. Anastopoulos G, Asimakopoulos A, Exarchou E, Pantazopoulos T. Closed interlocked nailing in comminuted and segmental femoral shaft fractures. Journal of Trauma and Acute Care Surgery. 1993;35(5):772-5.

484. Pihlajamäki HK, Salminen ST, Böstman OM. The treatment of nonunions following intramedullary nailing of femoral shaft fractures. Journal of orthopaedic trauma. 2002;16(6):394-402.

485. Yokoyama K, Itoman M, Nakamura K, Wakita R*, et al.* Contributing factors affecting initial bony healing in interlocking nailings for femoral shaft fractures. European Journal of Orthopaedic Surgery & Traumatology. 2003;13(1):33-7.

486. Wu C, Shih C. A small effect of weight bearing in promoting fracture healing. Archives of orthopaedic and trauma surgery. 1992;112(1):28-32.

487. Brumback R, Uwagie-Ero S, Lakatos R, Poka A*, et al.* Intramedullary nailing of femoral shaft fractures. Part II: Fracture-healing with static interlocking fixation. The Journal of Bone & Joint Surgery. 1988;70(10):1453-62.

488. Christie J, Kinninmonth A, Howie C. Intramedullary locking nails in the management of femoral shaft fractures. Journal of Bone & Joint Surgery, British Volume. 1988;70(2):206-10.

489. Riquelme A, Rodriguez A, Mino G, Sanmartin R. Treatment of the femoral and tibial fractures with Grosse and Kempf locking nails. Clinical orthopaedics and related research. 1992;283:86-9.

490. Sage FP. The Second Decade of Experience with the Kuntscher Medullary Nail in the Femur. Clinical orthopaedics and related research. 1968;60:77-86.

491. Eid AM, Deif A. Aetiological factors in non-union following Küntscher intramedullary nailing of the femur. Archives of orthopaedic and traumatic surgery. 1980;96(3):213-20.

492. Winquist RA, Hansen ST, Clawson DK. Closed intramedullary nailing of femoral fractures. A report of five hundred and twenty cases. The Journal of Bone & Joint Surgery. 1984;66(4):529-39.

493. Kempf I, Grosse A, Beck G. Closed locked intramedullary nailing. Its application to comminuted fractures of the femur. The Journal of Bone & Joint Surgery. 1985;67(5):709-20.

494. Im G, Shin S. Treatment of femoral shaft fractures with a titanium intramedullary nail. Clinical orthopaedics and related research. 2002;401:223-9.

495. Simmermacher R, Ljungqvist J, Bail H, Hockertz T*, et al.* The new proximal femoral nail antirotation (PFNA®) in daily practice: results of a multicentre clinical study. Injury. 2008;39(8):932-9.

496. Wiss DA, Brien W, Stetson W. Interlocked nailing for treatment of segmental fractures of the femur. The Journal of Bone & Joint Surgery. 1990;72(5):724-8.

497. Winquist R, Hansen Jr S. Comminuted fractures of the femoral shaft treated by intramedullary nailing. The Orthopedic clinics of North America. 1980;11(3):633-48.

498. Wehner T, Claes L, Ignatius A, Simon U. Optimization of intramedullary nailing by numerical simulation of fracture healing. Journal of Orthopaedic Research. 2012;30(4):569-73.

499. Wilson DJ, Morgan RL, Hesselden KL, Dodd JR*, et al.* A single-channel telemetric intramedullary nail for in vivo measurement of fracture healing. Journal of orthopaedic trauma. 2009;23(10):702-9.

500. Nemchand J, Anson A, Jones B, Wilson D*, et al.* D-4 Biomechanical Fracture Healing Simulation for Smart Implants Using Telemetry. Journal of Biomechanics. 2010;43:S69-S70.

501. Sedel L, Christel P, Dewas J, de Charentenay F*, et al.* Comparison of the effects of intramedullary nailing or plating on the mechanical properties of fracture callus. Journal of biomedical engineering. 1980;2(2):89-92.

502. Mølster A, Gjerdet N, Raugstad T, Hvidsten K*, et al.* Effect of instability on experimental fracture healing. Acta orthopaedica. 1982;53(4):521-6.

503. Henry A, Freeman M, Swanson S. Studies on the mechanical properties of healing experimental fractures. Proceedings of the Royal Society of Medicine. 1968;61(9):902.

504. Wehner T, Penzkofer R, Augat P, Claes L*, et al.* Improvement of the shear fixation stability of intramedullary nailing. Clinical Biomechanics (Bristol, Avon). 2011;26(2):147-51.

505. Mehboob H, Son D-S, Chang S-H. Finite element analysis of tissue differentiation process of a tibia with various fracture configurations when a composite intramedullary rod was applied. Composites Science and Technology. 2013;80:55-65.

506. English T, Kilvington M. In vivo records of hip loads using a femoral implant with telemetric output (a prelimary report). Journal of Biomedical Engineering. 1979;1(2):111-5.

507. Hodge W, Fijan R, Carlson K, Burgess R*, et al.* Contact pressures in the human hip joint measured in vivo. Proceedings of the National Academy of Sciences. 1986;83(9):2879-83.

508. Bergmann G, Graichen F, Rohlmann A. Hip joint loading during walking and running, measured in two patients. Journal of biomechanics. 1993;26(8):969-90.

509. Davy D, Kotzar G, Brown R, Heiple K*, et al.* Telemetric force measurements across the hip after total arthroplasty. The Journal of Bone & Joint Surgery. 1988;70(1):45-50.

510. Duda GN, Heller M, Albinger J, Schulz O*, et al.* Influence of muscle forces on femoral strain distribution. Journal of biomechanics. 1998;31(9):841-6.

511. Nemchand JL, Anson AW, Jones BJ, Wilson D*, et al.* D-4 Biomechanical Fracture Healing Simulation for Smart Implants Using Telemetry. Journal of Biomechanics. 2010;43, Supplement 1:S69-S70.

512. Brumback R, Toal T, Murphy-Zane M, Novak V*, et al.* Immediate Weight-Bearing After Treatment of a Comminuted Fracture of the Femoral Shaft with a Statically Locked Intramedullary Nail*. The Journal of Bone & Joint Surgery. 1999;81(11):1538-44.

513. Jones M, Parry M, Whitehouse M, Mitchell S. Radiologic Outcome and Patient-Reported Function After Intramedullary Nailing: A Comparison of the Retropatellar and Infrapatellar Approach. Journal of Orthopaedic Trauma. 2014;28(5):256-62.

514. Kuhn S, Hansen M, Rommers P. Extending the Indications of Intramedullary Nailing with the Expert Tibial Nail®. Acta chirurgiae orthopaedicae et traumatologiae Cechoslovaca. 2008;75(2):77.

515. Lovald S, Kurtz SM. Applications of Polyetheretherketone in trauma, arthroscopy, and cranial defect repair. PEEK Biomaterials Handbook. 2011:243.

516. Hak DJ, Mauffrey C, Seligson D, Lindeque B. Use of Carbon-Fiber-Reinforced Composite Implants in Orthopedic Surgery. Orthopedics (Online). 2014;37(12):825.

517. Weis JA, Miga MI, Granero-Molto F, Spagnoli A. A finite element inverse analysis to assess functional improvement during the fracture healing process. J Biomech. 2010;43(3):557-62.

518. Lacroix D, Prendergast P. A mechano-regulation model for tissue differentiation during fracture healing: analysis of gap size and loading. Journal of biomechanics. 2002;35(9):1163-71.

519. Mishra S. An Idealised Biphasic Poroelastic Finite Element Model of a Tibial Fracture. In: Jones PS, editor. Advanced Methods for Practical Applications in Fluid Mechanics2012.

520. Vetter A, Liu Y, Witt F, Manjubala I*, et al.* The mechanical heterogeneity of the hard callus influences local tissue strains during bone healing: a finite element study based on sheep experiments. Journal of biomechanics. 2011;44(3):517-23.

521. Shefelbine SJ, Simon U, Claes L, Gold A*, et al.* Prediction of fracture callus mechanical properties using micro-CT images and voxel-based finite element analysis. Bone. 2005;36(3):480-8.

522. Shefelbine SJ, Augat P, Claes L, Simon U. Trabecular bone fracture healing simulation with finite element analysis and fuzzy logic. Journal of biomechanics. 2005;38(12):2440-50.

523. Isaksson H, van Donkelaar CC, Huiskes R, Yao J*, et al.* Determining the most important cellular characteristics for fracture healing using design of experiments methods. Journal of theoretical biology. 2008;255(1):26-39.

524. Isaksson H, van Donkelaar CC, Huiskes R, Ito K. A mechano-regulatory bone-healing model incorporating cell-phenotype specific activity. Journal of theoretical biology. 2008;252(2):230-46.

525. Geris L, Gerisch A, Maes C, Carmeliet G*, et al.* Mathematical modeling of fracture healing in mice: comparison between experimental data and numerical simulation results. Medical and Biological Engineering and Computing. 2006;44(4):280-9.

526. Isaksson H, van Donkelaar CC, Huiskes R, Ito K. Corroboration of mechanoregulatory algorithms for tissue differentiation during fracture healing: comparison with in vivo results. Journal of Orthopaedic Research. 2006;24(5):898-907.

527. Andreykiv A, Van Keulen F, Prendergast P. Simulation of fracture healing incorporating mechanoregulation of tissue differentiation and dispersal/proliferation of cells. Biomechanics and modeling in mechanobiology. 2008;7(6):443-61.

528. Lin J, Lin SJ, Chen PQ, Yang SH. Stress analysis of the distal locking screws for femoral interlocking nailing. Journal of Orthopaedic Research. 2001;19(1):57-63.

529. Shih K, Hsu W, Fan C, Hou S. Stress analysis of locking screws for femoral antegrade and retrograde nailing constructs. Journal of the Chinese Institute of Engineers. 2005;28(5):837-48.

530. Wolinsky PR, McCarty E, Shyr Y, Johnson K. Reamed Intramedullary Nailing of the Femur: 551 Cases. Journal of Trauma and Acute Care Surgery. 1999;46(3):392-9.

531. Sojbjerg J, Eiskjaer S, Moller-Larsen F. Locked nailing of comminuted and unstable fractures of the femur. Journal of Bone & Joint Surgery, British Volume. 1990;72(1):23-5.

532. Roach MD, Williamson RS, Zardiackas LD. Comparison of the Corrosion Fatigue Characteristics of CPTi-Grade 4, Ti-6A1-4V ELI, Ti-6A1-7 Nb, and Ti-15 Mo. Journal of Testing and Evaluation. 2005;2(7).

533. Cózar-Bernal M, Rabasco A, González-Rodríguez M. Development and validation of a high performance chromatographic method for determining sumatriptan in niosomes. Journal of pharmaceutical and biomedical analysis. 2013;72:251-60.

534. Lyu S, TeWu W, Hou C, Hsieh W. Study of cryopreservation of articular chondrocytes using the Taguchi method. Cryobiology. 2010;60(2):165-76.

535. Sidambe A, Figueroa I, Hamilton H, Todd I. Metal injection moulding of CP-Ti components for biomedical applications. Journal of Materials Processing Technology. 2012;212(7):1591-7.

536. Claes LE, Heigele CA. Magnitudes of local stress and strain along bony surfaces predict the course and type of fracture healing. J Biomech. 1999;32(3):255-66.

537. Sarmiento A, Latta, I. I. Functional Fracture Bracing. Tibia, Humerus and Ulna. Berlin: Springer; 1995.

538. Eastaugh-Waring SJ, Joslin CC, Hardy JR, Cunningham JL. Quantification of fracture healing from radiographs using the maximum callus index. Clin Orthop Relat Res. 2009;467(8):1986-91.

539. Animating Plots: Dassault Systèmes; 2012. Available from: http://help.solidworks.com/2012/English/SolidWorks/cworks/idh_plan.htm?format=P&value=1.

540. Wiss DA, Fleming CH, Matta JM, Clark D. Comminuted and rotationally unstable fractures of the femur treated with an interlocking nail. Clinical orthopaedics and related research. 1986;212:35-47.

541. Tarr RR, Wiss DA. The mechanics and biology of intramedullary fracture fixation. Clinical orthopaedics and related research. 1986;212:10-7.

542. Roberts GL, Pallister I. Finite element analysis in trauma & orthopaedics – an introduction to clinically relevant simulation & its limitations. Orthopaedics and Trauma. 2012;26(6):410-6.

543. Seide K, Aljudaibi M, Weinrich N, Kowald B, *et al.* Telemetric assessment of bone healing with an instrumented internal fixator: A preliminary study. Journal of Bone & Joint Surgery, British Volume. 2012;94-B(3):398-404.

544. Moss C, Weinrich N, Sass W, Mueller J, editors. Integration of a telemetric system within an intramedullary nail for monitoring of the fracture healing progress. Applied Sciences in Biomedical and Communication Technologies (ISABEL), 2010 3rd International Symposium on; 2010 7-10 Nov. 2010.

545. Moiz F, Kumar S, Leon-Salas WD, Johnson M. An embedded multichannel telemetry unit for bone strain monitoring. EURASIP Journal on Embedded systems. 2013;2013(1):1-16.

546. Baker R. Journal of NeuroEngineering and Rehabilitation. Journal of NeuroEngineering and Rehabilitation2006. 2005;3(4).

547. Tadano S, Takeda R, Miyagawa H. Three dimensional gait analysis using wearable acceleration and gyro sensors based on quaternion calculations. Sensors. 2013;13(7):9321-43.

548. Wall-Scheffler CM, Chumanov E, Steudel-Numbers K, Heiderscheit B. Electromyography activity across gait and incline: The impact of muscular activity on human morphology. American journal of physical anthropology. 2010;143(4):601-11.

549. Franz JR, Kram R. The effects of grade and speed on leg muscle activations during walking. Gait & posture. 2012;35(1):143-7.

550. Slaughter S, Butler P, Capozzella H, Nguyen A, *et al.* The comparative gait effects of select walking surfaces using kinetic and EMG analyses. Human Movement. 2012;13(3):198-203.

551. Robertson A. Muscle Activity During Gait Transitions. Available from: asbweb.org/conferences/2011/pdf/32.pdf.

552. Galajdová A, Šimšík D, Madarász L, editors. Possibilities of gait parameters prediction from EMG data by Neural Networks. Proceedings of the 3rd International Symposium of Hungarian Researchers; 2002.

553. GAP Nail: Pega Medical; 2015. Available from: http://www.pegamedical.com/en/products/Gap-Nail-the-endo-exo-medullary-system.html.

554. PediNail™: OrthoPediatrics; 2015. Available from: http://www.orthopediatrics.co.uk/styled-2/styled-3/.

555. The Pediatric Proximal Femoral Nail, PediFIN®: Hexagon Ortho; 2015. Available from: http://www.hexagonortho.com/products/intramedullary-rods/pedifin-pediatric-proximal-femoral-nail/.

556. PLN: Biomet; 2015. Available from: http://www.biomet.co.uk/medhome-uk/trauma/paediatric-applications/pln-nail.

Appendix A. Presentations and Publications

A.1. Presentations

1. Angadi DS, Shepherd DE, Vadivelu R, Barrett T 'Adolescent Femoral Fracture Fixation with Lateral Trochanteric Entry Rigid Helical Intramedullary Nail - A Biomechanical Evaluation'. XXV Congress of the International Society of Biomechanics in Glasgow, UK, July 2015.
2. Angadi DS, Shepherd DE, Vadivelu R, Barrett T. 'Rigid Helical Intramedullary Nail Fixation of Paediatric Femur Fractures - A Biomechanical Evaluation'. 16th European Federation of National Association of Orthopaedic and Trauma Congress (EFORT), Czech Republic, May 2015.
3. Angadi DS, Shepherd DE, Vadivelu R, Barrett T 'Development and validation of a paediatric femur finite element model using orthogonal digital radiographs'. 7th World Congress of Biomechanics, USA, July 2014.
4. Angadi DS, Shepherd DET, Vadivelu R, Barrett T 'Orthogonal digital radiographs - a novel template for paediatric femur finite element model development'. 5th International Conference on Biomedical Engineering, Vietnam, June 2014.
5. Angadi DS, Shepherd DET, Vadivelu R, Barrett T 'Development and validation of a simplified paediatric femur finite element model using digital radiographs'. 21st SICOT Trainees Meeting, UK, June 2014.
6. Angadi DS, Shepherd DET, Vadivelu R, Barrett T 'Biomechanical Evaluation of Rigid Helical Intramedullary Nail Fixation Using Paediatric Femur Finite Element Model'. Annual Mechanical Engineering Symposium, University of Birmingham, May 2014

A.2. Publications

1. Angadi DS, Shepherd DET, Vadivelu R, Barrett T. Rigid intramedullary nail fixation of femoral fractures in adolescents: what evidence is available? J Orthopaed Traumatol (2014) 2013 15:147-153.
2. Angadi DS, Shepherd DET, Vadivelu R, Barrett T. 'Orthogonal digital radiographs - a novel template for paediatric femur finite element model development'. International Federation for Medical and Biological Engineering (IFMBE) Proceedings vol-46, 175-178.
3. Angadi DS, Shepherd DET, Vadivelu R, Barrett T. 'Biomechanical Evaluation of Rigid Helical Intramedullary Nail Fixation Using Paediatric Femur Finite Element Model' (manuscript under preparation)

Appendix B. Test Jigs And Alignment Molds

Custom-made test jigs were designed and fabricated based on the dimensions of the small composite femur in the initial phase of the study.

B.1. Axial compression

The test jig comprised of a base and top unit. The circular aluminium base had a flat surface to place the lower end of the composite femur and secured in place circumferentially by bolts during loading tests (Figure B-1). The top unit had a polymer block manufactured from the polymer Fullcure 720 using an Eden 250 3D Printing System (Objet GmbH, Rheinmünster, Germany). It contained a spherical cavity of radius 27 mm in which Polymethylmethacrylate (PMMA, Palacos®, Heuraeus, UK) was initially molded to mimic the acetabular socket of the hip joint (Figure B-2). This ensured an anatomical fit of the femoral head in the socket for all the femur specimens. The block was housed in a steel frame during testing with the Instron machine whereas it was secured in place by screws for the MTS machine tests. The composite femurs were aligned using customised split molds cast from PMMA. PMMA was selected as it is a viscoelastic material whose material properties have been extensively described (302, 303). The Palacos® package consists of a liquid monomer along with an activation agent and a polymer powder. The two are combined using vacuum mixing to avoid air voids and achieve uniform consistency. The polymerisation process is an exothermic reaction. Hence a layer of metal foil was used around the composite femur to act as a heat shield. The split molds were fabricated such that it allowed the axial load force to be transmitted along the mechanical axis of the femur (Figure B-3, Figure 4-11). As all the composite femur specimens had similar geometry and dimensions, the split molds also ensured a repeatable test setup.

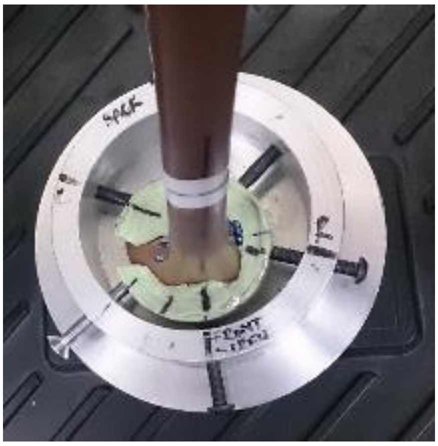

Figure B-1 Base unit with PMMA mold and screws securing distal end of femur

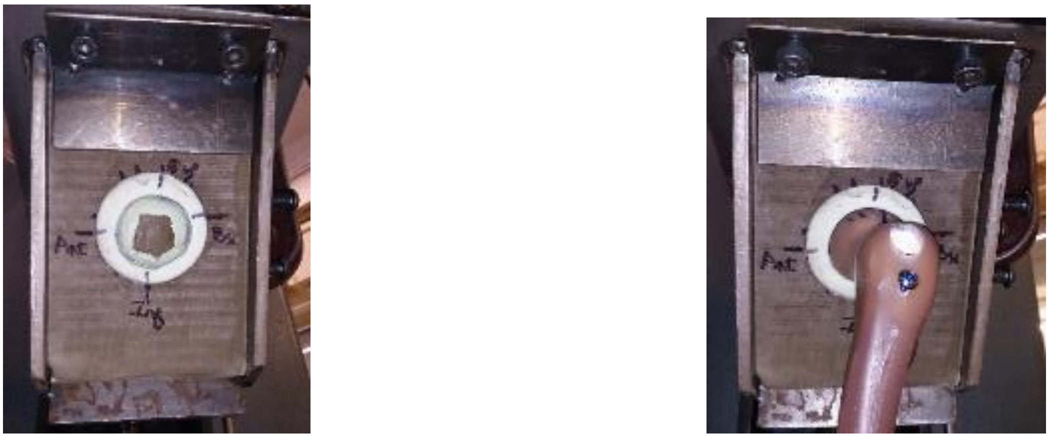

Figure B-2 Top unit (left-polymer block with PMMA in cavity replicating acetabular socket, right- anatomical fit of femoral head in socket)

Figure B-3 PMMA split mold at base aligning the femur along the mechanical axis

B.2. Four-point bending

The test jig comprised of a base and a top unit. The dimensions for the test jig were adopted based on the current ASTM guidelines (301). The base had the distal support set perpendicular and proximal support at 60° to the long axis to provide a stable support for the composite femur. The top unit for the Instron machine tests had a stainless steel plate with two rollers set perpendicular to the long axis of the plate with a gap of 70 mm (Figure B-4). The top unit for the MTS machine tests comprised of a solid aluminium rod with a centering joint. The loading points were welded onto the rod and were 70 mm apart (Figure B-5).

Figure B-4 Four-point bending test setup in the Instron machine

Figure B-5 Four-point bending test setup in the MTS machine showing top and base units

B.3. Torsion

Version 1

The initial test jig consisted of a stainless steel base plate of 500 mm length and 200 mm width. At the proximal end a rotating socket was mounted with a lever arm of 150 mm from the long axis. At the distal end a tapered metal pot allowed the femoral condlyes to be held securely. To minimise toggle during loading, split molds were cast from PMMA similar to the techinique described in axial test. The proximal molds extended from the head to just below the lesser trochnater of the femur. The distal mould encased the condyles and rose above the metaphyseal flares of the femur (Figure B-6).

Figure B-6 Torsion test jig version 1 (left-end on view, right-top view)

Following initial tests it was noted that several factors from this jig contributed towards inconsistent results. A closer analysis revealed some of the factors such as alignment of the femur, slippage in the PMMA split molds during loading, inadequate depth of the proximal cup designed to capture the femoral head and weight of the metal bar used as a lever arm. Hence this jig was abandoned and version 2 was fabricated to specifically overcome these limitations.

Version 2

In this jig, two aluminium cylindrical units were aligned to the mid-axis of a steel base plate and mounted to allow free rotation of the composite bone. The proximal unit was attached to an aluminium lever arm connected to a ball-bearing joint to allow rotation along the mid-axis. The distal unit was fixed onto the steel plate such that the open sections of the two cylindrical units faced each other. The mechanical axis of the composite femur was aligned to the mid-axis of the cylindrical units using PMMA split molds. The proximal mold completely encased the femoral head, greater and lesser trochanters and extended upto 20 mm below the lesser trochanter. During casting of the PPMA mold, the femoral head was aligned to the center of the proximal cylindrical unit and the mechanical axis of the femur was coincident with the axis of rotation of the jig (Figure B-7 and Figure B-8).

Figure B-7 Femoral head aligned to centre of the proximal cylindrical unit during casting of PMMA mold

 

Figure B-8 Alignment of femur during casting of PMMA molds to ensure mechanical axis of femur was coincident with axis of rotation of the jig

The distal mold completely encased the medial and lateral femoral condyles and extended up to 20 mm above the metaphyseal flare. The split molds were secured into the cylindrical units using circumferential grub screws. As the calibrated weights were attached to the lever arm torque was applied to the proximal aspect of the femur which then rotated along the mechanical axis. The degree of rotation was measured using a digital inclinometer (Digi-Pas DWL-130, resolution of 0.05° with accuracy 0.05° at 0° & 90°) mounted on the lever arm (Figure 4-13).

Engineering drawings of the axial (Figure B-9, Figure B-10 and Figure B-11), four-point bending (Figure B-12, Figure B-13 and Figure B-14) and torsion test jigs (Figure B-15) are shown below.

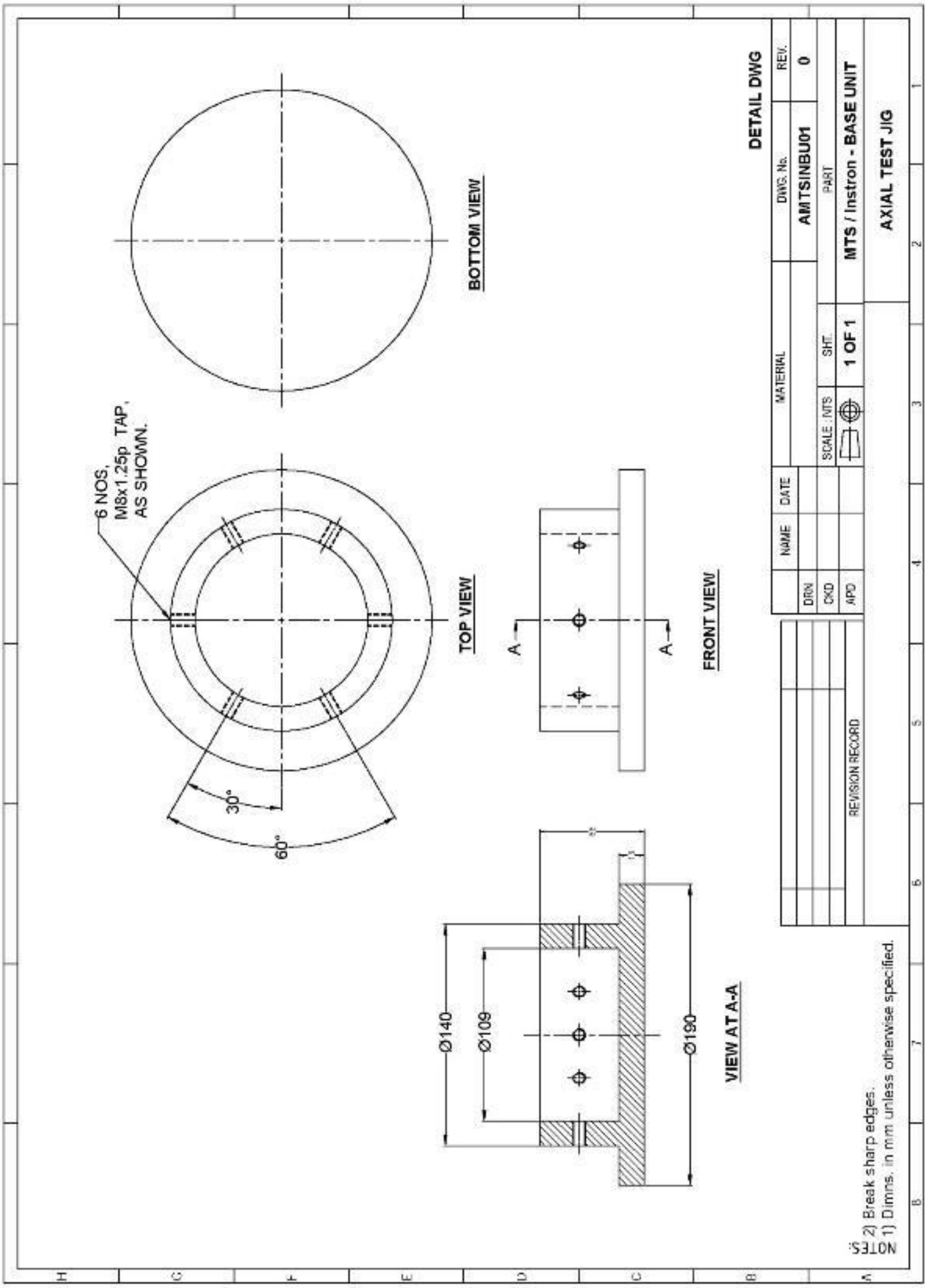

Figure B-9 Engineering drawing of axial compression test base unit

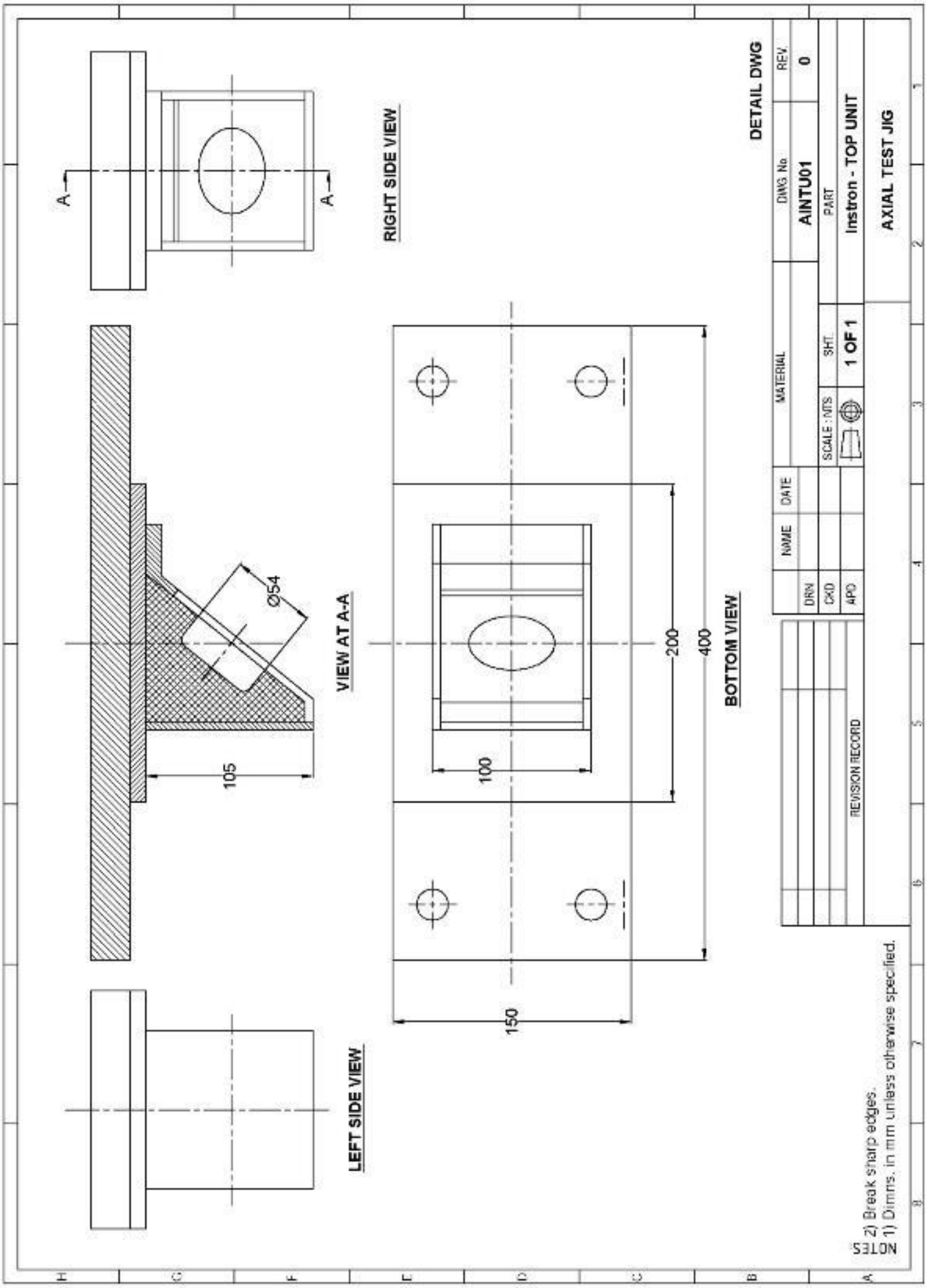

Figure B-10 Engineering drawing of axial compression test top unit used with Instron machine

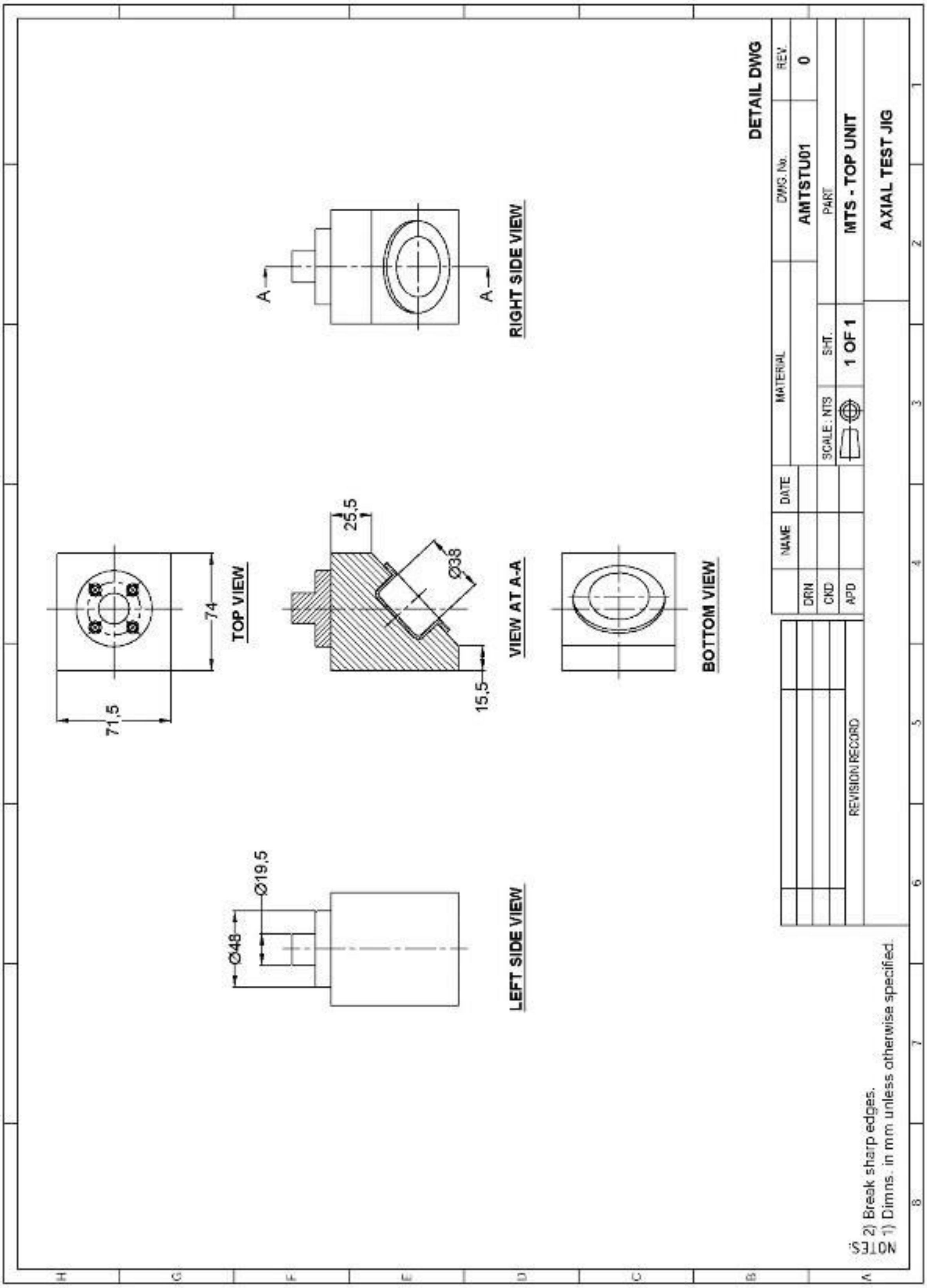

Figure B-11 Engineering drawing of axial compression test top unit used with MTS machine

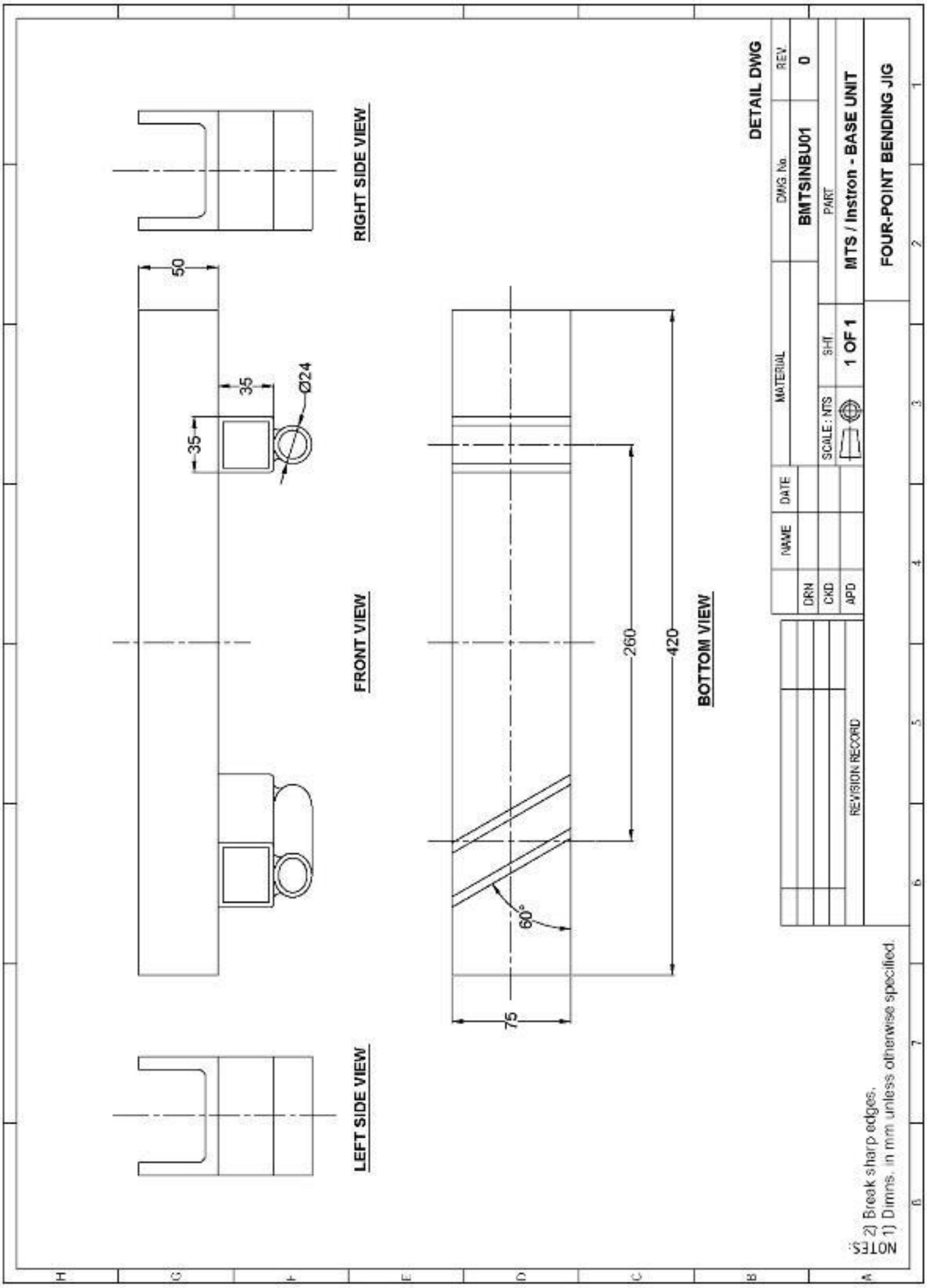

Figure B-12 Engineering drawing of four-point bending test base unit

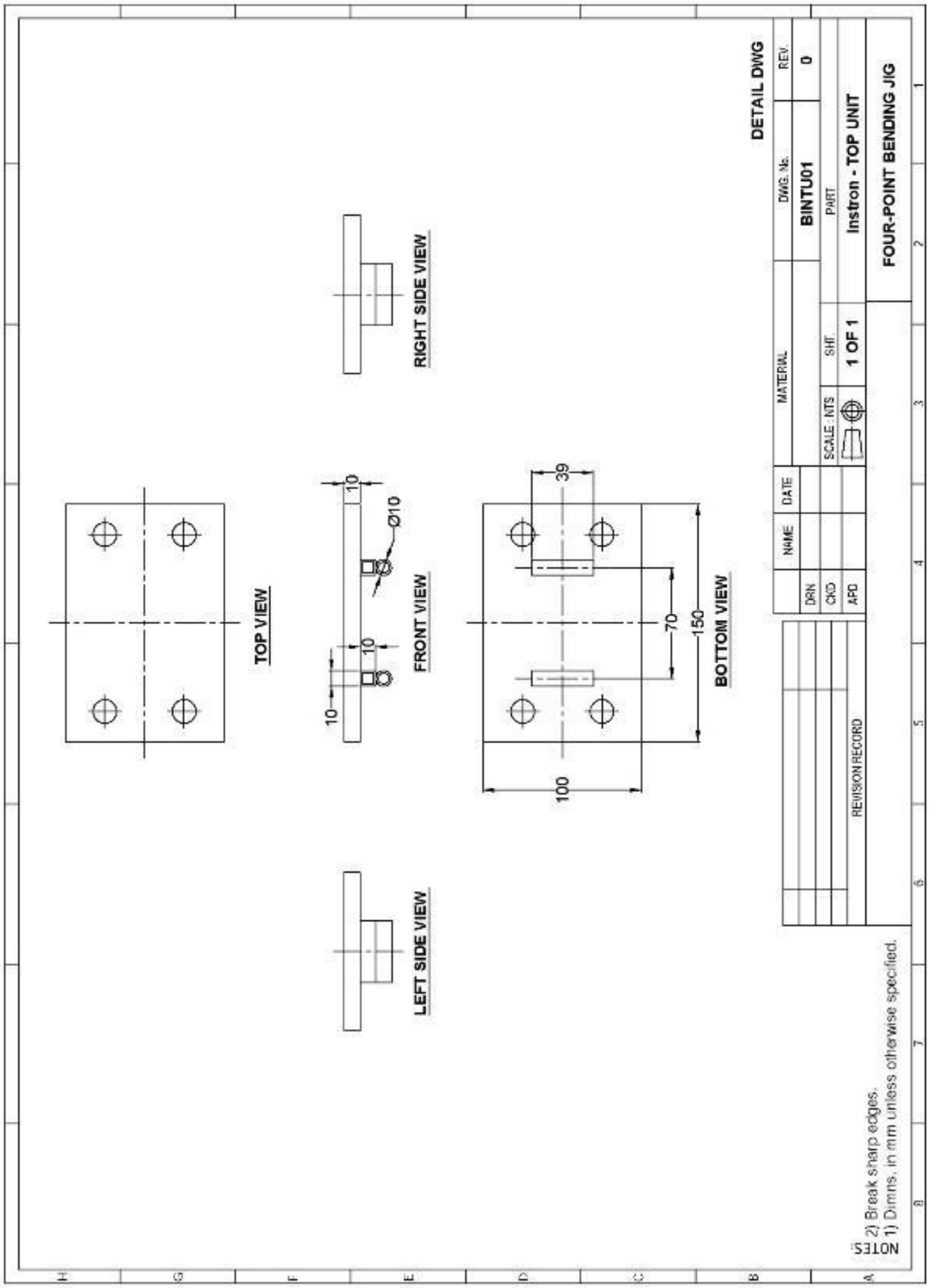

Figure B-13 Engineering drawing of four-point bending test top unit used with Instron machine

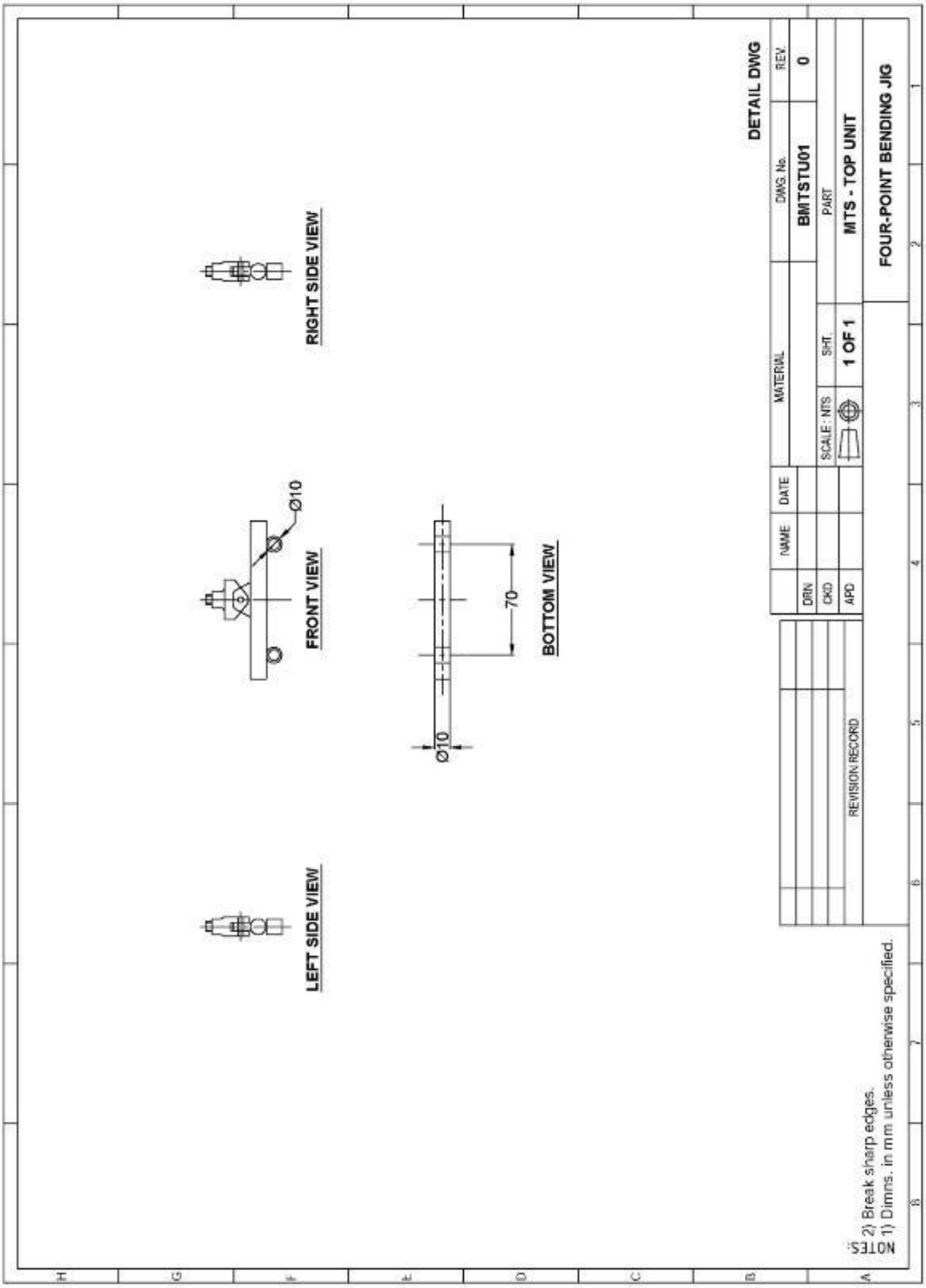

Figure B-14 Engineering drawing of four-point bending test top unit used with MTS machine

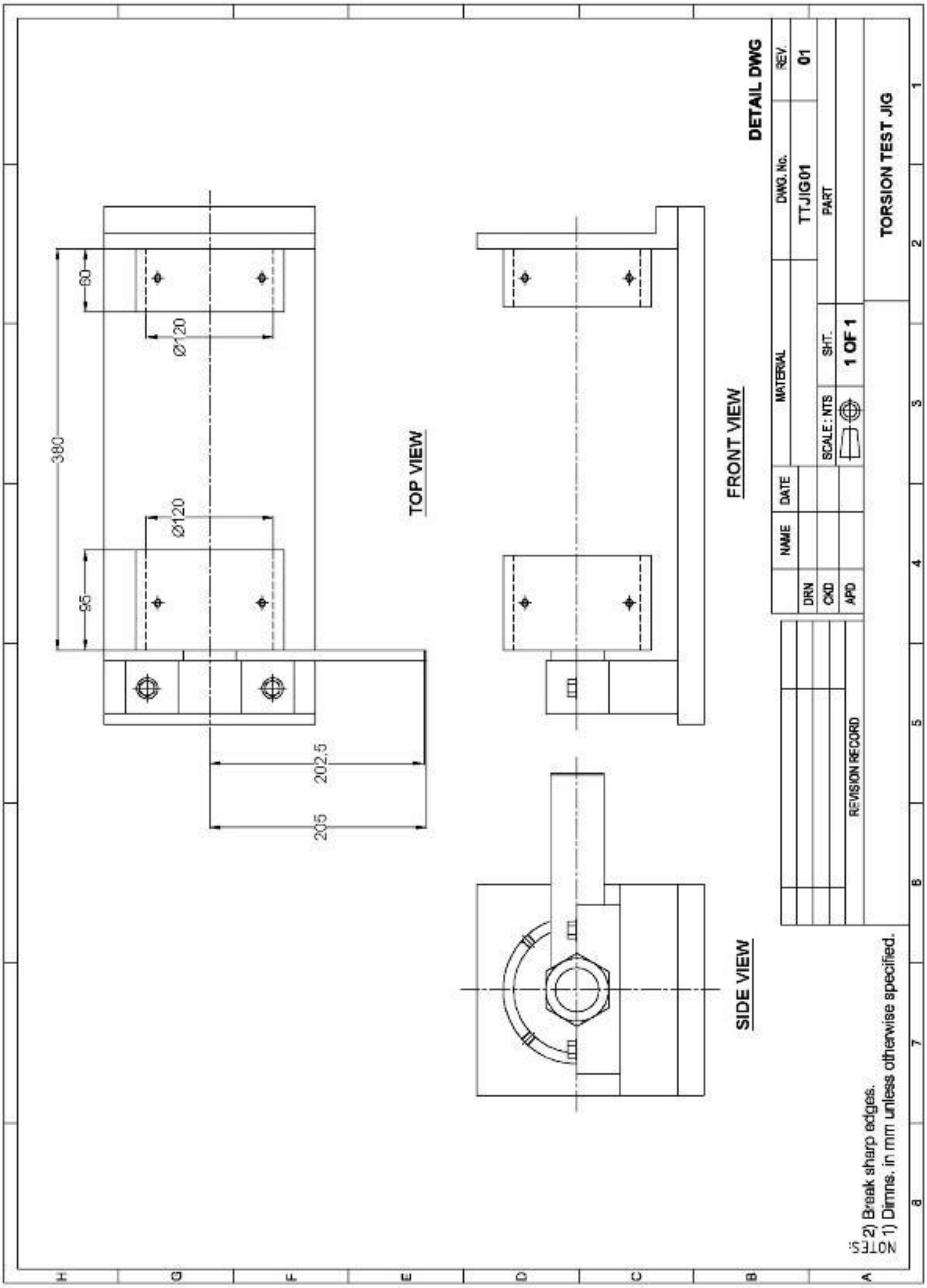

Figure B-15 Engineering drawing of torsion test jig

Appendix C. Summary of Data

Table C-1 Details of FEA model iterations tested during simulated axial compression test

DOF – degrees of freedom, Mesh quality = percentage of elements with aspect ratio < 3

FEA Model / Iteration	Maximum Element Size (mm)	Total Nodes	Total Elements	DOF	Mesh quality	U_X (mm)	Solution Time (s)
Transverse							
1	10.237	33664	18240	99993	91.10	0.041	34
2	5.118	62739	36816	182805	95.40	0.045	70
3	2.559	71392	42747	208752	96.10	0.046	82
4	1.279	122991	78973	363561	97.70	0.049	90
5	0.639	379117	261127	783381	99.20	0.049	304
6	0.500	567488	395773	1702464	99.50	0.049	414
Comminuted							
1	10.234	34232	18584	101775	90.50	0.042	44
2	5.117	71274	42271	207699	95.70	0.044	69
3	2.559	79762	48055	233163	96.10	0.048	81
4	1.279	128583	82279	379626	97.70	0.050	94
5	0.639	367154	251518	1095339	98.10	0.050	334
6	0.500	540929	375322	1622787	99.20	0.050	419
Segmental							
1	10.236	34464	18689	102519	90.60	0.042	41
2	5.118	65073	38377	189531	95.70	0.049	68
3	2.559	71943	43085	210075	95.80	0.050	78
4	1.279	121774	77974	359568	97.70	0.052	91
5	0.639	360775	247505	1076349	99.20	0.053	312
6	0.500	549435	382497	1648305	99.40	0.053	428
7	0.400	737491	517808	2212473	99.60	0.053	518
Healed							
1	10.242	33238	18069	98634	91.30	0.082	42
2	5.123	81130	48143	237849	97.60	0.083	67
3	2.561	89332	53684	262647	97.70	0.083	81
4	1.280	144771	92572	428856	98.60	0.083	126
5	0.640	414358	284175	1243074	99.50	0.083	298

Table C-2 Details of FEA model iterations tested during simulated four-point bending test

DOF – degrees of freedom, Mesh quality = percentage of elements with aspect ratio < 3

FEA Model / Iteration	Maximum Element Size (mm)	Total Nodes	Total Elements	DOF	Mesh quality	U_Y (mm)	Solution Time (s)
Transverse							
1	10.0000	34308	18561	102924	90.80	0.079	27
2	5.0000	41301	22933	123903	94.00	0.086	44
3	2.5000	47778	26806	143334	95.00	0.089	53
4	1.2500	77269	44801	231807	96.80	0.090	65
5	0.6250	145494	86565	436482	96.80	0.090	98
6	0.5000	237474	142328	712422	97.40	0.090	140
Comminuted							
1	10.2344	34764	18799	104292	90.40	0.084	37
2	5.1175	41700	23125	125100	94.00	0.092	55
3	2.5587	48593	27350	145779	94.70	0.092	65
4	1.2794	79549	46445	238647	96.60	0.093	84
5	0.6397	205736	124919	617208	97.50	0.094	102
6	0.5117	299444	184386	898332	97.90	0.094	160
7	0.4094	426799	270601	1280397	96.90	0.094	314
Segmental							
1	10.000	34133	18491	102399	90.50	0.081	37
2	5.000	50045	28242	150135	94.40	0.093	62
3	2.500	77108	44541	231324	94.50	0.097	91
4	1.250	143053	84235	429159	95.10	0.100	165
5	0.625	277680	165865	833040	96.00	0.101	272
6	0.500	337938	203328	1013814	96.50	0.101	380
7	0.400	429450	264538	1288350	96.90	0.101	434
Healed							
1	10.000	33069	17942	99207	91.70	0.085	18
2	5.000	34106	18639	102318	91.80	0.086	36
3	2.500	39558	21960	118674	93.60	0.086	41
4	1.250	55638	31648	166914	94.20	0.088	52
5	0.625	105961	61449	317883	93.50	0.091	69
6	0.500	156912	91373	470736	94.60	0.093	164
7	0.400	201146	117293	603438	96.80	0.093	196
8	0.3000	284978	167669	854934	96.80	0.093	294

Table C-3 Details of FEA model iterations tested during simulated torsion (internal rotation)

DOF – degrees of freedom, Mesh quality = percentage of elements with aspect ratio < 3

FEA Model / Iteration	Maximum Element Size (mm)	Total Nodes	Total Elements	DOF	Mesh quality	ϕ_{IR} (deg)	Solution Time (s)
Transverse							
1	10.233	34129	18578	99570	90.90	0.096	45
2	5.117	63769	38413	188490	95.40	0.101	47
3	2.558	68452	41137	202539	95.60	0.104	50
4	1.279	87061	51539	258366	96.00	0.104	54
5	0.639	162896	94518	488688	98.20	0.104	122
Comminuted							
1	10.2336	35168	19223	102264	91.90	0.099	46
2	5.1171	67359	40517	198837	94.50	0.102	55
3	2.5585	68720	41226	202920	95.60	0.104	60
4	1.2793	105885	63888	275265	97.20	0.105	63
5	0.6396	221659	134463	499374	98.00	0.105	196
6	0.5000	300243	180599	886287	98.60	0.105	235
Segmental							
1	10.2336	33938	18417	98670	90.20	0.102	45
2	5.1171	63194	37988	186450	92.50	0.104	50
3	2.5585	66541	39804	195507	93.60	0.107	58
4	1.2793	83659	49396	247845	98.20	0.107	64
5	0.6396	112397	61437	326837	99.00	0.107	189
Healed							
1	10.2465	34076	18600	97845	92.10	0.053	44
2	5.1235	63723	38438	186822	95.80	0.054	76
3	2.5617	66199	39665	194205	97.00	0.056	91
4	1.2809	86580	51310	255645	97.40	0.056	105
5	0.6404	164715	96269	494145	98.70	0.056	312

Table C-4 Details of FEA model iterations tested during simulated torsion (external rotation)

DOF – degrees of freedom, Mesh quality = percentage of elements with aspect ratio < 3

FEA Model / Iteration	Maximum Element Size (mm)	Total Nodes	Total Elements	DOF	Mesh quality	ϕ_{ER} (deg)	Solution Time (s)
Transverse							
1	10.2330	34129	18578	99570	90.90	0.096	45
2	5.1170	63769	38413	188490	95.40	0.101	48
3	2.5580	68452	41137	202539	95.60	0.104	52
4	1.2790	87061	51539	258366	96.00	0.104	58
5	0.6390	162896	94518	488688	98.20	0.104	131
Comminuted							
1	10.2336	35168	19223	102264	91.90	0.099	47
2	5.1171	67359	40517	198837	94.50	0.102	56
3	2.5585	68720	41226	202920	95.60	0.104	61
4	1.2793	105885	63888	275265	97.20	0.105	65
5	0.6396	221659	134463	499374	98.00	0.105	203
6	0.5000	300243	180599	886287	98.60	0.105	240
Segmental							
1	10.2336	33938	18417	98670	90.20	0.102	45
2	5.1171	63194	37988	186450	92.50	0.104	50
3	2.5585	66541	39804	195507	93.60	0.107	59
4	1.2793	83659	49396	247845	98.20	0.107	65
5	0.6396	112397	61437	326837	99.00	0.107	190
Healed							
1	10.2465	34076	18600	97845	92.10	0.053	45
2	5.1235	63723	38438	186822	95.80	0.054	78
3	2.5617	66199	39665	194205	97.00	0.056	92
4	1.2809	86580	51310	255645	97.40	0.056	106
5	0.6404	164715	96269	494145	98.70	0.056	314

Appendix D. Surgical Technique

Preoperative assessment and planning is undertaken on all patients prior to surgery with AP and lateral view radiographs of the femur.

The patient is appropriately positioned on a fracture table and the fracture is adequately reduced. The greater trochanter is exposed through a surgical incision and the entry point located lateral to the greater trochanter just above the piriform fossa is identified. Subsequently the guide wire is inserted at the entry point and the proximal femur is drilled upto depth of 75 mm to open the cortex starting with 8.5 mm reamer and ending with 13.0 mm reamer. Serial reaming of medullary canal is undertaken beginning with 8.5 mm reamer upto 9.5 mm in 0.5 mm increments. ALFN of appropriate size identified with surgical templates is inserted over the guide wire. Proximal and distal interlocking screws are inserted under image intensifier control.

Further details of surgical technique and instrumentation set of ALFN is available at http://emea.depuysynthes.com/hcp/trauma/products/qs/expert-adolescent-lateral-femora